ISBN 978-82-326-2088-3 (printed version)
ISBN 978-82-326-2089-0 (electronic version)
ISSN 1503-8181

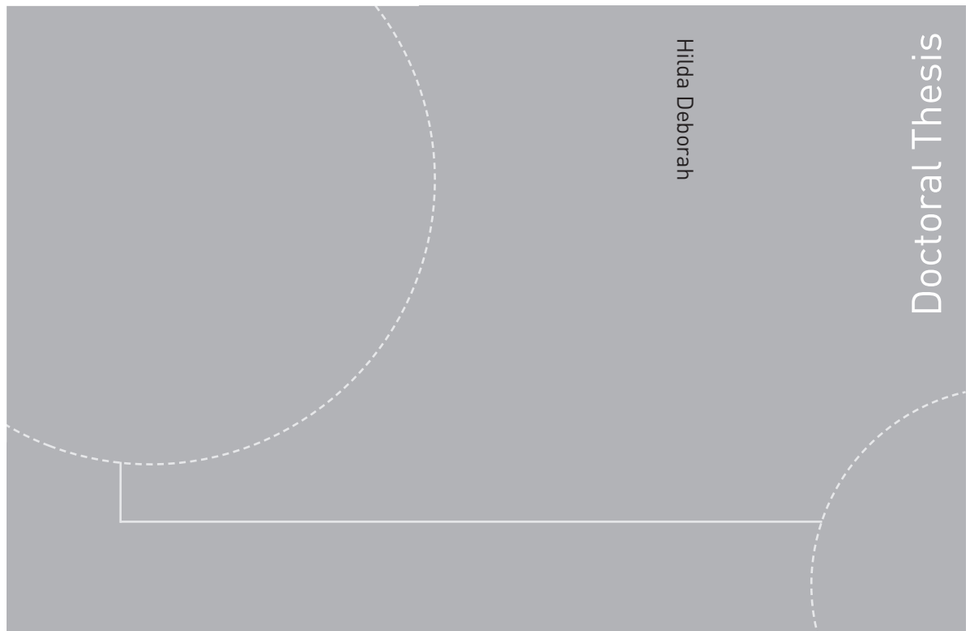

Doctoral theses at NTNU, 2016:372

Hilda Deborah

Towards Spectral Mathematical Morphology

NTNU
Norwegian University of Science and Technology

Doctoral theses at NTNU, 2016:372

NTNU

NTNU
Norwegian University of Science and Technology
Faculty of Computer Science and Media Technology

NTNU
Norwegian University of Science and Technology

Université de Poitiers

Hilda Deborah

Towards Spectral Mathematical Morphology

Thesis for the degree of Philosophiae Doctor

Gjøvik, November 2016

Norwegian University of Science and Technology
Faculty of Computer Science and Media Technology

University of Poitiers
Faculty of Fundamental and Applied Sciences
Doctoral School of Science and Engineering for Information

NTNU
Norwegian University of
Science and Technology

1431
Université
de Poitiers

Thesis for the degree of Philosophiae Doctor

Joint degree between:

Norwegian University of Science and Technology,
Faculty of Computer Science and Media Technology

Université de Poitiers
Faculté de Sciences Fondamentales et Appliquées
Ecole Doctorale Sciences et Ingénierie pour
l'Information (S2I)

ISBN 978-82-326-2088-3 (printed version)
ISBN 978-82-326-2089-0 (electronic version)
ISSN 1503-8181

Doctoral theses at NTNU, 2016:372

Printed by Skipnes Kommunikasjon as

Abstract

Providing not only spatial information but also spectral measures as a function of wavelength, hyperspectral imaging boasts a much greater accuracy than traditional grayscale and color imaging. For this capability, hyperspectral imaging has been employed increasingly for various applications such as quality control and inspection of materials. However, to fully exploit its potential, it is important to be able to validly process the spectral image data as a measure. This induces the need of metrology where accuracy, uncertainty, and bias are addressed and managed at every level of the image processing.

Aiming at developing a metrological image processing framework for spectral data, in this work we selected a nonlinear approach using the established mathematical morphology framework. We have extended this framework to the spectral domain by means of a distance-based ordering relation. Novel spectral distance function and spectral ordering relations are proposed, as well as new spectral image analysis tools using histograms of spectral differences.

To ensure the validity of the new spectral mathematical morphology framework, rigorous theoretical validation and metrological assessment are carried out at each stage of the development. Thus, new protocols for quality assessment of spectral image processing tools are also developed. These protocols consist of artificial datasets to validate the theoretical and metrological requirements, image datasets of known characteristics to assess the robustness and stability, and datasets from real cases to prove the usefulness of the framework in an applicative context. The chosen application tasks are within the cultural heritage domain, where the analyzed images include pigments and paintings.

Translations of The Abstract

The following translations of the abstract have been kindly provided by the supervisors, Jon Hardeberg (Norwegian translation) and Noël Richard (French translation).

Sammendrag (Norwegian translation) Hyperspektral avbildning muliggjør mye mer nøyaktige målinger enn tradisjonelle gråskala og fargebilder, gjennom både høy romlig og spektral oppløsning (funksjon av bølgelengde). På grunn av dette har hyperspektral avbildning blitt anvendt i økende grad ulike applikasjoner som kvalitetskontroll og inspeksjon av materialer. Men for å fullt ut utnytte sitt potensiale, er det viktig å være i stand til å behandle spektrale bildedata som målinger på en gyldig måte. Dette induserer behovet for metrologi, der nøyaktighet, usikkerhet og skjevhet blir adressert og kontrollert på alle nivå av bildebehandlingen.

Med sikte på å utvikle et metrologisk rammeverk for spektral bildebehandling valgte vi en ikke-lineær metodikk basert på det etablerte matematisk morfologi-rammeverket. Vi har utvidet dette rammeverket til det spektrale domenet ved hjelp av en avstandsbasert sorteringsrelasjon. En ny spektral avstandsfunksjon og nye spektrale sorteringsrelasjoner ble foreslått, samt nye verktøy for spektral bildeanalyse basert på histogrammer av spektrale forskjeller.

For å sikre gyldigheten av det nye spektrale rammeverket for matematisk morfologi, har vi utført en grundig teoretisk validering og metrologisk vurde-

Résumé (French translation) En fournissant en plus de l'information spatiale une mesure spectrale en fonction des longueurs d'ondes, l'imagerie hyperspectrale s'enorgueillit d'atteindre une précision bien plus importante que l'imagerie en niveaux de gris et couleur. Grace à cela, elle a été utilisée en contrôle qualité, inspection de matériaux, etc. Cependant, pour exploiter pleinement ce potentiel, il est important de traiter la donnée spectrale comme une mesure, d'où la nécessité de la métrologie, pour laquelle exactitude, incertitude et biais doivent être maitrisés à tous les niveaux de traitement.

Face à cet objectif, nous avons choisi de développer une approche non-linéaire, basée sur la morphologie mathématique et de l'étendre au domaine spectral par une relation d'ordre spectral basée sur les fonctions de distance. Une nouvelle fonction de distance spectrale et une nouvelle relation d'ordonnancement sont ainsi proposées. Un nouvel outil d'analyse des données spectrales a été proposé à partir d'histogrames de différences.

Afin d'assurer la validité des opérateurs, une approche théorique rigoureuse et une évaluation métrologique ont été mises en œuvre à chaque étage de dé-

ring på hvert trinn i utviklingen. Dermed er og-så nye protokoller for kvalitetsvurdering av spektrale bildebehandlingsverktøy utviklet. Disse protokollene består av kunstige datasett for å validere de teoretiske måletekniske kravene, bildedatasett med kjente egenskaper for å vurdere robustheten og stabiliteten, og datasett fra reelle anvendelser for å bevise nytten av rammeverket i en anvendt sammenheng. De valgte anvendelsene er innenfor kulturminnefeltet, hvor de analyserte bildene er av pigmenter og malerier.

veloppement. Des protocoles d'évaluation de la qualité des traitements morphologiques sont proposés, exploitant des jeux de données artificielles pour la validation théorique, des ensembles de données dont certaines caractéristiques sont connues pour évaluer la robustesse et la stabilité et des jeux de données de cas réels pour prouver l'intérêt des approches en contexte applicatif. Les applications sont développées dans le contexte du patrimoine culturel pour l'analyse de peintures et pigments.

Acknowledgments

First of all, I want to express my gratitude to my supervisors from both NTNU Gjøvik and University of Poitiers: Professor Jon Y. Hardeberg, Associate Professor Noël Richard, and Professor Christine Fernandez-Maloigne. Thank you for the invaluable feedback, support, and opportunities given to me throughout my study. I have learnt a lot from all of you, not only academically but also as a person.

Being in a co-tutelle program has exposed me to two different cultural norms at The Norwegian Colour and Visual Computing Laboratory (Colorlab) and Laboratory XLIM-SIC. It has certainly been a great experience to have in such a short time. And so I want to thank friends and colleagues I met along the way: Thomas Simon-Liedtke, Irina Ciortan, Kiran Raja, Sony George, Jana Blahova, Gerardo de la Riva, David Völgyes, Ferdinand Deger, and many more. I am also thankful for the lecturers whose courses I had attended: Professor Stephen Wolthusen, Professor Katrin Franke, Assoc. Professor Marius Pedersen, Assoc. Professor Faouzi Cheikh, and Professor Einar Snekkenes. Thank you for the guidance and invaluable discussions, and ultimately, because the challenging and highly demanding courses worth the knowledge I gained from them. I also want to thank the staffs who have been tremendously helpful and kind to me. Thank you, because without your help, I would not have been able to work on my research in peace.

I am extremely blessed to have these people as my family: Papa, Mama, Andre, Tabita, and Sarah. My parents have been constantly supporting me throughout my entire life, not just because that is what parents do, but because they love me. Thank you for your prayers and for always picking up the phone in the middle of the night to hear me panicking. I want to thank my siblings for the great teamwork in supporting each other. I could not ask for more, really. And congratulations, Tabita and Sarah, for finishing your theses.

Throughout my study, I have also been supported by these great people: Ronny Lukas, Tieta Antaresti, Ivonne Margi, Feraena Bibyna, Alice Renaud, and Ruth Ann and Ray Gorrell. Thank you, Ronny and Feraena, for always asking me how things are going from time to time. Thank you for being great travel companions and we should definitely plan for another. Thank you, Tieta and Ivonne, for the friendship and laughter and whatnot for this past decade. Here's to many more decades tolerating each other's eccentricities. I want to say that your visit, Ruth Ann and Ray, has been a great blessing to me. I really needed the encouragement you both gave me. But much more than that, I am grateful to have met both of you at beginning of my journey in Europe five years ago. Thank you because ever since then you have been a family to me in this land I do not call my own. Thank you, Tante Alice, for receiving me at your home, for being there during my difficult times, for being a friend, a sister, and a mother.

Last but not least, this PhD research work has been made possible by the funding from the Research Council of Norway and the Poitou-Charentes regional funds for research activities. I also want to acknowledge Norsk Elektro Optikk AS, The National Museum of Art, Architecture and Design of Norway, and The National Library of Norway for their collaboration during my study.

He named it Ebenezer, saying,
"*Thus far the LORD has helped us.*"
I Samuel 7:12b, New International Version

Notations

Set, Image, and Spectral Functions Related Terms

λ	Wavelength or spectral band, $\lambda \in [\lambda_{\min}, \lambda_{\max}]$.
S	Image value as a function of wavelength λ, where $S = \{s(\lambda),\ \lambda \in [\lambda_{\min}, \lambda_{\max}]\}$.
$I(x) = S$	Image function at spatial location x, $x \in \mathbb{Z}^2$, whose value is a spectral function S. Sometimes $I(i, j)$ notation is also used to explicitly state the two spatial coordinates of an image, $i, j \in \mathbb{Z}$.
$\tilde{I}(x) = S$	Artificially generated image function at spatial location x.
$I_g(x) = S$	Ground truth image function at spatial location x.
$L(x) = y$	Labeled image in the context of image segmentation, $y \in \mathbb{Z}$. When used in the context of crack detection, $y = \{0, 1\}$, where 0 and 1 are used to represent non-crack and crack pixels, respectively.
n_I	Numbers of pixels in an arbitrary image I.
S_{Bk}	Theoretical equi-energetic black spectral function, where $s_{Bk}(\lambda) = 0,\ \forall\lambda \in [\lambda_{\min}, \lambda_{\max}]$.
S_{Wh}	Theoretical equi-energetic white spectral function, where $s_{Wh}(\lambda) = 1,\ \forall\lambda \in [\lambda_{\min}, \lambda_{\max}]$.
S_{ref}	Spectral function employed as reference in the context of single reference distance function.
$\mathcal{C}$	Spectral function associated with a crack signal.
$\mathcal{N}$	Spectral function associated with a noise signal.
$\mathcal{S}$	A set of spectral functions. When it is written as $\mathcal{S}_I$, it should be read as a set of all spectral functions originating from image I.

$t(S, \theta)$	Transformation function modifying an arbitrary spectral function S with parameter θ.

Distance and Ordering Relations

$d(S_x, S_y)$	Distance between two arbitrary spectral functions S_x and S_y.
$div(S_x, S_y)$	Dissimilarity between two arbitrary spectral functions S_x and S_y, described in terms of divergence.
$sim(S_x, S_y)$	Similarity between two arbitrary spectral functions S_x and S_y.
$\bar{d}$	Normalized distance response.
$\mathcal{D}$	A set of distance values, $\mathcal{D} = \{d(S_{ref}, S_i),\ \forall S_i \in \mathcal{S}\}$.
$g(S)$	Ordering relation, with an arbitrary spectral function S as input.

Nonlinear Image Filtering

$F_{W,r,g}(S_x)$	Image filter function, with a predefined filter window W, rank r, and ordering relation g. Takes a spectral function S_x as input.
r	Selected rank in the context of rank order filters.
W	Spatial neighborhood associated with x as the spatial coordinate of its origin, over which a filter window is defined.
$\mathcal{S}_W$	Set of spectral functions within filter window W.
n_W	Number of spectral functions in $\mathcal{S}_W$.
$\mathfrak{c}_i$	Cardinality, or number of elements, associated with spectral function S_i.

Mathematical Morphology Terms

B	Structuring element. Will sometimes be written as a subscript of a morphological operator to explicitly state the use a particular structuring element. E.g., δ_B is to be read as "dilation with structuring element B." The rest of the mathematical morphology terms follow or are adapted from the written expression of Soille [159].
$S^{-\infty}$, $S^{+\infty}$	Spectral reference coordinates in CRA ordering relation, also referred to as minimum and maximum convergence coordinates.
ϵ, δ	Erosion and dilation operators, respectively.
ϱ	Beucher's gradient.
γ, ϕ	Opening and closing operators, respectively.
BTH, WTH	Black and white grayscale top-hat transforms, respectively.
$TH^{-\infty}$, $TH^{+\infty}$	Spectral top-hat transforms which retain objects whose spectral

	function converge towards the minimum and maximum convergence coordinates, respectively.
CTH	Combined spectral top-hat transforms, obtained by superimposing the results of $TH^{-\infty}$ and $TH^{+\infty}$ by a logical 'OR' operation.

Other General Terms

$\mathbb{Z}$, $\mathbb{Z}^n$	Set of integers and n-dimensional discrete space, respectively.
$\mathbb{R}$, $\mathbb{R}^n$	Set of real numbers and n-dimensional Euclidean space, respectively.
$\mu,\ \sigma$	Average and standard deviation, respectively.
$\wedge$, $\vee$	Minimum and maximum operators, respectively.
$\cap$, $\cup$	Set intersection and union, respectively.
$\bullet$, $\star$	Logical AND and OR, respectively.
Δ	Absolute difference operator.
$\mathbf{id}$	Identity operator.
$\mathcal{H}$	Heavyside function.
R	A random variable.
T	An arbitrary threshold value.

Abbreviations

ASF	alternating sequential filters
BHSD	bidimensional histogram of spectral differences
CCMM	Convergent Color Mathematical Morphology
CDF	cumulative distribution function
CLTR	color transformation employing D65 illuminant and CMF (Section 2.3)
CMF	CIE 1931 Color Matching Function (2°standard observer)
CRA	conditional ratio and angular distance ordering relation
CRA-SMF	CRA-based spectral median filter
ECS	Euclidean distance of cumulative spectrum
EMD	earth mover's distance
FIXED	Fixed bands color visualization (Section 2.3)
GFC	goodness-of-fit coefficient
GMC	Geman-McClure function
HMT	hit-or-miss transform
HSI	hyperspectral imaging
IR	infrared
Isomap	isometric feature mapping
KL	Kullback-Leibler divergence
KLPD	spectral Kullback-Leibler pseudo-divergence
LLE	Locally Linear Embedding
LWIR	long-wave infrared
MCW	marker-controlled watershed
MM	mathematical morphology

MSB	most significant bit
MWIR	medium-wave infrared
NIR	near-infrared
OCCO	open-close and close-open filters
PDF	probability density function
RMS	root mean square
ROF	rank order filters
ROI	region of interest
SAM	spectral angle mapper
SCM	spectral correlation mapper
SE	structuring element
SID	spectral information divergence
SWIR	short-wave infrared
THSD	tridimensional histogram of spectral differences
VMF	Vector Median Filters

Contents

Chapter 1

Introduction

1.1 Motivation

Spectral imaging, e.g., multispectral and hyperspectral, has been employed for quality control and inspections or diagnostics of materials for several decades. Originally developed for remote sensing tasks, nowadays it has found its place in a broad range of application fields. In agriculture, hyperspectral imaging has been employed for, e.g., quality assessment of fruits [71], grains and nuts [123, 158], meat [113, 185], and seeds [67]. The use of spectral imaging in art conservation was started in the early 90s [118], and has continued to develop ever since [58, 81, 144]. In the medical field, hyperspectral imaging has been employed to develop cancer detection algorithms [117, 135] and also to detect counterfeit drugs [184]. Other use of hyperspectral imaging can be found in aerial archeology [47], plastic waste sorting [89], and oil spillage detection [7].

Despite the great potential of hyperspectral imaging, unfortunately, the image processing side does not quite follow the advances of this imaging technology. Generally, due to the size of a hyperspectral image which poses a significant computational burden, the image processing step is carried out after dimensionality reduction or band selection procedures. Indeed, these approaches have their merit and can be appropriate in certain cases, e.g., when diagnostic bands are known. However, they do not allow to fully exploiting the gain of accuracy that hyperspectral imaging has to offer. Often times, dimensionality reduction is conducted by assuming the existence of noise. However, this procedure will not only remove the noise but also important spectral variations within the data. And so, this pre-processing step is done at the cost of losing the accuracy, by which argument the expensive acquisition is carried out in the first place. In order to fully exploit

the potential of hyperspectral imaging, we believe that hyperspectral image processing must be carried out metrologically. By introducing metrology to image processing, the following question will always be at the center of consideration, i.e., how to manage accuracy, uncertainty, and bias at every step of the processing chain. But in order to construct this metrological image processing framework, an understanding of the physical properties of spectral data is required. This is because the framework will be developed based on the physical properties of spectral data, rather than only considering them as numerical objects.

Spectral images should rather not be processed with linear image processing techniques. This is because, in general, spectral images do not satisfy the widely used hypotheses of Gaussianity and stationarity which are usually assumed to validate linear models [122]. Furthermore, linear processing approach requires that there is a valid addition and multiplication with a scalar for spectral data, see Fig. 1.1, which is an erroneous assumption to make. But then again, it is also not only a matter of whether the operations are available. Rather, both addition and multiplication with a scalar should be physically meaningful. And looking at the problem from this point of view, such operations do not exist for spectral data. Thus, even though the linear approach has been employed to solve image processing tasks for spectral data, one must be conscious that this approach is not theoretically valid. A valid spectral image processing can be obtained through the nonlinear approach. In nonlinear image processing approach, only a complete lattice is required, which will be enabled through ordering relation.

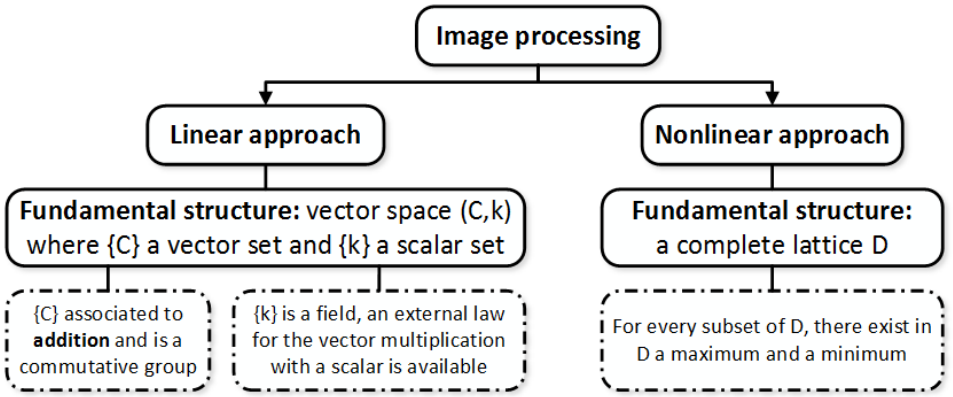

Figure 1.1 – Fundamental structures and requirements of linear and nonlinear image processing approaches.

Mathematical morphology (MM) is a theory and full framework for the analysis of spatial structures in an image. The theory was laid by the works of Math-

eron [119, 120] and Serra [154, 156] on the fundamentals of ordering relations and complete lattice theory. As an image processing framework, MM provides tools such as image filtering, image segmentation, image measurements, etc. Morphological filters cover application tasks such as non-uniform illumination correction [180], edge enhancement [153], and noise reduction [86, 108]. Watershed algorithm is a morphological approach to image segmentation and it has been employed in, e.g., extracting features for content-based image retrieval [4] and extracting text-line features for document image analysis [133]. As a framework for image measurements, MM provides tools for analysis of directions, texture analysis, shape descriptors [159]. The popularity and success of MM are mainly attributed to its rigorous mathematical foundation and ability to exploit spatial relationships of pixels, i.e., connected components, shape, size, and orientations. However, it should also be noted that the framework has only been fully developed for binary and grayscale images. The extension of mathematical morphology framework to the multivariate domain remains an open research question.

1.2 Mathematical Morphology, A State of The Art

1.2.1 Advanced Morphological Image Processing Tools

The scope of what MM framework can offer is extensive. At its basic level of processing, erosion and dilation operators can be employed for tasks such as hole-filling and the removal of noise or small objects in an image. These examples are, however, a small fraction to the potential of the full MM framework. With the purpose of describing the potential of the framework, in the following we present two examples of advanced image processing tools which can be achieved by MM.

1.2.1.1 Morphological Gradients

The term gradient can be described as a slope, i.e., where there is change in magnitude. In image processing, a gradient can be a useful identifier of region boundaries or edges, in turn making it useful for segmentation algorithm such as watershed. This is because pixels belonging to the same region typically have homogeneous values. And, thus, an edge can be found when the magnitude of a gradient is high. Or in other words, an edge occurs when there is a significant variation in the values of neighboring pixels.

Computed based on the outputs of the basic morphological operators, i.e., erosion and dilation, morphological gradients enhance local variations within an image. Several morphological gradients have been proposed, which are essentially arithmetic difference between either of the following combinations, i.e., dilation and erosion, dilation and the original image, and the original image and erosion [159].

Beucher's gradient is an arithmetic difference between dilation and erosion. Other morphological gradients are the *half gradients* [146], which consists of *internal gradient* and *external gradient*. A morphological Laplace filter was also proposed based on the arithmetic difference between external and internal gradients [173]. Then, there is also *directional gradient*, which is Beucher's gradient obtained using line structuring element [99].

The aforementioned morphological gradients were, however, limited to the grayscale domain. Challenges arise when the input image is multivariate, e.g., color or spectral images. Many researchers approach the challenge by simplifying the image. For example, the grayscale gradient would be applied on each individual image channel, which would be followed by strategies combining the resulting gradient images [32, 62]. A color image is considered in a vectorial way through a bit mixing paradigm, allowing the use of grayscale morphological gradient in the context of watershed transformation [44].

1.2.1.2 Morphological Filters

Morphological opening and closing operators allow obtaining a set of morphological filters, e.g., open-close and close-open (OCCO) filters and alternating sequential filters (ASF) [155, 163]. OCCO filters are a set of filters which are composed by a sequence of opening and closing operators, i.e., open-close, close-open, close-open-close, and open-close-open filters[1] This class of morphological filtering is particularly suitable to filter an image which is disturbed by bright and dark noisy structures [159]. ASF is also composed of sequential opening and closing operators, but in this set of filters, the structuring element size is gradually increased from 1 to n. This makes ASF particularly useful for a multiscale analysis. ASF has been used for fractal analysis [29, 166], impulse noise removal [20], and the segmentation of retinal images [157]. An extension of morphological filters to the multivariate domain can be found in [43] using bit mixing approach. In this article, results are provided for the case of ASF applied on color images.

1.2.2 Existing Color Mathematical Morphology

The main challenge of extending MM framework to the multivariate domain is in identifying which ordering relation to employ, since there exist multitudes of multivariate ordering relation [12, 23]. And this selection should be made by considering the nature of the image at hand and also the application goal. When it comes to color images, color is not a valid Euclidean metric space [91]. As a consequence, addition and multiplication with a scalar cannot be applied to color images. And,

[1] Open-close is to be read opening followed by closing operators.

apart from the theoretical constraints to be satisfied, the nature of color images makes not just any arbitrary vectorial ordering valid for color images.

Color images were initially processed by applying grayscale operations independently on its channels, which was inevitable due to technological constraints at the time. Nevertheless, Pitas [138] argued that multichannel images had to be processed with multichannel processes. Then, color image filters were developed using the marginal approach [96, 136, 182]. The same marginal ordering relation has also been employed in a color mathematical morphology that is independent from the choice of color space [66]. This morphology is applied on the reconstructed spectral image of a given color image. Despite being more preferable than other ordering relations due to its lower computational complexity [136], marginal ordering relation is not to be considered a suitable ordering relation for color images. This is because it does not consider the correlation which exist between the channels of a color image, which in turn causes the generation of *false colors*. False colors are values which do not exist in the initial image.

Then, there is a group of approaches which divide data into sub-groups, either by employing the marginal properties of an image or reduction functions. The ordering relation is then applied independently in each sub-group. Generally, the challenge with this approach lies in the fact that there is no order between the sub-groups. Two examples of this approach is ordering relations developed based on random projection depth [177] and cost function incorporating distance and color co-occurrences [45]. In [177], the existence of background and foreground representations in an image is assumed. Even though the study was limited to color images, it was claimed that the results were valid for any metric spaces. In [45], to tackle the issue of having to compute too big of color co-occurrences, the input image is clustered into a number of clusters, followed by a minimization algorithm.

Conditional ordering approach conducts ordering on the marginal components sequentially according to certain conditions or priorities. The marginal components can be the original components of the data [9, 13, 15, 131] or ones obtained after a preliminary coordinate transformation [110]. Also known as *lexicographic* ordering [23, 177], it is particularly suitable where natural or artificial priorities exist among the marginal components of the data, e.g. in color images [13]. However, there is a significant drawback, i.e. excessive prioritization of the first few channels. This implies that the importance of the rest of the channels are almost negligible and the inter-channel relation is not efficiently exploited.

Several strategies have been proposed to tackle the excessive prioritization issue of the lexicographic approach. α-lexicographical ordering, originally developed for the HSI (hue, saturation, and intensity) color space, was proposed to reduce

the effect of excessive prioritization of the classical lexicographic ordering relation [131]. A factor α is introduced on the first cascade, i.e. I channel, allowing the lexicographic approach to reach the subsequent marginal component. α-modulus lexicographic ordering is an α-based approach which reduces the dynamic range of the first channel and consequently allows reaching the second channel in the ordering procedure [9]. Another approach that tries to shift prioritization from the first channel is the α-trimmed lexicographical approach [12]. Then there are quantization-based α-lexicographical ordering and marker-based lexicographical ordering [13], which were developed to reduce the excessive prioritization issue in an image with much larger channel count than the color images.

The notions of distance or similarity is one of the most common approach to extend mathematical morphology framework to the color domain [10, 106, 178, 189]. In [10, 178], the order of a color is determined through its distance to a reference color. In [106], two reference colors are employed, aiming to reach total ordering property which is required by MM framework. In [189], the notion of similarity is combined with a conditional ordering approach to develop a hybrid ordering relation. Other approaches in extending mathematical morphology to the color domain include graph-based approach [111], the bit-mixing paradigm [43], fuzzy approaches [94, 107], probabilistic color morphology [51], and color morphology based on Pareto-dominated hypervolume measure [93, 95].

1.3 Research Objectives

The main objective of this study is to develop a metrological image processing framework for spectral data based on mathematical morphology. Thus, a multivariate ordering relation suitable for spectral data must be defined. Selecting to base the ordering relation on the notion of distance, we claim that the metrological constraints of the image processing framework to be developed can be maintained.

The first theoretical objective of this study is to identify the most suitable distance function for spectral images, with the end goal of developing a distance-based spectral mathematical morphology. In a previous research work, a distance-based mathematical morphology for color images has been constructed [103]. Then, in a more recent study, the potential of its extension to the multispectral domain has also been explored [104]. To follow this direction, selection criteria which comprises both theoretical and metrological constraints will be developed. Then, based on the predefined criteria, a comprehensive evaluation will be carried out on the existing distance functions. If none of the existing ones is found to be suitable for spectral data, having identified the selection criteria, a suitable spectral distance function will be constructed.

Having identified a suitable spectral distance function, a distance-based spectral ordering relation will be constructed. And this is the second theoretical objective defined for the study. In addition to constructing a novel spectral ordering relation, existing approaches for the spectral domain will be considered and evaluated. Thus, for this purpose, evaluation criteria consisting of both theoretical and metrological constraints will be developed.

After the theoretical developments of spectral distance function and spectral ordering relation, we will develop at the same time a set of tools for image analysis and the fundamental operators for spectral MM framework. Given a hyperspectral image, spectral distance function can be directly employed to construct tools useful for the analysis of its spectral distribution. Then, having obtained spectral ordering relation, rank order filters can be extended to the spectral domain and this will also be carried out. Finally, as the main goal of the study, both spectral distance function and spectral ordering relation will be employed to extend mathematical morphology framework to the spectral domain. Each of the aforementioned processing tools will be assessed according to certain criteria, and employed to address tasks in cultural heritage field, with datasets coming from paintings, manuscripts, etc. To summarize, the main development stages in the study is as depicted in the first column Fig. 1.2. In the second column are image processing operators which can be obtained at the corresponding development stage. Then, related to this figure is Fig. 1.3, providing the metrological criteria to assess at each stage of the image processing framework development.

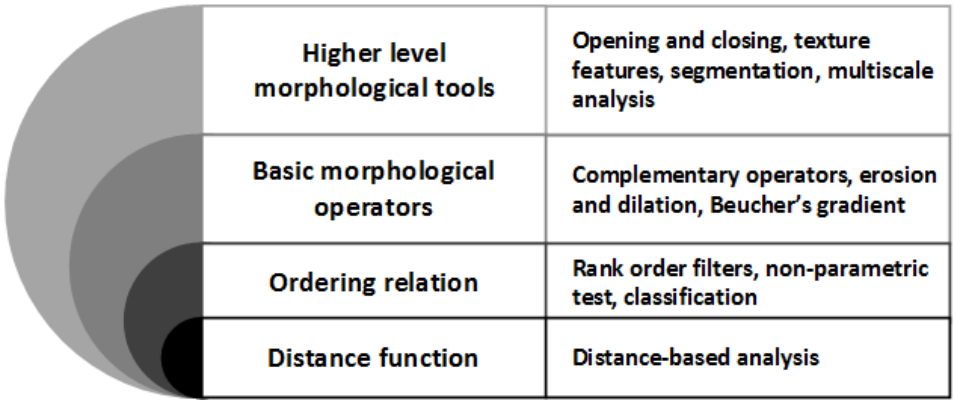

Figure 1.2 – Hierarchical organization of the scientific concepts leading to the construction of distance-based spectral mathematical morphology framework. The core development stages are depicted in the first column. In the second column are operators which can be obtained at the corresponding level of development.

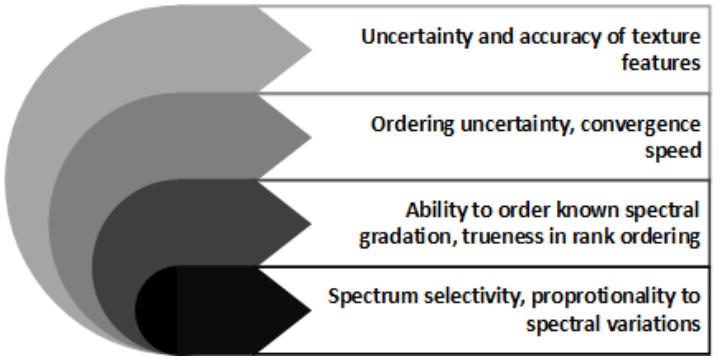

Figure 1.3 – Metrological criteria associated to each level of spectral mathematical morphology framework development shown in Fig. 1.2.

1.4 List of Published Articles

Throughout the span of this study, a number of articles have been published, see the list below. The main topics of each article relative to the goals of the research can be observed through Fig. 1.4.

Article A H. Deborah, N. Richard, and J. Y. Hardeberg. A comprehensive evaluation of spectral distance functions and metrics for hyperspectral image processing. *Selected Topics in Applied Earth Observations and Remote Sensing, IEEE Journal of*, 8(6):3224–3234, Jun 2015

Article B H. Deborah, N. Richard, and J. Y. Hardeberg. On the quality evaluation of spectral image processing algorithms. In *Signal-Image Technology and Internet-Based Systems (SITIS), 2014 Tenth International Conference on*, pages 133–140, Nov 2014

Article C H. Deborah, N. Richard, and J. Hardeberg. Spectral impulse noise model for spectral image processing. In A. Trémeau, R. Schettini, and S. Tominaga, editors, *Computational Color Imaging*, volume 9016 of *Lecture Notes in Computer Science*, pages 171–180. Springer International Publishing, Feb 2015

Article D H. Deborah, N. Richard, and J. Y. Hardeberg. Spectral ordering assessment using spectral median filters. In J. A. Benediktsson, J. Chanussot, L. Najman, and H. Talbot, editors, *Mathematical Morphology and Its Applications to Signal and Image Processing*, volume 9082 of *Lecture Notes in Computer Science*, pages 387–397. Springer International Publishing, May 2015

Article E H. Deborah, N. Richard, and J. Y. Hardeberg. Vector crack detection for cultural heritage paintings. In *Traitement et Analyse de l'Information Méthodes et Applications (TAIMA)*, May 2015, Hammamet, Tunisia.

Article F H. Deborah, N. Richard, and J. Y. Hardeberg. Hyperspectral crack detection in paintings. In *Colour and Visual Computing Symposium (CVCS)*, pages 1–6, Aug 2015, Gjøvik, Norway.

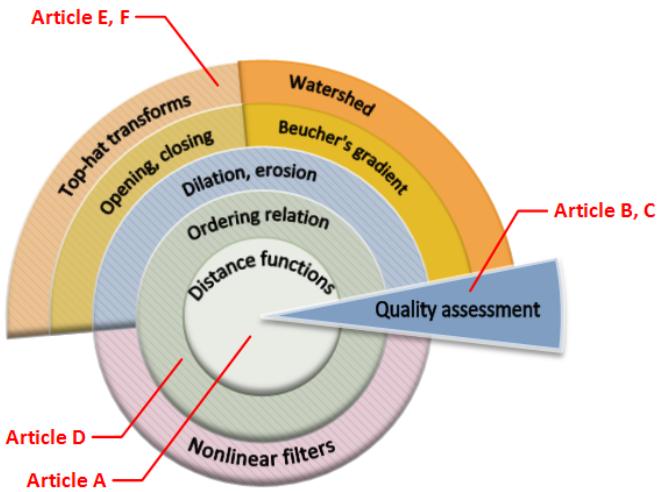

Figure 1.4 – Publication list in the context of thesis development. The main topics of article A are spectral distance function and its quality assessment. Article B and C proposed elements for the quality assessment of spectral image processing tools. In article D, several multivariate ordering relations were assessed using a proposed criterion. Article E and F provide applications of top-hat transforms to crack detection task in cultural heritage domain. Note that all elements from distance function to opening and closing are obtained prior to top-hat transforms.

1.5 Thesis Organization

The content of the thesis is organized around the flowchart shown in Fig. 1.5. Part I of the thesis consists of 3 chapters. Background notions related to the digital construction of a spectral image will be provided in Chapter 2. In the same chapter, color visualization methods which will be used throughout the thesis will also be elaborated. In Chapter 3, an extensive study is carried out considering the question of spectral function definition, and consequently, which difference measure is the most suitable for spectral data. A significant portion of this chapter has been published in **Article A**, where a new measure has also been proposed. The study of

spectral ordering relation is given in Chapter 4, where based on spectral difference function defined in the preceding chapter, a new spectral ordering relation is proposed. Quality assessment protocols used in this chapter are taken from elements published in **Article B** and **D**.

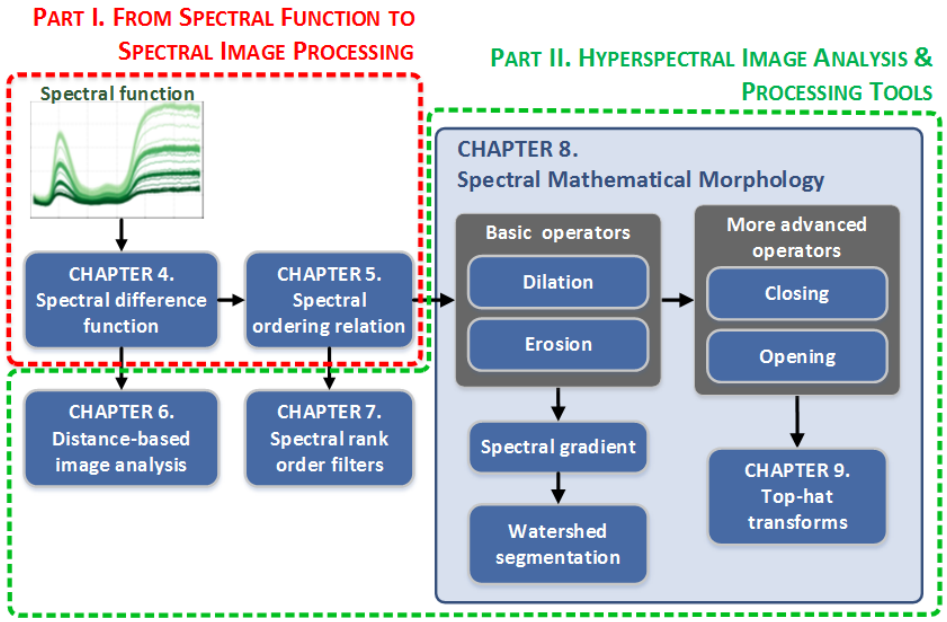

Figure 1.5 – Thesis organization flowchart within the context of image processing framework to be developed.

Part II of the thesis begins with Chapter 5, where graphical representations of spectral differences are introduced as tools for hyperspectral image analysis. Since the notion of reference is central to the computation of spectral differences, formulation of reference selection is also provided in the chapter. Still in the same chapter, noise and numerical problems are identified using the introduced graphical representations, which in turn allows adjusting the programming implementation accordingly. Chapter 6 provides the construction and application of spectral rank order filters, which are enabled by the spectral difference function and ordering relation previously studied in Chapter 3 and 4, respectively. Parts of the quality assessment protocols used in this chapter have been published in **Article B**, **C**, and **D**. The construction of the first levels of a spectral mathematical morphology framework can be found in Chapter 7. Basic morphological operators, i.e., erosion and dilation, are defined which in turn allows the construction of spectral morphological gradient. Using the constructed gradient, watershed segmentation algorithm will be applied to spectral data. As a base for morphological filters, the extension of

opening and closing can also be found in this chapter. One advanced morphological filter is also extended to the spectral domain in this chapter, i.e., top-hat transforms. As the final chapter of Part II, Chapter 8 provides a study centered around an application task, i.e., crack detection for cultural heritage paintings. Differing from its preceding chapters, the chapter will focus on the application and how the morphological tools which have been developed so far can solve the problem. This chapter is a complete version of the preliminary studies published in **Article E** and **F**. Finally, the study will be concluded in Chapter 9.

In the final part of the dissertation, an exhaustive list of spectral distance functions evaluated in Chapter 3, including their mathematical expressions, is provided in Appendix A. In Appendix B, the hyperspectral image datasets employed throughout the study will be described in more details.

1.6 Metrological Terms and Notions

The list of metrological terms and notions which will be employed throughout the monograph can be found in Table 1.1. Measurement uncertainty and trueness will be frequently used as for quality assessment in Chapter 4 and 6. The rest of the terms are provided to avoid confusions of their definitions. Especially since they are commonly used without reference to the vocabulary of metrology.

Table 1.1 – Definition of several qualitative terms used in metrology as seen in [171].

measurand	*quantity* intended to be measured
measurement accuracy	closeness of agreement between a *measured quantity value* and a *true quantity value* of a measurand
measurement trueness	closeness of agreement between the *average of an infinite number of replicate measured quantity values* and a *reference quantity value*
measurement precision	closeness of agreement between *indications* or *measured quantity values obtained by replicate measurements on the same or similar objects* under specified conditions
measurement uncertainty	non-negative parameter characterizing the *dispersion of the quantity values* being attributed to a measurand, based on the information used

Part I

From Spectral Function To Spectral Ordering Relation

Chapter 2

From Surface To Spectral Images

Digital imaging works by recording electromagnetic radiation as it travels through space and interacts with objects, e.g., absorbed or reflected. Based on the types of electromagnetic radiation being captured, there are different modes of digital imaging. For instance, given a scene or object, color imaging records visible electromagnetic radiation falling to its sensor, i.e., radiation ranging from approximately 380 to 780 nm. Computer tomography (CT) and radiography are digital imaging technologies commonly used in the medical field. They capture X-rays, i.e., radiation around 0.01 to 10 nm. Positron emission tomography (PET) is a functional imaging technique that takes in gamma rays, i.e., electromagnetic radiation with wavelengths less than 10 pm (or 10^{-11} meters). There are also digital imaging modes which capture other types of waves, e.g., sound and radio waves. Regarding this study, the focus is on electromagnetic radiation-based digital imaging, mostly within the visible and a portion of near infrared spectral ranges. Throughout the rest of this chapter, we provide necessary fundamental knowledge required to understand digital images captured by a spectral imaging device.

2.1 Electromagnetic Radiation

2.1.1 Electromagnetic Waves

All matters with temperature above absolute zero emits electromagnetic radiation. Not only that, matters also reflect radiations emitted by other matters. But what is electromagnetic radiation? Electromagnetic radiation is energy which is propagated through space as well as materials in the form of electromagnetic waves. Electromagnetic waves consist of two components, i.e., electric and magnetic components. The electrical field (E) varies in magnitude in direction perpendicular to the

propagation direction. The magnetic field (H) is propagated in phase with the electrical field [35], see Fig. 2.1.

Different properties can be used to characterize electromagnetic energy. These properties are *wavelength*, *amplitude*, *frequency*, and *phase*. In this study, we will mainly use wavelength property. And as can be seen in the illustration in Fig. 2.1, wavelength is the distance between crests of one wave and the next one. When dealing with electromagnetic waves, this distance is actually really small. In general we will use nanometer (nm) unit, i.e., 1 nm is equal to 10^{-9} meters.

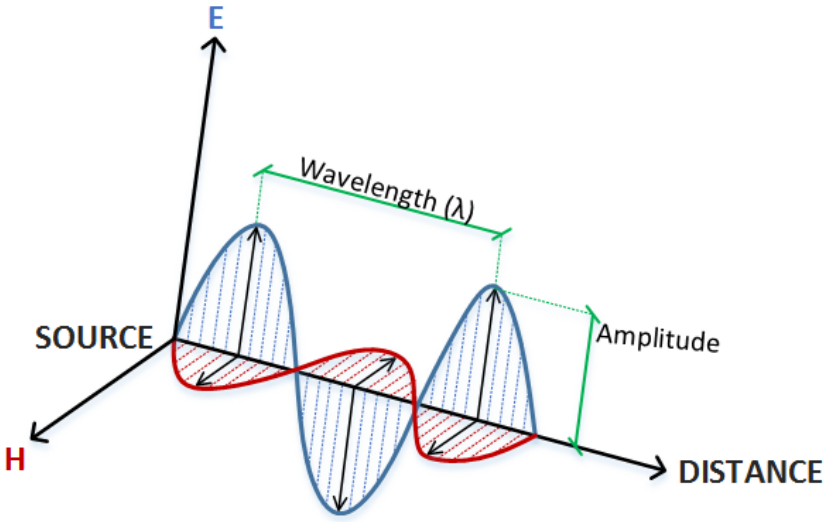

Figure 2.1 – Illustration of an electromagnetic wave traveling through space in the form of electric (E) and magnetic (H) fields, which are perpendicular to each other and the direction of propagation. Shown illustration is derived from [35].

2.1.2 Divisions of the Electromagnetic Spectrum

The range of the electromagnetic spectrum can be divided into several groups based on its wavelength, see Fig. 2.2. Note that such sharp breaks do not exist in a full spectrum of solar energy. These divisions are established mainly for practical purposes and could be defined differently in different disciplines. Images which will be employed throughout the study covers the visible and near-infrared spectral ranges. The visible range is where light becomes visible to the human visual system. From shorter to longer wavelengths, light is perceived as colors from violet to red by the human eye. Characteristics of pigments within this range have been found to be useful for pigment identification tasks [58]. The infrared

(IR) range can be divided further into near-infrared (NIR), short-wave infrared (SWIR), medium-wave infrared (MWIR), and long-wave infrared (LWIR) ranges.

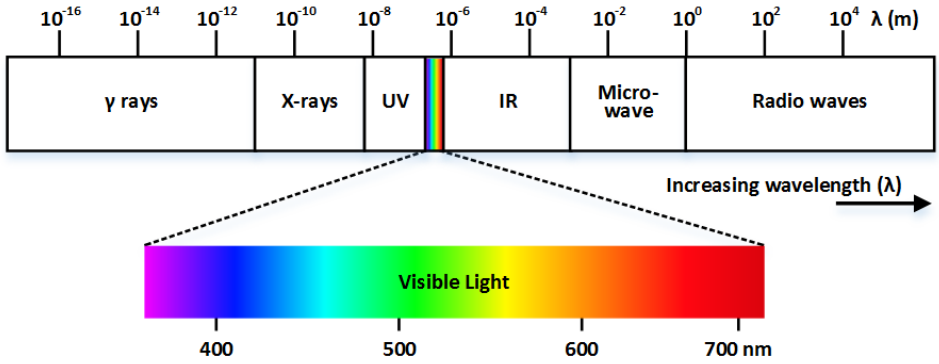

Figure 2.2 – Principal divisions of the electromagnetic spectrum based on wavelength. Illustration is derived from [183].

2.1.3 Radiometric and Spectral Quantities

Radiometry is the science of measuring electromagnetic radiation in any portion of the electromagnetic spectrum. When it comes to visible light and human visual system, photometry measures electromagnetic radiation whose units are weighted according to the sensitivity of human visual system. Hyperspectral imaging, which is the scope of this study, is concerned with radiometry rather than photometry. Radiometric quantities, their units, and descriptions are provided in Table 2.1. Quantities mentioned in the table are broadband quantities obtained from **integrating** quantities over a wavelength range. The distribution of these quantities in each wavelength is called **spectral quantities**. **Spectral radiance** is radiance as a function of wavelength, with unit of (W $m^{-2}sr^{-1}$). **Spectral reflectance** is reflectance as a function of wavelength. It is sometimes expressed as a ratio, with values ranging from 0 to 1.

Table 2.1 – List of radiometric quantities and their corresponding units and definitions. Definitions are obtained from [169].

Radiometric quantity	Unit	Description
Radiant energy	joule (J)	The amount of energy carried out by electromagnetic waves.
Radiant power	watt (W)	The radiant energy emitted, reflected, transmitted, or received per unit time, also known as radiant flux.
Radiant intensity	W sr^{-1}	The radiant power from a point source.
Radiance	W m^{-2} sr^{-1}	The amount of energy being emitted or reflected from a particular area per unit solid angle and per unit time.
Irradiance	W m^{-2}	The amount of incident energy on a surface per unit area and per unit time.
Radiant exitance	W m^{-2}	The power emitted from a surface, also known as radiant emittance.
Reflectance	-	The portion of the incident energy on a surface that is reflected, usually expressed as percentage or as value between 0 and 1. $$\text{Reflectance} = \frac{\text{Observed brightness}}{\text{Irradiance}}$$

2.2 Hyperspectral Images

Hyperspectral imaging is an imaging technology combining the power of digital imaging and spectroscopy. An acquired hyperspectral image captures not only spatial information, but also spectral measures that typically spans over hundreds of contiguous spectral bands. In this study, in addition to the number of spectral bands, we differentiate multispectral and hyperspectral imaging in that the multispectral bands can overlap and their bandwidths are non-uniform. More detailed explanations regarding hyperspectral imaging can be read from [36, 68].

2.2.1 Digital Image Formation

A grayscale image can be defined as a two-dimensional function $I(i, j)$ where i, j describes the spatial coordinates of the corresponding object or scene and I describes the intensity of light at any arbitrary pair of (i, j) coordinates. Such representation of a grayscale image means that the image is considered as a continuous

object. However, when it comes to digital images, both the spatial coordinates (i, j) and intensity I are of finite values and discrete quantities.

2.2.1.1 Image sampling and quantization

Image sampling is the digitization of continuous spatial dimension of the real world into discrete coordinates (i, j). Then, digitization of the continuous intensity values I into the discrete world is called *image quantization*. The two digitization processes allow to express digital image as an approximation of a real world as follows.

$$I(i,j) \approx \begin{bmatrix} I(0,0) & I(0,1) & \cdots & I(0,M-1) \\ I(1,0) & I(1,1) & \cdots & I(1,M-1) \\ \vdots & & & \\ I(N-1,0) & I(N-1,1) & \cdots & I(N-1,M-1) \end{bmatrix}$$

In the expression above, the continuous image $I(i, j)$ is approximated by a digital construction, which is an $N \times M$ array of equally spaced samples. Each individual element of the array is called an *image element*, *picture element*, *pel*, or most commonly known as *pixel*.

Digitizing the spatial continuity of an object into a discrete $N \times M$ plane requires decision about how big or small are the N and M, and subsequently the number of intensity values n_I which can be represented by a digital device. Resolution of a digital image, i.e., degree of discernible details, depends strongly on the choice of N, M, and n_I parameters. If values of the parameters are increased, the obtained digital image will be a closer approximation of the real scene it represents. Which, of course, comes at the price of increasing the byte size of the image.

To observe the impact of various sampling and quantization choices to a color image, see Fig. 2.3 and 2.4. With the scene shown in the image, we have a fixed size of area in the real world which we want to represent as a digital image. A pixel captures average information of the whole area it covers. Consequently, if it covers a larger area, many details will be smoothed due to the averaging procedure. By increasing the number of pixels an image can have, resolution of the image will increase and more details can be perceived, see Fig. 2.3. Having a reduced numbers of colors which can be represented by a digital device will make a digital image look unrealistic, see Fig. 2.4. More importantly, colors belonging to the same object tend to be more homogeneous. And due to this, object boundaries will be harsher and more of a step function rather than a smooth ramp. However, when this number is increased, there will be a certain point where the human visual system will not be able to perceive the color differences anymore.

(a) 512 × 512 (b) 128 × 128 (c) 32 × 32

Figure 2.3 – Illustration of the impact of image sampling choices to a color image. Reducing spatial resolution will cause a pixel to cover a larger area and, consequently, smaller details in the scene are not captured.

(a) Initial number of colors (b) 128 colors (c) 8 colors

Figure 2.4 – Illustration of the impact of image quantization choices to a color image. Reducing the numbers of colors which can be represented by a digital device causes the image to look less realistic. The same object tends to have homogeneous colors and object boundaries will also be more of a step function rather than a smooth ramp.

2.2.1.2 Spectral image sampling and image cube

When it comes to spectral images, sampling is not only carried out for the spatial domain but also the spectral domain. Unlike a grayscale image whose smallest unit is represented by a single value, one pixel in a spectral image is represented by many values. The number of values representing a pixel is determined by the *spectral sampling interval* $\Delta\lambda$, or what is more commonly known as *spectral bandwidth*, and the spectral range in which a camera operates $\Delta(\lambda_{\max}, \lambda_{\min})$. Spectral bandwidth specifies the spectral interval, typically in nanometer unit, which are

used to record brightness as a function of wavelength [37]. Due to this, a digital spectral image is represented by a three-dimensional matrix $I(i, j, \lambda)$, which is also called an *image cube*. See also illustration in Fig. 2.5.

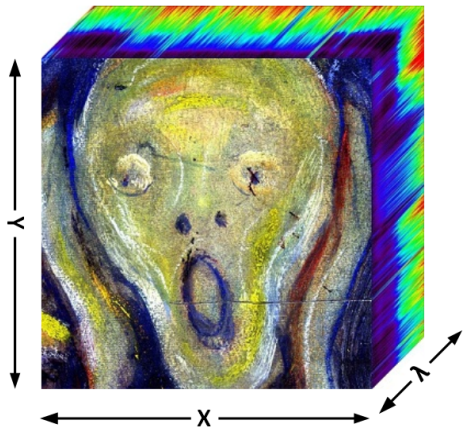

Figure 2.5 – Illustration of a hyperspectral image cube using a cutout of *The Scream* (1893) by Edvard Munch, which was hyperspectrally acquired in 2012 [81]. An image cube consists of three dimensions. Two of them capture spatial coordinates. The other dimension captures spectral measures as a function wavelength λ.

2.2.1.3 The impact of image sampling

Due to an averaging process which follows image sampling in the formation of a digital image, the values of neighboring pixels are not independent. Moreover, the closer two pixels are in the spatial arrangement of the image, the more correlated they are. And this applies for all digital images, be it grayscale, color, or the spectral ones. As a consequence, the color of a spatial region will be relatively homogeneous as neighboring pixels only vary a little.

For spectral image sampling, in reality the spectral bandwidths do not define a discrete limit in the spectral range captured by a camera sensor. And due to spectral sensitivity of the sensor[1], neighboring spectral channels in a hyperspectral image are known to be highly correlated. In turn, these known characteristics of hyperspectral data will impact the discrimination of objects and regions in a spectral image. Rather than having clear edge boundaries, spectral values along borders of a region will be characterized by a mixture of spectral characteristics of the region it belongs to and the neighboring ones.

[1]Read [37] for more explanations regarding spectral sensitivity of optical sensors.

2.2.2 Spectral Values as Measures of Electromagnetic Radiation

As mentioned previously, every pixel in an image cube is represented by a series of measures where each correspond to the amount of energy received for a specific spectral band or wavelength λ. Due to this, spectral measures describing an image pixel can be represented as a function of wavelength, or simply *spectral function*. Then, rather than describing a spectral image with $I(i, j, \lambda)$, the following expression will be employed throughout the monograph.

$$I(i, j) = S = \{s(\lambda),\ \lambda \in [\lambda_{\min}, \lambda_{\max}]\}$$

Looking at the spectral function S, it is composed of measured quantity values of electromagnetic radiation which are obtained from a spectral acquisition. Then, since in this case the measurand is energy, the measured quantity values are positive. Due to this, a spectral function can be mathematically defined as a measure, i.e., a function which assigns a non-negative real number to a subset Σ of X defined on a σ-algebra[2]. For a spectral function s to be a measure from wavelength λ to the extended real number line, it has to satisfy the following properties.

- **Non-negativity**, $s(\lambda) \geq 0,\ \forall \lambda \in [\lambda_{\min}, \lambda_{\max}]$
- **Null empty set**, $s(\emptyset) = 0$
- **Countable additivity**, for all countable collections $\{E_i\}_{i=1}^{\infty}$ of pairwise disjoin sets in Σ, Eq. 2.1 holds.

$$s\left(\bigcup_{i=\lambda_{\min}}^{\lambda_{\max}} \lambda_i\right) = \sum_{k=1}^{\infty} s(E_k) \tag{2.1}$$

[2] σ-algebra on a set X is a collection of Σ subsets of X, including $\emptyset$, which is closed under complement and union/ intersection of countably infinite many subsets. The pair (X, Σ) of a set X and its σ-algebra is called a measurable space [167].

2.3 Color Visualization of Hyperspectral Images

A hyperspectral image typically consists of hundreds of channels. In order to generate a color visualization of a hyperspectral image, it must be reduced to a three-channel color image. In the following are three different color visualization methods employed throughout the study.

FIXED visualization In this method, three spectral band images from a hyperspectral image are directly used as RGB channels. The band selection is made according to information provided by each hyperspectral scanner, i.e., the spectral bands which correspond to peak-sensitivity band of the camera sensor.

ENVI visualization Color images are generated using the default visualization method of ENVI software platform [69].

CLTR visualization Color images generated by CLTR method, which is a short for *color transformation*, are approximation of how the scene/ objects captured by the hyperspectral camera would be perceived by the human visual system. Having a spectral reflectance function as a function of wavelength $s(\lambda)$, the first step of the color transformation is given in Eq. 2.2, where $s_{D65}(\lambda)$ is the spectral power distribution of D65 illumination and the CIE 1931 Color Matching Function (2°standard observer) (CMF) is represented by $\overline{x}(\lambda)$, $\overline{y}(\lambda)$, and $\overline{z}(\lambda)$ [1]. Finally, the sRGB coordinate of spectral function $s(\lambda)$ is given by the matrix multiplication shown in Eq. 2.3. In the case of a calibrated display, a more suitable $XYZ \rightarrow RGB$ matrix can be employed in order to use the whole display gamut.

$$\begin{aligned} X &= \int_{380}^{780} s(\lambda) \cdot s_{D65}(\lambda) \cdot \overline{x}(\lambda)\, d\lambda \\ Y &= \int_{380}^{780} s(\lambda) \cdot s_{D65}(\lambda) \cdot \overline{y}(\lambda)\, d\lambda \\ Z &= \int_{380}^{780} s(\lambda) \cdot s_{D65}(\lambda) \cdot \overline{z}(\lambda)\, d\lambda \end{aligned} \tag{2.2}$$

$$\begin{bmatrix} R \\ G \\ B \end{bmatrix} = \begin{bmatrix} 3.2404542 & -1.5371385 & -0.4985314 \\ -0.9692660 & 1.8760108 & 0.0415560 \\ 0.0556434 & -0.2040259 & 1.0572252 \end{bmatrix} \begin{bmatrix} X \\ Y \\ Z \end{bmatrix} \tag{2.3}$$

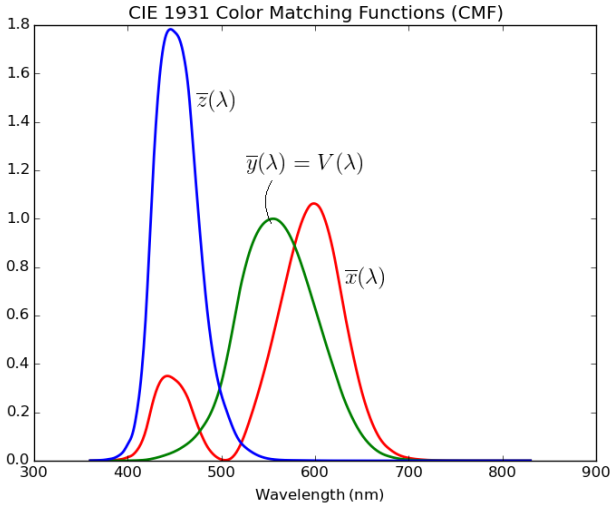

Figure 2.6 – CIE 1931 Color Matching Functions (CMF), 2°standard observer.

Chapter 3

From Definition of Spectral Function to Spectral Difference

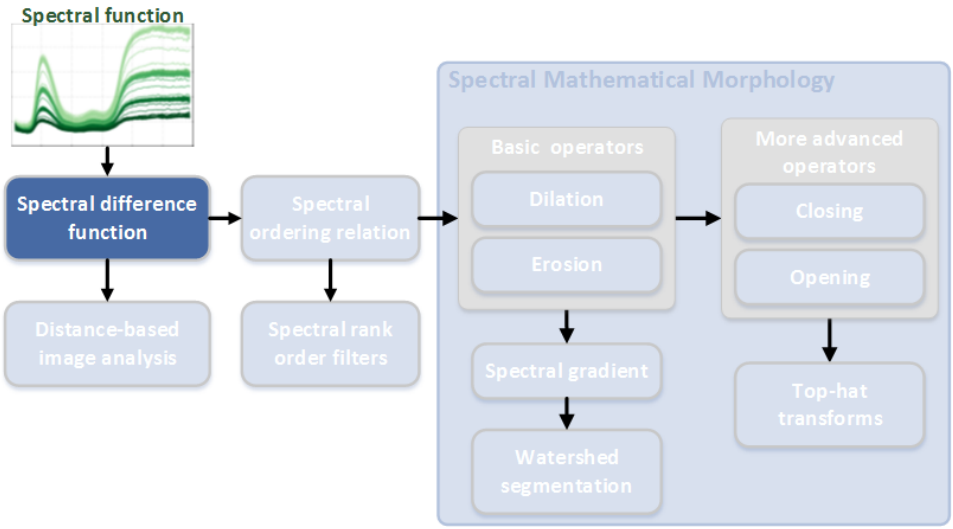

3.1 Introduction

A spectral function is an n-dimensional measure. So does a color measure obtained from a traditional color imaging, typically with three or four channels. In this regard, the difference between a spectral and color measures lies solely in their numbers of channels. Should the two measures then have the same definition? Quantities obtained from different measurements can be combined into an n-dimensional

feature vector. Both, a spectral function coming from a single spectral acquisition and a feature vector of different measurements, are essentially composed of measured quantities. Then, should the two measures have the same definition?

In mathematics, there are several possible definitions for an n-dimensional measure. It is most commonly considered as a vector in the Euclidean space given that the components are independent, which then implies that their order of arrangement does not matter. On the other hand, if the components are correlated, the notion of probability density function can be an alternative. When the order of components must be maintained, the questioned measure could possibly be a sequence such as in DNA matching task, or similar to that of time series. Another possible definition is to regard an n-dimensional measure as a sample in manifold. While there are many possibilities to properly defining a spectral function, in this study the aim is to find the most suitable definition for a spectral function for its use in spectral difference.

The question of mathematical definition of a spectral function can be translated into the question of spectral differences, e.g., distance, similarity, or divergence. Such is because a difference function implicitly defines what a spectral function is in its formulation. As a consequence, validating a difference function requires to validate its inherent assumption of a spectral function. And thanks to this, the validation of whether the spectral function definition is suitable can be carried out through evaluating the response of the questioned difference function. Finally, since both spectral function definition and spectral difference must be validated, the necessity of objective criteria has become indispensable. Another point to consider lies in the fact that a spectral function is not only a mathematical object, but also a measure coming from a physical reality. Therefore, objective criteria to define must incorporate both theoretical criteria and metrological criteria enabling physical validity of the difference function.

In this chapter, after defining the objective criteria, various difference functions are categorized based on their inherent definition of a spectral function and further evaluated with the predefined objective criteria. Organization of the chapter is as follows. Criteria used in evaluating spectral difference functions is provided in Section 3.2. Then, various difference functions are grouped based on their definition of a spectral function, allowing their discussions and evaluations, as given from Section 3.3 to 3.7. Finally, conclusions are drawn in Section 3.8. Note also that mathematical expressions of each distance function that are not found in this chapter will be provided in Appendix A. The core part of this chapter has been published in Article A [56].

3.2 Expected Properties of Distance Function

3.2.1 Theoretical Properties

The notion of difference is a general term used to describe dissimilarity between two objects. And in mathematics, there are several ways in which differences between two objects can be defined and quantified. Among the different ways are, e.g., *distance* (or *dissimilarity*), *similarity*, and *divergence*. The notion of *metric* is often encountered to describe object differences, but in this study its definition is considered to be identical to that of distance[1]. Regardless of which definition of difference is to be employed, we limit the choice to ones that satisfy the properties of a measure, i.e., non-negativity, null empty set, and countable additivity. See Section 2.2.2 for mathematical definition of a measure adapted to the case of spectral function.

With the objective of identifying the most suitable difference function for spectral data, a difference function on a set of spectral functions $\mathcal{S}$ is defined as

$$d\colon \mathcal{S} \times \mathcal{S} \to [0, \infty),$$

where $\forall S_x, S_y, S_z \in \mathcal{S}$ the following holds:

- **Reflexivity**, $d(S_x, S_x) = 0$
- **Non-negativity**, $d(S_x, S_y) \geq 0$
- **Symmetry**, $d(S_x, S_y) = d(S_y, S_x)$
- **Identity of indiscernibles**, $d(S_x, S_y) = 0 \Leftrightarrow S_x = S_y$
- **Triangular inequality** or **subadditivity**, $d(S_x, S_y) \leq d(S_x, S_z) + d(S_z, S_y)$

Note that the properties above are expected properties of a distance function. When it comes to similarity function, their main differences lie in the fact that a similarity function is a distance function which is bounded by 1 from above, e.g., through transformation $d = 1 - sim$. Therefore a similarity function requires $sim(S_x, S_y) \leq sim(S_x, S_x)$ with equality only in the case of $S_x = S_y$. Nevertheless, in the rest of this chapter a difference function will be strictly evaluated based on the properties of a distance. In the rest of this chapter the term *distance* will be used as to generally mean the difference between two spectral functions, without adhering to whether it is strictly distance with respect to the above theoretical properties. The term *difference* will be used when distinction is necessary.

[1] Metric and distance are most often considered as identical, although different definitions can also be found, e.g., as in [65].

3.2.2 Simulated Spectral Functions for the Assessment of Theoretical Properties of Distance

Distance between two arbitrary spectral functions can be described as the transformation it requires to change one spectral function into another, see illustration in Fig. 3.1. In the case of spectral functions S_x and S_y, their magnitudes are identical but S_y can be considered as S_x that is right-shifted by the amount of θ_1. On the other hand, the shapes of S_x and S_z are identical but S_z can be regarded as S_x multiplied by a factor of θ_2. In this regard, the relationship between two arbitrary spectral functions S_x and S_y can be expressed as

$$S_y = t(S_x, \theta),$$

where t is a transformation function with parameter θ, whose evolution is given by a function $f(\theta)$. Then, given a simulated spectral function S, transformation function t, and parameter evolution $f(\theta)$, a set of simulated spectral functions $\mathcal{S}$ with known characteristics can be generated, i.e.,

$$\mathcal{S} = \{t(S, \theta_i),\ \theta_i \in [\theta_{\min}, \theta_{\max}]\}.$$

As the evolution within generated spectral set is controlled, we know that distance between any two spectral functions within the set should be proportional to parameter evolution, i.e.,

$$d(S, t(S, \theta)) \propto f(\theta).$$

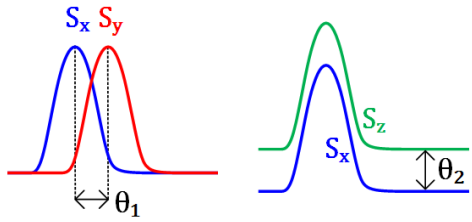

Figure 3.1 – Illustration of distance function as the transformation it requires to change a spectral function into another.

In the following, three transformations t are defined, i.e., magnitude change, translation, and standard deviation change. Magnitude and standard deviation changes in the spectral domain can be considered as the simulation of intensity differences, while translation simulates hue changes in the color domain. Then, in order to focus on the behavior of distance functions against these transformations, a simple function must be used to simulate spectral function S. With such purpose, Gaussian-like distribution function in the following is employed.

$$s(\lambda) = e^{-\frac{1}{2}\left(\frac{\lambda-\mu}{\sigma}\right)^2}$$

The Gaussian-like function is chosen instead of a pure Gaussian function due to the following reasons. A pure Gaussian function is expressed as

$$ae^{-\frac{1}{2}\left(\frac{\lambda-\mu}{\sigma}\right)^2}, \text{ where } a = \frac{1}{\sigma\sqrt{2\pi}}.$$

Due to normalization factor a, imposing a magnification factor in the Gaussian function will not only modify the intensity of a spectral function. It will also slightly modify the shape of a spectral functions since the standard deviation will be modified. Eventually, this does not allow evaluating each individual transformation t, which is only enabled when the normalization factor is removed. With respect to this Gaussian-like function, the aforementioned transformations can now be expressed as follows,

$$t_m(S,\theta) = \theta \cdot \exp -\frac{1}{2}\left(\frac{x-\mu}{\sigma}\right)^2,$$
$$t_t(S,\theta) = \exp -\frac{1}{2}\left(\frac{x-(\mu+\theta)}{\sigma}\right)^2, \text{ and}$$
$$t_{std}(S,\theta) = \exp -\frac{1}{2}\left(\frac{x-\mu}{\theta\cdot\sigma}\right)^2,$$

where θ is given by a monotonically increasing $f(\theta)$. t_m, t_t, and t_{std} are transformations corresponding to magnitude change, translation, and standard deviation change, respectively. Their corresponding spectral sets $\mathcal{S}_m$, $\mathcal{S}_t$, and $\mathcal{S}_{std}$ are as illustrated in Fig. 3.2. Each of these generated spectral sets allows to evaluate the behavior of a difference function with regards to theoretical constraints of distance. Then, if the red-colored spectral function is chosen as the reference, regardless of which set is employed, a questioned difference function is a suitable one if its response is either of the ones shown in Fig. 3.3a. Note that even though in this illustration the responses are symmetrical, the symmetry of response is not required. Difference functions with behavior similar to those depicted in Fig. 3.3b are not the suitable ones for spectral data. Detailed explanation behind the improperness of 'Response 4' in the figure will be given in the next subsection. As for 'Response 5', such behavior demonstrates violation of *identity of indiscernible* property, since

$$d(S_{ref}, S_i) = 0,\ \forall S_i \in \mathcal{S},\ S_i \neq S_{ref}.$$

This response can also be interpreted as the inability of a difference function to detect any differences between two distinct spectral functions.

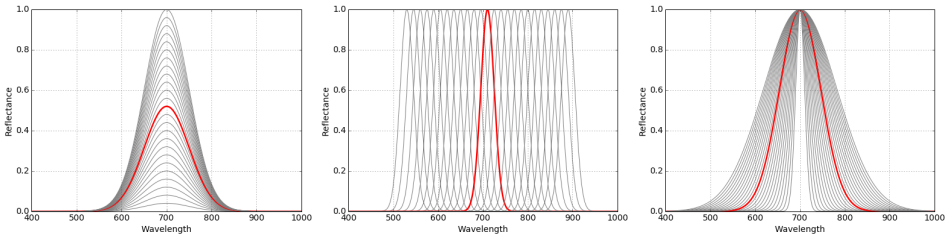

(a) Magnitude change (b) Translation (c) Standard deviation change

Figure 3.2 – Gaussian-like functions (red curves) modified using 3 different transformations, i.e., magnitude change, translation, and standard deviation change, creating 3 spectral sets to be used in the evaluation of distance functions.

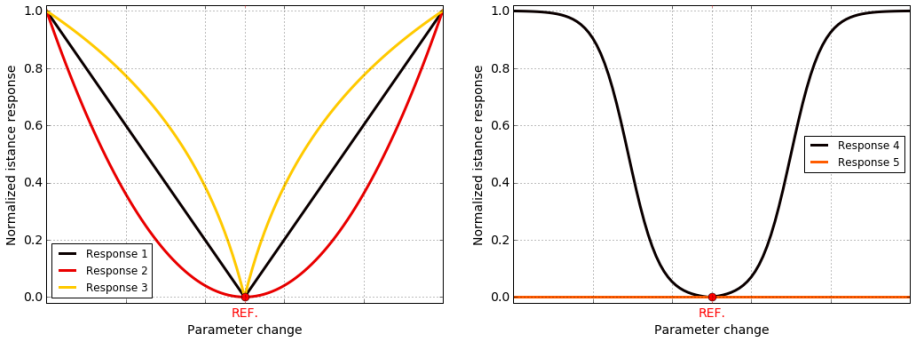

(a) Expected distance responses (b) Inadequate distance responses

Figure 3.3 – The behavior of a suitable spectral distance function must be in one of the three forms shown in (a), with no strict requirement of the symmetry of response. On the other hand, it is not suitable if the distance response matches either of the two cases shown in (b), i.e., stationary or saturating responses.

3.2.3 On Strictly Monotonic Distance Function

Two required properties of a distance function, i.e., *non-negativity* and *triangular inequality*, induce *monotonicity* property. Given a simulated spectral function S, a transformation function t, and two arbitrary parameters θ_1 and θ_2, monotonicity property can be described as

$$d(S, t(S, \theta_i)) \leq d(S, t(S, \theta_j)) \Leftrightarrow \theta_i \leq \theta_j.$$

As a consequence, not only behaviors depicted in Fig. 3.3a are acceptable, but also those in Fig. 3.3b. However, recalling from the previous subsection, 'Response 5'

in Fig. 3.3b is rejected by the *identity of indiscernible* property. Regarding 'Response 4', if a difference function demonstrates such behavior, it means that its sensitivity has a limit. Given a spectral reference, if two distinct spectral functions are 'farther' than this limit, then they would be deemed as identical by the distance function. In other words, after this certain limit, the difference between two spectral functions saturates or can also be regarded as approaching infinity. In order to avoid choosing a distance function which saturates, *strict monotonicity* property below has to be imposed.

$$d(S, t(S, \theta_i)) < d(S, t(S, \theta_j)) \Leftrightarrow \theta_i < \theta_j$$

As will be discovered later in the evaluation of various distance functions, this saturation phenomenon cannot always be avoided. Thus, rather than strictly requiring a difference function to never saturate, it would be judged based on how soon the phenomenon occurs.

3.2.4 Quality Assessment Using Pigment Spectral Sets

Simulating spectral functions by means of a Gaussian-like function and basic mathematical transformations allows evaluating the theoretical behavior of a distance function in a wide range of cases. Albeit a useful protocol, its use cannot imply for the users the validity and usefulness of the function in case of real spectral data. This is because in the real case, a spectral function can rarely be described as a simple Gaussian-like function, not to mention variations and noise that may also occur. Instead, a spectral function can be modeled as a combination of several Gaussian-like functions as well as their integrals.

Spectral reflectance functions originating from three pigment patches are shown in Fig. 3.4, where none is composed of a single Gaussian-like function S_G. Rather, their spectral decompositions could be approximated by

$$\begin{aligned} S_{Orange} &= t(S_S, \theta_i), \\ S_{Blue} &= t\left(S_G^{(1)}, \theta_i\right) + t\left(S_G^{(2)}, \theta_j\right), \text{ and} \\ S_{Green} &= t\left(S_G^{(1)}, \theta_i\right) + t\left(S_G^{(2)}, \theta_j\right) + t(S_S, \theta_k), \end{aligned}$$

where S_S is the integral of S_G. Spectral reflectance function of orange pigment S_{Orange} can be approximated by one integral of S_G. On the other hand, decompositions for S_{Blue} and S_{Green} express that the mathematical transformations occur in combination.

By employing pigment spectral reflectance sets shown in Fig. 3.4, validity and usefulness of a distance function in a real case will be evaluated. For each spectral set, spectral function originating from pixel located in the leftmost of each red

horizontal line will serve as the spectral reference. Then, the expected distance response will be a step function as illustrated in Fig. 3.5, where each step corresponds to color group in the pigment patch. Since spectral variations exist within the data, it follows that there will also be small fluctuations in the step function. Finally, a better distance function will better separate the four groups of spectral reflectance functions, i.e., interclass distance being larger than intraclass variation.

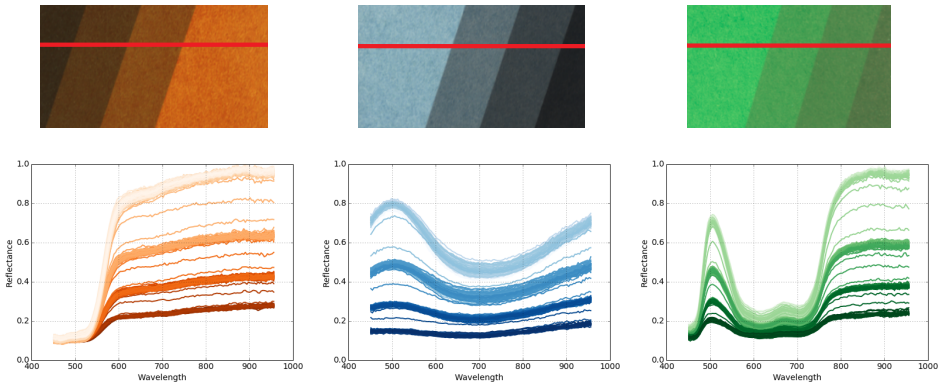

(a) Orange pigment (b) Blue pigment (c) Green pigment

Figure 3.4 – Three pigment patches and their corresponding spectral reflectance functions obtained from pixels under the red horizontal lines. Each pigment patch consists of 4 color groups.

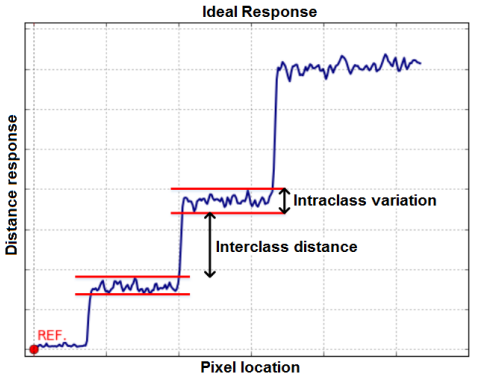

Figure 3.5 – Illustration of an ideal response of a distance function when given spectral reflectance sets shown in Fig. 3.4. Better distance function will give interclass distance which is larger than intraclass variation.

3.3 Spectral Function as Vector in Euclidean Space

3.3.1 Hypothesis of Validity

In the Euclidean space, a vector is represented as n-tuples where each of the axes or dimensions are independent. Therefore, if a spectral function is defined as such, its spectral bands are assumed to be independent. This also implies that the order in which the spectral bands are arranged have no significance. Thus, given any two spectral functions, their distance will remain unchanged regardless of how the spectral bands are arranged.

The aforementioned assumptions are, however, inaccurate. Spectral bands represent the wavelengths of an electromagnetic spectral function. Furthermore, neighboring bands in a hyperspectral image are known to be highly correlated [147]. Finally, as a consequence, the use of a distance function which considers a spectral function as vector in the Euclidean space will yield erroneous measurements.

3.3.2 Consequences on Possible Distance Functions

Many distance functions that fall within this category are derived from the L_p norms (Eq. 3.1). By varying the order p, we obtain Manhattan (p=1), Euclidean (p=2), and Chebyshev (p=∞) distance, which are also metrics. Another variation is when $p < 1$, which was shown by Aggarwal, *et al.* [5] to significantly improve the effectiveness of clustering algorithms for high dimensional data. However, strictly speaking, these fractional variations are not distances since the triangular inequality property is violated [84].

$$d_{L_p}(S_1, S_2) = \left(\int_{\lambda_{\min}}^{\lambda_{\max}} |s_1(\lambda) - s_2(\lambda)|^p \, d\lambda \right)^{\frac{1}{p}} \tag{3.1}$$

Other than varying the order p, other distance functions introduce different weighting function, see equations in Appendix A.1. Such variations can be generalized into, e.g., weighted Manhattan and weighted Euclidean. Examples of weighted Manhattan distance are Canberra [101], Sørensen [161], Kulczynski [65], and Lorentzian [65] distance functions. Root mean square (RMS) distance, Geman-McClure [75], and 2 variations of χ^2 functions are examples of weighted Euclidean distance.

Besides the L_p variations, several other functions can be generalized into angular-based functions, e.., cosine distance and spectral angle [97]. Both functions are based on cosine similarity. Bounded by 1, the values of cosine distance range from 0 for identical spectral functions to 1 for completely different ones. For spectral angle, its value is given in radians.

3.3.3 Validation of Theoretical Behavior

3.3.3.1 The impact of magnitude change to distance measurements

With spectral set $\mathcal{S}_m$ as input, normalized responses of distance functions that consider a spectral function as vector in the Euclidean space can be observed in Fig. 3.6. Note that the normalization is carried out by the following formula:

$$\bar{d} = \frac{d - \min(\mathcal{D})}{\max(\mathcal{D}) - \min(\mathcal{D})},$$

where $\bar{d}$ and $\mathcal{D}$ are normalized distance response and the set of all distance responses, respectively. L_p norm-based distance functions differing only in order of

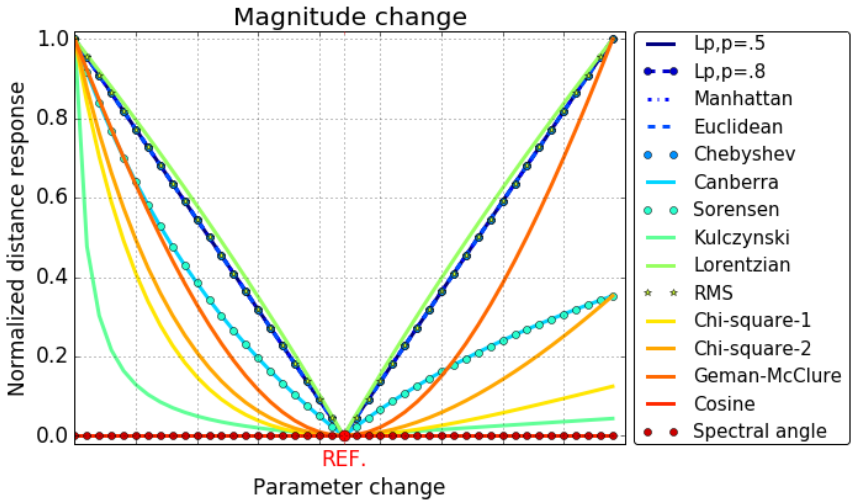

Figure 3.6 – Normalized responses of distance functions that consider a spectral function as vector in the Euclidean space with regards to magnitude change. Responses of fractional Minkowski L_p, Manhattan, Euclidean, Chebyshev, and RMS distance functions are identical and linear. Symmetric and nonlinear responses are given by Lorentzian and Geman-McClure functions. Responses of Canberra and Sørensen functions are identical, asymmetric, and nonlinear. χ^2_1 and χ^2_2 functions are also asymmetric and nonlinear. Stationary zero responses are given by cosine distance and spectral angle.

p yield symmetrical and linear response. The functions are Manhattan, Euclidean, Chebyshev, and the two fractional L_p with $p \in \{0.5, 0.8\}$. Their differences mainly lie in the dynamic ranges of distance values. And as observed in Table 3.1, smaller p generates larger dynamic range. Symmetrical and linear response is also

demonstrated by RMS, which is basically a Euclidean distance weighted by a constant value. Angular-based functions return stationary zero responses. In other words, they do not perceive any differences in 2 spectral functions having different intensity. This is as expected since they are designed to account for shape differences and to suppress magnitude variations.

Table 3.1 – Dynamic ranges of L_p norm-based distance functions. With identical numbers of spectral channels, function of smaller p will have larger dynamic range.

Distance functions	p	**Dynamic range**
Fractional L_p	0.5	4.26×10^4
	0.8	4.46×10^2
Manhattan	1	1.02×10^2
Euclidean	2	5.94×10^0
Chebyshev	∞	4.89×10^{-1}

Lorentzian and Geman-McClure functions yield symmetrical and nonlinear responses, see also Fig. 3.7. Lorentzian modifies the Manhattan distance formulation with a natural logarithm, which explains the nonlinearity and symmetry of the response. Geman-McClure is basically Euclidean distance normalized by itself plus a constant value at each wavelength, and as such, the response is as expected.

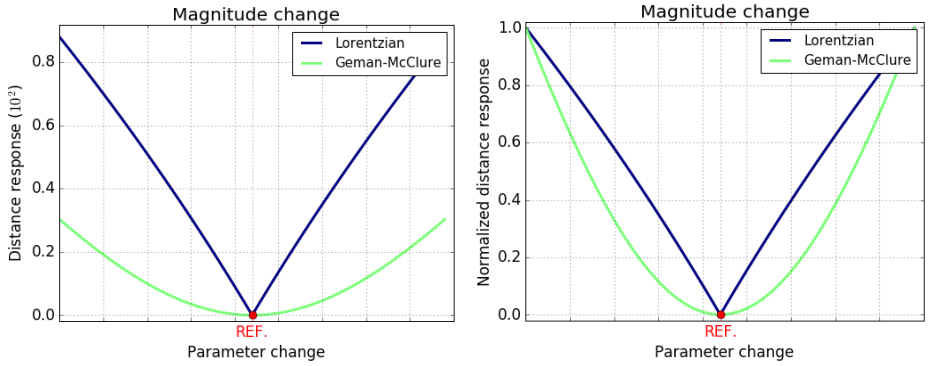

Figure 3.7 – Responses of Lorentzian and Geman-McClure functions to magnitude change, given in real and normalized values.

In Fig. 3.8, nonlinear and asymmetrical responses are presented by Canberra, Sørensen, Kulczynski, χ^2_1, and χ^2_2 functions. Observing their formulations (see details in Appendix A.1), these results are expected. This is because the functions are either weighted Manhattan or Euclidean, with total intensity or region of overlap between two functions as their weighting factors.

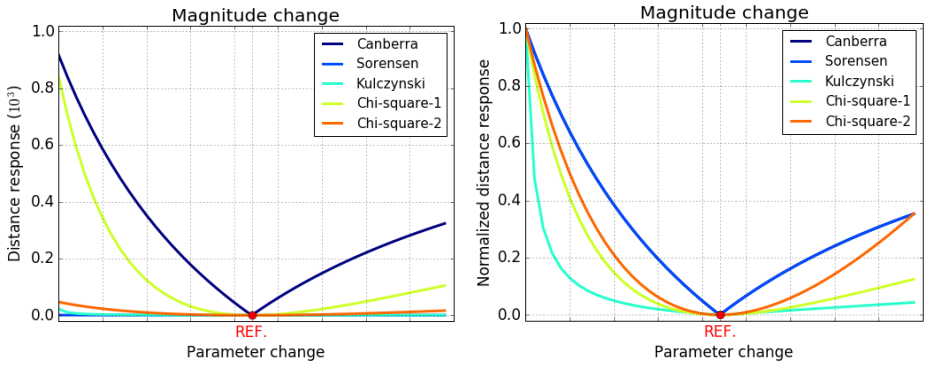

Figure 3.8 – Nonlinear and asymmetrical vector distance responses to magnitude change obtained from Canberra, Sørensen, Kulczynski, χ_1^2, and χ_2^2 functions, given in real and normalized values.

3.3.3.2 The impact of translation to distance measurements

Responses of vector distance functions with respect to translation are shown in Fig. 3.9. As observed, all distance functions saturate, except for Kulczynski. The observed behavior is caused by the calculation of area difference, see Fig. 3.10 where it is shown as the sum of two gray regions. All of the saturating distance functions in Fig. 3.9, except for the angular ones, compute spectral difference by measuring the area difference between two spectral functions S_1 and S_2 through their different variations of $\mid s_1(\lambda) - s_2(\lambda) \mid$. And if we go back to the illustration, this can be expressed as in Eq. 3.2.

$$d(S_1, S_2) \propto \mid s_1(\lambda) - s_2(\lambda) \mid \propto f(\theta) \tag{3.2}$$

In the case of Fig. 3.10a, Eq. 3.2 still holds true with $\theta = \theta_1$. However, this relationship is violated when two spectral functions does not overlap. Or as illustrated in Fig. 3.10b and 3.10c, the translation parameter θ becomes irrelevant as $f(\theta_2) = f(\theta_3) = \text{k}$ where k is a constant value.

For the angular functions, i.e., cosine distance and spectral angle, dot product has the same saturating effect as area difference calculation. And finally, none of the functions that have been discussed so far are strictly monotonic. For Kulczynski function, the normalized response shown in Fig. 3.9 is caused by its weighting factor that takes the element-wise minimum of two spectral functions. Then, as the minimum value converges to 0, which would often be the case for spectral reflectance values of dark objects, the distance value would reach infinity. And for this exact reason, Kulczynski function would not be suitable for spectral data.

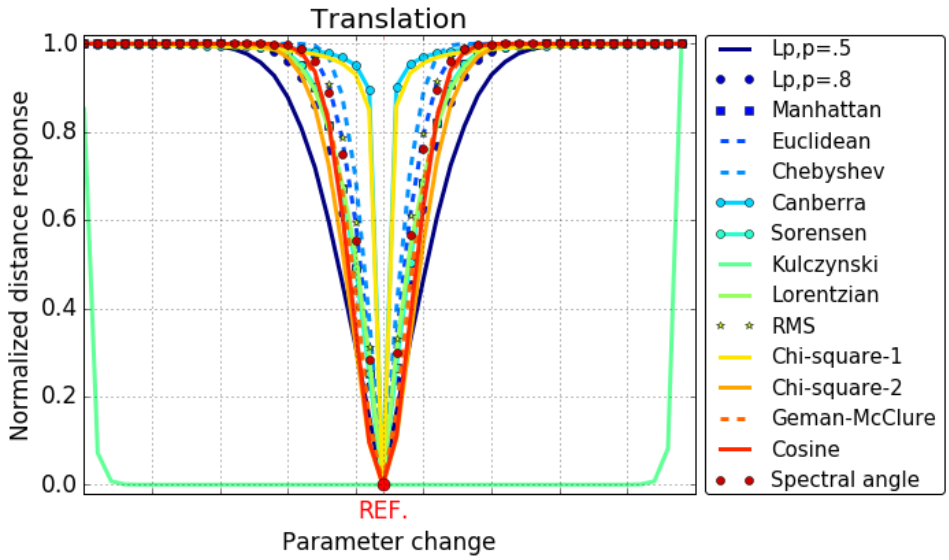

Figure 3.9 – Normalized responses of distance functions which consider a spectral function as vector in the Euclidean space with regards to translation. All distance functions saturate, except for Kulczynski.

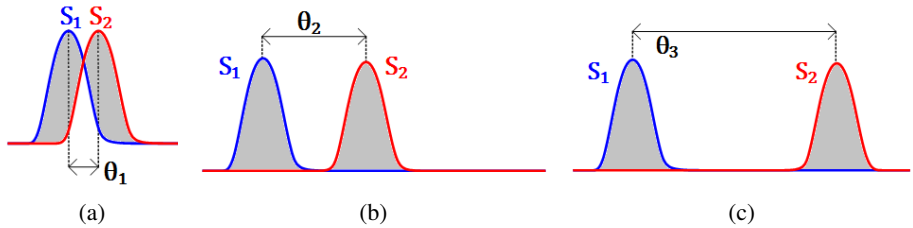

(a) (b) (c)

Figure 3.10 – Illustration explaining saturation phenomenon on functions that compute spectral distance based on difference of area between two spectral functions as what L_p norm does, i.e., the sum of two gray regions in each of the shown cases. In (a), distance between S_1 and S_2 is proportional to the function of translation parameter $f(\theta_1)$. In (b) and (c), translation parameters θ_2 and θ_3 become irrelevant to the sum of gray regions.

3.3.3.3 The impact of standard deviation change to distance measurements

Responses of difference functions that consider a spectral function as vector in the Euclidean space is shown in Fig. 3.11. As observed in the figure, none of the functions faces any particular challenge as in the previous case of translation. The responses are nonlinear and asymmetric which, again, are due to distance calculation that is based on area difference. Nevertheless, the response is still proportional to the function of parameter change, in the sense that distance magnitude increases when parameter value increases.

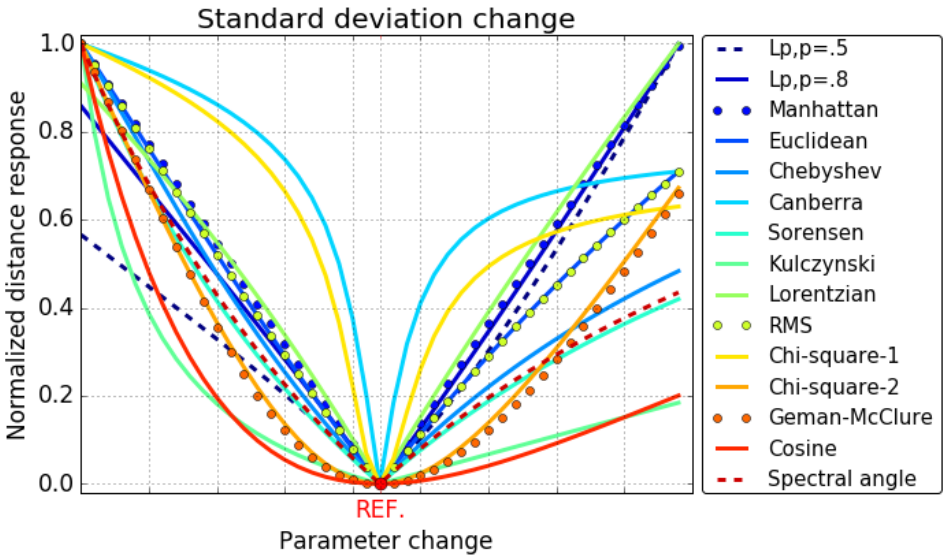

Figure 3.11 – Normalized responses of distance functions which consider a spectral function as vector in the Euclidean space with regards to standard deviation change. Responses of Euclidean distance and RMS are identical. All distance functions yield non-saturating, nonlinear, and asymmetric responses.

3.3.4 Quality Assessment Using Pigment Spectral Sets

Responses of distance functions to the 3 pigment spectral sets previously shown Fig. 3.4 can be found in Fig. 3.12. As observed, in general these functions are able to separate the four groups of color that exist in the pigment judging by four steps in the responses. However, a closer observation in Fig. 3.13a shows that the angular distances demonstrate poor performances. For the blue pigment, intra-class variations produced by the two functions are significantly larger than their interclass distances. Showing the responses in their real values, see Fig. 3.13b, eventually all spectral functions under evaluation are considered as highly similar

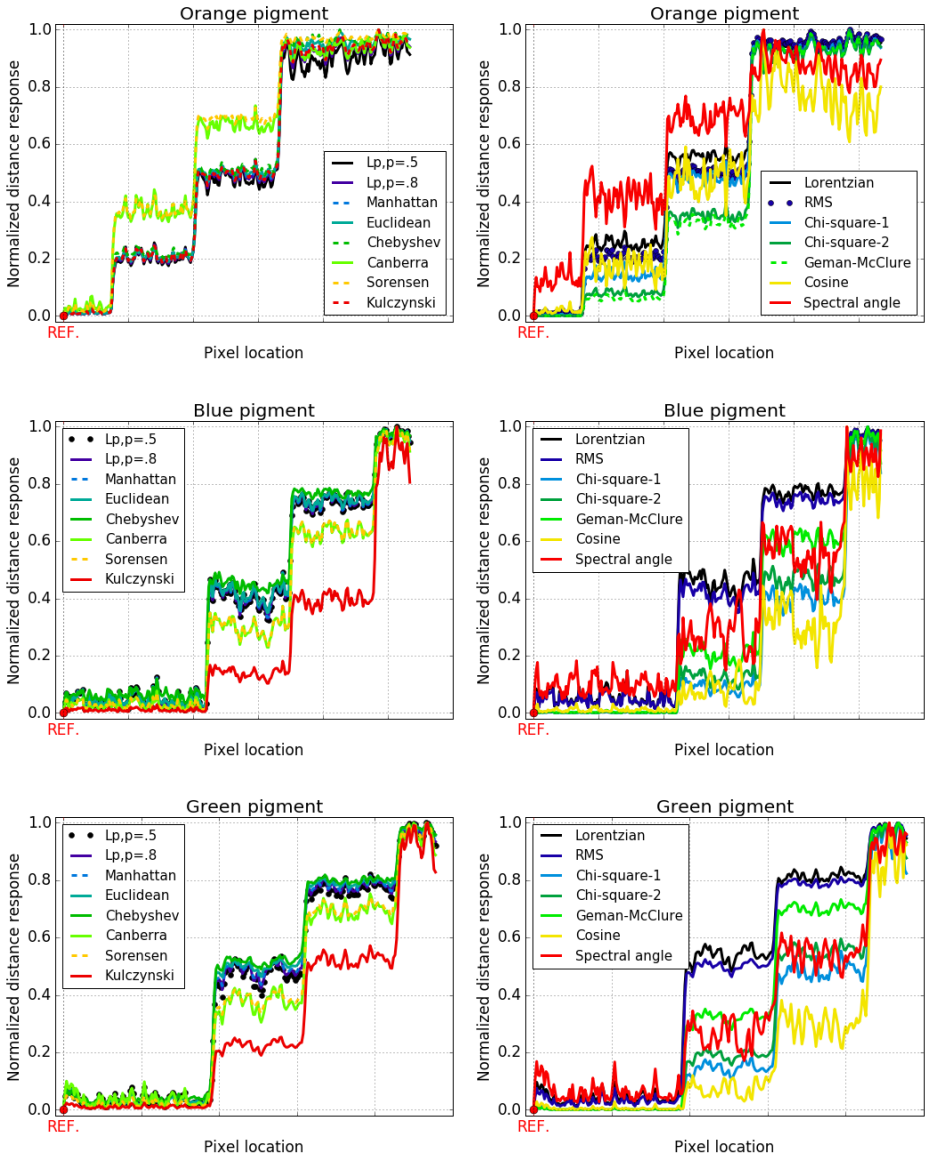

Figure 3.12 – Responses of vector distance functions to pigment spectral sets shown in Fig. 3.4 where spectral function from the leftmost pixel is used as reference. Generally, distance functions in this category are able to separate the 4 groups of colors in each pigment patch, judging by the 4 steps in each distance response.

since their distance values are close to zero. Bearing in mind that variations in the spectral sets are mainly governed by magnitude differences, the observed behaviors are as expected. Angular distances are sensitive to shape differences, e.g., translation, but not to magnitude differences.

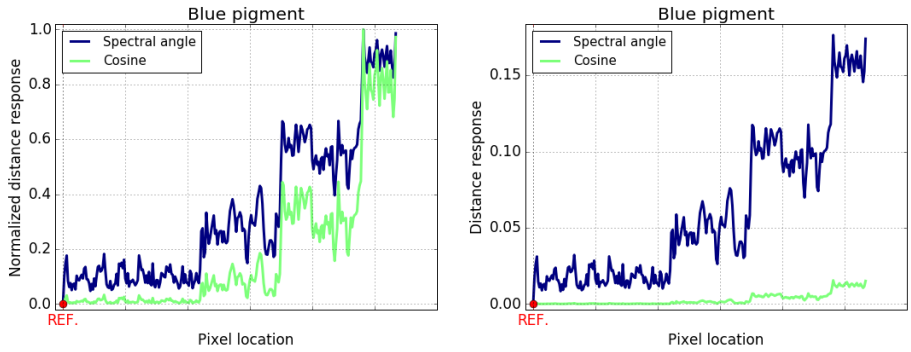

Figure 3.13 – Responses of angular distance functions to the blue pigment, with spectral function originating from the leftmost pixel as reference, shown in normalized and real values.

To summarize, the theoretical properties of each distance functions that have been discussed in this section are provided in Table 3.2. Among the evaluated difference functions, only Manhattan, Euclidean, Chebyshev, and RMS functions that are strictly distance functions. These distance functions, however, failed to satisfy strict monotonicity property since they saturate in the case of translation. The only function that is strictly monotonic is Kulczynski function, which however is not a distance function since it violates the triangular inequality property.

Table 3.2 – Summary of theoretical properties of difference functions which consider a spectral function as vector in the Euclidean space. Among the shown functions, only Manhattan, Euclidean, Chebyshev, and RMS are strictly distance functions. However, they are not strictly monotonic.

Distance functions	RF	NN	SY	II	TI	SM
L_p norm-based functions						
Fractional, p=0.5	✓	✓	✓	✓	✗	✗
Fractional, p=0.8	✓	✓	✓	✓	✗	✗
Manhattan	✓	✓	✓	✓	✓	✗
Euclidean	✓	✓	✓	✓	✓	✗
Chebyshev	✓	✓	✓	✓	✓	✗
Weighted Manhattan						
Canberra	✓	✓	✓	✓	✗	✗
Sørensen	✓	✓	✓	✓	✗	✗
Kulczynski	✓	✓	✓	✓	✗	✓
Lorentzian	✓	✓	✓	✓	✗	✗
Weighted Euclidean						
Root mean square (RMS)	✓	✓	✓	✓	✓	✗
χ^2_1	✓	✓	✓	✓	✗	✗
χ^2_2	✓	✓	✓	✓	✗	✗
Geman-McClure	✓	✓	✓	✓	✗	✗
Angular-based functions						
Cosine	✓	✓	✓	✗	✓	✗
Spectral angle	✓	✓	✓	✗	✓	✗

RF–reflexivity, **NN**–non-negativity, **SY**–symmetry, **II**–identity of indiscernible, **TI**–triangular inequality, **SM**–strict monotonicity

3.4 Spectral Function as N-Dimensional Data in Manifold

3.4.1 Hypothesis of Validity

While assuming that a spectral function is a vector in the Euclidean space is incorrect, it can possibly be assumed as an n-dimensional data whose spectral variations form a manifold. In addition to the classical approach of directly measuring the difference between two spectral functions, another approach considers a spectral function within the entire deployment of spectral set in a graph. In this way, rather than directly measuring distance between two spectral functions, the approach is centered around the assessment of local distance between neighboring spectral functions within the graph.

3.4.2 Consequences on Possible Difference Functions

Goodness-of-fit coefficient (GFC) is one example of the straightforward distance expressions in this category, which was originally used to test the accuracy of reconstructed spectral functions of daylight [82]. If GFC is to be used with data which is assumed to be vector in the Euclidean space, it will be equivalent to cosine distance. See mathematical expression of GFC in Appendix A.2.

In parallel, Tenenbaum *et al*. [170] and Roweis *et al*. [148] proposed a new way to consider a set of spectral functions, i.e., as manifolds where each spectral function is represented by a node in a graph. With this new point of view, the dimensionality of spectral variations can be reduced using either of the proposed algorithms, i.e., isometric feature mapping (Isomap) [170] and Locally Linear Embedding (LLE) [148]. Several more advanced algorithms are Locally Linear Coordination (LLC) [168] and manifold charting [31]. See mathematical expression of Isomap in Appendix A.2.

The LLE algorithm considers that each spectral function is a weighted combination of a trusted set of nearest neighbors. It then computes the minimally distorting low-dimensional barycentric embedding [31, 148]. The main idea behind LLE algorithms is that the n-dimensional values mostly consist of noise or inaccurate features and that the lattice or neighborhood structure is more important than data values. In Isomap, a distance between two spectral functions can be expressed as a sum of local distances between the two spectral functions and their immediate neighbors in a trusted set of spectral functions; local distances are typically computed with Euclidean distance or dot product. Isomap is considered as a global method as it preserves the global geometric features of the initial spectral set. Several applications of Isomap for hyperspectral images are available [31, 50]. In the following evaluation, it is only the Isomap construction that is to be considered as valid measure since it preserves the global structure of the spectral functions lattice.

3.4.3 Validation of Theoretical Behavior

Responses of GFC when given the three basic transformations can be observed in Fig. 3.14. GFC cannot detect differences in magnitude resulting in zero distance despite the different spectral functions. This stationary zero response demonstrate the inability of GFC to satisfy identity of indiscernibles property. Hence, GFC is not a measure of distance. For translation, GFC saturates and violates strict monotonicity. Its response to standard deviation change does not present any apparent problem. In summary, the behavior of GFC is identical to that of cosine distance and it is not a distance.

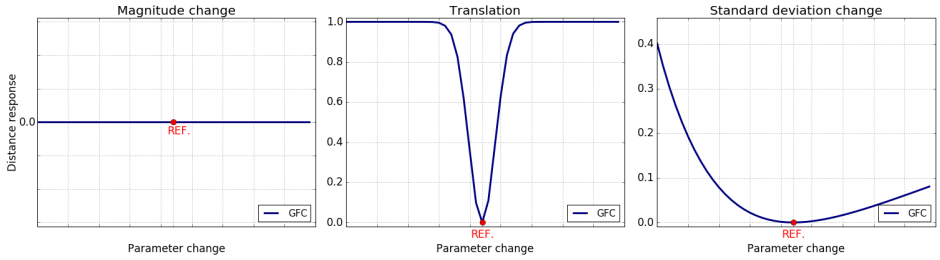

Figure 3.14 – Responses of GFC to magnitude change, translation, and standard deviation change. Vertical axes of all plots corresponds to distance response. Stationary zero response to magnitude change shows that GFC is not a distance measure since it violates the identity of indiscernible property. Its response to translation saturates and violates strict monotonicity. Response to standard deviation change does not present any apparent problem.

Regarding Isomap, distance between two spectral functions must be assessed inside a lattice structure. Thus, in order to evaluate its theoretical behavior, a lattice structure as illustrated in Fig. 3.15 is constructed. Beginning with a spectral function S, simulated spectral functions located in the same row as S, i.e., $S_{t1}, S_{t2}, \ldots, S_{tn}$, are S modified by increasing translation parameters given by $f(\theta_t)$. Simulated spectral functions $S_{m1}, S_{m2}, \ldots, S_{mn}$ which are located on the same column as S are obtained by modifying S with increasing magnitude change parameter given by $f(\theta_m)$. The rest of spectral functions in the lattice are obtained by modifying S by both translation and magnitude change parameters. This lattice is then passed onto Isomap, together with the numbers of neighbors and components, for it to carry out dimensionality reduction. The number of neighbors dictates how many adjacent spectral functions are allowed in the graph constructed by Isomap, while number of components is the number of channels in the reduced dimension. It is only after this dimensionality reduction that Isomap can compute local distances between neighboring spectral functions.

Taking one row from the lattice shown in Fig. 3.15 as target and spectral function located in the middle as reference, performance evaluation of Isomap with respect to translation is obtained, see Fig. 3.16. Three distance functions are chosen arbitrarily to compute the local distances, i.e., Euclidean, Canberra, and GFC. In this figure, distance responses obtained with varying numbers of neighbors and components are also given. By observing each subfigure, we know that depending on the chosen local distance function, the performance of Isomap will vary. However, rather than the distance function, it is the lattice structure that bears more importance in Isomap. Its significance can be seen by observing how much a curve

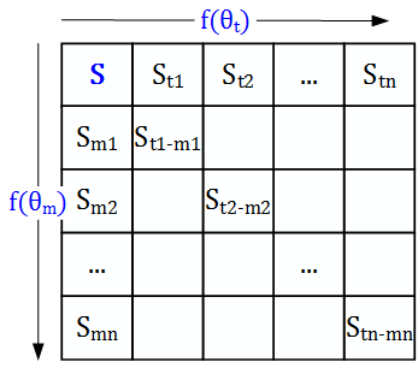

Figure 3.15 – Lattice structure of simulated spectral functions constructed using translation and magnitude change transformations. Spectral functions along the same row as S are obtained by modifying S with increasing translation parameters given by $f(\theta_t)$. For those located on the same column, they are obtained by modifying S with increasing magnitude change parameter given by $f(\theta_m)$. The rest of spectral functions in the lattice are obtained by modifying S by both translation and magnitude change parameters.

produced by a single distance function changes when the number of neighbors or components are modified. Due to this, the use of Isomap is not always appropriate. It could potentially be a good choice when the distance between two spectral functions are to be assessed, taking into consideration their pixel locations in a given image. Furthermore, lattice density of the image in which these two spectral functions are contained will also affect the accuracy of computed distance. When the lattice is dense, the obtained local distances will be closely related to the chosen local distance function. On the other hand, when lattice is sparse, computed distance will be more closely related to the Isomap algorithm itself. Finally, due to the aforementioned considerations, theoretical properties of Isomap cannot always be guaranteed and Isomap will not be further considered in the following evaluation. Summary of theoretical properties of manifold distance functions is provided in Table 3.3.

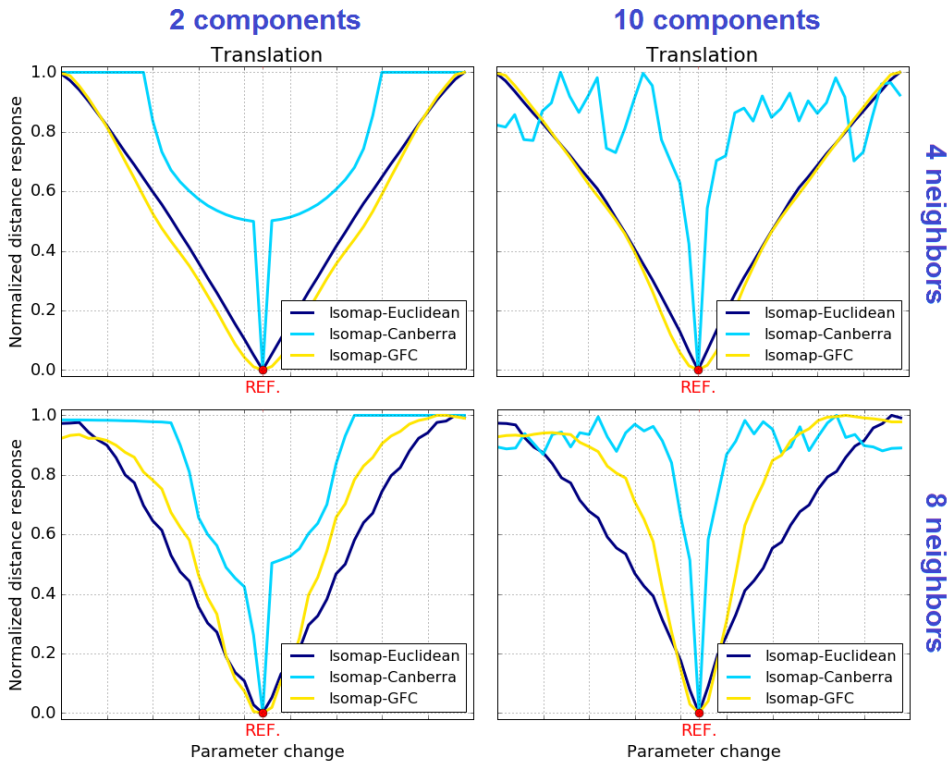

Figure 3.16 – Normalized responses of Isomap combined with 3 distance functions with respect to translation transformation, and with varying numbers of neighbors components. All axes are with identical units and dynamic ranges.

Table 3.3 – Summary of theoretical properties of difference functions which consider a spectral function as n-dimensional data in manifold. Despite Isomap-Euclidean satisfying the properties of distance function, it is not suitable for spectral data since the distance computation depends on the density of input lattice.

Distance functions	**RF**	**NN**	**SY**	**II**	**TI**	**SM**
GFC	✓	✓	✓	✗	✓	✗
Isomap-Euclidean	✓	✓	✓	✓	✓	✗
Isomap-Canberra	✓	✓	✓	✓	✗	✗
Isomap-GFC	✓	✓	✓	✗	✓	✗

RF–reflexivity, **NN**–non-negativity, **SY**–symmetry, **II**–identity of indiscernible, **TI**–triangular inequality, **SM**–strict monotonicity

3.4.4 Quality Assessment Using Pigment Spectral Sets

When given spectral sets coming from pigment patches in Fig. 3.4, GFC respond as shown in Fig. 3.17. It can be observed that, generally, GFC manages to detect the four different color shades existing in the spectral set. However, it is rather challenged in one case of where blue pigment is the target. Observing the two steps in the middle of response to the blue pigment, their intraclass variations are larger than the interclass distance. Then, in a closer observation, values returned by GFC are very reduced and close to zero. Considering the dynamic range of GFC distance that would reach unity, these values are rendered insignificant. Nevertheless, this behavior is in line with the purpose of GFC, i.e., to measure shape rather than magnitude differences. And to recall, variations in the pigment spectral set is mainly governed by magnitude differences.

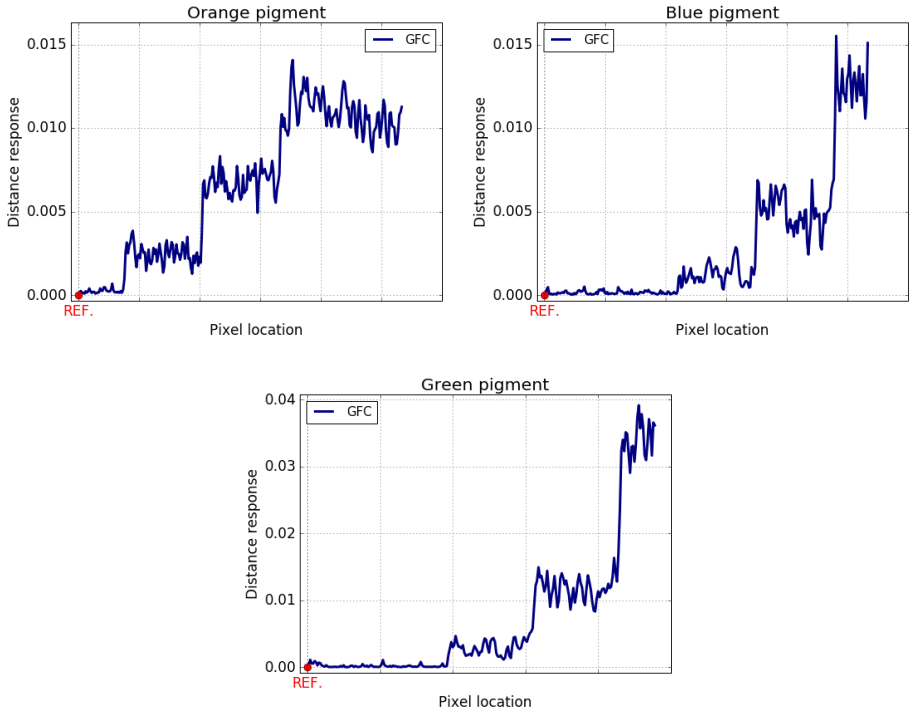

Figure 3.17 – Responses of GFC to 3 spectral sets originating from pigment patches shown in Fig. 3.4. Generally, GFC is able to detect the 4 different color shades existing in the spectral set. However, the intraclass variations between the two middle shades of the blue pigment are larger than the interclass distance. Then, values returned by GFC are also significantly reduced and close to 0.

3.5 Spectral Function as Distribution

3.5.1 Hypothesis of Validity

By assuming that a spectral function is a distribution, it is also assumed that the spectral bands are ordered. Not only that, neighboring spectral bands are considered to be more correlated than those which are further away. These assumptions do agree with the common knowledge about spectral data, i.e., highly-correlated neighboring spectral bands [147]. As distribution, a spectral function could then be represented as probability density function (PDF), cumulative distribution function (CDF), or discrete probability distribution (or more commonly known as *histogram*). However, note that neither spectral reflectance nor radiance functions can be considered as PDF because their integrals are not 1.

3.5.2 Consequences on Possible Distance Functions

Spectral correlation, initially developed for spectral correlation mapper (SCM) [54] in the remote sensing field, is a measure of similarity. Aiming to minimize the effect of shading in the processing of remotely-sensed images, spectral correlation was designed to not account for magnitude differences. Although this characteristic is identical to that of spectral angle (see Section 3.3), spectral correlation was claimed to be more accurate than spectral angle. Pearson χ^2, or also known as χ^2 statistics [142, 149], is a function that measures the likelihood of one distribution to be drawn from population distribution as represented by the average.

Another way of computing distance between two PDFs or histograms is considering the area under curves. Generally there are two slightly different approaches to measure the area under curves, see illustration in Fig. 3.18. In the first approach, the difference between two spectral functions is calculated through the overlapping area under the two curves, or $\min_\lambda(S_1, S_2)$. See also illustration in Fig. 3.18a. An example of such measure is Smith distance [165]. Then, the 2nd approach can be generally considered as computing area difference between two curves as follows:

$$\mid S_1 - S_2 \mid = \mid s_1(\lambda) - s_2(\lambda) \mid, \ \forall \lambda \in [\lambda_{\min}, \lambda_{\max}]$$

See illustration in Fig. 3.18b. Manhattan distance and its variations (see Section 3.3) can be considered as taking this approach, albeit with different assumptions of the definition of spectral function.

Then there is a family of difference measure, e.g., f-divergences. Strictly, these functions are divergence and not distance functions. Many divergence measures are not symmetrical, e.g., Kullback-Leibler (KL) divergence [98] and K-divergence, and therefore will not be considered as a suitable difference function for spectral data. The symmetric ones are, e.g., Jeffrey divergence [85], Jensen-Shannon di-

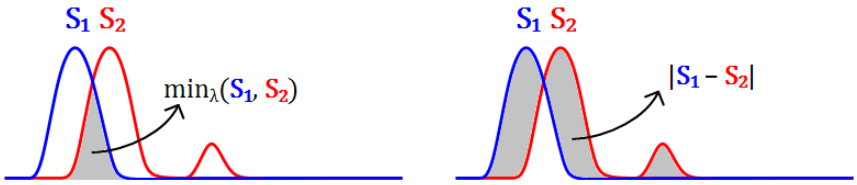

(a) Overlapping area (b) Area difference

Figure 3.18 – Illustration of two different approaches in measuring spectral differences by means of area under curves.

vergence [112], and empirical Jeffrey-divergence which was initially developed to deal with histogram bins [142]. Spectral information divergence (SID) [42], which is essentially Jeffrey divergence, is a divergence measure commonly used in the remote sensing field. Other difference functions include squared-chord distance [74, 132], earth mover's distance (EMD) [149], and Combined EMD [104]. See mathematical expressions of the aforementioned functions in Appendix A.3.

3.5.3 First Proposal of Spectral Distance Function

After studying the behavior and limitation of distance functions that are based on L_p norm, see illustration in Fig. 3.10, we know that the proper use of these functions are when two spectral functions have similar shape. This similarity in shape can further be described as having overlapping regions under the two spectral curves. In order to overcome this limitation, we have an early proposal of a suitable spectral distance function in which a spectral function is considered as a CDF, i.e., Euclidean distance of cumulative spectrum (ECS) [56].

As seen in the mathematical expression of ECS in Eq. 3.3, each input spectral function is transformed into its cumulative version by $\int_{\lambda_{\min}}^{\lambda} s(\lambda)\ d\lambda$, in which the integration (or summation in discrete case) goes from shorter to longer wavelengths. The distance computation will only be carried out after this transformation. As a consequence, despite the fact that the distance function is still insensitive to shape differences, we make sure that both shape and magnitude differences are integrated in the transformed spectral function. Thanks to this, saturation phenomenon suffered by the L_p norm based functions is no longer an issue in ECS.

$$
\begin{aligned}
d_{ECS}(S_1, S_2) &= \left(\int_{\lambda_{\min}}^{\lambda_{\max}} \left(s_1'(\lambda) - s_2'(\lambda) \right)^2 \ d\lambda \right)^{\frac{1}{2}} \\
s_i'(\lambda_c) &= \int_{\lambda_{\min}}^{\lambda_c} s_i(\lambda)\ d\lambda
\end{aligned}
\tag{3.3}
$$

To give better understanding, illustration is also provided in Fig. 3.19. Two pairs of spectral functions, S_1 and S_2, are given where in each pair the two functions have identical shape but different displacement. Ideally, the two pairs will yield different distance values. But we know that this is not the case for L_p norm based functions since the sum of area under the two spectral curves, as marked by green color, are identical. Considering a spectral function by its cumulative or integrals allows to diminish the limitation. Area under the two cumulative spectral curves becomes different, as marked by the blue regions, and therefore properly reflecting the real displacement in each pair of spectral functions.

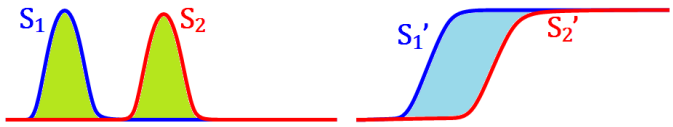

(a) Spectral function pair, #1, in their (**left**) original and (**right**) cumulative forms.

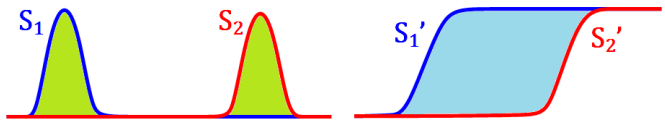

(b) Spectral function pair, #2, in their (**left**) original and (**right**) cumulative form.

Figure 3.19 – Two pairs of spectral functions S_1 and S_2 with identical shape but different displacement. Despite the different displacement, computing spectral differences in the original form of the spectral functions yields identical distance, as marked by the green area. However, the distance will differ if its computed in the cumulative form of the spectral functions, as marked by the blue area.

Despite being superior to other distance functions due to its avoidance of saturation phenomenon, ECS is not without limitation. Its integration that goes from shorter to longer wavelengths inherently assumes more importance to the shorter wavelengths. Or, if wavelength is expressed as a discrete sequence $\lambda_0, \lambda_1, \ldots, \lambda_n$, the importance of a wavelength λ_i would be equivalent to $(n-i)$. Indeed, the integration can be flipped over such that it goes from longer to shorter wavelengths, giving more importance to the longer wavelengths. But the bigger issue lies on the prioritization of the wavelengths. When integration goes from shorter wavelengths, it means that shape differences in this spectral range is more important than those on the other spectral ranges. This prioritization of certain spectral range can be correct when priorities are known beforehand or when it can be correctly imposed on the spectral data. In most cases, however, priorities over the wavelengths are unknown therefore risking inaccurate distance measurements. Due to this inherent prioritization, ECS is similar to lexicographic ordering relation in Section 4.3.3.

3.5.4 Validation of Theoretical Behavior

3.5.4.1 The impact of magnitude change to distance measurements

Theoretical behaviors of distance functions in this category with respect to magnitude change can be observed in Fig. 3.20. Functions that give zero responses when given spectral set with magnitude variations violate identity of indiscernible property. They are spectral correlation, Smith distance, Jeffrey divergence (or SID), and Jensen-Shannon divergence. The desired responses areobtained by Pearson χ^2, ECS, squared-chord, and empirical Jeffrey divergence functions.

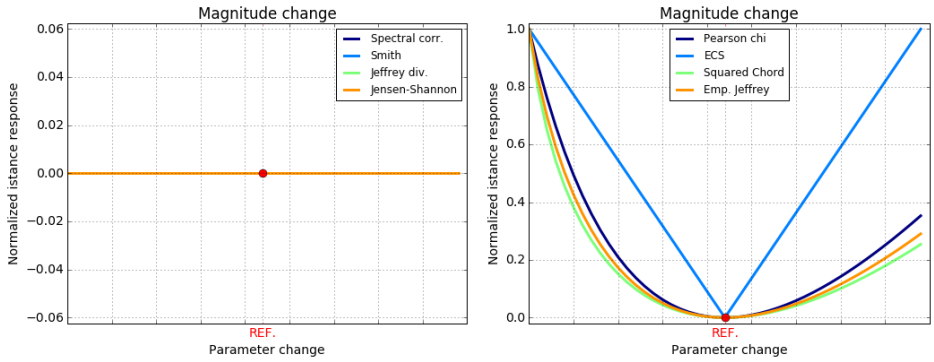

(a) Functions violating identity of indiscernible

(b) Functions with expected behavior

Figure 3.20 – Normalized responses of distance functions that consider a spectral function as distribution with regards to magnitude change. Spectral correlation, Smith distance, Jeffrey divergence, and Jensen-Shannon divergence violate the property of identity of indiscernible. Thus, they are not distance functions.

3.5.4.2 The impact of translation to distance measurements

The impact of translation to difference functions in this category can be observed in Fig. 3.21. Note that only values in Fig. 3.21a that are normalized and the response of Jeffrey divergence in Fig. 3.21b is scaled down with a factor of 100. All difference functions found in Fig. 3.21a violates strict monotonicity property, and finally only Jeffrey divergence and ECS do not saturate.

3.5.4.3 The impact of standard deviation change to distance measurements

Given a set of spectral functions with variations of standard deviation, the responses of distance functions under evaluation are as shown in Fig. 3.22. These distance responses are given in normalized values. Upon observation, only Smith distance does not give the desired behavior. Observed behavior is due to its use of

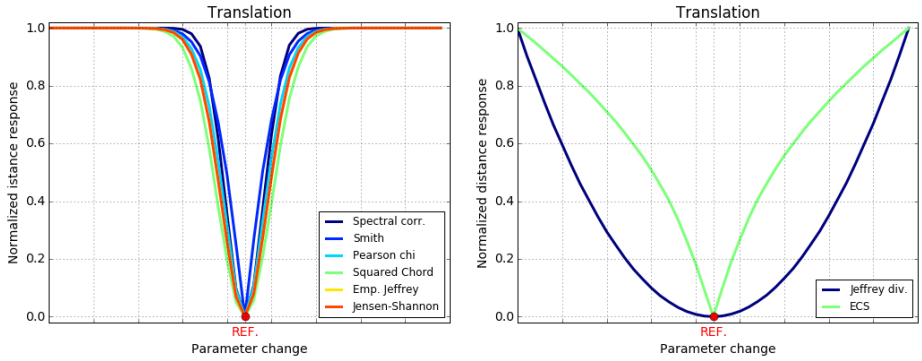

(a) Functions violating strict monotonicity (b) Functions with expected behavior

Figure 3.21 – Normalized responses of distance functions that consider a spectral function as distribution with regards to translation. Among the shown functions only Jeffrey divergence and ECS satisfy the strict monotonicity property.

minimum function, see equation in Appendix A.3. And since in the spectral set that corresponds to standard deviation change one spectral curve is always marginally larger than the other, or $s_1(\lambda) \leq s_2(\lambda),\ \forall\lambda \in [\lambda_{\min}, \lambda_{\max}]$, Smith distance will always return 0 distance for every pair of spectral functions. Finally, a summary of theoretical properties of functions in this category can be found in Table 3.4.

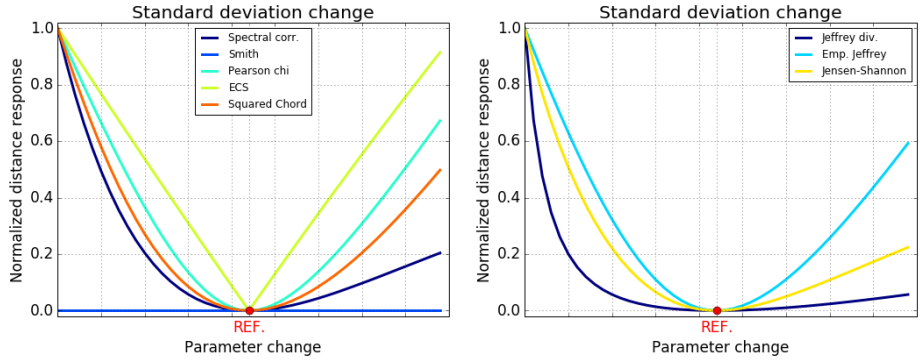

(a) Distance/ similarity functions (b) Divergence functions

Figure 3.22 – Normalized responses of difference functions that consider a spectral function as distribution in case of standard deviation change. Smith function violates identity of indiscernible property due to its stationary zero response. The other functions do not show apparent problem.

Table 3.4 – Summary of theoretical properties of difference functions which consider a spectral function as distribution. The proposed ECS is a distance function and is strictly monotonic, making it a suitable choice for use with spectral data.

Distance functions	RF	NN	SY	II	TI	SM
Correlation-based functions						
Spectral correlation	✓	✓	✓	✗	✓	✗
Pearson χ^2	✓	✓	✓	✓	✗	✗
Measure of area under curves						
Smith	✓	✓	✓	✗	✓	✗
ECS	✓	✓	✓	✓	✓	✓
f-divergences						
Jeffrey divergence	✓	✓	✓	✗	✗	✗
Empirical Jeffrey	✓	✓	✓	✓	✗	✗
Jensen-Shannon divergence	✓	✓	✓	✗	✓	✗
Other functions						
Squared chord	✓	✓	✓	✓	✗	✗

RF–reflexivity, **NN**–non-negativity, **SY**–symmetry, **II**–identity of indiscernible, **TI**–triangular inequality, **SM**–strict monotonicity

3.5.4.4 On distance functions requiring optimization step

In this category of distance between two distributions, it has been previously mentioned that EMD and Combined EMD will be evaluated. What separates the two functions from the others from this category is their use of an optimization loop in finding the minimum necessary cost to transform one distribution to another. The responses of these two functions in the three spectral sets can be observed in Fig. 3.23. Note that for Combined EMD, the parameter α is set to 0.5, see equation in Appendix A.3. In the cases of magnitude change and translation, there is no significant problem as the growth of their distance values reflect the evolution within the spectral sets, even though they are neither linear nor symmetric. Problems do arise in the case of standard deviation change and this is due to the optimization procedure that is required by EMD.

Generally, the challenge with requiring an optimization loop is in the risk of reaching a local minimum. Thus, in addition to the actual constraints of the function to be optimized, another stopping criteria is needed for when a local minimum is reached, i.e., maximum number of iteration. Apart from the technical solutions that could be implemented to avoid the local minimum, the risk of losing accuracy is always apparent. Furthermore, it also induces that the theoretical properties of

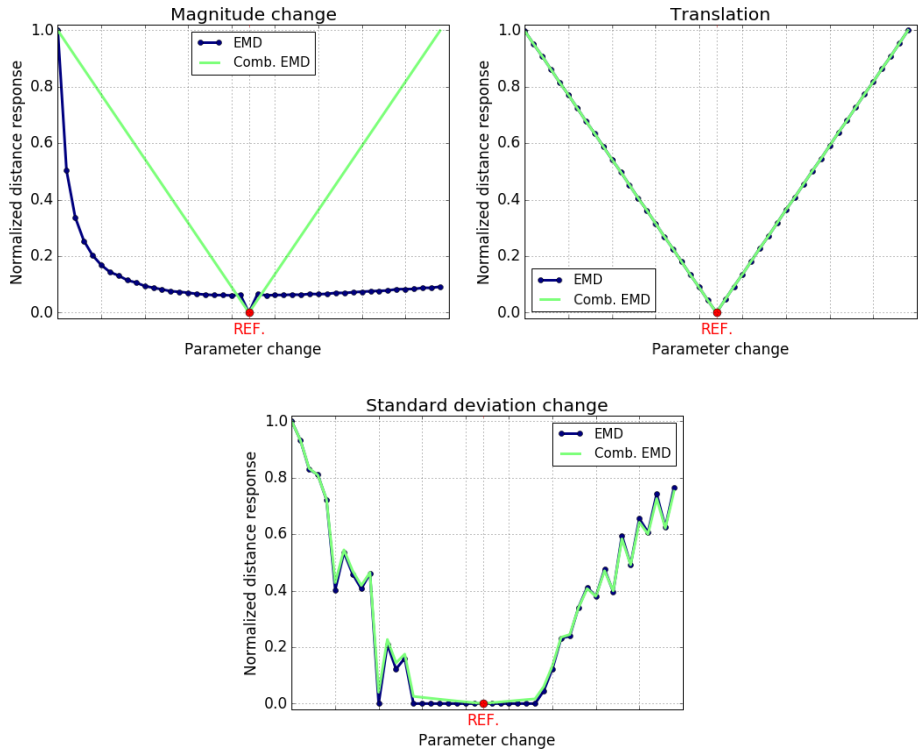

Figure 3.23 – Normalized distance responses of EMD and Combined EMD to spectral sets corresponding to magnitude change, translation, and standard deviation change. Due to its optimization procedure, both distance functions become unstable as demonstrated by the case of standard deviation change.

distance cannot always be guaranteed. For this reason, EMD and Combined EMD will not be taken into further considerations.

3.5.5 Quality Assessment Using Pigment Spectral Sets

Given spectral reflectance sets as shown in Fig. 3.4, the responses of difference functions in this category which are less sensitive to magnitude differences can be observed in Fig. 3.24. In this figure, responses for all pigments are shown in real values and normalized values. In figures providing responses in real values (images in the first column), it can be observed that the responses are relatively close to zero, demonstrating a reduced capability in detecting spectral differences that are mainly governed by magnitude. Although there is also an exception, i.e., the response of spectral correlation with respect to the blue pigment. Also, note

that for spectral correlation, the maximum value is 1. These responses are not unexpected since it is exactly what is intended by their respective mathematical expressions, i.e., to suppress the effect of magnitude differences. This is also the main reason why the intraclass variations are generally larger than the interclass distance, see images in the second column of Fig. 3.24. These kinds of difference functions can generally find their use in the remote sensing field, where in many cases the effect of shading are to be eliminated. Although, if among the four functions one is to be selected for such purpose, Smith distance would be a better candidate since in all shown cases it generally gives much closer responses to zero.

Difference functions with better capability in separating the four color shades in the pigment spectral set shown in Fig. 3.4 are Pearson χ, ECS, squared-chord, and empirical Jeffrey divergence. Their normalized distance responses can be observed in Fig. 3.25. As for ECS, as previously mentioned, distance response would differ depending on whether the integration goes from shorter to longer wavelengths or vice versa. This effect can be observed in Fig. 3.26, in which spectral set of the green pigment is employed.

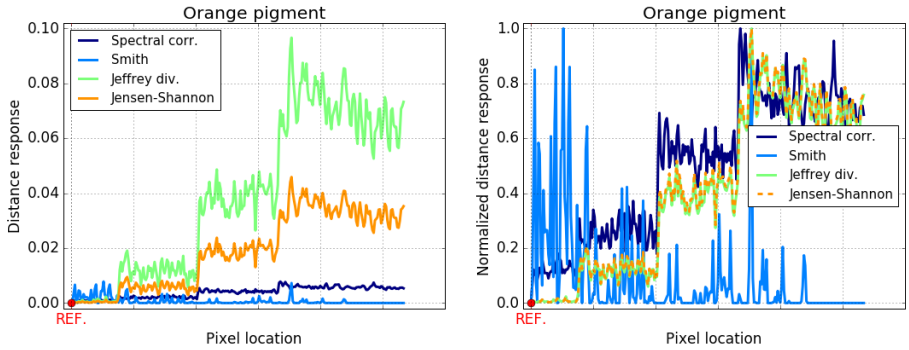

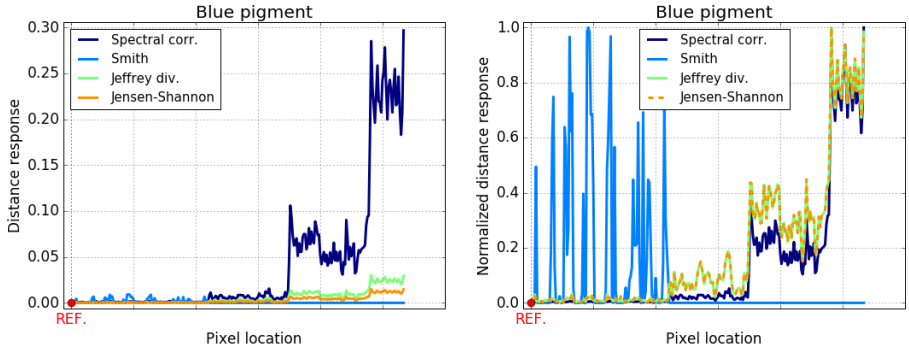

(c) (d)

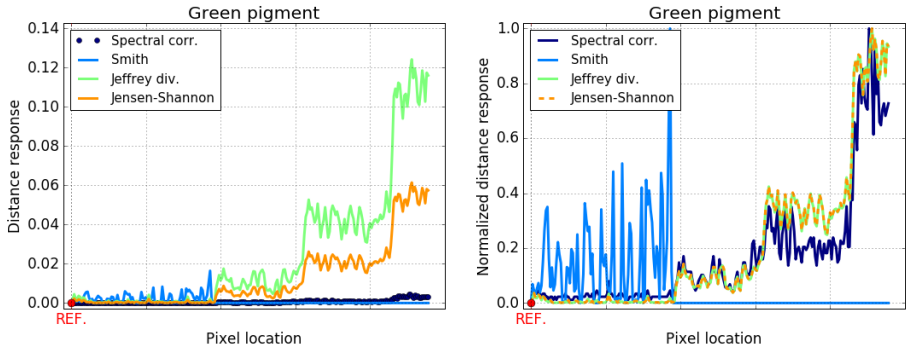

(e) (f)

Figure 3.24 – Responses of spectral difference functions that are less sensitive to magnitude differences to pigment spectral sets shown in Fig. 3.4. In the normalized values, responses of Jeffrey and Jensen-Shannon divergence functions are almost identical. Responses of Smith function is very close to 0. However, in the normalized version, it can be observed that the response is rather noisy.

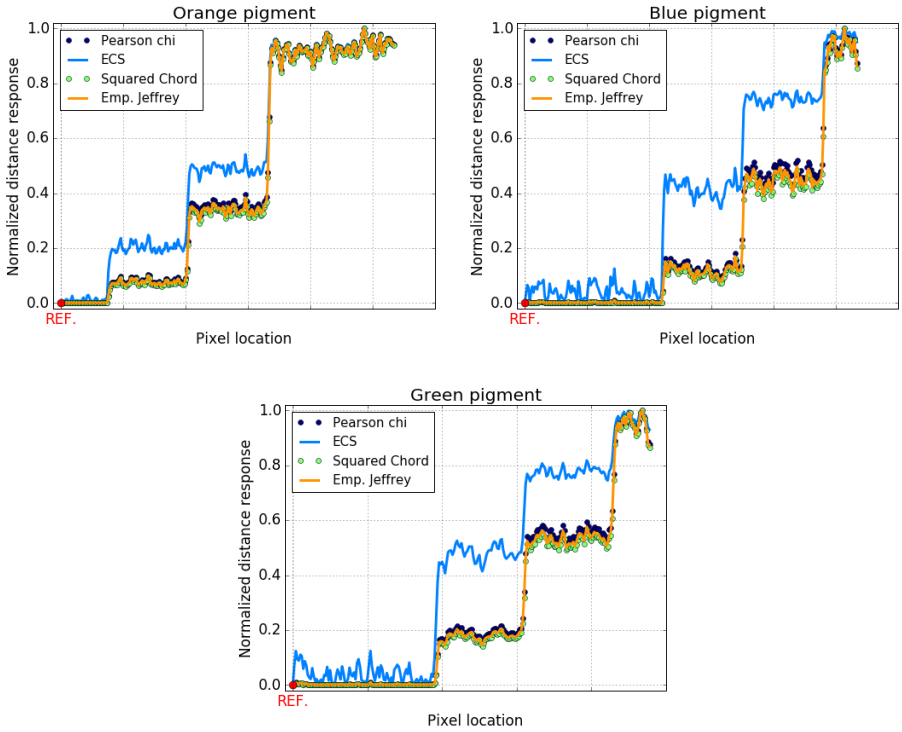

Figure 3.25 – Normalized responses of difference functions which are able to separate 4 color shades which exist within pigment spectral sets shown in Fig. 3.4. Obtained intraclass variations are always smaller than interclass distance between the color shades.

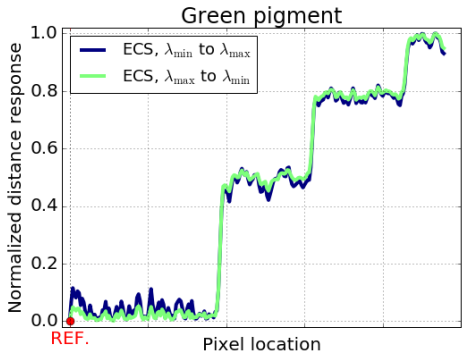

Figure 3.26 – ECS distance function would give different response depending on whether integration goes from shorter to longer wavelengths or vice versa. The shown graphs are obtained from the spectral set of green pigment given in Fig. 3.4.

3.6 Spectral Function as Sequence

3.6.1 Hypothesis of Validity

This category is inspired by distance functions used in the task of matching DNA sequences [83, 152]. If a spectral function is considered as a sequence, it means that its spectral bands or channels are ordered by its position in the sequence. Its other assumption is that the spectral function values come from a finite set. The latter assumption is incorrect since spectral data is represented by real numbers which is an infinite set of values.

3.6.2 Consequences on Possible Distance Functions

Distance functions that fall into this category come from those that are mainly used for string matching. Hamming distance [80] measures differences between two sequences based on the minimum number of character substitutions required to transform one string into another. This distance is only applicable if the two sequences are of the same length. In Levenshtein distance [109], instead of only taking into account character substitution, it considers all single character edit, i.e., insertion, deletion, and substitution. Levenshtein distance is therefore suitable for spectral functions or sequences of unequal length. Damerau-Levenshtein [52] adds another operation to those considered in Levenshtein, i.e., transposition of two adjacent characters, with a justification saying that it corresponds to human misspelling.

3.6.3 Validation of Theoretical Behavior

Theoretical behaviors of the three distance functions in this category with respect to magnitude change, translation, and standard deviation change can be observed in Fig. 3.27. Note that the unit and dynamic ranges of all Y-axes are identical. In case of magnitude and standard deviation changes, all distance functions saturate as soon as the target spectral function is different from the spectral reference. If spectral reference and the target are considered as S and $t(S, \theta)$, and their values as sets, the two transformations causes the two value sets to be

$$\{s(\lambda)\} \cap \{t(s(\lambda), \theta)\} = \emptyset, \ \forall \lambda \in [\lambda_{\min}, \lambda_{\max}].$$

To recall, distance functions in this category assume finite value set and repetition of values. Finally, due to all these, distance responses to magnitude and standard deviation changes saturates. For the case of translation, this transformation only shifts the spectral values. This means that there are still common values between the reference and the target, although their wavelength positions have changed. Then, depending on how many values are shifted, the distance response will vary.

The observed fluctuations, rather than the expected monotonicity, are due to optimization procedure that is embedded in Levenshtein and Damerau-Levenshtein distance functions. Note that their responses are identical. More explanations of distance functions requiring optimization loop can be read in Section 3.5.4.4. Finally, summary of theoretical properties of distance functions which consider a spectral function as sequence is provided in Table 3.5.

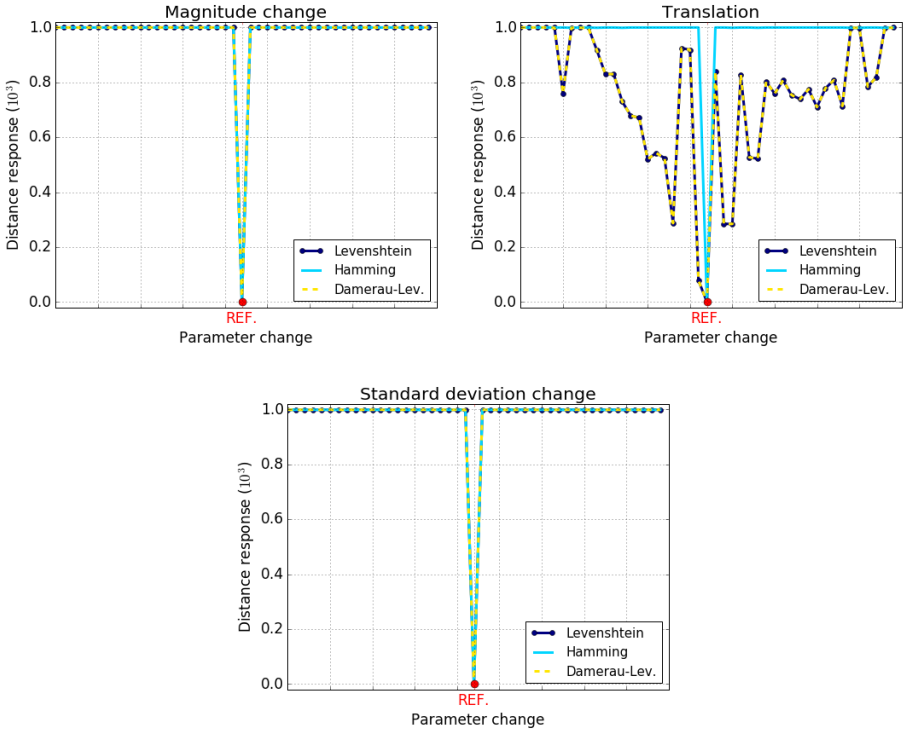

Figure 3.27 – Theoretical behaviors of Hamming, Levenshtein, and Damerau-Levenshtein distance functions with respect to magnitude change, translation, and standard deviation change. Responses to magnitude and standard deviation changes for all distance functions saturate as soon as a spectral function differ from the reference. Fluctuations observed in the responses of Levenshtein and Damerau-Levenshtein to translation are due to their uses of optimization loop.

Table 3.5 – Summary of theoretical properties of difference functions which consider a spectral function as sequence. Even though the evaluated functions are strictly distance functions, they do not satisfy the property of strict monotonicity.

Distance functions	RF	NN	SY	II	TI	SM
Hamming	✓	✓	✓	✓	✓	✗
Levenshtein	✓	✓	✓	✓	✓	✗
Damerau-Levenshtein	✓	✓	✓	✓	✓	✗

RF–reflexivity, **NN**–non-negativity, **SY**–symmetry, **II**–identity of indiscernible, **TI**–triangular inequality, **SM**–strict monotonicity

3.6.4 Quality Assessment Using Pigment Spectral Sets

Given pigment spectral reflectance sets described in Fig. 3.4 as inputs, responses of three distance functions in this category can be found in Fig. 3.28. As expected, their responses are identical to those of magnitude and standard deviation changes in the previous subsection, i.e., saturation of distance values. The reason to this is also the same, that there is no repetition of values between the spectral reference and the target spectral functions.

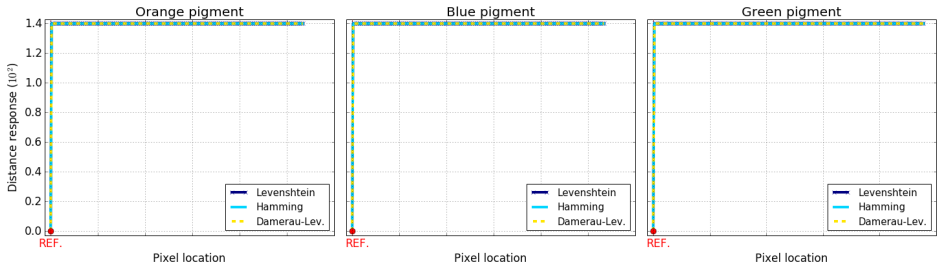

Figure 3.28 – Responses of Hamming, Levenshtein, and Damerau-Levenshtein distance functions to three spectral reflectance sets described in Fig. 3.4. Dynamic ranges and vertical axes of all 3 plots are identical. Distance functions saturate as soon as target spectral function is different from the reference. These results demonstrate their inability to discriminate spectral functions in the real setting.

3.7 Spectral Function as Series

3.7.1 Spectral Kullback-Leibler Pseudo-Divergence

In a recent study, Richard *et al*. [145] proposed a new spectral difference function in which a spectral function is considered as a series or function, i.e., spectral

Kullback-Leibler pseudo-divergence (KLPD). KLPD is only a pseudo-divergence because spectral reflectance and radiance cannot be considered as probability density function that is assumed by divergence functions. Unlike Euclidean distance of cumulative spectrum (ECS) (Section 3.5.3) which integrates shape and intensity differences in one measure, in KLPD the two measures are separate components, see Eq. 3.4 and 3.5.

$$\text{shape}: k_1 \cdot \mathrm{KL}(\bar{S}_1, \bar{S}_2) + k_2 \cdot \mathrm{KL}(\bar{S}_2, \bar{S}_1) \tag{3.4}$$

$$\text{energy or intensity}: (k_1 - k_2) \log \left(\frac{k_1}{k_2} \right) \tag{3.5}$$

Then, the complete mathematical expression of KLPD becomes as in Eq. 3.6, where $\bar{S}$, k, and KL are normalized spectral function, its corresponding normalizing factor, and Kullback-Leibler divergence function. See Appendix A.3 for how to compute the three variables.

$$\begin{aligned} div_{\mathrm{KL}'}(S_1, S_2) = k_1 \cdot \mathrm{KL}(\bar{S}_1, \bar{S}_2) + k_2 \cdot \mathrm{KL}(\bar{S}_2, \bar{S}_1) + \\ (k_1 - k_2) \log \left(\frac{k_1}{k_2} \right) \end{aligned} \tag{3.6}$$

3.7.2 Validation of Theoretical Behavior

Response of KLPD measure to three basic transformations can be observed in Fig. 3.29. In all 3 cases of basic transformations, KLPD is strictly monotonic. However, regarding its theoretical properties, it does not satisfy triangular inequality hence it is strictly not a distance function, see also Table 3.6.

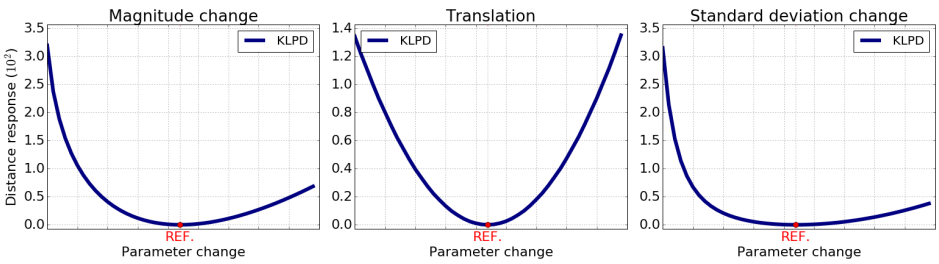

Figure 3.29 – Behavior of spectral Kullback-Leibler pseudo-divergence (KLPD) function to 3 basic transformations, i.e., magnitude change, translation, and standard deviation change. Scales of dynamic ranges from left to right are 10^2, 10^4, and 10^3. In all cases, KLPD is strictly monotonic.

Table 3.6 – Theoretical properties of KLPD function. It is not a distance function due to violation of the triangular inequality property. However, KLPD is a strictly monotonic function.

Distance functions	RF	NN	SY	II	TI	SM
KLPD	✓	✓	✓	✓	✗	✓

RF–reflexivity, **NN**–non-negativity, **SY**–symmetry, **II**–identity of indiscernible, **TI**–triangular inequality, **SM**–strict monotonicity

3.7.3 Quality Assessment Using Pigment Spectral Sets

The validity and usefulness of KLPD is also assessed using pigment spectral sets described in Fig. 3.4. Its performance can be observed through Fig. 3.30, where in all three cases it is successfully separating the four groups of colors.

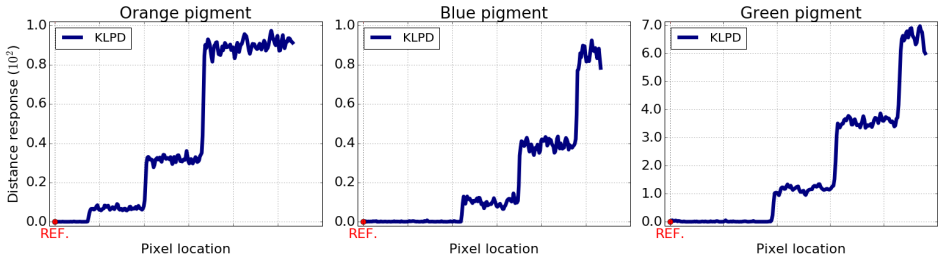

Figure 3.30 – Behavior of KLPD function to three spectral reflectance sets shown in Fig. 3.4. Scales of dynamic ranges from left to right are 10^2, 10^2, and 10^1. In all cases, it is shown that KLPD successfully separates the 4 groups of colors within each pigment patch.

3.8 Conclusions

Before it is a mathematical object, spectral data is a capture of electromagnetic radiation reflected by a surface or emitted by a light source. Therefore, a spectral data cannot be separated from its physical aspects. As a consequence, for a spectral data to be processed correctly ensuring the accuracy and relevance of its results, this physical aspect must be taken into account. And not only that, it has to be considered in every step of the processing chain.

Spectral distance is at the core of many image processing tools. While there seems to be plenty of distance functions to choose from, not every one of them is suitable for spectral data. This is because each distance function gives a mathematical

definition to what a spectral function is. In various distance functions, a spectral function is assumed to be either a vector in the Euclidean space, an n-dimensional data in manifold, a distribution, a sequence, or a series. Additionally, many existing distance functions are only sensitive to shape or intensity differences, and not the two together. After evaluating the existing distance functions with the proposed protocol and criteria, a new distance function capable of measuring both shape and intensity differences was constructed, i.e., Euclidean distance of cumulative spectrum (ECS). Although ECS has been shown to be suitable for spectral data, it is not without limitation, i.e., its inherent prioritization over the spectral channels.

After our first proposal of spectral distance function, i.e., ECS, Richard *et al*. [145] proposed a newer one, i.e., spectral Kullback-Leibler pseudo-divergence (KLPD) function. Although strictly KLPD is not a distance function due to its violation of triangle inequality property, it demonstrates strict monotonicity which is crucial for the suitability of spectral distance function. Then, despite ECS is superior in terms of the theoretical properties, KLPD has the advantage of not prioritizing the spectral channels. Also, unlike ECS, KLPD separates the components which measure shape and intensity differences.

Summary of Contributions.

- ✓ Evaluation protocol and criteria for selecting a suitable distance function for spectral data.
- ✓ Categorization of various distance functions based on their inherent assumptions of a spectral function.
- ✓ First proposal of a spectral distance function which integrates both shape and intensity differences in one measure, i.e., Euclidean distance of cumulative spectrum (ECS).
- ✓ Comparison of spectral distance functions using color scales, i.e., pigment patches of varying shades, to assess their selectivity and/ or discrimination ability.

Chapter 4

Spectral Ordering Relation and Its Expected Properties

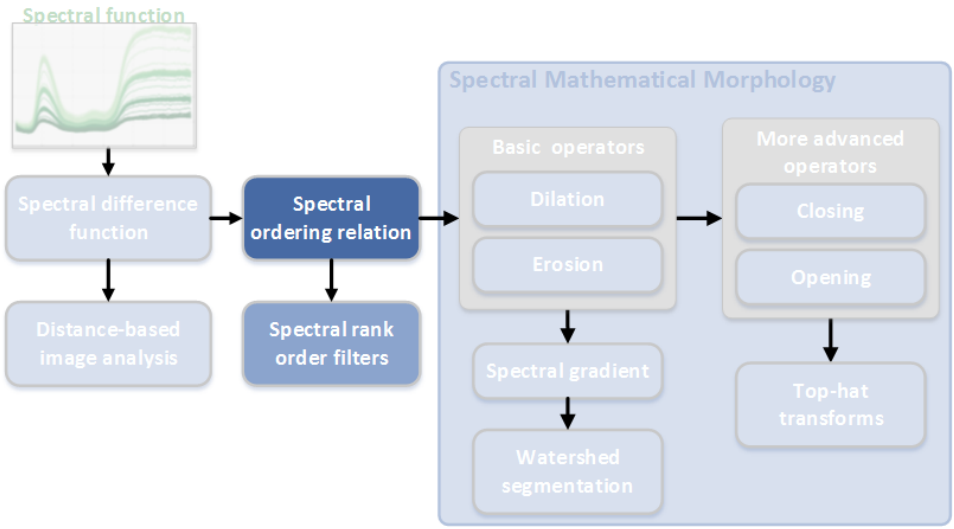

4.1 The Sense of Ordering in Hyperspectral Data

Ordering relation is an important concept in digital image processing. It is a fundamental theory in which a significant part of nonlinear image processing tools, e.g., mathematical morphology and rank-order filters, is built upon. Understanding the sense of order in the grayscale domain is trivial. If intensity level is to be represented by scalar values, large numbers would signify pixels with high energy and

vice versa. This representation makes the ordering of grayscale values straightforward since the scalar domain is equipped with the concept of rank or order, i.e., the natural '$\leq$' or 'less than or equal to' relationship.

Ordering in the multivariate domain is not as trivial as in the scalar domain. It is because ordering relation does not naturally exist in the multivariate domain [23, 27, 90]. An illustration is given in Fig. 4.1 for a two dimensional color space, i.e., CIE 1931 Chromaticity Diagram (2°Standard Observer). If any arbitrary colors are taken from this space, we know that it is highly unlikely that rank or order is readily available for the colors. This, however, does not mean that the concept of order is entirely absent from the multivariate domain. A set of spectral reflectance functions originating from a pigment patch is shown in Fig. 4.2. In the spectral set, in addition to the highly similar spectral shape, there is a certain progression of magnitude or intensity changes among the spectral functions. This observed progression allows us to see the set as an ordered list of spectral reflectance functions from, e.g., darker to brighter ones. This example is a demonstration that order can and do exist in the multivariate domain. Other examples of physical phenomena that can induce order in the color and spectral domain are provided in Table 4.1.

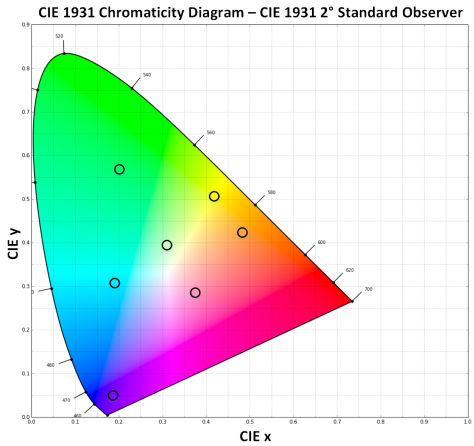

Figure 4.1 – Several arbitrary colors with no apparent ranks or orders, shown in two-dimensional CIE 1931 Chromaticity Diagram (2°Standard Observer).

The aforementioned instances of order in the color and spectral domains show us that multivariate ordering relation does not have the same strict sense of 'less than or equal to' as in the scalar domain. Nevertheless, this pre-existing order equally allows us to arrange values as a series or an ordered list, as in the scalar domain. But rather than the order extending to infinity, in the multivariate domain an ordering relation is only valid within a certain range. Fig. 4.3 illustrates how an existing

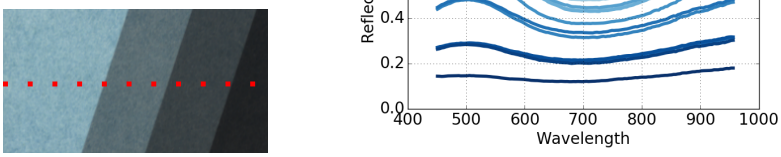

Figure 4.2 – A pigment patch and its spectral reflectance functions, as obtained from pixels approximately located under the red dots. As observed, brightness level in the pigment patch translates to variations in intensity and shape in the spectral reflectance domain.

Table 4.1 – Several physical parameters and the impact of their modifications in the perception of color and in the spectral reflectance space.

Parameters in physical domain	**Impact on**	
	Color perception	**Spectral reflectance function**
Paint layer thickness	Opacity	Mostly intensity variations
Pigment mixture	Hue, lightness	Variations in intensity and shape
Effect of shading in remote sensing data	Brightness level	Magnitude differences

order in the multivariate domain can be formulated. Given a set of colors $\mathcal{C}$, color ordering relation on the set can be expressed as a monotonic function of parameter change applied to color C_0, i.e., $C_i = g(C_0, \theta_i),\ i \in [a, b]$ where θ is controlled by a monotonic function f. Since f is defined over the range $[a, b]$, it induces limit to the ordering function g and allows to obtain colors at the extremities, i.e., C_a and C_b. Finally, the ordering function g over the color set $\mathcal{C}$ allows defining the set as a series or ordered list of colors that it produces.

Generally, given a set of multivariate data, determining order within the set is a great challenge. In cases such that is shown in Fig. 4.2, the underlying order is evident. But more often than not, this is not the case, leaving us with the task of identifying a suitable ordering relation. However, note that arbitrary ordering relations can be applied to the given set of data and each would generate a different ordered list. But which one is the most suitable one and according to which

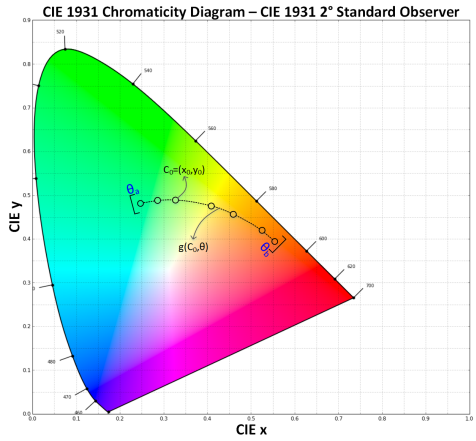

Figure 4.3 – Illustration of an existing ordering relation given a set of colors in the CIE 1931 Chromaticity Diagram (2°Standard Observer).

criteria? Setting out to find the most suitable ordering relation for developing a metrological image processing framework for hyperspectral data, the rest of this chapter is organized as follows. Definition and expected properties of the sought after ordering relation is given in Section 4.2. The expected properties encompass not only the theoretical properties of an ordering relation, but also requirements imposed by metrology. Then, the state of the art of existing ordering relations that have been used for hyperspectral data are provided in Section 4.3, using a categorization formulated by Barnett [23]. It is then followed by a proposal of hyperspectral ordering relation in Section 4.4. Employing criteria defined in Section 4.2, metrological evaluations of existing and proposed ordering relations are carried out in Section 4.5. Regarding total ordering constraint imposed by mathematical morphology, discussions will be provided in Section 4.6. Finally, conclusions are drawn in Section 4.7.

4.2 Spectral Ordering: Definition and Properties

Ordering relation is a mathematical construction allowing to describe a set of values as a series or an ordered list. Then, as it produces a series, the notion of extrema is obtained since the series is bounded by minimum and maximum values. When it comes to hyperspectral data, in addition to it being a series and not a vector (see conclusion of Chapter 3), the accuracy of its processing results must be able to justify the high cost and complexity of its acquisition. With this consideration, a suitable spectral ordering relation is not only satisfying the required mathematical properties but also the metrological ones, see Fig. 4.4.

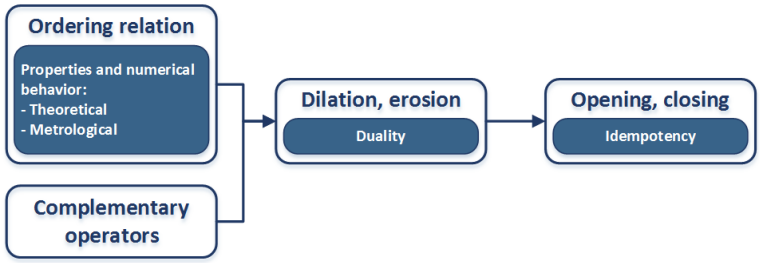

Figure 4.4 – Expected properties of a suitable hyperspectral ordering as imposed by the different levels of processing.

4.2.1 Definition

Suppose that $\mathcal{S}$ is a set, an ordering relation is a binary relation defined over $\mathcal{S}$, providing definition for the statement "x *precedes* y" or "x *is less than* y" for $x, y \in \mathcal{S}$. In the scalar domain, this binary relation is automatically obtained through operator "*less than or equal to*" $\leq$ or the stricter "*less than*" operator $<$. Expressing it as a function g, an ordering relation in the scalar domain can be expressed as in Eq. 4.1.

$$g(x) = x, \ \forall x \in \mathbb{R} \tag{4.1}$$

In the multivariate domain, an ordering relation g can be regarded as a function that maps values from the multivariate to the scalar domain where ordering is direct, see Eq. 4.2. Thus, any arbitrary function can be an ordering relation, given that the theoretical properties in Section 4.2.2 are satisfied.

$$g \colon \mathbb{R}^n \to \mathbb{R} \tag{4.2}$$

Then, provided a multivariate ordering relation g, the order of two arbitrary multivariate values $\mathbf{x} = \{x_1, x_2, \ldots, x_n\}$ and $\mathbf{y} = \{y_1, y_2, \ldots, y_n\}$, $\mathbf{x}, \mathbf{y} \in \mathbb{R}^n$ are as in Eq. 4.3.

$$\mathbf{x} \preceq_g \mathbf{y} \Leftrightarrow g(\mathbf{x}) \leq g(\mathbf{y}) \tag{4.3}$$

In the hyperspectral domain, we are dealing with measures of energy, typically in terms of spectral reflectance or radiance. And since this measure only comes in positive values, hyperspectral ordering relation can be expressed as in Eq. 4.4.

$$g \colon (\mathbb{R}^+)^n \to \mathbb{R}^+ \tag{4.4}$$

Finally, any two spectral functions S_1 and S_2 can be ordered through a function g, as shown in Eq. 4.5.

$$S_1 \preceq_g S_2 \Leftrightarrow g(S_1) \leq g(S_2), \ \forall S_1, S_2 \in \mathcal{S} \tag{4.5}$$

4.2.2 Theoretical Requirements

Given any arbitrary spectral functions $S_1, S_2, S_3 \in \mathcal{S}$, the following are theoretical requirements a function g has to satisfy in order for it to be an ordering relation.

- **Reflexivity**, $S_1 \preceq_g S_1$.
- **Transitivity**, if $S_1 \preceq_g S_2$ and $S_2 \preceq_g S_3$ then $S_1 \preceq_g S_3$.
- **Anti-symmetry**, if $S_1 \preceq_g S_2$ and $S_2 \preceq_g S_1$ then $S_1 = S_2$. In other words, if S_1 both precedes and succeeds S_2 according to g, then S_1 and S_2 must be identical spectral functions.
- **Trichotomy** [159] is where exactly one of the following holds: $S_1 \prec_g S_2$, $S_2 \prec_g S_1$, or $S_1 =_g S_2$.

Achieving reflexivity and transitivity allows a function to be a *pre-order*. When it also satisfies anti-symmetry property, it becomes an *ordering* or, more precisely, a *partial ordering*. Partial ordering relation enables the extraction of extrema, however without ensuring their uniqueness. The uniqueness of an extremum is guaranteed by trichotomy, which expresses that one of two spectra can always be defined as the minimum (or maximum). When a function satisfies all four requirements, it is called a *total ordering*.

Up to this point, spectral ordering relation has only been considered in terms of its theoretical properties. As mentioned previously, mathematical properties are insufficient since they do not regard the physical sense of spectral data, which can only be ensured by metrological constraints. The first entry point to metrology is the *trichotomy* property. With trichotomy, given any arbitrary pair of spectral functions S_1 and S_2, an ordering relation will always be able to order the two. On the other hand, when trichotomy is not satisfied, the order of the two spectral functions will end up being random selection. And this random selection procedure does not allow managing uncertainties as it is required by metrology.

4.2.3 Spectral Ordering Uncertainty

In the beginning of this chapter (Section 4.1), it has been mentioned that there are cases where the underlying ordering relation in a given spectral set is evident. Such cases can be employed to develop metrological tests for spectral ordering relation. Ledoux *et al*. [105] developed ordering uncertainty test for color data by generating ordered lists of colors. Further on, this ordered list will be referred to as *gradation*. See Fig. 4.5 for the illustration of its procedure. Looking at the color set shown in the figure, we can perceive a gradual change from green to yellow and then to red. According to our perception, we know that there is an underlying

order in this color set even though it is difficult to pinpoint exactly what they are. Nevertheless, since it is a gradual change, the ordering response $g(x)$ must behave like either of the curves 1, 2, or 3.

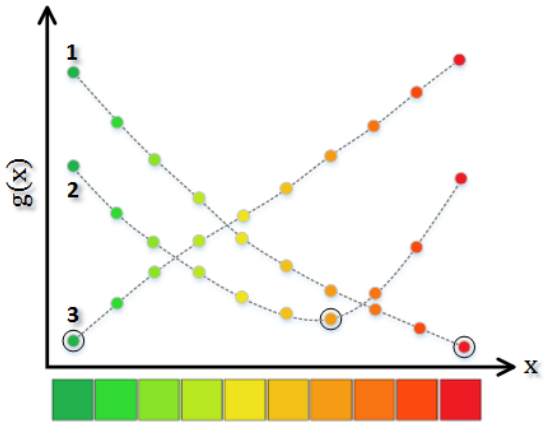

Figure 4.5 – Illustration of ordering uncertainty using a set of colors. Knowing that there is an underlying order in the color set according to our perception, the behavior of a suitable color ordering relation must be either of the three curves. In each curve, the global minimum is marked in a black circle.

The ordering uncertainty[1] test can be extended to the spectral domain. This test is formulated as in Eq. 4.6, where $\mathcal{S}_t$ is an ordered list or spectral gradation of $p+1$ unique spectral functions generated by a certain transformation t.

$$\exists! S_m \in \mathcal{S}_t \mid S_m = \bigwedge_{i:0\ldots p} g(S_i), \quad \text{where } g(S_{i-1}) > g(S_i),\ \forall i < m \text{ and } g(S_{i+1}) > g(S_i),\ \forall i > m \tag{4.6}$$

Interpretation. In a given ordered list of spectral functions $\mathcal{S}$, *there exist a unique global minimum* spectral function S_m according to the ordering relation under evaluation g. Then, g must order spectral functions whose location in the given list precede and succeed S_m in a strictly monotonic progression.

In its original construction, color gradation is generated by selecting an arbitrary initial color in a given color space and then the set is produced by varying, e.g., hue or brightness of the initial color. To extend this construction to the spectral domain, two considerations are to be taken. In the color domain, generating an arbitrary color value within a specific color space means that this color does exist. In the spectral domain, random generation of a spectral function does not always lead to a

[1]The notion of uncertainty is taken from metrology, i.e., measurement uncertainty in Section 1.6.

meaningful representation of the physical domain. Any arbitrary spectral function can be generated but it does not mean that the spectral function will have a physical sense, other than it is a digital construction. Thus, the first constraint in extending color gradation to the spectral domain lies in selecting an initial spectral function which is representative of the real physical world. And rather than generating an artificial one, it will be taken from images acquired by a spectral sensor.

Having defined the constraint for the initial spectral function, what remains in obtaining a spectral gradation is the transformation used to generate the gradation itself. And the second constraint lies in having a transformation function which is meaningful in the physical domain. An example in Fig. 4.2 demonstrates how the perception of brightness translates to spectral reflectance functions varying in their shapes and intensities. To simulate these spectral variations, as well as those mentioned in Table 4.1, three basic transformations previously introduced in Section 3.2.2 will be adapted to allow the modification of the initial spectral function.

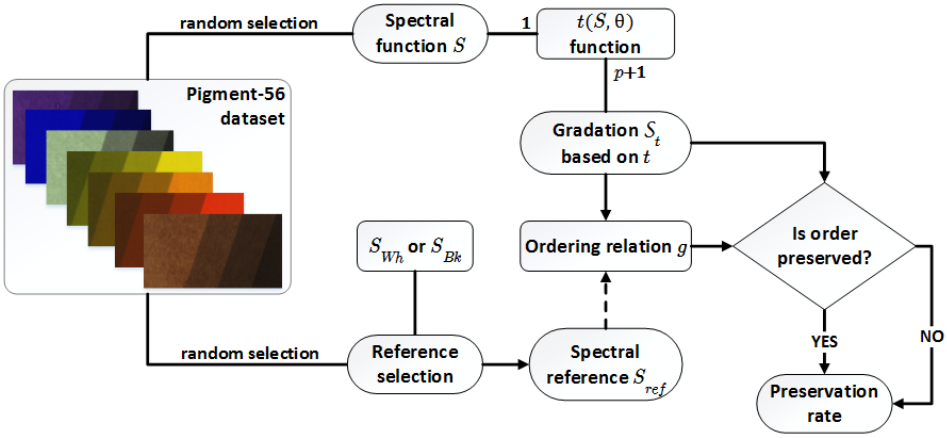

Figure 4.6 – Spectral ordering uncertainty test flowchart. Spectral gradation is generated based on a spectral function obtained from Pigment-56 dataset, see Appendix B.1, and t function. Depending on ordering relation under evaluation g, a spectral reference S_{ref} might be required.

Taking the aforementioned constraints into account, the design of spectral ordering uncertainty test is as shown in Fig. 4.6. The initial spectral function S used in generating gradation $\mathcal{S}_t$ in Eq. 4.7 is selected randomly from images of the pigment patches in Pigment-56 dataset (Appendix B.1).

$$\mathcal{S}_t = \{t(S,\theta_i),\ \theta \in [\theta_0,\theta_p]\} \tag{4.7}$$

Function t is also randomly selected from one of the following basic transformations, i.e., magnitude change, translation, and standard deviation change. Trans-

lation is implemented by shifting S over its wavelength, while magnitude t_m and standard deviation t_{std} changes are implemented according to Eq. 4.8, where k is a constant. Note that these t functions are not aimed at modeling the spectral transformations, but rather to produce sequences of ordered spectral functions. See examples of obtained spectral gradations in Fig. 4.7.

$$t_m(S) = k \int_{\lambda_{\min}}^{\lambda_{\max}} s(\lambda)\, d\lambda, \quad t_{std}(S) = k \int_{\lambda_{\min}}^{\lambda_{\max}} s(\lambda)^2\, d\lambda \tag{4.8}$$

Finally, depending on the ordering relation under evaluation, a spectral reference might be required. It can be one of the equi-energetic black and white spectral functions, S_{Bk} and S_{Wh}, shown in Eq. 4.9. Another option would be by randomly selecting a spectral function from the Pigment-56 as the reference.

$$\begin{aligned} S_{Bk} &= \{s_{Bk}(\lambda) = 0,\ \forall\lambda \in [\lambda_{\min}, \lambda_{\max}]\} \\ S_{Wh} &= \{s_{Wh}(\lambda) = 1,\ \forall\lambda \in [\lambda_{\min}, \lambda_{\max}]\} \end{aligned} \tag{4.9}$$

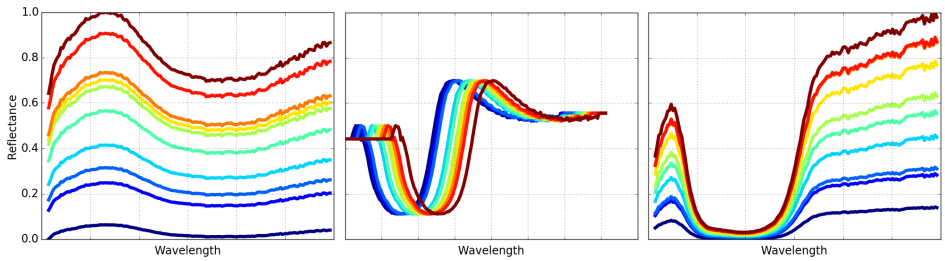

Figure 4.7 – Examples of spectral gradation generated by three transformation t, i.e., magnitude change, translation, and standard deviation change. Units and dynamic ranges of all three plots are identical.

Procedure shown in Fig. 4.6 is for a single test. Later in Section 4.5, this test will be carried out 500 times for each ordering relation under evaluation. Then, a table will be produced where under each ordering relation there will be a percentage number. This percentage number represents how many times out of 500, an initial ordering is preserved after an ordering relation is applied to the spectral gradation.

4.2.4 Trueness in Median Filtering

Rank order filters (ROF) is a set of filters which can be developed directly after defining an ordering relation, see formal definition in Chapter 6. An ROF works by iteratively sliding a filter window over the entire spatial dimension of an image, each time replacing value at the origin with one that is associated with rank r. Median filter is an example of ROF in which $r = \frac{n_W - 1}{2}$, n_W being the number of pixels within filter window W.

Because ordering relation is the core of ROF, its properties will also impact the performance and properties of the constructed ROF. Median filter is an instance of ROF whose properties are well identified for the scalar domain [88, 172]. Aiming to measure the indirect impact of an ordering relation g in its corresponding g-based spectral median filter, a trueness[2] test in median filtering is developed. The test allows to obtain an estimate of the performance of various ordering relations [59]. Given an image target, the test is essentially a comparison between two images, before and after filtering. Target images to employ originate from the Pigment-56 and Subsets-250 datasets, see Appendix B. In addition, as the notion of truesness requires the existence of a reference (see definition in Section 1.6), there has to be images that play the role of references. For that, target images filtered by Vector Median Filters (VMF) [18] will be used as the references. VMF, with cumulative distance as its ordering relation, has been shown to be the most statistically robust multivariate median filter. Spectral Kullback-Leibler pseudo-divergence (KLPD) function (Section 3.7.1), which has been concluded as the most suitable spectral difference function in Chapter 3, is chosen to be the spectral difference function of VMF. The general procedure of this trueness test can also be seen in Fig. 4.8. Ordering relation with smaller average pixel-by-pixel differences is considered as a better one, as it provides a more similar performance to VMF as the reference.

[2]The notion of trueness is taken from metrology, i.e., measurement trueness in Section 1.6.

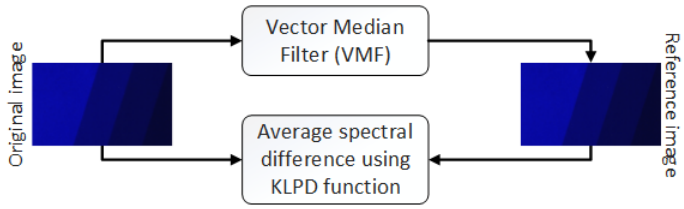

(a) Computation of average spectral difference between original image and its VMF-filtered image which is considered as the reference.

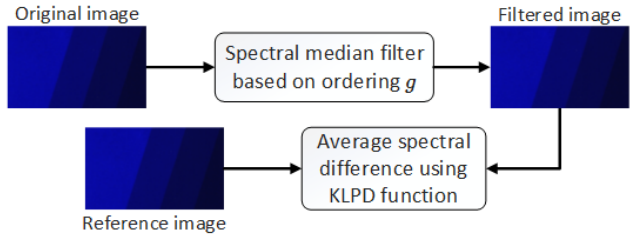

(b) Computation of average spectral difference between g-based spectral median filtered images and the references, i.e., VMF-filtered ones.

Figure 4.8 – Performance assessment of spectral ordering relation using trueness in rank ordering test. With VMF-filtered images as references, g ordering relation is considered to have a good performance if the average spectral difference to reference image is reduced after the filtering process.

4.3 Existing Hyperspectral Ordering Relations

A comprehensive study of multivariate ordering was carried out in the 70s by Barnett [23]. In his work, multivariate ordering relations were categorized into four non-mutually exclusive categories based on their approaches in reducing n-dimensional value into a single scalar. Following this classification, in the following are the state of the art of hyperspectral ordering relations, classified into marginal, partial, conditional, and reduced approaches.

4.3.1 Marginal Ordering (M-Ordering)

M-ordering approach orders multivariate data channel-wise. Its main interest is in taking an inference or summarizing the distribution of each data channel, and not to represent characteristics of a multivariate data point [23]. Marginal ordering has been employed in the color [66, 96, 136, 182] and multispectral [16] domain. Adapting the approach to the continuous nature of spectral function, its mathematical expression is rewritten as in Eq. 4.10.

$$S_1 \preceq_{marg} S_2 \Leftrightarrow s_1(\lambda) \leq s_2(\lambda),\ \forall\lambda \subset [\lambda_{\min}, \lambda_{\max}] \tag{4.10}$$

Interpretation. Spectral function S_1 precedes spectral function S_2 if and only if all of its elements are smaller than those of S_2 at every wavelength λ.

According to Eq. 4.10, M-ordering requires binary relation $\leq$ to be satisfied in the entire range of the data. This case is found in, e.g., one that is shown in Fig. 4.9a. However, when the spectral functions are as shown in Fig. 4.9b, M-ordering will not be able to determine which out of the two precedes the other. In such a case, S_1 neither precedes nor succeeds S_2. To be exact, $S_1 \not\prec S_2$, $S_1 \not\succ S_2$, and $S_1 \neq S_2$. Hence, marginal ordering only satisfies partial ordering property.

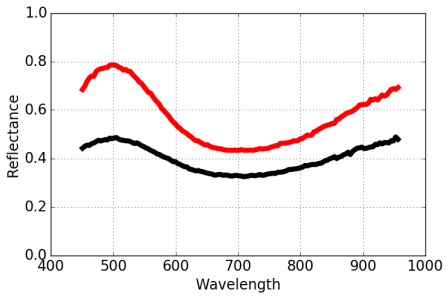

(a) Marginal minimum and maximum will be obtained from the initial set

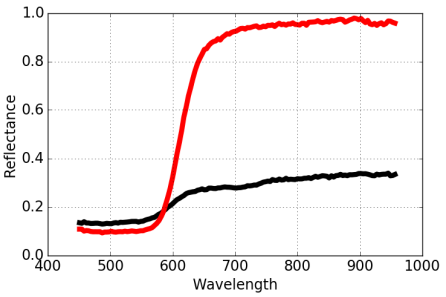

(b) Marginal minimum and maximum will be false colors

Figure 4.9 – Two spectral sets demonstrating when marginal ordering relation would (a) succeed and (b) fail in ordering the corresponding spectral function. In (b), marginal ordering relation will generate false colors.

The previous challenge where marginal ordering cannot always order two spectral functions by no means prevents its use. Marginal ordering finds the minimum between two spectral functions by taking minimum values at each wavelength, see Eq. 4.11. Going back to the example shown in Fig. 4.9b, the minimum spectral function of the set would be a new spectral function that does not exist in the initial set. This introduction of a new data is called *false color* problem.

$$\bigwedge_{marg} \{S_1, S_2\} = \bigwedge \{s_1(\lambda), s_2(\lambda)\},\ \forall\lambda \in [\lambda_{\min}, \lambda_{\max}] \tag{4.11}$$

False color problem is due to the fact that M-ordering approach assumes independent image channels, which we know is not true for hyperspectral images since their neighboring spectral channels are highly correlated. Thus, the only way to correctly employing M-ordering approach is by ensuring to have independent image

channels. And this can be done by decorrelating the data prior to ordering [12], e.g., by maximum noise fraction transform (MNF) or principal component analysis (PCA). However, these preprocessing steps would require additional computational resources which could be a burden in the case of hyperspectral images with hundreds of channels. Not to mention whether the employed method has a correct definition of a spectral function, e.g., not as a vector in the Euclidean space.

4.3.2 Partial Ordering (P-ordering)

P-ordering is a highly data-driven approach since it considers "*the overall inter-relational properties in the total deployment of the sample*" [23]. P-ordering divides input data into equivalence groups, either by employing marginal properties or reduction functions, followed by independently applying ordering function to each subgroup. Generally, this ordering approach is challenged by non-existent order between the sub-groups, in which case the ordering relation is not total.

The main reason which hinders the use of P-ordering approach for spectral data is in the precondition of having a certain number of equivalence groups. Such equivalence groups can be of particular interest in cases where, e.g., background-foreground [177] or pure-mixed pixels representations can be assumed. However, obtaining background-foreground representations in an image of natural scene is not a trivial matter. And even though pure-mixed pixels representations are commonly assumed in remotely-sensed images, it will still be a great challenge when dealing with textured images. Or in the case of hyperspectrally acquired paintings, the question of pigment mixtures become more difficult since chemical mixing has to be taken into account [3, 58] in addition to the optical mixing model which is commonly assumed in remote sensing images.

4.3.3 Conditional Ordering (C-Ordering)

C-ordering approach, also known as *lexicographic* ordering, orders multivariate data sequentially on its marginal components according to certain conditions or priorities. This approach can be applied to data in its original domain [8, 13–15, 131] or after a preliminary coordinate transformation [110]. In the lexicographical sense, a spectral function S cannot be considered as a continuous function but rather as a set of values, i.e., $S = \{s_{\lambda_i},\ i \in [0, n_\lambda - 1]\}$. Thus, lexicographical ordering can be expressed as in Eq. 4.12.

$$\begin{aligned} S_1 \preceq_{Lex} S_2 \ \Leftrightarrow \exists i \in [0, n_\lambda - 1], \\ (\forall j < i,\ s_{1,\lambda_j} = s_{2,\lambda_j}) \ \wedge \ (s_{1,\lambda_i} < s_{2,\lambda_i}) \end{aligned} \tag{4.12}$$

Interpretation. Spectral function S_1 precedes spectral function S_2 if and only if (1) its values at the first j channels are equal to those of S_2 and (2) its value at channel $j+1$ is smaller than that of S_2.

Lexicographic ordering is popular for its total ordering property, which is achieved when all image channels are used. This ordering approach is particularly suitable in cases where priorities among the marginal components of the image are known, e.g., in color images [15]. However, when this is not the case, the prioritization concept can easily become a drawback, especially when dealing with data of a much higher dimensionality.

When it comes to hyperspectral images, the use of lexicographical ordering suggests that only very few spectral channels are of high importance, and the rest will be considered negligible. This problem is demonstrated through an example in Fig. 4.10. According to a lexicographical approach which gives more priorities to shorter wavelengths, the black spectral function succeeds (is 'larger' than) the red one. This decision is made based on reflectance value obtained only from the shortest wavelength (see Fig. 4.10b), rendering the rest of the spectral information (see Fig. 4.10a) irrelevant. In addition to this excessive prioritization issue, lexicographic approach often yield inefficient exploitation of inter-channel relations [15].

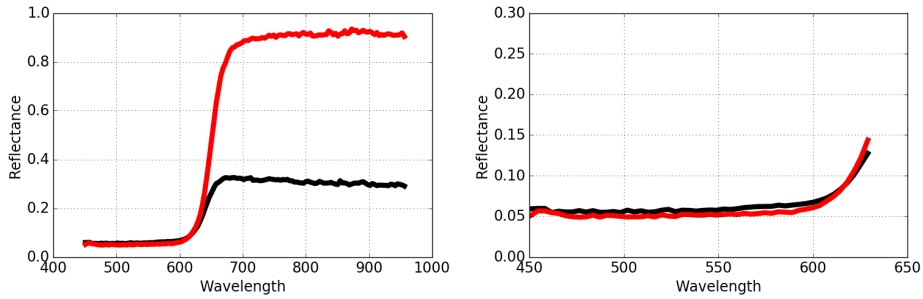

(a) Spectral functions in full spectral range (b) Portions of spectral functions shown in (a)

Figure 4.10 – Two spectral functions where S_1 (in red) can be considered as 'larger' than S_2 (in black) due to their overall magnitudes, see (a). However, a lexicographic ordering relation which prioritizes shorter wavelengths will say otherwise since $s_1(\lambda_{\min}) < s_2(\lambda_{\min})$, see (b).

Strategies employed in surpassing the limitation of classical lexicographic ordering are mainly in decreasing priority attributed to the first channel. Various attempts were made for three-channel color domain [8, 13, 14, 131], which however would not be of significant improvement for the hyperspectral domain due to its large channel count. Other strategies that could be of interest for multivariate data in general involves creating equivalence groups for the image channels and the use of marker images in a preprocessing step [15].

If lexicographic ordering is to be adapted to the most suitable definition of spectral data, i.e., as a series, its formulation can be expressed as in Eq. 4.13, where $f(\lambda)$ is a prioritization function of the marginal components. Prioritization function of the original lexicographical ordering can be defined as $f(\lambda) = k^{(\lambda_{\max}-\lambda)},\ k \in \mathbb{R}$. With this expression, lexicographic ordering essentially belongs to the family of R-ordering in Section 4.3.4.

$$\begin{aligned} S_1 \preceq_{Lex} S_2 \Leftrightarrow g_{Lex}(S_1) < g_{Lex}(S_2), \\ g_{Lex}(S) = \int_{\lambda_{\min}}^{\lambda_{\max}} f(\lambda) \cdot s(\lambda)\ d\lambda \end{aligned} \tag{4.13}$$

Interpretation. Lexicographic ordering relation as a form of ordering relation based on prioritization function. The order of a spectral function S is determined by the function of priorities over the wavelength $f(\lambda)$.

To the best of our knowledge, the original construction of lexicographic ordering has not been employed for hyperspectral image analysis. However, lexicographical cascade is still frequently used to resolve classification ties in supervised ordering [174] or to allow R-ordering approaches, which are generally only partial orders, in reaching the total ordering property [59, 176].

4.3.4 Reduced Ordering (R-Ordering)

The main idea behind R-ordering approach is to reduce a multivariate data into a scalar value by means of combining its components, aiming to imply a restricted overall ordering on the data [23]. Various reduced ordering relations that have been used in the spectral domain are given in the following.

Images in the grayscale domain can be considered as intensity images. If a spectral function is regarded as energy, one function is larger than another if its total amount of energy is bigger, see Eq. 4.14. Thus, as in the grayscale domain, a 'white' spectral function always succeeds a 'black' one [59].

$$g_{Esum}(S) = \int_{\lambda_{\min}}^{\lambda_{\max}} s(\lambda)\ d\lambda \tag{4.14}$$

Due to its energy point of view, the previous ordering relation assumes theoretical equi-energetic black and white spectral functions as the extrema. Consequently, its ability to process color information is very limited. This can be overcome by using a distance function since it explicitly requires to define a reference point S_{ref}, see Eq. 4.15. If theoretical equi-energetic white spectral function is selected as the reference point, the behavior of g_{d1} will be similar to g_{Esum} [59]. This approach has been employed in the color [10,178] and hyperspectral [179] domain.

If Euclidean distance of cumulative spectrum (ECS) (Section 3.5.3) is employed as the distance function, the obtained ordering relation will belong to the group that is based on prioritization function, see Eq. 4.13.

$$g_{d1}(S) = d(S, S_{ref}) \tag{4.15}$$

Ordering relations in Eq. 4.14 and 4.15 are only pre-orders since they cannot ensure anti-symmetry. Furthermore, if the two relations are to be employed in a morphological process, they do not allow to fully control the convergence of the value set. One solution to this could be by employing two reference points. Convergent Color Mathematical Morphology (CCMM) [106] employs the two references separately for minimum and maximum values extraction. CCMM can be directly extended to the hyperspectral domain, see Eq. 4.16 where $S^{-\infty}$ and $S^{+\infty}$ are the spectral references for minimum and maximum extraction, respectively. Due to this different use of references, if ordering relation of CCMM is used to determine any arbitrary rank r other than the extrema, essentially it will be reduced to ordering relation g_{d1} in Eq. 4.15.

$$\begin{aligned} g^{-}_{CCMM}(S) &= d(S, S^{-\infty}) \\ g^{+}_{CCMM}(S) &= d(S, S^{+\infty}) \end{aligned} \tag{4.16}$$

Median can be defined as the point where sum of its distance to all other points in the neighborhood is minimum [19]. Vector Median Filters (VMF) [18] was developed using this notion, i.e., multivariate median as the point having minimum aggregate distance. Considering that the pixels in a remote sensing image can be characterized by their mixed nature, cumulative distance using spectral angle distance was employed to extend the grayscale mathematical morphology to the hyperspectral domain [139, 140]; although strictly they are median/ anti-median filters [177]. Cumulative distance approach has also been used to construct mathematical morphology for hyperspectral data in [139], with spectral information divergence (SID) and hidden Markov model-based information divergence (HMMID).

In bit mixing ordering approach [43], the value $s(\lambda)$ of a spectral function S is considered as a binary word that consists of p bits. The relation works by transforming the multivariate value into a scalar of $(\Delta\lambda \times l)$ bits long. The ordering function can be written as in Eq. 4.17.

$$g_{BM}(S) = \sum_{j=0}^{l-1} \left\{ 2^{\lambda_{\max}-(l-1-j)} \int_{\lambda_{\min}}^{\lambda_{\max}} 2^{\lambda_{\max}-\lambda} \cdot s(\lambda)_{\{j\}}\, d\lambda \right\} \tag{4.17}$$

Bit mixing approach can also be considered as ordering relation with a prioritization concept. Although rather than only taking into account the wavelength arrangement as the lexicographic approach, it also considers the bit arrangement. The main challenge of its use for the hyperspectral domain lies in the number of channels and bits a hyperspectral image might require. Let us assume a hyperspectral image with 100 spectral channels where each value is represented by a 64-bit floating point number. Applying bit mixing order in its original form would result in each value having to be represented in 64×100 bits. Furthermore, taking also into account the typical spatial dimension of a hyperspectral image, the use of the original bit mixing approach is not feasible. Bearing this technological limitation in mind, three different bit mixing implementations are constructed, i.e., BM4, BM8, and BM16. Implementation details of each ordering relation is provided in Table 4.2, where differences between the three bit mixing functions lie in the number of considered bands, the number of most significant bit (MSB), and the total bits required to represent each value. Illustration of bit mixing procedure BM4 is also provided in Fig. 4.11.

Table 4.2 – Implementation details of 3 ordering relations employing bit mixing paradigm that are to be evaluated in this study. Implementation of each ordering relation vary in the number of spectral bands to take into account, the number of most significant bit (MSB), and the number of bits required to represent one value.

Ordering relation	Considered bands	Considered MSB	Bits per value
BM4	$[\lambda_{\min}, \lambda_{\min+3}]$	[0, 7]	32
BM8	$[\lambda_{\min}, \lambda_{\min+7}]$	[0, 7]	64
BM16	$[\lambda_{\min}, \lambda_{\min+15}]$	[0, 3]	64

4.3.5 Supervised Ordering Approaches

In addition to ordering relations that have been discussed in Section 4.3.4, there are supervised R-ordering relations originally developed for classification purposes. Similar to P-ordering approach, supervised ordering relations require the knowledge of sub-groups that exist within an image. Then, a preprocessing step would be carried out to obtain a representation for each of the sub-groups. Given a spectral function, its order will be determined by an R-ordering relation relative to the sub-groups. This ordering approach will not be considered in our study since our concern is order between spectral functions rather than order relative to a region or class. Nevertheless, in the following are some ordering relations belonging in this category of supervised reduced ordering approach.

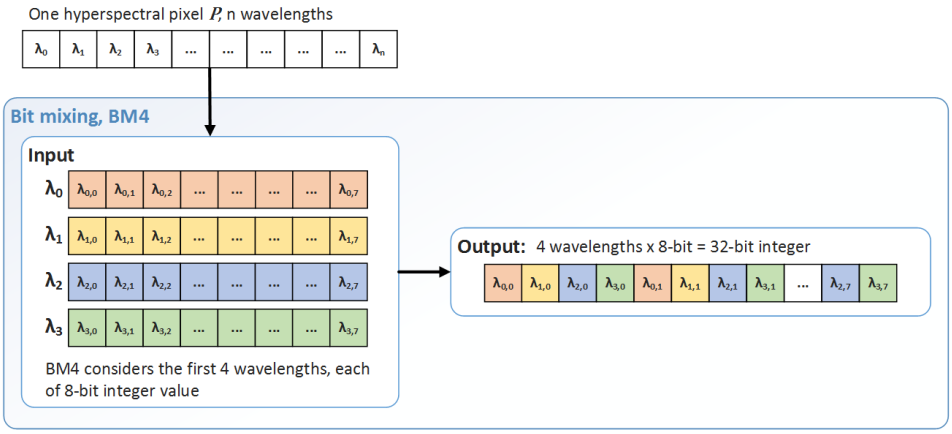

Figure 4.11 – Detailed implementation of bit mixing ordering relation BM4. For BM8, first 8 wavelengths are taken into account and thus the output is of 8×8=64-bit integer. For BM16, since 64-bit integer is the maximum, only the first 4 bits are considered for each of the 16 wavelengths.

Assuming background-foreground representations in an image, supervised reduced ordering were developed in [176]. Given a training set consisting of the background-foreground pixels, in the study kriging interpolation and support vector machine (SVM) were employed to learn the ordering. When background and foreground sets are both unitary, the ordering relation becomes the difference between kernelized distances, see Eq. 4.18. In this equation, S_b and S_f are spectral functions corresponding to background and foreground pixels, respectively.

$$g_{\{S_b,S_f\}}(S) = \frac{K(S_f,S) - K(S_b,S)}{K(S,S) - K(S_f,S_b)} \tag{4.18}$$

The previous two-class construction was further developed into a multiclass supervised ordering [175] as shown in Eq. 4.19, where g^* is a normalized two-class function, e.g., one-vs-all SVM evaluation function.

$$g_{\{\mathcal{S}\}}(S) = \max_i g^*(S;\mathcal{S}_{-i},\mathcal{S}_i) \tag{4.19}$$

Another supervised R-ordering was developed based on Lattice Auto-Associative Memories (LAAM), incorporating Chebyshev distance function. In this framework, lexicographic approach is employed to resolve cases of classification ties [174]. Two other supervised ordering relations employ a marginal approach [49] and where end-member ordering relation is developed based on the concept of spectral purity [11].

4.3.6 Ordering Relation on Reduced Spectral Data

Up to this point, discussions of various ordering relations have mostly been in the context of full-band approach. In such ordering relations, a hyperspectral image is taken as input in its entirety. Or it could also be after a decorrelating step if the employed ordering relation cannot take into account intercorrelated spectral channels, e.g., marginal and lexicographic approaches. But nevertheless, the dimensionality of data to be processed remains high.

Computational cost is often an important consideration when dealing with hyperspectral images. The large channel count of a hyperspectral image poses a challenge not only in terms of memory size but also computational time and complexity. Thus, it is not uncommon to apply dimensionality reduction [143, 164, 188] or band selection [187, 190] prior to ordering relation, or any image processing tasks for that matter. However, if computational cost is the main reason to carrying out the aforementioned data reduction steps, such approaches are easily out of our consideration. Bearing in mind the metrological aspects of image processing we are striving for, these approaches lose the interest of hyperspectral imaging (HSI). With these data reduction purposes, a metrological image processing framework cannot be achieved since the accuracy HSI has to offer will be lost during the data reduction process.

4.4 Proposed Hyperspectral Ordering Relation

In the following, a hyperspectral ordering relation based on the notion of ratio of distance is proposed, i.e., conditional ordering of ratio and angular ratio of distances. Further on, this ordering relation will be referred to as CRA. CRA expresses minimum and maximum extractions separately, as respectively shown in Eq. 4.20 and 4.21. Definitions of g_R^-, g_R^+, and g_A are provided in Eq. 4.22, where $S^{-\infty}$ and $S^{+\infty}$ are two spectral functions to serve as references.

$$S_1 \preceq_{CRA} S_2 \Leftrightarrow \begin{cases} g_R^-(S_1) > g_R^-(S_2) \text{ or} \\ g_R^-(S_1) = g_R^-(S_2) \text{ and } g_A(S_1) < g_A(S_2) \end{cases} \tag{4.20}$$

Interpretation. Spectral function S_1 precedes S_2 if and only if its ratio of distance according to g_R^- is larger than that of S_2. In case where they are identical, angular ratio of distance g_A of S_1 must be smaller than that of S_2.

$$S_1 \succeq_{CRA} S_2 \Leftrightarrow \begin{cases} g_R^+(S_1) > g_R^+(S_2) \text{ or} \\ g_R^+(S_1) = g_R^+(S_2) \text{ and } g_A(S_1) > g_A(S_2) \end{cases} \tag{4.21}$$

Interpretation. Spectral function S_1 succeeds S_2 if and only if its ratio of distance according to g_R^+ is larger than that of S_2. In case where they are identical, angular ratio of distance g_A of S_1 must be greater than that of S_2.

$$g_R^-(S) = \frac{d(S, S^{+\infty})}{d(S, S^{-\infty})}, \quad g_R^+(S) = \frac{d(S, S^{-\infty})}{d(S, S^{+\infty})},$$
$$g_A(S) = 2 \cdot \frac{d(S, S^{-\infty})}{d(S^{-\infty}, S^{+\infty})} \tag{4.22}$$

To understand the concept behind mathematical construction of ratio and angular ratio of distance shown in Eq. 4.22, see illustration in Fig. 4.12 where the notion of distance is expressed geometrically. Suppose there are two spectral references

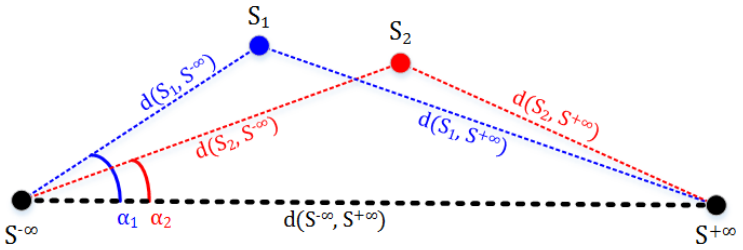

Figure 4.12 – Illustration explaining the concept behind conditional ratio and angular ratio of distance (CRA), where a distance function d and two references $S^{-\infty}$ and $S^{+\infty}$ are required.

$S^{-\infty}$ and $S^{+\infty}$, where each could be interpreted as convergence coordinates for minus and plus infinity. Any arbitrary spectral function S_1 can be considered as smaller than S_2 if its distance to plus infinity $S^{+\infty}$ is larger than that of S_2. Or it can also be expressed as S_1 being closer to minus infinity $S^{-\infty}$ than S_2. In either case, whether S_1 is closer to $S^{-\infty}$ or $S^{+\infty}$ can be determined by the ratio of distance of S_1 to these two references. Indeed, minimum and maximum extractions are given separate expressions in CRA, see Eq. 4.20 and 4.21. However, note that relationship between the two ratio of distances can be written as follows.

$$g_R^- = \frac{1}{g_R^+}$$

In Fig. 4.12, angular ratio of distance $g_A(S_1)$ and $g_A(S_2)$ are given in terms of α_1 and α_2, respectively. Note that this ratio of distance is not an angle, *per se*. Rather, it is a measure that is proportional to angle. In the case illustrated in the figure, g_A computation is not needed since $S_1 \prec S_2$ according to g_R^-. And in this case the proposed ordering relation is only a reduced approach rather than conditional. This, however, does not imply that g_A is unnecessary. When it comes to ratio, for any arbitrary scalar values x and y, there are $x' = c \cdot x$ and $y' = c \cdot y$ where the following holds $\forall c \in \mathbb{R}$.

$$\frac{x}{y} = \frac{x'}{y'}$$

An illustration of such a case is given in Fig. 4.13, where S_1 and S_2 are aligned in an axis that is perpendicular to $S^{-\infty}S^{+\infty}$. For this example, the first condition of CRA will be identical, i.e., $g_R^-(S_1) = g_R^-(S_2)$. Thus, the need of the second condition of CRA emerges, where the ties in distance ratio can be solved since $\alpha_1 \neq \alpha_2$.

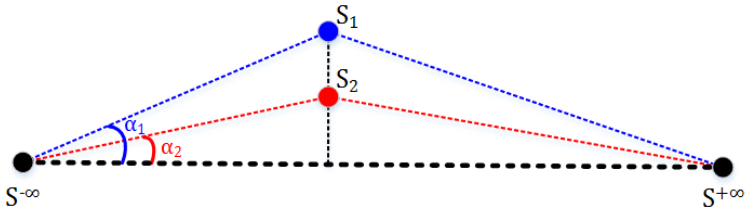

Figure 4.13 – Illustration for the necessity of the second component of CRA, i.e., angular ratio of distance.

4.5 Metrological Evaluation of Hyperspectral Ordering Relations

In this section, metrological evaluations of all ordering relations introduced in the previous section will be carried out. To recall, the proposed metrological tests are spectral ordering uncertainty (Section 4.2.3) and trueness in median filtering (Section 4.2.4). Also, note that evaluation and discussion will be carried out according to the following categorization of ordering relation, i.e., energy-based and marginal ordering relations (Section 4.5.1), ordering relations with prioritization concept (Section 4.5.2), distance-based ordering relations employing a single reference point (Section 4.5.3), and various other distance-based ordering relations (Section 4.5.4).

4.5.1 Energy-Based and Marginal Ordering Relations

An energy-based ordering relation can be found in Eq. 4.14, further on the ordering relation will be referred to as Esum. Given a spectral function S, Esum will determine the order of S based on its total sum of energy. In this evaluation, Esum will be compared to marginal ordering relation shown in Eq. 4.10.

4.5.1.1 Spectral ordering uncertainty

Results of ordering uncertainty test for Esum and marginal ordering relation are provided in Table 4.3. For Esum, it returns 100% preservation rate. On the other hand, marginal ordering relation can only preserve 65.6% out of 500 randomized spectral gradations, while the remaining causes generation of false colors. Examples of marginally-preserved and false color inducing spectral gradations en-

countered during the test can be observed in Fig. 4.14. By considering only this metrological test, Esum is more favorable than marginal ordering relation since it is order-preserving and does not generate false colors.

Table 4.3 – Results of ordering uncertainty tests for Esum and marginal ordering relation, shown in unit of percentage. Esum successfully preserves order in all the given spectral gradation. Marginal ordering relation cannot order a significant amount of the given gradation, in which it has to resort to producing false colors.

Ordering relation	Preserved order	False color
Esum	100	-
Marginal	65.6	34.4

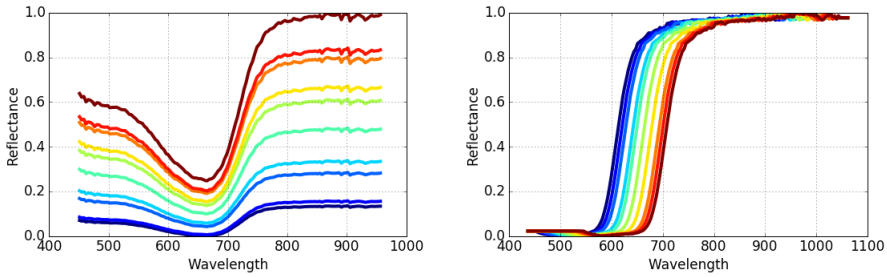

(a) Spectral gradation whose initial order can be preserved

(b) Initial order cannot be preserved, hence inducing false colors

Figure 4.14 – Two instances of spectral gradations encountered by marginal ordering relation in spectral ordering uncertainty test.

4.5.1.2 Trueness in median filtering

Performance of Esum and marginal ordering relations in trueness test employing Pigment-56 and Subsets-250 datasets can be observed through Fig. 4.15. To recall, the results were computed using VMF-filtered images as reference images. Thus, lower values are better since it can be considered that the performance of ordering relation under evaluation is closer to that of VMF. Upon observing the figure, comparing to the unfiltered images, both Esum and marginal ordering relations were able to construct well-performing median filters. If the two median filters are compared, marginal always outperforms Esum ordering relation. This, however, is not unexpected. Marginal ordering relation selects marginal medians which approximate the average spectral function (or average value at every wavelength). And VMF, with its statistical median, is also a good estimator of the average spec-

tral function [18, 88]. Thus, marginal ordering relation will always lead to smaller spectral differences to VMF-filtered images.

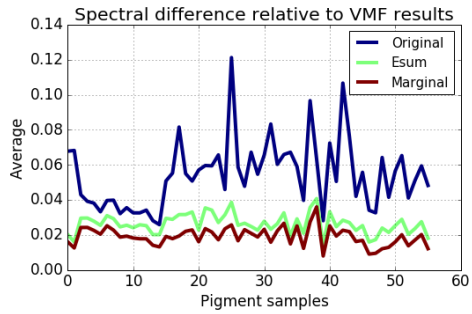

(a) Pigment-56, average

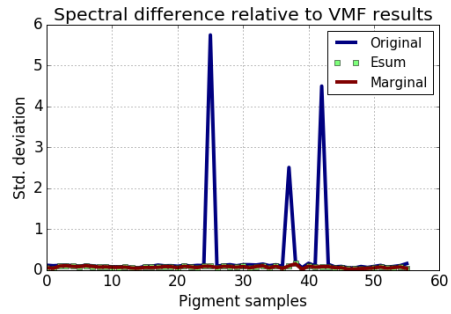

(b) Pigment-56, standard deviation

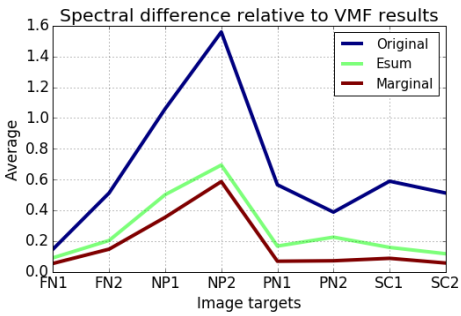

(c) Subsets-250, average

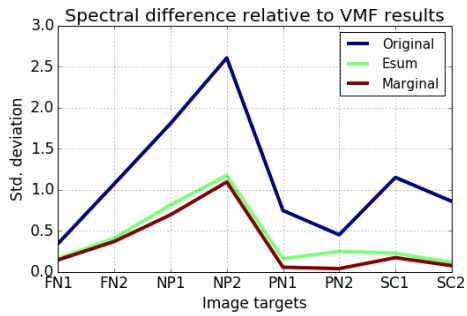

(d) Subsets-250, standard deviation

Figure 4.15 – Spectral differences computed between reference and target images, in which VMF-filtered images are used as reference. As for the targets, they are original (unfiltered) images, and those filtered by median filters based on Esum and marginal ordering relations. Judging from how the average and standard deviation of spectral differences to the references are reduced, Esum and marginal ordering relation performs well in median filtering, with marginal as the most efficient.

4.5.1.3 Discussion

In the ordering uncertainty test, it was concluded that Esum is to be preferred rather than marginal ordering relation. However, the opposite was concluded in trueness in median filtering test. Marginal ordering relation performs median filtering better than Esum. Then, which one is to be selected as a more suitable hyperspectral ordering relation? None of them.

Esum only computes the total energy of a given spectral function. This entails that its capability to account for shape information is very limited. Spectral functions of

different shapes can have identical total energy, see example in Fig. 4.16. Despite evident shape differences, Esum will deem the 3 spectral functions as identical.

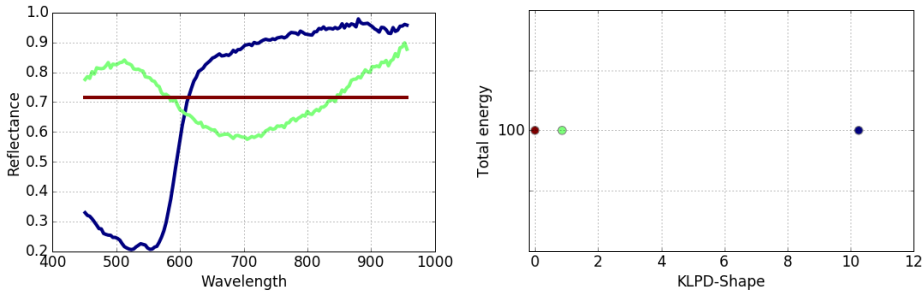

(a) Spectral reflectance functions (b) Their spectral variations

Figure 4.16 – Three spectral reflectance functions of different shape but identical total amount of energy. The shape difference is computed with KLPD-Shape with equi-energetic black spectral function S_{Bk} as reference.

Despite its closeness to performance of VMF, the false color problem of marginal ordering relation persists. For example, all pixels in a marginally-filtered FN1 shown in Fig. 4.17 are actually false-colored, despite the absence of apparent perceptual distortion of the image. This might lead to a doubt whether false colors is indeed a serious problem or if to some extent it can be acceptable. To better understand the impact of false color, see illustration in Fig. 4.18. Five spectral reflectance functions were randomly selected from Pigment-56 and marginal ordering relation was employed to obtain minimum, median, and maximum of the given set. As observed in the figure, none of the spectral functions that are associated to the ranks comes from the initial spectral set. Color difference between ranked spectral functions and the initial set is also provided in Table 4.4.

Table 4.4 – Color differences between colors of the initial spectral set shown in Fig. 4.18 and colors of spectral functions associated with the rank minimum, median, and maximum. The colors are obtained using CLTR method. CIELAB color difference was employed to compute the differences. All ranked spectral functions are false colors since no $\Delta E_{ab} = 0$.

ΔE_{ab}	S_1	S_2	S_3	S_4	S_5
S_{min}	36.40	26.23	39.05	26.27	12.85
S_{median}	21.16	32.78	21.78	25.21	25.25
S_{max}	30.09	24.64	32.14	14.83	38.48

(a) **Reference**, VMF-filtered (b) Filtered FN1, marginal (c) Filtered FN1, Esum

Figure 4.17 – Performance of marginal and Esum ordering relations in filtering image FN1 as compared to the reference, i.e., VMF-filtered FN1. Note that despite the absence of perceptual distortion, all pixels of the marginally filtered FN1 are actually false colors.

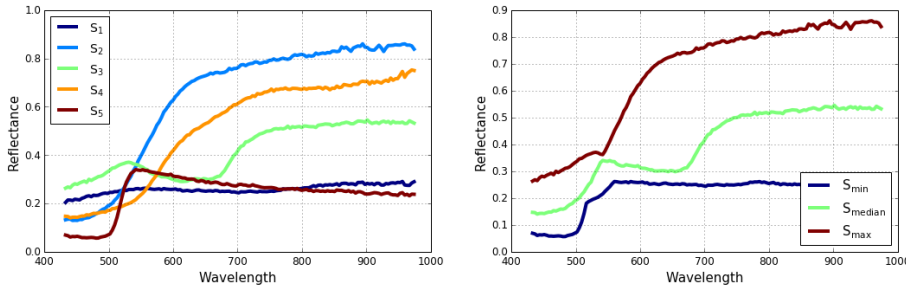

(a) Spectral reflectance set randomly selected from Pigment-56 dataset

(b) Spectral reflectance functions associated with minimum, median, and maximum

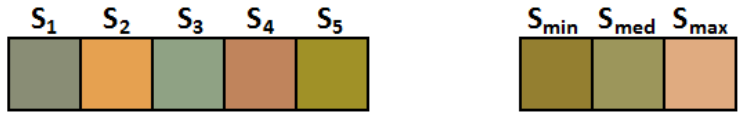

(c) Colors of the initial spectral reflectance set shown in (a)

(d) Colors of spectral functions associated with ranks as in (b)

Figure 4.18 – Given an (a) initial set of spectral reflectance functions, (b) three spectral functions associated to minimum, median, and maximum are obtained using the marginal approach. All spectral reflectance functions are converted to the sRGB space and the colors are shown in (c) and (d).

4.5.2 Ordering Relations with Prioritization Concept

Ordering relations to be evaluated in this category are the lexicographic and bit-mixing approaches. Two different lexicographic ordering relations are considered, i.e., with priorities given to shorter (Lex-$\lambda_{\min}$) and longer (Lex-$\lambda_{\max}$) wavelengths. Then, in order to demonstrate the excessive prioritization problem of the approach, the two will be contrasted with ordering relations that are only based on the shortest ($\lambda_{\min}$) and longest ($\lambda_{\max}$) wavelengths, respectively. Other ordering relations to be considered are the bit mixing approaches BM4, BM8, and BM16. Distance-based ordering relation with ECS will also be evaluated. The aforementioned ordering relations, except for ECS, assumes the equi-energetic black spectral function S_{Bk} to be the global minimum of the value space. Thus, in order to be comparable, S_{Bk} will be employed as reference for ECS. Further on, this last ordering relation will be referred to as ECS-S_{Bk}.

4.5.2.1 Spectral ordering uncertainty

Five hundred ordering uncertainty tests were carried out for ordering relations with prioritization concept and their results can be seen in Table 4.5. Lexicographic ordering relations Lex-$\lambda_{\min}$ and Lex-$\lambda_{\max}$ are both able to preserve existing order in the given spectral gradations. And if compared to $\lambda_{\min}$ and $\lambda_{\max}$, it shows that more than one spectral band is employed by the lexicographic relations to determine the order of a spectral function. Through this test, however, excessive prioritization issue of the lexicographic approach cannot be demonstrated. For bit mixing ordering relations, limitation of their approach becomes evident, especially since their rates of order preservation never reach 50%. ECS-S_{Bk} is able to preserve the order of all given spectral gradations. Rather than the previous approaches where measures from all spectral bands are, in practice, not always used, ECS-S_{Bk} incorporates all of them through its use of distance computation.

Table 4.5 – Order preservation rate (in unit of percentage) of various ordering relations with prioritization concept, obtained from 500 ordering uncertainty tests.

Lex-$\lambda_{\min}$	**Lex-$\lambda_{\max}$**	$\lambda_{\min}$	$\lambda_{\max}$	**BM4**	**BM8**	**BM16**	**ECS-S_{Bk}**
100	100	60.2	60.2	39.2	44	17.6	100

4.5.2.2 Trueness in median filtering

Average and standard deviation of pixel-by-pixel differences for lexicographic ordering relations are shown in Fig. 4.19, in which they are compared to ordering relations based on single band image. Between the lexicographic ordering relations Lex-$\lambda_{\min}$ and Lex-$\lambda_{\max}$, it can be observed that in the case of these pigments

datasets, higher priorities should be given to longer wavelengths rather than to shorter ones. Incorrect function of prioritization would result in the filter introducing more errors (as compared to the curve associated to unfiltered images) rather than reducing it. The two lexicographic ordering relations demonstrate how this approach heavily relies on the correct prioritization function. In the color domain, obtaining such priorities over the image channels is less of a challenge. Depending on the image at hand, higher priority can be given to, e.g., hue or saturation channels. But when it comes to the hyperspectral domain, inferring priorities over the hundreds of spectral bands might not always be possible, and in many cases such information is not known beforehand.

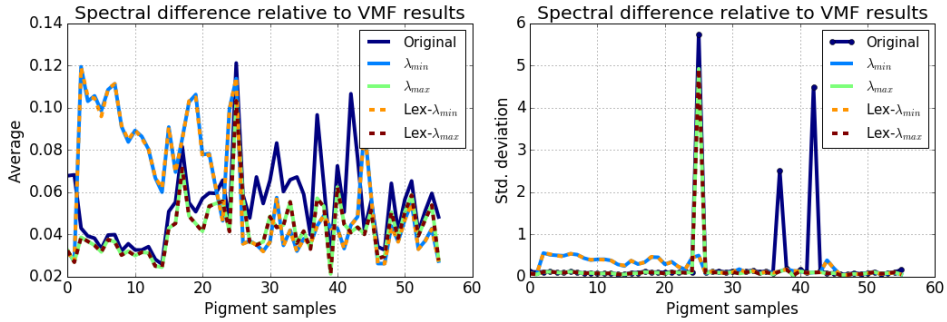

Figure 4.19 – Average and standard deviation of spectral differences of Pigment-56 images before and after median filtering, with VMF-filtered images as the reference. Performances of Lex-$\lambda_{\min}$ and Lex-$\lambda_{\max}$ are almost identical to $\lambda_{\min}$ and $\lambda_{\max}$, respectively, showing the excessive prioritization problem of their approach. Prioritizing shorter wavelengths is also not a good choice since it introduces more errors in almost half of the images, as compared to curve of the original images.

$\lambda_{\min}$ and $\lambda_{\max}$ utilizes only the first and last spectral bands, respectively, when determining the order of a given spectral function. As observed in Fig. 4.19, the two are almost identical to Lex-$\lambda_{\min}$ and Lex-$\lambda_{\max}$, respectively. These responses are as expected. Unlike spectral functions employed in the ordering uncertainty test, where no additional variations are added even in the smallest amounts, real spectral functions are rich of small variations. But even the smallest variations would have a great impact on lexicographic ordering. The almost identical response between the pairs of lexicographic and single band image based ordering relations demonstrate the excessive prioritization given by the traditional lexicographic ordering. Hence, lexicographic ordering is not a suitable hyperspectral ordering relation as it considers a significant number of band images as insignificant.

Performances of the three different implementations of bit mixing approach is shown in Fig. 4.20. Comparing the different implementations, including more spectral bands seem to improve the performance. Nevertheless, if compared to the curve corresponding to unfiltered images, in approximately half of the pigment samples bit mixing approach introduces more errors rather than reducing them. Similar conclusion to that of lexicographic ordering relation, this shows the importance of knowing where the priorities actually exist or where optimum one should be implied.

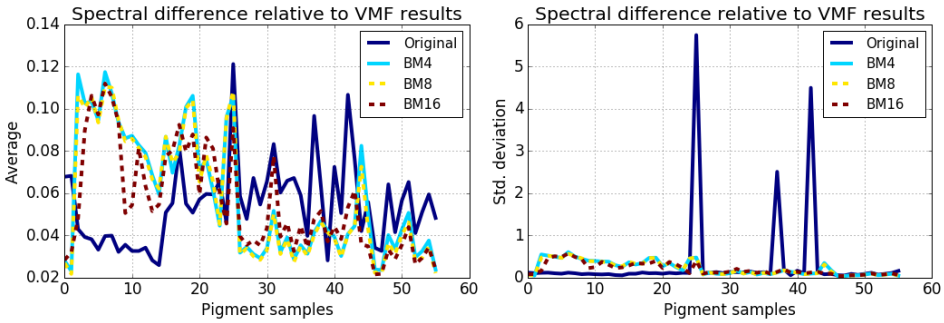

Figure 4.20 – Average and standard deviation of spectral differences of Pigment-56 images before and after median filtering, with VMF-filtered images as the reference. Including more spectral bands seem to improve the performance of the obtained median filters, e.g., BM16 is better than BM8. Although in almost half of the pigment samples, more errors are introduced by all ordering relations (compare to the curve which corresponds to original images).

Despite using different techniques, ECS-S_{Bk}, Lex-$\lambda_{\min}$, and BM8 ordering relations give more priorities to shorter wavelengths. In order to compare the three ordering relations, their performances are obtained in the context of trueness in rank ordering tests, see Fig. 4.21. As observed in the figure, BM8 performs slightly better than Lex-$\lambda_{\min}$. This is because BM8 incorporates more spectral bands rather than Lex-$\lambda_{\min}$ which, in practice, mostly considers only the first spectral band. Considering ECS-S_{Bk}, it significantly outperforms the other two ordering relations. Also, it always reduces the spectral difference of the original image, in both, average and standard deviation values. Finally, despite also having prioritization concept, ECS-S_{Bk} do not perform poorly as Lex-$\lambda_{\min}$ and BM8 do. And this is because with a distance-based approach, in practice all spectral bands are taken into account thus avoiding the excessive prioritization problem.

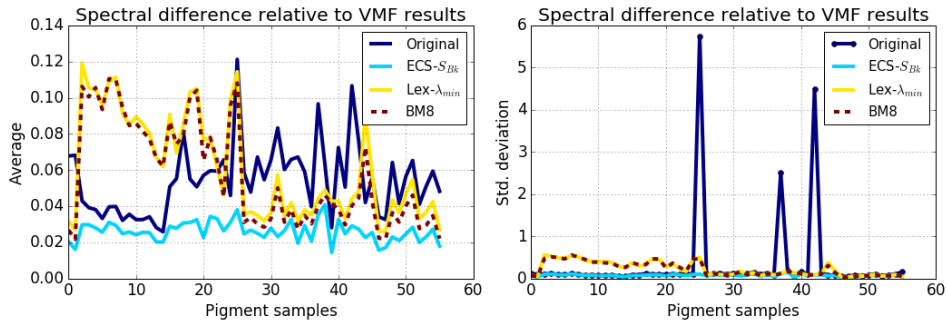

Figure 4.21 – Average and standard deviation of spectral differences of Pigment-56 images before and after median filtering, with VMF-filtered images as the reference. Ordering relation used to construct the median filters are ECS-S_{Bk}, Lex-$\lambda_{\min}$, and BM8, all giving higher priorities to the shorter wavelengths. ECS-S_{Bk} is the best performing ordering relation since in all cases it improves spectral differences to the reference images, i.e., VMF-filtered ones. This is because ECS avoids the excessive prioritization problem by its distance approach.

In addition to Pigment-56, the test is also carried out for the Subsets-250 dataset. Performances of ordering relations with prioritization concept in the context of this dataset are provided in Fig. 4.22. As observed, the trend of performance with regard to the Subsets-250 dataset remains highly similar to the previous dataset. Lex-$\lambda_{\min}$ and Lex-$\lambda_{\max}$ are almost identical to $\lambda_{\min}$ and $\lambda_{\max}$, respectively. Between the bit mixing approaches there are almost no significant difference. Then, it can also be inferred that in this dataset, more priorities should be given to longer rather than shorter wavelengths. Nevertheless, prioritization using distance based approach ECS-S_{Bk} proves to be the best performing ordering relation out of the rest. Fig. 4.23 allows side-by-side comparison of unfiltered, reference, and filtered images obtained from various ordering relations, example is shown for image NP1 from the dataset. Observing the figure, it is evident that the lexicographic and bit mixing approaches introduce grainy artifacts to the filtered images. On the other hand, it is only ECS-S_{Bk} which demonstrates perceptually similar performance to that of VMF.

4.5.2.3 Discussion

From our analysis we may conclude that, generally, lexicographic ordering relations are not a suitable choice for hyperspectral image processing. This is because they suffer from excessive prioritization problem, which has been demonstrated through trueness in rank ordering test. In the test, their performances are almost

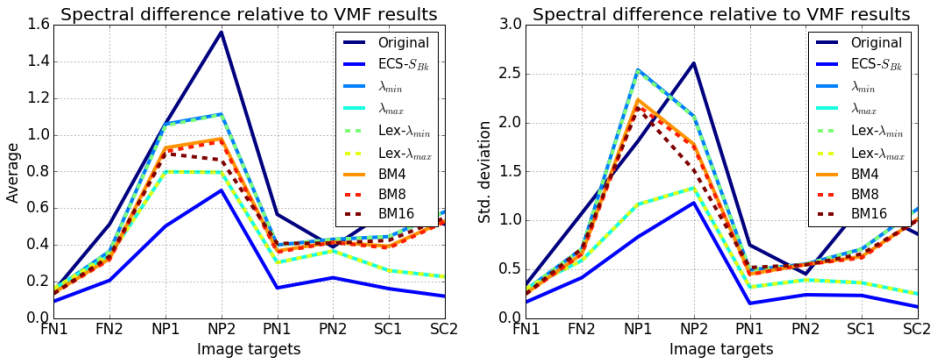

Figure 4.22 – Average and standard deviation of spectral differences of Subsets-250 images before and after median filtering, with VMF-filtered images as the reference. The median filters are developed based on ordering relations with prioritization concept. Among all ordering relation, ECS-S_{Bk} is the best performing one as it avoids excessive prioritization problem by its distance approach.

identical to ordering relations which are based on only single band images. And this shows that in many cases lexicographic ordering relation was essentially reduced to being a first-priority ordering relation, rendering the rest of the components useless. Bit mixing approach is not significantly different from the lexicographic one, in its excessive prioritization problem. Indeed, this problem was even more magnified because the implementation only allows taking information from very few spectral bands. But this is yet another reason why bit mixing approach is not to be selected for full-band hyperspectral image processing. It is simply not feasible considering size of a hyperspectral image, that is typically of hundreds of spectral bands and large spatial dimension. Finally, the only remaining candidate from this group of ordering relations is ECS-S_{Bk}. It reduces the prioritization problem, while at the same time incorporates information from all spectral bands.

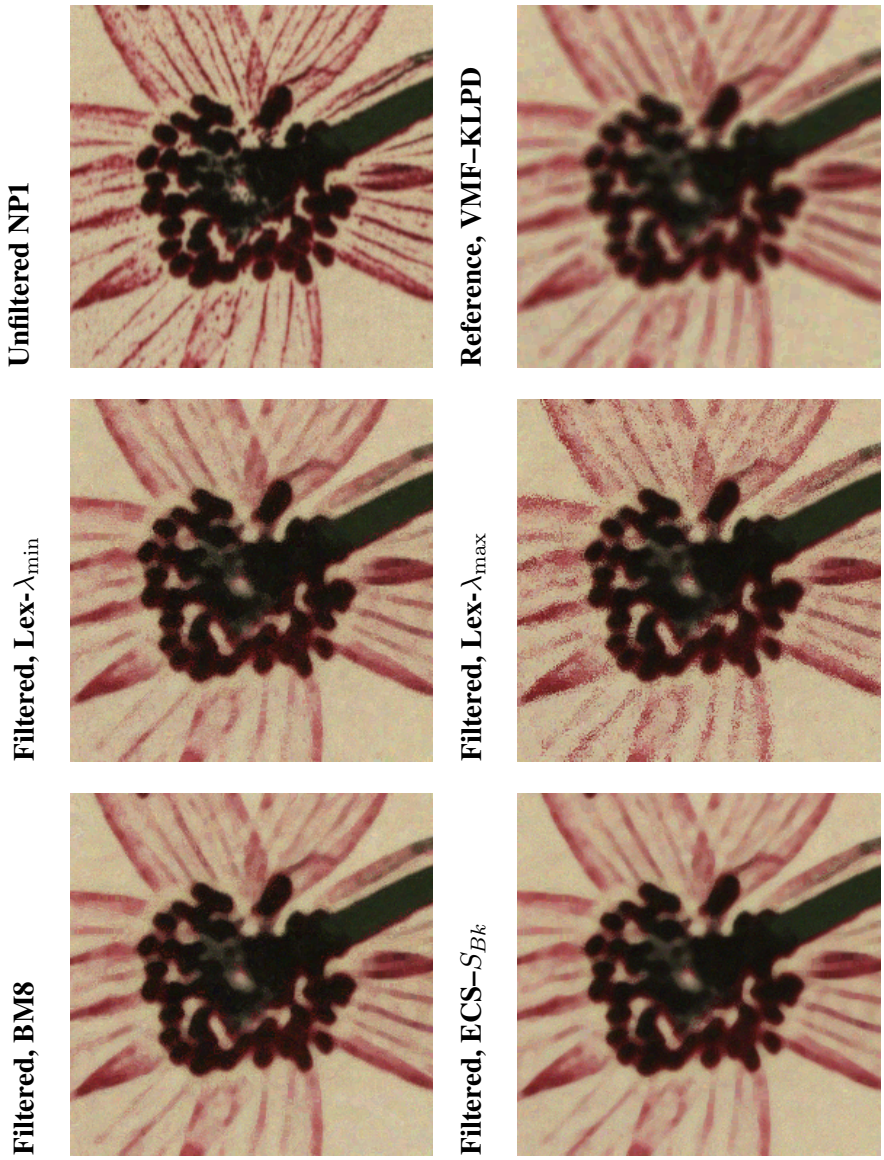

Figure 4.23 – Side-by-side comparison of unfiltered NP1, its VMF-filtered reference, and its filtered images obtained from various ordering relations with prioritization concept. Compared to the reference, lexicographic and bit mixing approaches introduce grainy artifacts and only ECS-S_{Bk} seem to approach the performance of VMF. Shown color images are produced using FIXED method.

4.5.3 Single Reference Distance-Based Ordering Relations

The performance of a distance-based ordering relation will be partially influenced by the distance function it employs. And despite having concluded the most suitable distance function for spectral data in Chapter 3, in the following we will demonstrate the impact of several distance functions on distance-based ordering relation which requires to define a reference point. The functions to evaluate are Euclidean distance, spectral angle (SAM), ECS (Section 3.5.3), and KLPD (Section 3.7.1).

4.5.3.1 Spectral ordering uncertainty

Performance comparison of 4 distance-based ordering relations in spectral ordering uncertainty test is given in Table 4.6, where the reference choice is varied (see protocol in Section 4.2.3). Consistently lower performances are given by SAM, which is as expected due to its suppression of magnitude differences. Other difference functions only perform slightly different in each case of reference choice.

Table 4.6 – Percentage rate of preserved order obtained by single reference distance-based ordering relations, where the reference choice is varied.

Reference	Euclidean	SAM	ECS	KLPD
S_{Bk}	100	82.6	100	100
S_{Wh}	100	88.8	98.8	100
Randomized	99.0	88.6	99.4	98.2

4.5.3.2 Trueness in median filtering

Performances of the four distance-based ordering relations for trueness in median filtering test can be seen in Fig. 4.24. Note that in this test, only one spectral reference is employed, i.e., equi-energetic black spectral function S_{Bk}. In agreement with spectral ordering uncertainty test, among the four distance-based ordering relations, SAM gives the lowest performance. As for the rest, if compared to the curves which correspond to spectral differences between original and reference images, they produce lower differences to VMF-filtered images. Furthermore, in the context of Pigment-56 and Subsets-250 datasets, their performances are highly similar, with only slight differences for Euclidean in the case of Pigment-56.

Performances of the considered ordering relations in the spatial dimension of target images can be observed through a side-by-side comparison provided in Fig. 4.25. Observing these images, it is evident that SAM is not a suitable ordering relation for hyperspectral images, it introduces noise and artifacts to the filtered image.

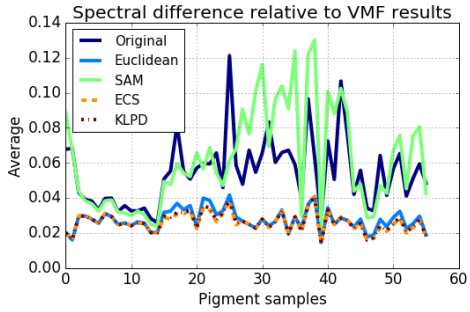

(a) Pigment-56, average

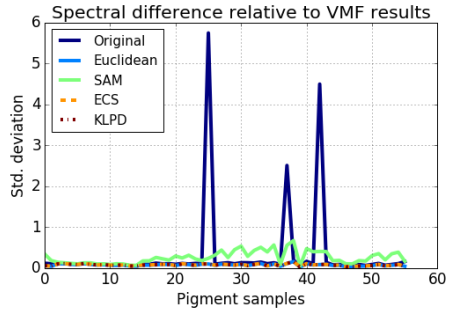

(b) Pigment-56, standard deviation

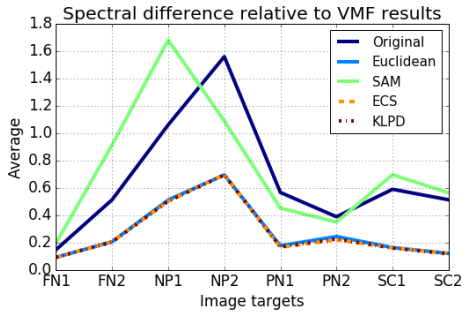

(c) Subsets-250, average

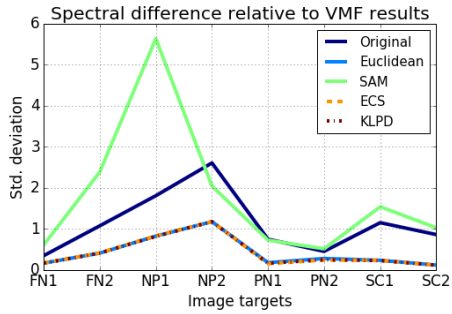

(d) Subsets-250, standard deviation

Figure 4.24 – Spectral differences of Pigment-56 and Subsets-250 images before and after median filtering, with VMF-filtered images as the reference. Single reference ordering relations are employed, i.e., using Euclidean, spectral angle (SAM), ECS, and KLPD functions. S_{Bk} is used as spectral reference.

On the other hand, the three other ordering relations perform as expected from a median filter, i.e., gives smoothing effect without destroying edges in the image.

4.5.3.3 Discussion

To conclude, this subsection has been more of a validation for spectral distance functions rather than spectral ordering relations. Nevertheless, it has shown the impact a distance function has on the ordering relation. Euclidean, spectral angle, ECS, and KLPD functions have been evaluated. Despite its popularity in remote sensing field, it has been shown that spectral angle is not to be selected in hyperspectral image processing due to its inability to account for magnitude differences. In addition to its reduced performance in detecting existing order in a spectral set, it also introduces artifacts when it is employed to construct a spectral median filter. For other difference functions, their performances were not significantly different.

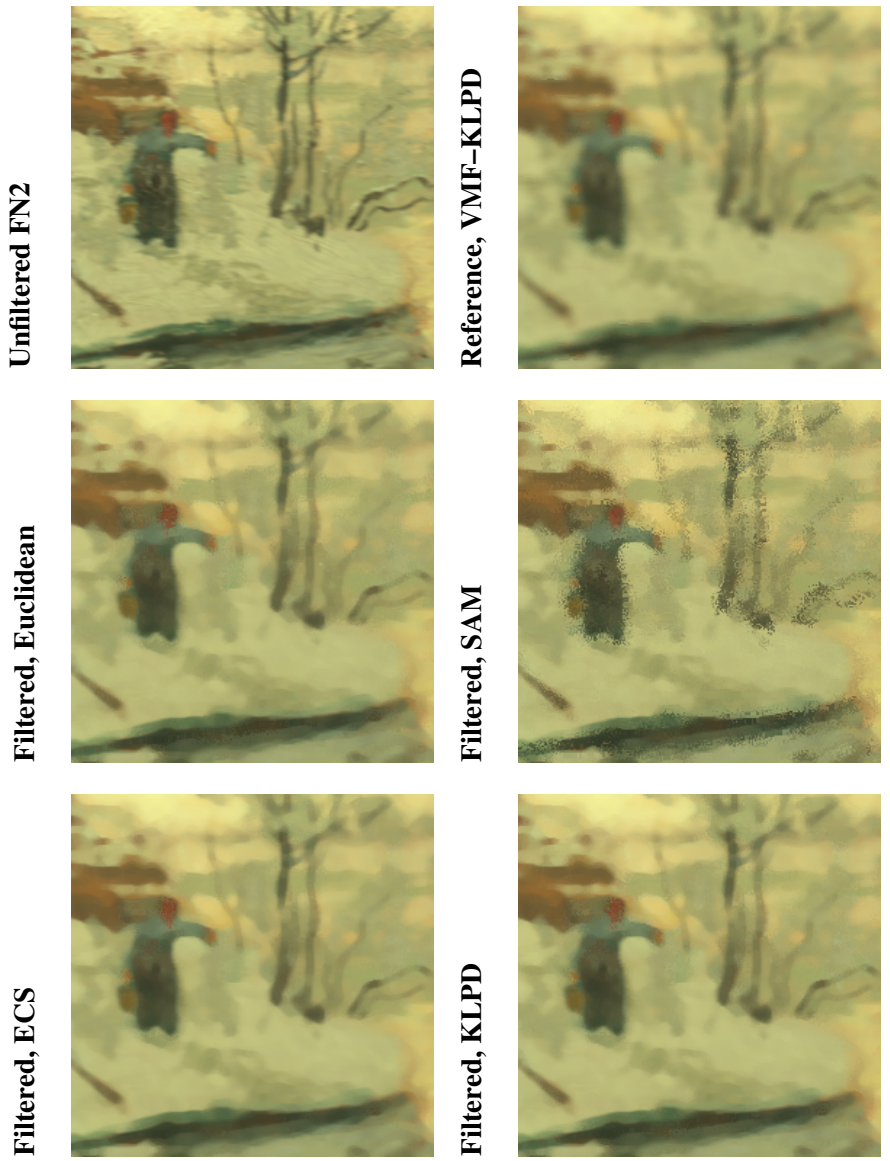

Figure 4.25 – Side-by-side comparison of unfiltered FN2, its VMF-filtered reference, and its filtered images obtained from various single reference distance-based ordering relations. All distance-based ordering relations employ S_{Bk} as reference. Among the evaluated ordering relations, worst performance is given by SAM as grainy artifacts are introduced to the filtered image. Shown color images are produced using CLTR method.

4.5.4 Various Distance-Based Ordering Relations

In addition to single reference distance-based ordering relations, there are various other distance-based approaches. In the following, metrological evaluations will be carried out for distance based ordering relations, including the new conditional ratio and angular distance ordering relation (CRA) which has been proposed in Section 4.4. Details regarding which ordering relations are to be evaluated can be seen in each metrological test. KLPD function is chosen as the distance function and S_{Bk} and S_{Wh} are employed as references.

4.5.4.1 Spectral ordering uncertainty

Ordering relations evaluated in this part are single reference distance-based (KLPD-B and KLPD-W), ratio of distance (Ratio-BW)[3], proposed CRA ordering relation (CRA-BW), distance-based ordering relation originally found in CCMM construction [106] (CCMM-BW), and one that is based on cumulative or aggregate distance (CumDist). Note that -B, -W, and -BW refer to spectral reference used, i.e., S_{Bk}, S_{Wh}, and when both are used together, respectively.

Table 4.7 – Preservation rate of various distance-based ordering relations in spectral ordering uncertainty tests. -B and -W denote the employed spectral reference, i.e., S_{Bk} and S_{Wh}, respectively.

KLPD-B	KLPD-W	Ratio-BW	CRA-BW	CCMM-BW	CumDist
100	100	100	100	100	98.6

Performances of the aforementioned ordering relations in spectral ordering uncertainty tests can be seen in Table 4.7. As observed, five ordering relations provide excellent performances with the given datasets. It is only the cumulative distance approach CumDist which demonstrates a slightly worse performance than the rest. This, however, is not surprising. CumDist approach, which is the ordering relation behind VMF [18], cannot differentiate minimum and maximum since the two are mixed together in the maximum value returned by CumDist; the minimum value of CumDist relates to the median. But this does not entail that CumDist would fail in this test, because its response would resemble curve 2 shown in Fig. 4.5. CumDist would, however, fail when its assumption of data distribution [18] is not met. On the other hand, rather than relying on a certain assumption of data distribution, other distance-based ordering relations employ spectral references to imply the order in a given dataset. And the selected references in this test have partially contributed to the success of these ordering relations.

[3]It is ordering relation based on only the first part of proposed CRA ordering relation

4.5.4.2 Trueness in median filtering

In this test, the evaluated ordering relations are KLPD-B, KLPD-W, Ratio-BW, and CRA-BW. CCMM-BW cannot be evaluated due to its alternating use of references which does not allow computation of median, see Eq. 4.16. As for CumDist, it is not evaluated as the other but rather used as reference, i.e., VMF. Performances of the remaining distance-based ordering relations in this metrological test are presented in Fig. 4.26. Comparing to the spectral differences between original images and the references, i.e., VMF-filtered ones, all ordering relations are successfully lowering the spectral differences after filtering. However, performances of the four are almost identical. See also the side-by-side comparison of resulting images in Fig. 4.27.

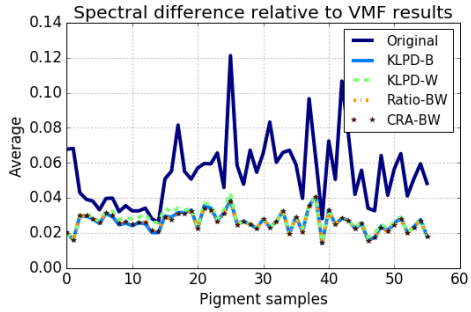

(a) Pigment-56, average

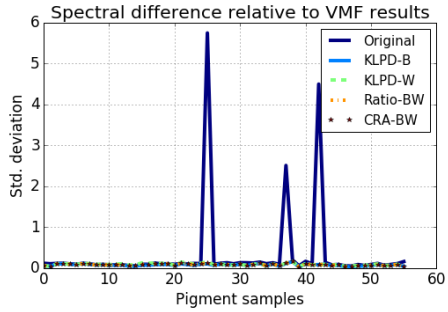

(b) Pigment-56, standard deviation

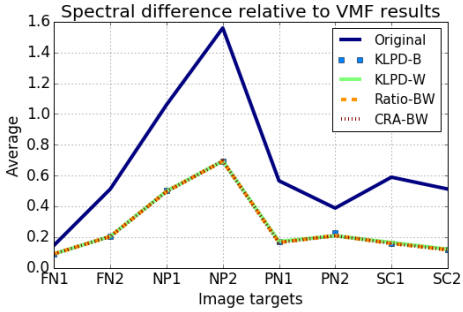

(c) Subsets-250, average

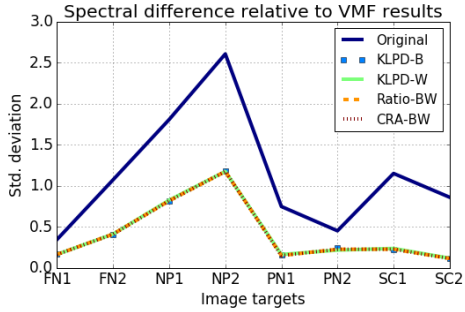

(d) Subsets-250, standard deviation

Figure 4.26 – Spectral differences of Pigment-56 and Subsets-250 images before and after median filtering, with VMF-filtered images as the reference. Various distance-based ordering relations are employed to construct the median filters. Performances of all ordering relations are almost identical.

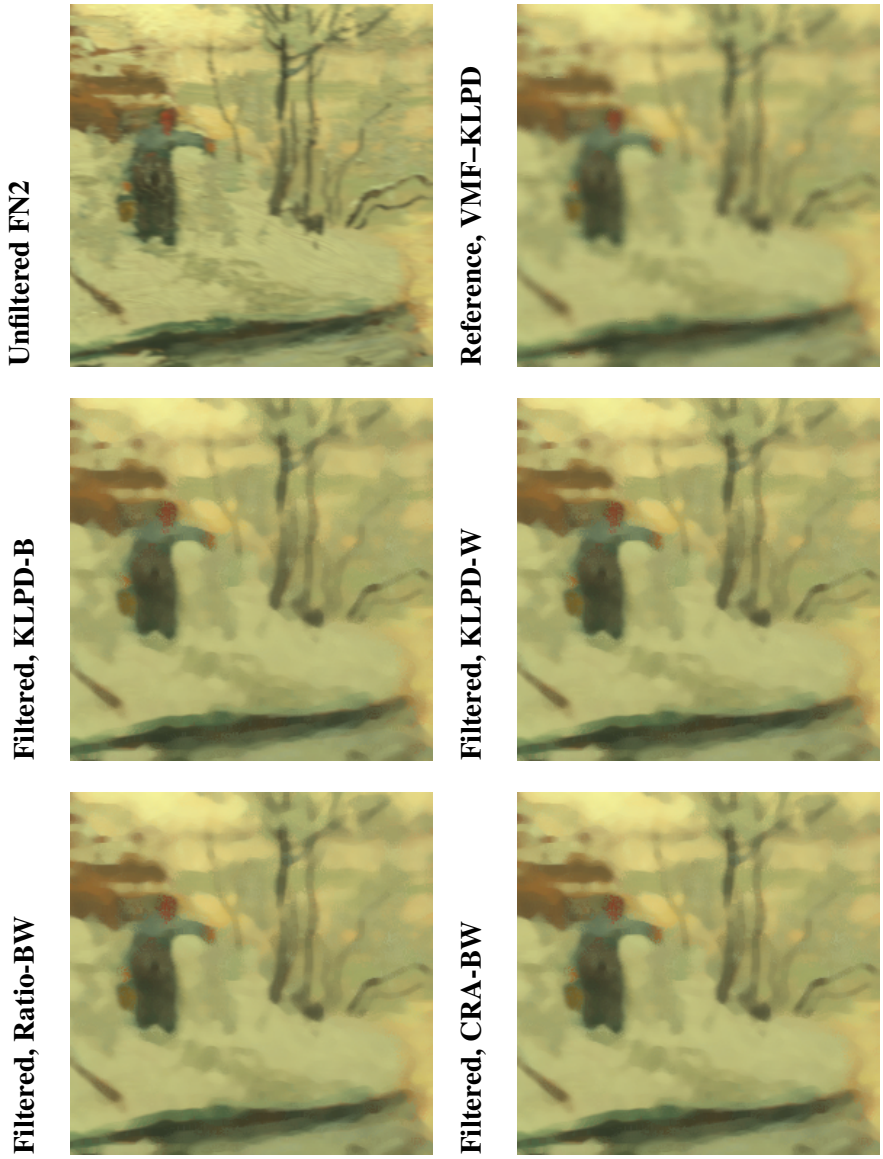

Figure 4.27 – Side-by-side comparison of unfiltered FN2, its VMF-filtered reference, and its filtered images obtained from various distance-based ordering relations. Performances of the evaluated ordering relations are almost identical. Shown color images are produced using CLTR method.

4.5.4.3 Discussion

Various distance-based ordering relations have been evaluated and none of them are clearly superior to the others. In the ordering uncertainty test, CumDist ordering relation was slightly less performing than the other approaches due to its assumption of data distribution that could not always be satisfied. In the trueness in median filtering test, CumDist and CCMM were not evaluated for reasons that have been described before. Then, for the rest of the ordering relations, their performances were almost identical.

4.6 On Mathematical Morphology and Total Ordering Property

Mathematical morphology (MM) is a framework for the analysis of structures in an image. Its foundation is laid upon the notion of a complete lattice, which can be obtained by just having a partial ordering relation, see Section 4.2.2. However, total ordering property is indispensable in the context of metrology. This is because in partial ordering, there is a risk of extrema selection being a randomized process since the employed ordering relation cannot decide the order between two inputs.

Marginal ordering approach can only satisfy partial ordering property. Lexicographic approach is, by definition, total. However, the metrological tests in Section 4.5.2 have shown how lexicographic ordering relations perform almost identically to those that are based on a single band image. As an impact of this excessive prioritization problem, the ordering relation produces undesirable artifacts in the median filtering results of spectral images. To further demonstrate the problem, two images from Pigment-56 and Subsets-250 are filtered with a minimum filter constructed using Lex-$\lambda_{\min}$ ordering relation. With a 5×5 filter window, the relative use of each spectral band can be seen in Fig. 4.28. In this demonstration, it is clearly shown that spectral bands associated with wavelength longer than 460 nm are never used. Therefore, despite being a theoretically valid ordering relation, lexicographic approach is not to be selected for further development of MM framework.

Trichotomy property (Section 4.2.2) is generally satisfied by the distance-based ordering relations. However, they are typically challenged by the anti-symmetry property. This theoretical property requires that if $(S_1 \leq_g S_2)$ and $(S_2 \leq_g S_2)$ then S_1 and S_2 must be identical spectral functions. In other words, anti-symmetry demands for unique minimum and/ or maximum. However, due to mathematical conjecture shown in Eq. 4.23, obtaining unique minimum and/ or maximum in the hyperspectral domain is easier than in, e.g., three-channel color domain. Then, due to the small spectral variations, the chance of two different spectral functions having the same distance value to a specific reference is very reduced. Even if this

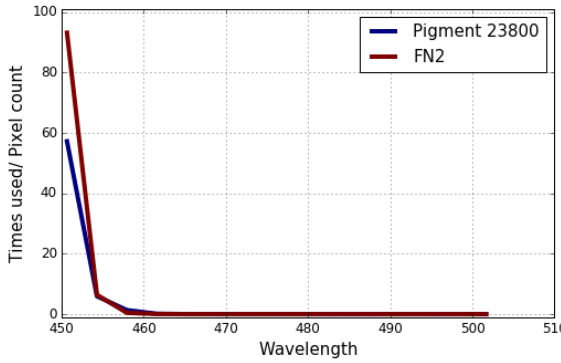

Figure 4.28 – Percentage of the number of spectral bands (or wavelengths) being used in a minimum filter of window size 5×5 pixels, when a Lex-$\lambda_{\min}$ is employed as the ordering relation of the filter. In each image, the first spectral channel is almost always the determining factor of the ordering of values within a filter window. Spectral channels after 460 nm are never used in the ordering process.

condition is reached, the proposed CRA ordering relation will be able to differentiate the two functions through its second condition, i.e., angular ratio of distance. See construction of CRA ordering relation in Section 4.4. For cumulative distance approach (CumDist) which is employed in VMF, it does not have the ability to differentiate minimum and maximum. This is because CumDist only allows detecting median and extrema. As for the CCMM construction, it can also reach total ordering property due to its conditional ordering approach. However, this ordering relation is not idempotent, which later in Chapter 7 will be shown as a necessary requirement for reaching morphological filters.

$$\text{prob}\left(\#\Big\{\bigcap_{\lambda_{\min}}^{\lambda_k} s_i(\lambda)\Big\} > 1\right) > \text{prob}\left(\#\Big\{\bigcap_{\lambda_{\min}}^{\lambda_l} s_i(\lambda)\Big\} > 1\right) \tag{4.23}$$
$$\lambda_k = \lambda_{\min} + n \cdot \Delta\lambda,\ \lambda_l = \lambda_{\min} + (n+1) \cdot \Delta\lambda, \forall S_i \in \mathcal{S}$$

Interpretation. Given a set of spectral functions $\mathcal{S} = \{S_1, S_2, \ldots, S_i\}$, the probability that in the set there are two spectral functions whose values are identical at every wavelength is reduced as the number of spectral channels are increased. In other words, the probability of obtaining unique spectral functions is increased as the number of spectral channels increases.

To conclude, CRA ordering relation is the most suitable ordering relation for spectral image processing. Despite being theoretically unable to satisfy the anti-symmetry property, in the hyperspectral domain it is possible to reach due to the large channel count which induces spectral uniqueness. The idempotency of this

ordering relation, which makes it superior to CCMM construction, will be given in Chapter 7.

4.7 Conclusion

The multivariate domain, such as that of hyperspectral images, is not naturally equipped with the notion of order or rank. While this does not mean that order is meaningless, hyperspectral ordering relation can only be constructed in a restricted form, by summarizing or combining features of the spectral measure. In this chapter, relevant existing and proposed multivariate ordering relations have been evaluated regarding their suitability for use in hyperspectral image processing. In addition to theoretical constraints, metrological tests have been proposed as evaluation protocol.

The proposed metrological evaluations rejected several ordering relations, i.e., marginal, lexicographic, and bit mixing approaches. A reduced ordering approach which is based on total amount of energy (Esum) was also evaluated. Even though it performed well during the metrological tests, it has a significant drawback which has also been demonstrated. Esum has a very reduced capability in taking into account spectral shape information. Various distance based ordering relations have also been evaluated and they generally deliver good performances. A particular note has to be made regarding cumulative distance based ordering relation. Its obtained minimum and maximum corresponds the notion of median and extrema, respectively. And due to that, it cannot distinguish minimum and maximum since they are mixed as extrema.

Aiming to construct a metrological image processing framework, it entails that total ordering property has to be satisfied. However, apart from the lexicographic approach, none of the relevant ordering relations are theoretically total ordering. Even for the lexicographic approach, it has been shown to be unable to satisfy the metrological constraints. The evaluated distance-based ordering relations face a challenge with the anti-symmetry property. Fortunately, as described by a mathematical conjecture, in the hyperspectral domain it is easier to obtain unique maximum and/ or minimum as demanded by the anti-symmetry property. The proposed ordering relation, i.e., conditional ratio and angular distance ordering relation (CRA), better ensures the spectral uniqueness than other distance-based ordering relations due to its use of two different conditions.

Regarding distance based ordering relations, they are generally more advantageous in application-driven image processing than other ordering approaches. In one sense, they provide flexibility in deciding which spectral features are to be taken into account and consequently a more suitable spectral distance function can be

used. Distance-based ordering relations which require spectral references would further allow expert users to define these references. Distance-based ordering relations requiring two references give even more flexibility, in the way that they allow mathematical morphology with user-defined convergence coordinates rather than assuming convergence to, e.g., black and white. However, this last point will be of a latter discussion which can be found in Chapter 7.

Summary of Contributions.

- ✓ Two metrological criteria were proposed, i.e., spectral ordering uncertainty and trueness in median filtering. These criteria are used to assess the performance of ordering relation.
- ✓ A hyperspectral ordering relation was proposed, i.e., conditional ratio and angular distance ordering relation (CRA). CRA is based on the ratio of distance values relative to two spectral references. Its first component is ratio between to distances, while its second is measure of ratio which is proportional to the notion of angle.

Part II

Hyperspectral Image Analysis and Processing Tools

Chapter 5

Hyperspectral Image Analysis through Spectral Differences

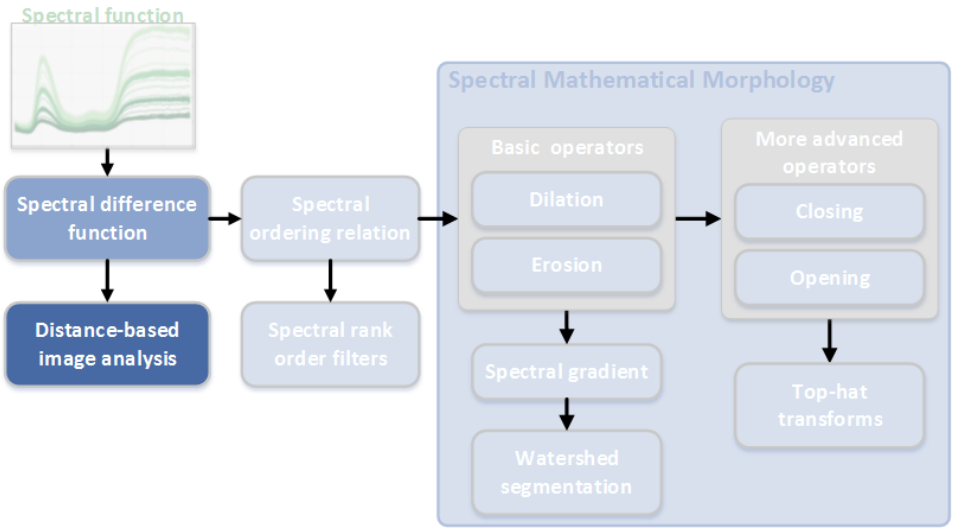

5.1 Introduction

Hyperspectral imaging (HSI) technology is a good news for the field of image processing since it offers a far greater potential than the traditional color imaging does. In addition to its high spatial sampling, HSI provides a high spectral sampling. As a spectral sampling increases, more data are obtained and color change assessment can be carried out with more accuracy. With such gain in accuracy, we believe that many image processing tasks can be addressed at a basic processing level.

And unlike what have been carried out for color and multispectral images, many hyperspectral image processing tasks would not need a complex classification or learning systems. But this comes at the cost of processing hyperspectral images at a metrological level.

Image analysis can be regarded as the first level of a complete image processing chain. At this low level of processing, measures can be managed and process quality and accuracy can be evaluated. Image analysis itself covers a broad range of application field, e.g., pigment identification in paintings [3, 58], land cover mapping [53,77], detection of melanoma from dermoscopic images [124,151], and many more. But despite its extensive range of applications and algorithms, image analysis tasks are generally addressed by means of classification and/ or unmixing approaches. In image classification, the similarities of an unidentified pixel to a set of well-identified spectral functions are computed. Then, the unknown pixel will be determined as belonging to the class to which it is the most similar. In an unmixing task, an unknown pixel is considered as a mixture of the known ones. Estimations are then generated by employing a certain mixing model. Then, the final concentration of the mixture is determined by an estimation which produces the smallest error to the pixel in question. It can be seen that in the two different approaches, the notion of similarity or distance plays a key role. It has been studied in Chapter 3 that the existing distance functions have different properties. And as a consequence, the choice of distance function will determine the quality of its subsequent processing steps and, finally, the end results.

Limiting the scope of study to hyperspectral image analysis by means of spectral differences, organization of the chapter is as follows. Section 5.2 introduces a graphical representation where features of a spectral image are described by means of spectral differences, i.e., bidimensional histogram of spectral differences (BHSD). The notion of reference is central in the context of spectral differences. Selecting an optimal reference is as important as selecting the correct distance function. In Section 5.3, discussions and directions of how to select an optimal spectral reference relative to the image at hand will be provided. Then, the combination of references allows to construct a higher dimensional graphical representation of spectral differences, i.e., tridimensional histogram of spectral differences (THSD). This graphical representation will be introduced in Section 5.4, as well as how to select the optimal combination of references. The previously introduced BHSD is employed as a tool to identify noise in a spectral image in Section 5.5. In the same section, numerical problems encountered in the calculation of spectral differences and their impact on the quality of results will be discussed. Finally, the chapter will be closed by a concluding perspectives in Section 5.6.

5.2 Graphical Representation of Spectral Differences

Let us now consider a painting subset which is shown in Fig. 5.1. By visual inspection, the image seems to have four main groups of pigments which roughly corresponds to the colors of blue, white, red, and yellow. But how should the spectral diversity and complexity of the content of this image be represented? Working with statistical distribution for each wavelength will not provide us with the different color groups and variations that exist within the image. Three one-dimensional histogram obtained from band images which roughly correspond to the red, green, and blue wavelengths are shown in Fig. 5.2. And as previously mentioned, none of the histogram is able to portray the complexity of image SCC01-1.

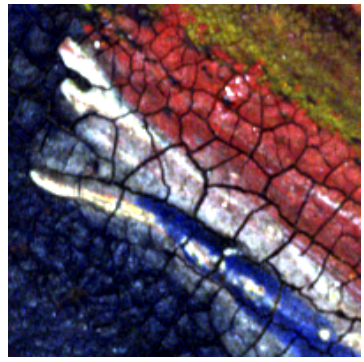

Figure 5.1 – Image SCC01-1 from Cracks-200 dataset. Shown color image was generated using ENVI software platform.

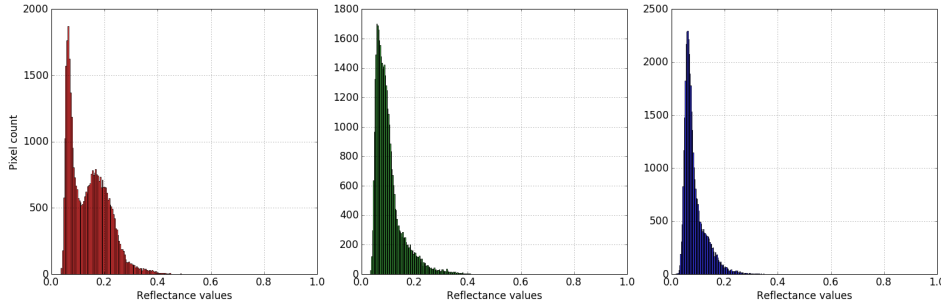

(a) Band image #45, 614.52 nm (b) Band image #31, 563.63 nm (c) Band image #2, 458.24 nm

Figure 5.2 – One-dimensional histograms of spectral reflectance values obtained from the band images of image SCC01-1. Horizontal axes of all plots are given in the full dynamic range of spectral reflectance values, i.e., from 0 to 1. As for the vertical axes, they are all of identical units, i.e., pixel count.

Rather than analyzing the content of a spectral image through its individual band images, we propose to employ spectral difference space as the feature space. In Chapter 3, spectral Kullback-Leibler pseudo-divergence (KLPD) has been concluded as the most suitable distance function for spectral data. Using S_{Wh} as the reference for KLPD function, a one-dimensional histogram of spectral differences of image SCC01-1 is obtained and shown in Fig. 5.3. However, this graphical representation is still not able to valorize the rich content of the spectral image in question. The obtained histogram shows two main color groups, despite there being four main groups which can be visually identified.

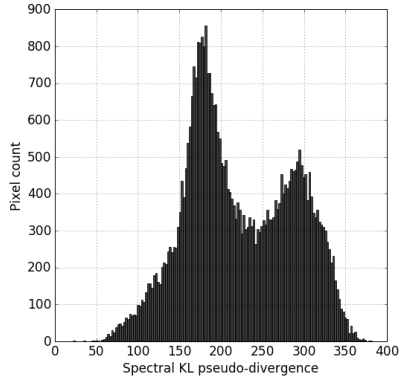

Figure 5.3 – One-dimensional histogram of spectral differences of image SCC01-1, obtained with KLPD and S_{Wh} as reference. Compared to the four color groups which can be identified visually, the histogram provides two main groups of colors.

If we recall the conclusion of Chapter 3, one of the reason why KLPD was chosen over Euclidean distance of cumulative spectrum (ECS)[1] was because KLPD combines as separate components the measures of shape and intensity differences. On the contrary, in ECS, the two are integrated without the ability to perceive which spectral variation is more predominant. And since KLPD combines measures of shape and intensity differences through an addition operation, the one-dimensional histogram shown in Fig. 5.3 can be easily expanded to a two-dimensional histogram of spectral differences by splitting its two individual components. This two-dimensional expansion of histogram of spectral differences can be seen in Fig. 5.4, where the horizontal and vertical axes correspond to shape and intensity components of KLPD function, respectively. Note that this graphical representation was first proposed by Richard *et al.* [145] in the context of KLPD function construction

[1]ECS was the first proposal of a suitable spectral distance function whose limitation has been identified since, and has been overcome by another development of spectral difference function, i.e., KLPD function.

and will, further on, be referred to as bidimensional histogram of spectral differences (BHSD). Observing the obtained BHSD, it is evident that discrimination of the spectral content of image SCC01-1 has improved since the pixels start to form different clusters.

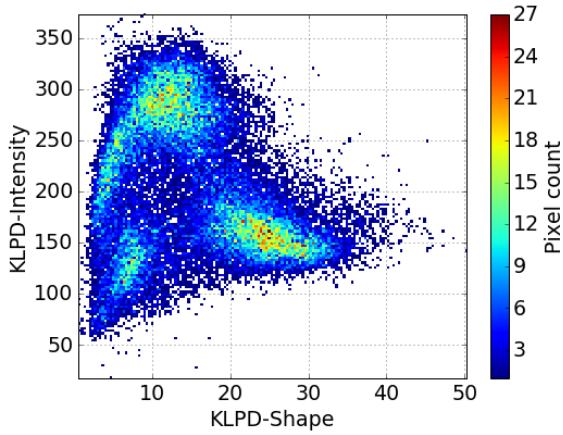

Figure 5.4 – Bidimensional histogram of spectral differences (BHSD) of image SCC01-1, obtained using the shape and intensity components of KLPD function and S_{Wh} as reference.

The one example provided in Fig. 5.4 demonstrates the great potential of using spectral differences as a feature space for image analysis. However, apart from the bidimensional representation, is KLPD construction superior than other spectral difference functions which also measure shape and intensity differences?

Euclidean distance measures intensity differences, although by assuming that a spectral function is a vector in the Euclidean space. Replacing KLPD-Intensity axis with this distance measure, a BHSD in Fig. 5.5a is obtained. Comparing this BHSD with the one shown in Fig. 5.4, it can be said that KLPD-Intensity is a better measure of intensity differences than Euclidean distance. Spectral angle [97], a popular measure in the remote sensing field, is capable of discounting the effect of shading. Thus, spectral angle can be regarded as a measure of shape differences. Replacing KLPD-Shape axis in Fig. 5.4 with spectral angle, Fig. 5.5b is obtained. In this BHSD, a relatively good discrimination of the spectral content of image SCC01-1 is demonstrated. Just as the one shown in Fig. 5.4, there are roughly 4 main clusters in the BHSD. However, KLPD-Shape is still superior to spectral angle since it provides better determination of the clusters. In other words, distribution of the pixels are closer to the center of each cluster than what is obtained by spectral angle. Superior performances of the 2 components of KLPD function is

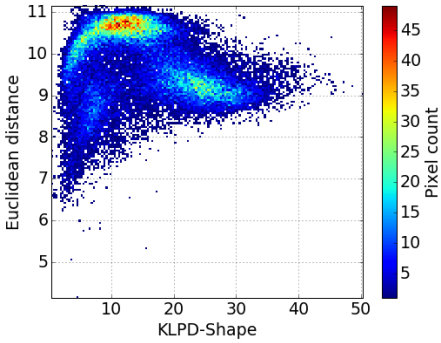

(a) KLPD-Shape & Euclidean distance

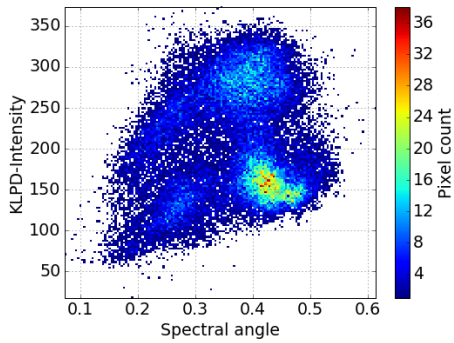

(b) Spectral angle & KLPD-Intensity

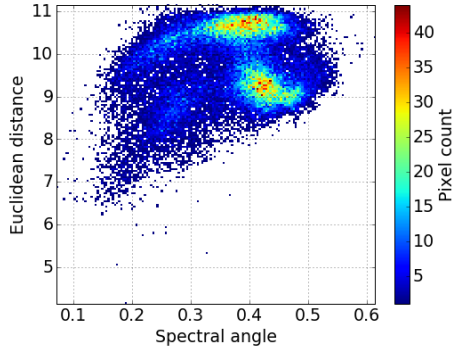

(c) Spectral angle & Euclidean distance

Figure 5.5 – BHSDs of image SCC01-1 obtained using various pairs of shape and intensity difference measures, and S_{Wh} as reference. Compared to BHSD shown in Fig. 5.4, none of the ones shown in this figure gives better discrimination.

as expected since KLPD function has a more suitable definition of what a spectral function is. On the other hand, both Euclidean distance and spectral angle erroneously assume that a spectral function is a vector in the Euclidean space, causing less performance in spectral content discrimination. In fact, if the two are employed to discriminate the content of image SCC01-1, significantly less discrimination power can be observed in Fig. 5.5c. Moreover, spectral angle and Euclidean distance are not uncorrelated [145], unlike the two components of KLPD function. Finally, after the previous results, we claim that many image processing tasks can be solved at the level of image analysis without having to employ more advanced image processing tools. And all of these potentials are enabled by employing the most suitable measures of spectral differences, i.e., KLPD. Note that KLPD function will be employed for the rest of the chapter, unless stated otherwise.

5.3 On Spectral Reference Selection

Defining a suitable distance function is one step toward a powerful hyperspectral image analysis. But a distance function further requires to define a reference. And depending on the choice of reference, image analysis results will differ.

Fig. 5.6 is generated to show the impact of reference selection to the discrimination of content in image SCC01-1. Two spectral functions are randomly selected from the target image and then used as references for KLPD. As observed, the use of different references leads to different discrimination ability of the image content. And if the two are further compared to the one shown in Fig. 5.4, it becomes evident that S_{Wh} which is employed to obtain the latter BHSD is a better reference. S_{Wh} allows the discrimination of four different groups of pixels rather than the previous ones where there is no clear grouping of the pixels in their respective BHSDs. In the following, we will show how an optimal spectral reference can be selected such that the obtained BHSD provides a good discrimination capability of the image content.

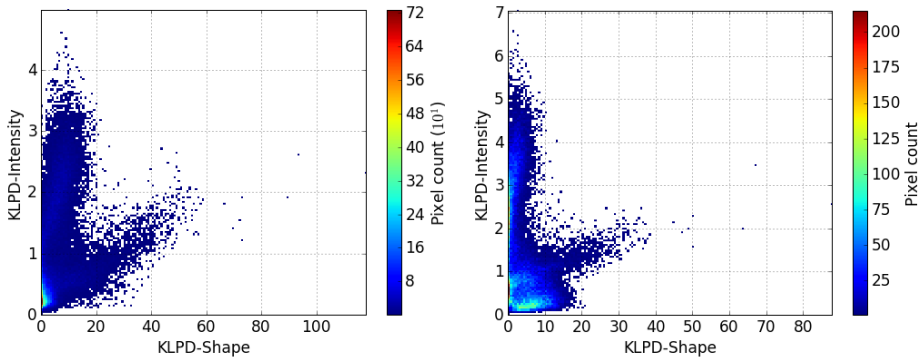

Figure 5.6 – BHSDs of image SCC01-1, obtained using KLPD function and two spectral functions which are randomly selected from the initial set of image SCC01-1 as references.

5.3.1 Selection Criteria

Distribution of spectral variations within a given image can be expressed in terms of a convex hull. And the convex hull of this initial spectral set can be obtained through a BHSD. See illustration given in Fig. 5.7. Suppose that in a given image, the pixels can be grouped into 3 clusters, whose centers are A, B, and C. Together, these clusters form a single convex hull. If we are to find a reference point such that the three clusters are well-identified, then there are several options to explore.

In the first case, see Fig. 5.7a, a reference point located far from the convex hull is selected. In such a case, the employed distance function could potentially end up 'seeing' the clusters as 'equally far' since it becomes saturated[2]. As a consequence, the different clusters are being perceived as a single cluster. Another option would be choosing one of the centers (or any point which belong to the initial clusters) as the reference. The risk of this selection is illustrated through Fig. 5.7b. Choosing a reference from any of the initial clusters might well-identify the cluster in which the reference belongs to. However, if the two other clusters are at considerably equal distance to the reference cluster, they might be recognized as the same one. Expected histogram of the illustrated case is represented by multimodal distributions, see the bottom row of Fig. 5.7b. This is to illustrate that differences between cluster B and C might still be perceived by the distance function, although with less discrimination. Similar discrimination ability will also be obtained if a reference point fall within the convex hull, even if it does not necessarily belong to any of the initial clusters, see Fig. 5.7c.

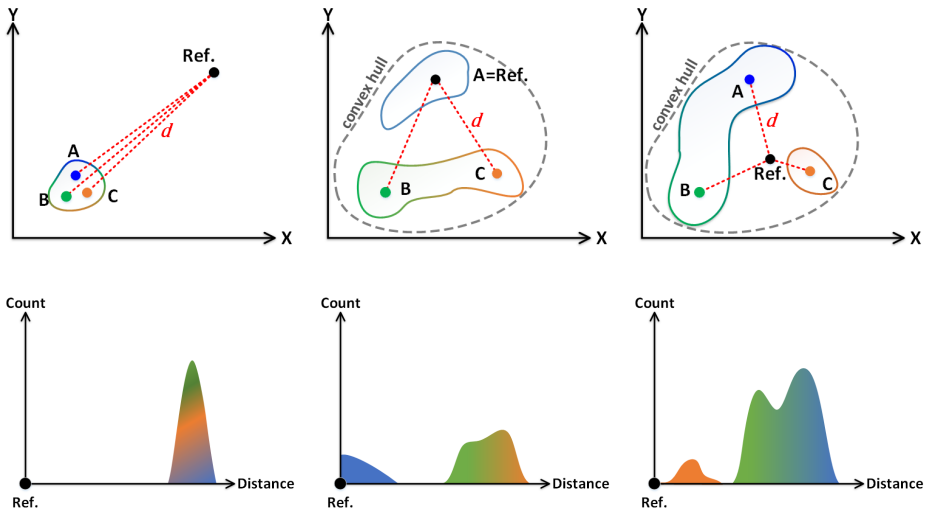

Figure 5.7 – Illustrations of **(top row)** non-optimal reference selection in a two-dimensional space and **(bottom row)** their corresponding expected distance histograms. A, B, and C are 3 points belonging to 3 different clusters and are considered as the centers. Together, the 3 clusters form a single convex hull. An optimal reference point should not be located 'far' from or fall within the initial convex hull.

[2]The saturation of distance function can be regarded as a certain point where the obtained distance values start to reach infinity. See Section 3.3 for more explanation.

An optimal selection of spectral reference is as illustrated in Fig. 5.8a. First, the reference point should fall outside the convex hull. Then, in the distance plane, it should be located 'close enough' in terms of magnitude to the convex hull such that it falls near the edge (or on the surface of a three-dimensional convex hull). But since measure of distance is always positive, there is still a risk of multiple clusters being recognized as one. Nevertheless, with this selection the distance values will be better distributed across the entire dynamic range, allowing to obtain a histogram as illustrated in Fig. 5.8b.

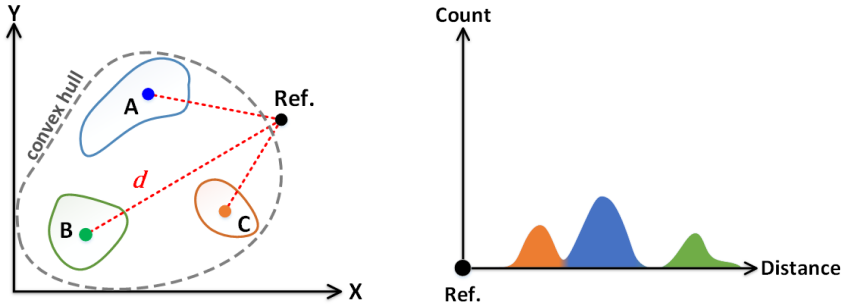

(a) Suggested selection of reference (b) Expected distance histogram of (a)

Figure 5.8 – Illustration of optimal reference selection in a two-dimensional space and its expected distance histogram. The reference should be chosen from outside the convex hull, considerably near to its edge. This will allow the distance of all pixels to be well-distributed along the dynamic range of the distance values.

As illustrated in Section 5.2, one component of spectral differences is insufficient to describe the complexity and diversity of the content of a spectral image. In addition to intensity variations, BHSD also considers shape variations one of its components. Thus, when considering a spectral reference, its shape variations should also be taken into account. Illustrations of non-optimal reference selection in an angular space can be observed in Fig. 5.9. As it is the case when using a measure of distance, a good reference should not be located 'too far' from the convex hull of the initial spectral set. And this is to avoid the case illustrated in Fig. 5.9a, where the employed measure of angle becomes insensitive to differences between the clusters. Then, a good reference should also not come from the initial spectral set because it will lead to what is illustrated in Fig. 5.9b. The optimal selection of reference in an angular space is illustrated in Fig. 5.10, where the reference is located 'close enough' to the edge of the convex hull. And as observed, the three different clusters of A, B, and C will be recognized correctly by the angular measure.

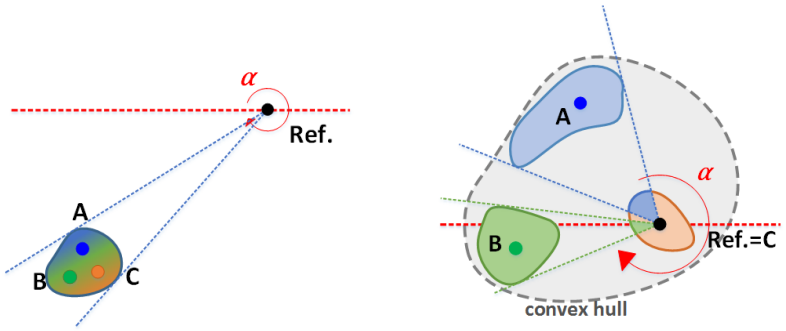

(a) Selected reference is far from the convex hull of the initial spectral set

(b) Selected reference belongs to the initial spectral set

Figure 5.9 – Illustrations of non-optimal reference selection in an angular space. A, B, and C correspond to the centers of three clusters in the initial spectral set.

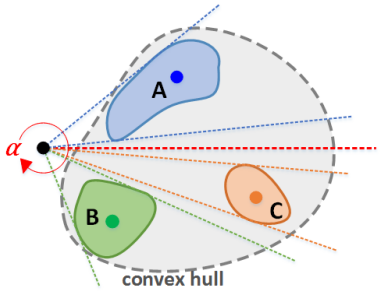

Figure 5.10 – Illustration of an optimal reference selection in an angular space. A good reference is located near the edge of the convex hull of the initial spectral set. A, B, and C are the centers of the three clusters.

To summarize, an optimal spectral reference which would allow a good discrimination of the spectral content of an image is one that does not fall within the convex hull of the initial spectral set. Rather, it should be one which is located 'near' the edge of the convex hull, as measured in terms of intensity and shape variations through a BHSD. The implementation of this concept in a real applications task will be provided in the following section.

5.3.2 Reference Selection in A Pigment Discrimination Task

To demonstrate the selection of an optimal spectral reference, image SCC01-2 from Cracks-200 dataset (see Appendix B.3) is employed, see Fig. 5.11a. Upon visual observation, there are roughly five clusters of color pigments, i.e, white, orange, brown, yellow, and red. For each cluster, one spectral reflectance function whose location is indicated by a blue arrow is extracted and plotted, see Fig. 5.11b.

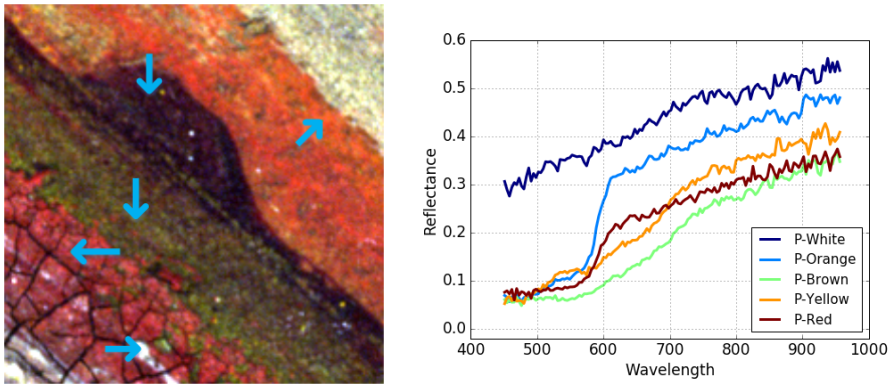

(a) Image SCC01-2

(b) Spectral reflectance functions

Figure 5.11 – Image SCC01-2 from Cracks-200 dataset (Appendix B.3) and 5 spectral reflectance functions originating from pixels indicated by the blue arrows.

Previously, it has been mentioned that the reference should not be taken from the initial spectral set. To demonstrate the impact, two spectral reflectance functions from Fig. 5.11b are employed as references, i.e., P-White and P-Orange. BHSDs of image SCC01-2 with the two as references are shown in Fig. 5.12. When P-White is employed as reference, the obtained BHSD in Fig. 5.12a gives a considerably good discrimination of the image content. Through visual observation, roughly 4 pigment clusters can be estimated. Then, since the reference is a white colored pigment, the small group of pixels located around the origin of both axes of the BHSD corresponds pixels of this color. For a reference which originates from the initial dataset, P-White demonstrates a good performance. However, this is not surprising. Comparing P-White with other spectral reflectance functions shown in Fig. 5.11b, its shape is significantly different from the rest.

Let us now consider P-Orange as reference, whose shape is considerably similar to the majority of spectral functions shown in Fig. 5.11b. Comparing its BHSD which is shown in Fig. 5.12b to the one previously obtained by P-White, its discrimination ability is significantly reduced. And through a visual observation, only 3 clusters of pigments can be identified. Moreover, among the three, 2 clusters are

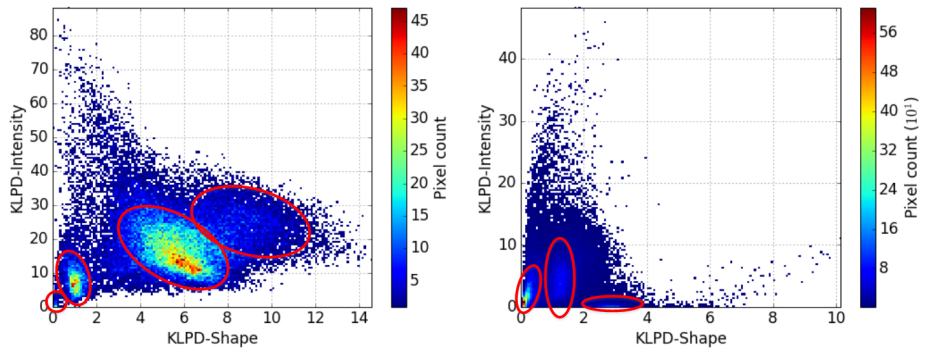

(a) P-White as reference, 4 pigment clusters are roughly estimated

(b) P-Orange as reference, 3 pigment clusters are roughly estimated

Figure 5.12 – BHSDs of image SCC01-2 obtained using 2 spectral references originating from the image itself, i.e., P-White and P-Orange shown in Fig. 5.11b. Pigment cluster estimation is carried out manually through visual observation.

of faint cyan colors. And this means that the clusters are only slightly formed, with small portions of the entire pixels being concentrated around the center of these 2 clusters. Then, in terms of intensity variations, P-Orange is also considerably similar to the majority of content in image SCC01-2, except for the white colored pigments. Finally, the poor discrimination is due to P-Orange being too similar to the majority of contents in both shape and intensity variations, see Fig. 5.11b.

It has been said that an optimal spectral reference must be located 'outside' the convex hull of the initial spectral set. In the context of a BHSD, this means a spectral function whose shape and intensity features are different from the content of image SCC01-2. With such considerations, 3 artificial spectral functions are generated, see Fig. 5.13. They are constructed such that their intensities fall outside the dynamic range of the initial spectral set, i.e., for the spectral functions shown in Fig. 5.11b to be bounded from above and below. As for the shapes of these artificial spectral functions, selections are made by considering the spectral functions from the initial spectral set as combinations of Gaussian-like functions and their integrals. For example, the shape of R1 is generated to resemble the parts of P-Yellow and P-Red, see Fig. 5.13a. P-Yellow itself has a slight Gaussian-like shape whose peak located around 540 nm. Then, a portion of P-Red from around 560 nm onward can be approximated by the integral of a Gaussian-like function whose peak is located around 600 nm. By combining the two basic functions and modifying the intensity of the combination, R1 is obtained. R2 and R3 in Fig. 5.13b are generated as approximations of P-Brown and P-Yellow, respectively.

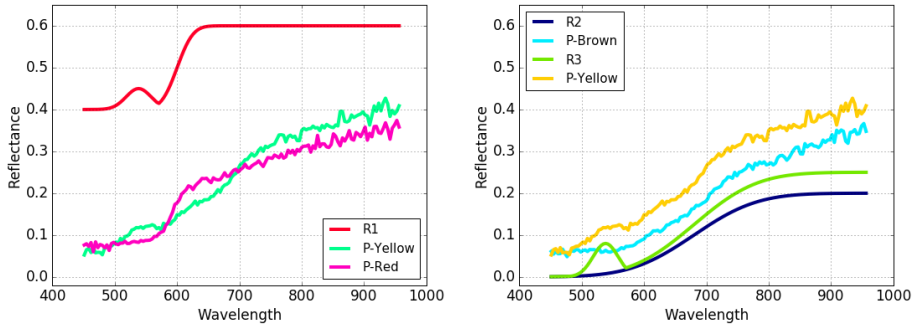

(a) Spectral shape of R1 to resemble parts of P-Yellow and P-Red

(b) Spectral shapes of R2 and R3 to resemble P-Brown and P-Yellow, respectively

Figure 5.13 – Artificial spectral functions R1, R2, and R3, to be used as references in discriminating the content of image SCC01-2. Their intensities are selected such that they bound the spectral set from below and above.

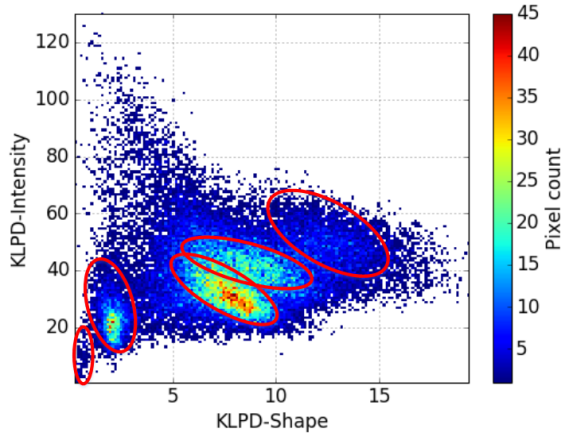

Figure 5.14 – BHSD of SCC01-2 obtained using artificial spectral function R1 shown in Fig. 5.13 as reference. Five pigment clusters are manually estimated through a visual observation.

Using the artificial spectral functions in Fig. 5.13 as references, BHSDs in Fig. 5.14 and 5.15 are obtained, where estimations of pigment clusters are carried out manually through visual observations. R1 and R2 demonstrate good performances in discriminating the content of SCC01-2. Five pigment clusters can be estimated through their corresponding BHSDs in Fig. 5.14 and 5.15a. Comparing these two BHSDs, R1 is considered a better choice than R2 since more pixels are distributed

across the obtained dynamic ranges of both axes. Rather than in the BHSD of R2 where majority of pixels are located in half of the obtained dynamic ranges for both intensity and shape axes. The intensity of R1 is larger enough in magnitude than most of the spectral content of the image. On the other hand, R2 bounds the initial spectral set from below with a smaller margin than R1 does bound from above, see Fig. 5.13. And it seems that intensity differences between R2 and the initial spectral set are not significant enough, resulting in a reduced discrimination between the pigment clusters across the intensity axis, see Fig. 5.15a and 5.15b. Due to similar reason, BHSD obtained by R3 also has a reduced discrimination along the intensity axis, see Fig. 5.15c and 5.15d.

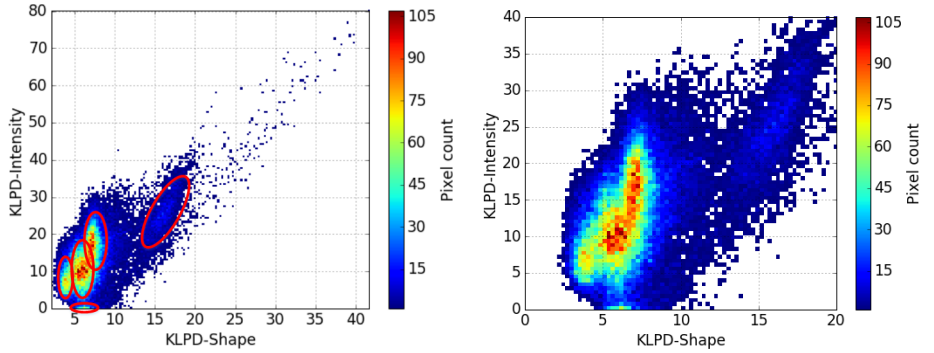

(a) R2 as reference

(b) R2 as reference, a zoomed view

(c) R3 as reference

(d) R3 as reference, a zoomed view

Figure 5.15 – BHSDs of SCC01-2 obtained using 2 of the artificial spectral functions shown in Fig. 5.13 as references. The estimations of pigment clusters in each BHSD is carried out manually by visual observation. Zoomed views of the BHSDs are also provided without estimations of the pigment clusters.

By observing Fig. 5.15, we can conclude that discrimination of the spectral content of image SCC01-2 is mostly due to shape differences. And comparing the three choices of spectral references, agreeing with the previous discussion, R1 is a better reference for the task. Albeit with a comparably reduced dynamic range, the obtained shape differences are better distributed in the BHSD obtained by R1, see Fig. 5.14. Comparing the performances of R2 and R3 in Fig. 5.15b and 5.15d, respectively, R2 leads to a slightly better discrimination of the pigment clusters. The observed performance is mainly due to the peak it has around 540 nm, which does not exist in R3. Although it is only an insignificant portion of the entire spectral range, it allows to better discriminate pigments which have similar shape around this wavelength, e.g., the yellow and orange pigments.

5.4 Tridimensional Histogram of Spectral Differences

A BHSD is limited in the sense that it can only display spectral differences relative to one spectral reference. In some cases, this might be sufficient provided that the reference selection is carried out properly. An example of such a case can be observed in Section 5.3.2. But in a case where the spectral content is more complex and diverse, using a single reference may lead to inefficient exploitation of the available information. By combining two spectral references, a tridimensional histogram of spectral differences (THSD) can be obtained.

For a single reference, we know that it must be selected from outside around the edge of the convex hull, see Section 5.3.1. But which two spectral functions are to be combined to construct a THSD? Will any arbitrary spectral functions make an optimal pair of references? To demonstrate how to select a good pair of spectral references, image SCC01-1 in Fig. 5.16a will be employed as a target in the task of pigment discrimination. By visual observation, 5 pigment clusters can be identified in the image, i.e., blue, white, red, yellow, and brown. Spectral reflectance functions corresponding to the pigments are also provided in Fig. 5.16b.

An optimal reference can be determined by generating a spectral function whose shape and intensity variations are considerably different from the content of image SCC01-1. Spectral function R1 (Fig. 5.17a) is selected as one reference. Its shape is made to resemble portions of P-Yellow until approximately 580 nm and of P-Red from 580 nm onward. Its intensity is chosen to bound the other spectral functions shown in Fig. 5.17a from above. The BHSD obtained by R1 can be seen in Fig. 5.17b, where roughly 4 pigment clusters can be estimated.

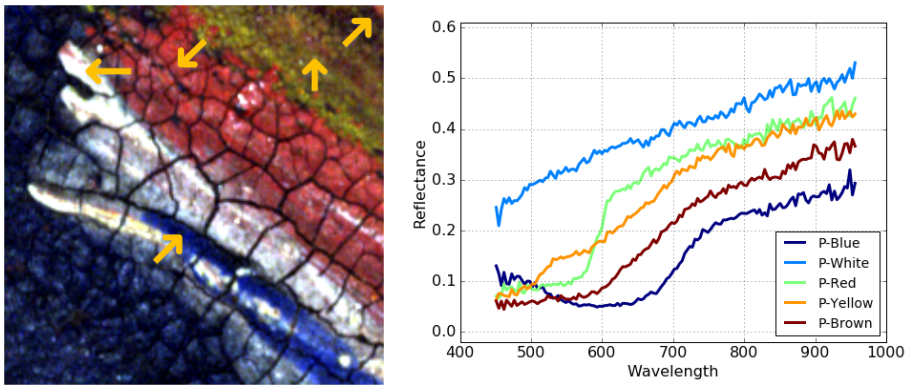

Figure 5.16 – Image SCC01-1 from Cracks-200 dataset and its spectral reflectance functions obtained from locations indicated by the yellow arrows. Shown color image is generated using ENVI software platform.

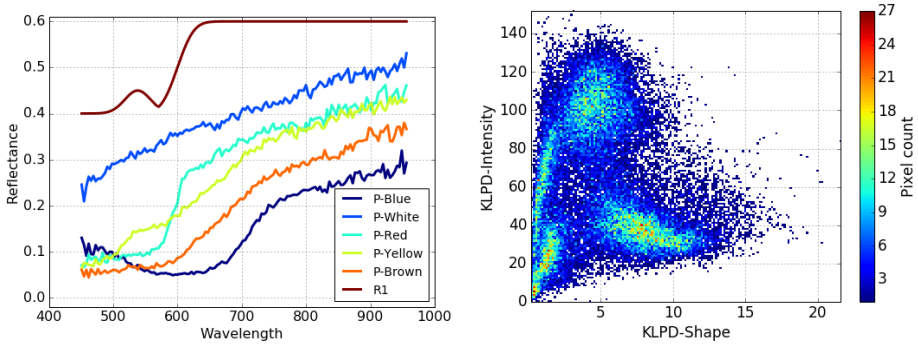

(a) Reference R1

(b) BHSD produced by R1

Figure 5.17 – Spectral function R1 shown relative to the content of image SCC01-1 and the BHSD it produces. Roughly 4 pigment clusters can be estimated from the obtained BHSD.

Selection of the other reference starts from the convex hull generated by R1, i.e., the BHSD it obtains. In Fig. 5.18, a modified BHSD is shown where each dot corresponds to each pixel in the image, colored according to the pixel color given in Fig. 5.16. Note that the limitation of this BHSD lies in the fact that entries superpose each other. Thus, not all colors which exist in the image will be visible in the modified BHSD. Nevertheless, this BHSD will help in determining the shape and intensity variations the next reference should have. And by observing this modified BHSD, we know that a dark blue spectral function would lie outside the

convex hull. Aiming to resemble the shape of P-Blue in Fig. 5.17b and with a slightly lower intensity level, an artificial spectral function R2 is generated, see Fig. 5.19a. The location of R2 relative to the convex hull of image SCC01-1 as obtained by R1 can also be observed in Fig. 5.18.

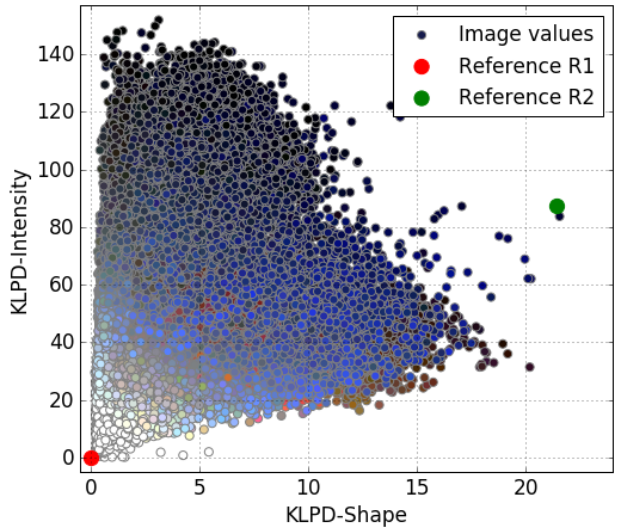

Figure 5.18 – The selection of reference R2, relative to the convex hull of image SCC01-1 as obtained by a predetermined reference R1. Shown is a modified BHSD, where each dot corresponds to each pixel in the image. Colors of the dots are obtained from colors of each pixel in Fig. 5.16a.

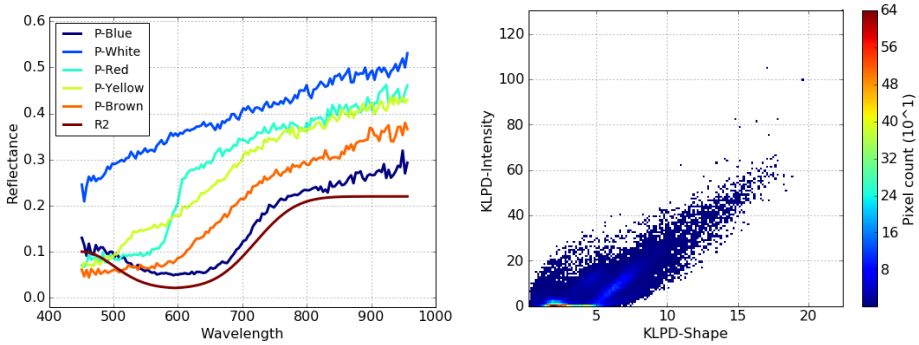

(a) Reference R2

(b) BHSD produced by R2

Figure 5.19 – Spectral function R2 shown relative to the content of image SCC01-1 and the BHSD it produces.

According to the previously formulated criteria of how to select an optimal spectral reference in Section 5.3, R2 should provide a good discrimination for image SCC01-1. But it does not seem to be the case if we observe its corresponding BHSD in Fig. 5.19b. Not obtaining a good discrimination in the two-dimensional representation of spectral differences, however, does not automatically eliminate R2 as a reference candidate. Employing R2 in combination with R1 could potentially improve the discrimination power R1 has to begin with.

Through Fig. 5.17b, we know that both spectral difference components obtained by R1 are good features for discriminating the content of SCC01-1. Thus, the two are selected as two axes in the THSD we are constructing. Then, in Fig. 5.19b, we can see that R2 provides a good distribution along the shape axis. Thus, the shape component of BHSD obtained by R2 will be chosen as the third axis of THSD. The constructed THSDs can be observed in Fig. 5.20, where 4 different views are provided. Note that the 4 views are constructed using the same references but varying on the minimum histogram count to show.

All of the histogram entries are shown in Fig. 5.20a, where no pigment groups are evident. Then, from Fig. 5.20b to 5.20d, the minimum histogram count to show are increased in order to better observe pigment groups that are detected. Choosing to show histogram entries with minimal count of 4, Fig. 5.20b allows us to see that in this THSD there are two pigment clusters. The two clusters are manually estimated and are marked in yellow and red dotted lines. Aiming to better observe the centers of each pigment clusters, the minimum histogram count is increased to 7 in Fig. 5.20c. With this visualization, we can see that there are actually two smaller clusters inside the one marked inside yellow dotted line in Fig. 5.20b. Then, we also start to see that there might also be smaller clusters inside the one marked by red dotted line. Aiming to observe potential clusters, the minimum histogram count is further increased to 12 and Fig. 5.20d is obtained. Finally, in this visualization it is revealed that the pigment cluster within the red dotted line indeed consists of 3 smaller pigment clusters. Therefore, according to THSD obtained by R1 and R2, 5 pigments clusters are estimated within image SCC01-1. And this agrees to what has been estimated through visually observing its color image in Fig. 5.16a.

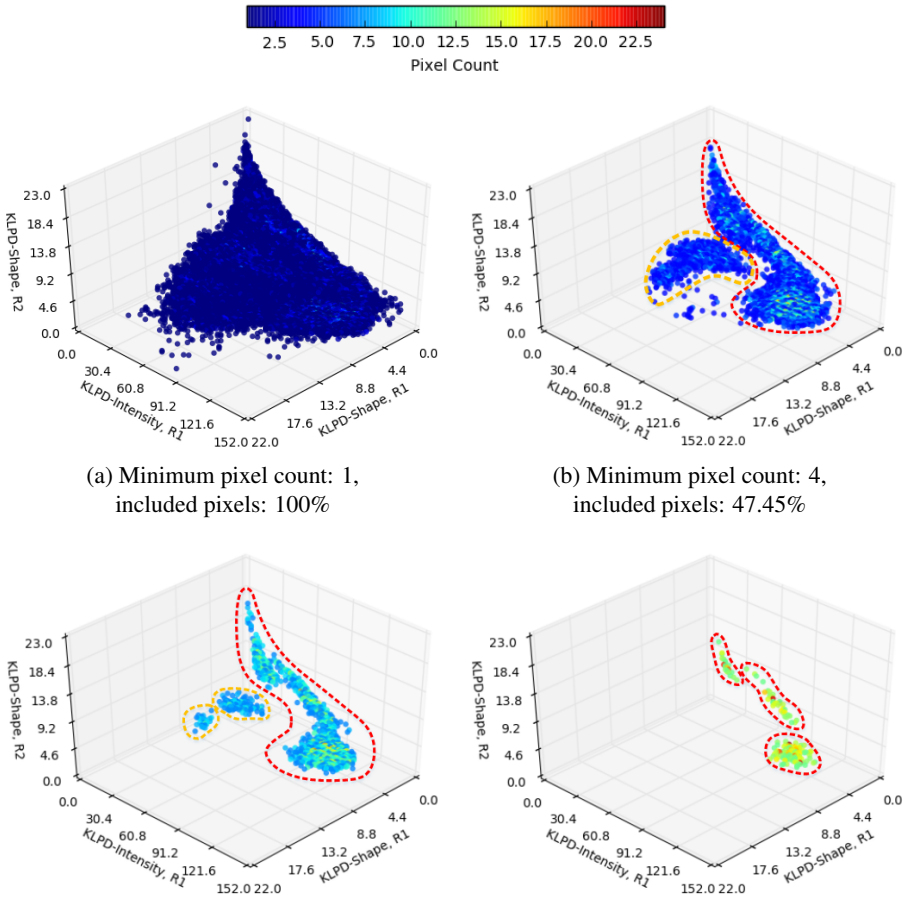

(a) Minimum pixel count: 1, included pixels: 100%

(b) Minimum pixel count: 4, included pixels: 47.45%

(c) Minimum pixel count: 7, included pixels: 23.05%

(d) Minimum pixel count: 12, included pixels: 5.11%

Figure 5.20 – Tridimensional histograms of spectral differences (THSDs) of image SCC01-1 obtained using R1 (Fig. 5.17a) and R2 (Fig. 5.19a) as references. The different views are obtained by choosing different minimum histogram count to show. Estimation of pigment clusters are carried out manually by visual observation. Initially, two pigment clusters are estimated in (b). Closer observations then reveal that each of the clusters consists of several smaller ones, making in total 5 clusters of pigments.

To contrast the previous selection of spectral reference pair where each of the artificial spectral functions lie outside the convex hull of image SCC01-1, two spectral functions originating from the image will be employed as references. They are P-Red and P-Blue, see Fig. 5.16b. Their corresponding THSDs can be observed in Fig. 5.21. Showing all of the histogram entries, just as previously observed in the R1-R2 generated THSDs, only one big pigment cluster can be observed in Fig. 5.21a. Nevertheless, this visualization gives an idea of a three-dimensional shape of the convex hull of image SCC01-1. By increasing the minimum histogram count to 4, roughly 3 pigment clusters can be estimated in Fig. 5.21b. The detected clusters are marked within the red, green, and yellow dotted lines. Aiming to better observe the cluster within the red dotted line, the minimum histogram count to show is further increased to 7 and Fig. 5.21c is obtained. This visualization allows us to see that the cluster we are interested in consists of two smaller pigment clusters. To see if yet another closer observation would lead to more detection of pigment clusters, the minimum histogram count is increased to 12 in Fig. 5.21d. And in this THSD, no new pigment cluster can be observed. Finally, this selection of reference pair leads to an estimation of only 4 pigment clusters.

To conclude shortly on the hyperspectral image analysis by means of a BHSD and THSD, even if the reference selection seems delicate, they are actually not complicated and can be decided quickly. In majority of cases, a BHSD is sufficient to observe pigment variations within a given image. Nevertheless, a THSD provides a possibility to observe the content of a more complex image, such as those coming from paintings.

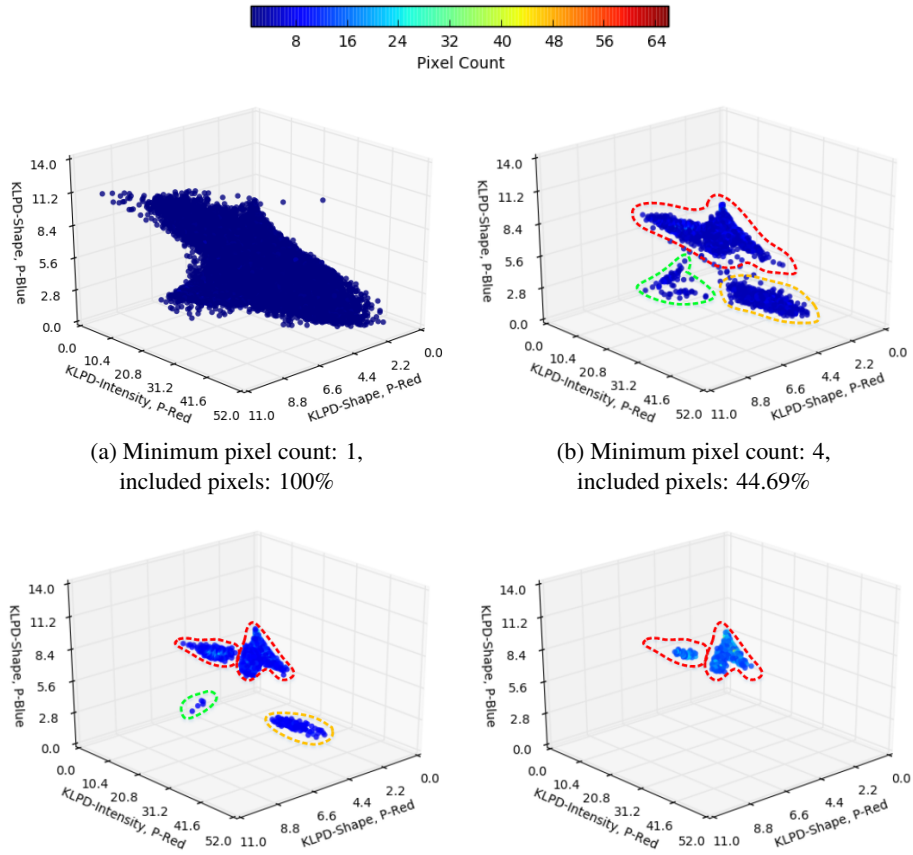

(a) Minimum pixel count: 1, included pixels: 100%

(b) Minimum pixel count: 4, included pixels: 44.69%

(c) Minimum pixel count: 7, included pixels: 38.93%

(d) Minimum pixel count: 12, included pixels: 19.22%

Figure 5.21 – THSDs of image SCC01-1 obtained using P-Red and P-Blue (Fig. 5.16b) as references. The different views are obtained by choosing different minimum histogram count to show. Estimation of pigment clusters are carried out manually by visual observation. Initially, three clusters can be identified, i.e., those marked in red, green, and yellow dotted lines. Closer observations then revealed that the cluster within the red dotted line is composed of two smaller ones, making an estimated total of 4 pigment clusters.

5.5 Implementation Notes and Noise Impact in Spectral Differences

Note that programming language used in the following are Python. Nevertheless, implementation considerations that are given are independent and can be adapted to functions that are relevant to the chosen programming language.

5.5.1 Log of Zero in Spectral Kullback-Leibler Pseudo-Divergence

Inside the mathematical expression of KLPD function (see Eq. 3.6), there is a logarithm function written as follows.

$$\log\left(\frac{s_1(\lambda)}{s_2(\lambda)}\right)$$

This expression could potentially induce numerical problems, especially when a spectral function has zero values. When $s_2(\lambda) = 0$, Python would return a runtime error. But when it is $s_1(\lambda)$ who is 0, the logarithm function will become $\log(0)$, which is yet another numerical problem. To recall, logarithm $\log(x)$ is only defined for $x > 0$. In Python, instead of returning a runtime error, the interpreter would return `nan`, short for 'not a number'. One potential workaround is by calling `numpy.nan_to_num()` function after computing the spectral difference, which would convert every `nan` it encounters to 0. But as a consequence, the shape difference, in which the logarithmic expression is incorporated, of every spectral function which contains zero values to the chosen reference will be zero. This case is well illustrated in Fig. 5.22, where image NP2 and SCC01-1 and S_{Wh} reference are employed. As observed in this figure, there is a significant amount of pixels with zero shape differences to the reference, see areas circled in red. The employed reference S_{Wh} is equi-energetic, or in other words, a flat spectral function. But none of the spectral reflectance functions in the two images are equi-energetic. Thus, this workaround is not to be chosen.

$\log(0)$ should be avoided prior to difference computation, rather than handling it post-computation. And as explained previously, this issue is caused by spectral functions having zero values. To avoid the problem, these zero values should be replaced by a small constant value ε. The impact of ε selection to the BHSD of NP2 and SCC01-1 can be observed in Fig. 5.23. After replacing the zero values, zero-valued shape entries are completely removed. However, this strategy leads to another numerical issue to tackle, i.e., the unrealistic periodical distribution of shape differences. It can also be observed that as ε becomes smaller, more periodic waves are introduced. Then, which ε value is to be selected? Zero reflectance or radiance value can be interpreted as the absence of energy. Thus, the only acceptable replacement value is one that respect similar physical meaning. This

(a) Image NP2

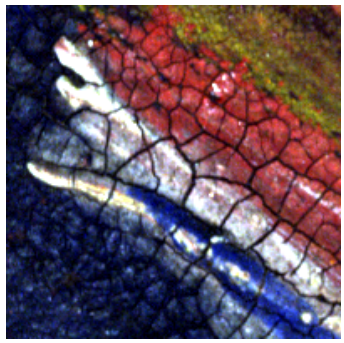

(b) Image SCC01-1

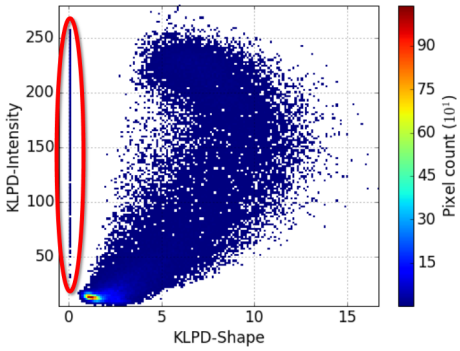

(c) BHSD of NP2, unhandled $\log(0)$

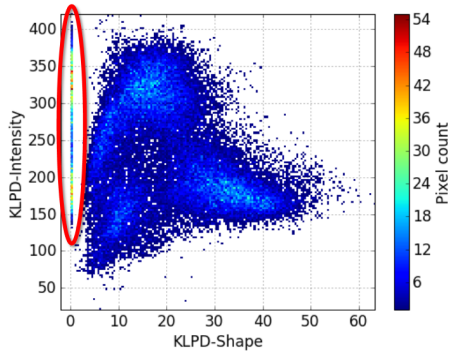

(d) BHSD of SCC01-1, unhandled $\log(0)$

Figure 5.22 – Two image targets having zero reflectance values and their corresponding BHSDs obtained with S_{Wh} as the reference. Histogram entries circled in red are caused by unhandled $\log(0)$ which results in zero shape differences.

means that ε must be significantly small compared to the general dynamic range of the spectral functions. For this reason, in our implementation $\varepsilon = 10^{-32}$ is chosen. Discussion and implementation strategy regarding the observed periodics in Fig. 5.23 will be provided in following section. In this later section, we will discover that the periodic waves are not due to numerical artifacts related to the log of zero, but rather due to sensor noise.

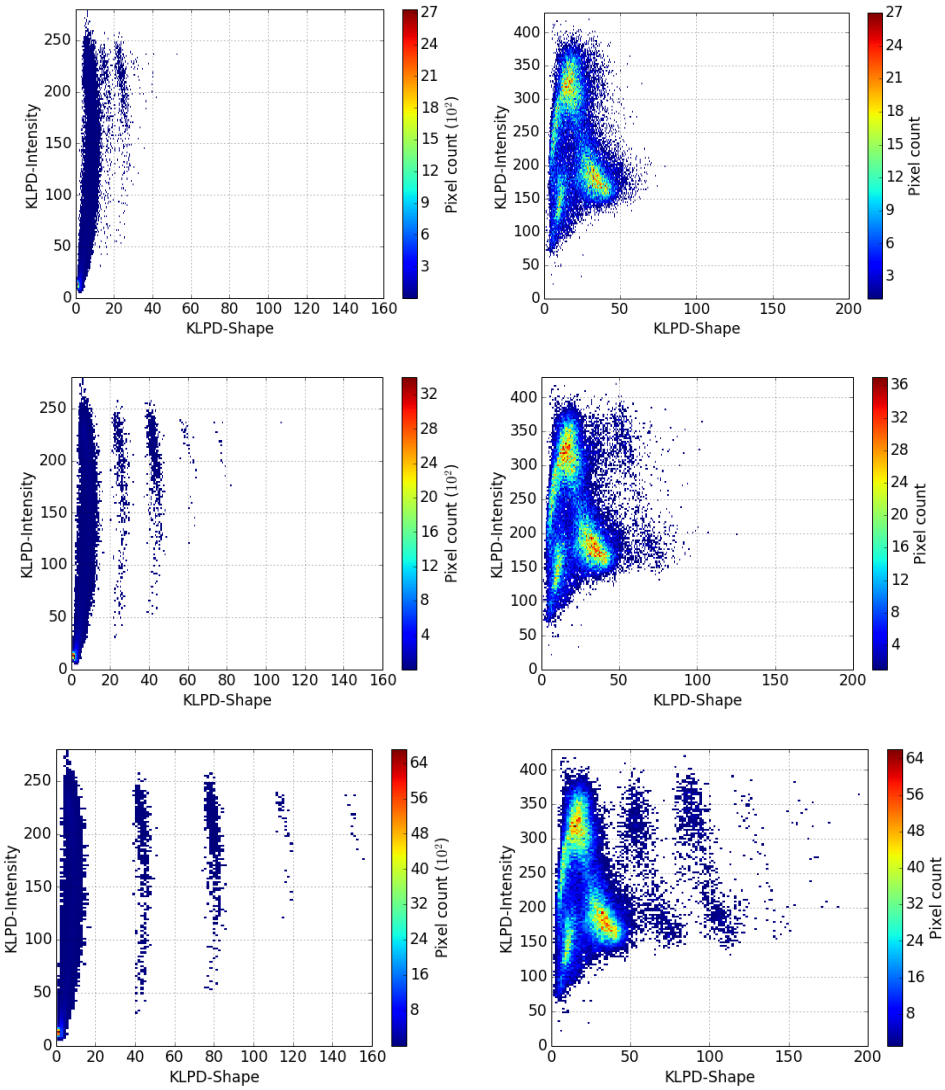

(a) BHSDs of image NP2

(b) BHSDs of image SCC01-1

Figure 5.23 – Three BHSDs obtained for image NP2 and SCC01-1, in which S_{Wh} are employed as spectral reference. From top to bottom, constant value ε replacing zero values are 10^{-8}, 10^{-16}, and 10^{-32}. Note that the periodic waves that appear in all BHSDs are due to sensor noise and will be discussed in Section 5.5.2.

5.5.2 Noise Identification using BHSD

Depending on the sensitivity of a hyperspectral sensor, an obtained hyperspectral image might be noisy at certain wavelengths, typically at the extremities of the spectral range[3]. While other types of noise can also be present, the existence of the former type can be detected through the use of BHSD. It has been identified that the hyperspectral scanner employed to capture datasets used in this study are noisy at both extremities, i.e., around 400 and 1000 nm. Thus, several spectral bands at these regions should be ignored during computation and thus introducing the notion of band cutoff, i.e., numbers of ignored spectral bands at each extremity.

The impact of various band cutoffs on the BHSDs of image NP2 and SCC01-1 can be observed in Fig. 5.24 and 5.25. Shown BHSDs were obtained with KLPD, S_{Wh} as reference, and zero value replacement $\varepsilon = 10^{-32}$. As seen in the figure, by gradually adding band cutoff, the periodical distribution is removed. However, there is also a trade off with removing spectral bands at the extremities. Indeed, noise can be removed, but at the same time information at the ignored bands are also lost. Thus, the band cutoff should not be too big. Finally, with such considerations, band cutoff of 10 is selected for processing all images in this study.

5.5.3 Other Implementation Notes

In the following are other implementation choices made to avoid numerical problems that could raise during computation.

Floating point representation Double instead single precision should be chosen.

Division in logarithm When there is a division operation within a computation of logarithm, it is decomposed into subtraction as follows.

$$\log \frac{x}{y} = \log x - \log y$$

Logarithm of reflectance values When a hyperspectral image is represented as reflectance, its values range from 0 to 1. To avoid losing computation accuracy as induced by the precision of these small reflectance values, each of these values are multiplied by a factor c as follows.

$$\log x = \log \frac{x \cdot \mathrm{c}}{\mathrm{c}} = \log(x \cdot \mathrm{c}) - \log \mathrm{c},\ \mathrm{c} = 10^6$$

Value rounding in angular distances In angular distance, distance values of less than 10^{-5} will be rounded as 0.

[3] Noise in the lower wavelengths can be caused by low energy of the used light source in this particular spectral range. Noise in the higher ones is typically due to low sensitivity of the sensor.

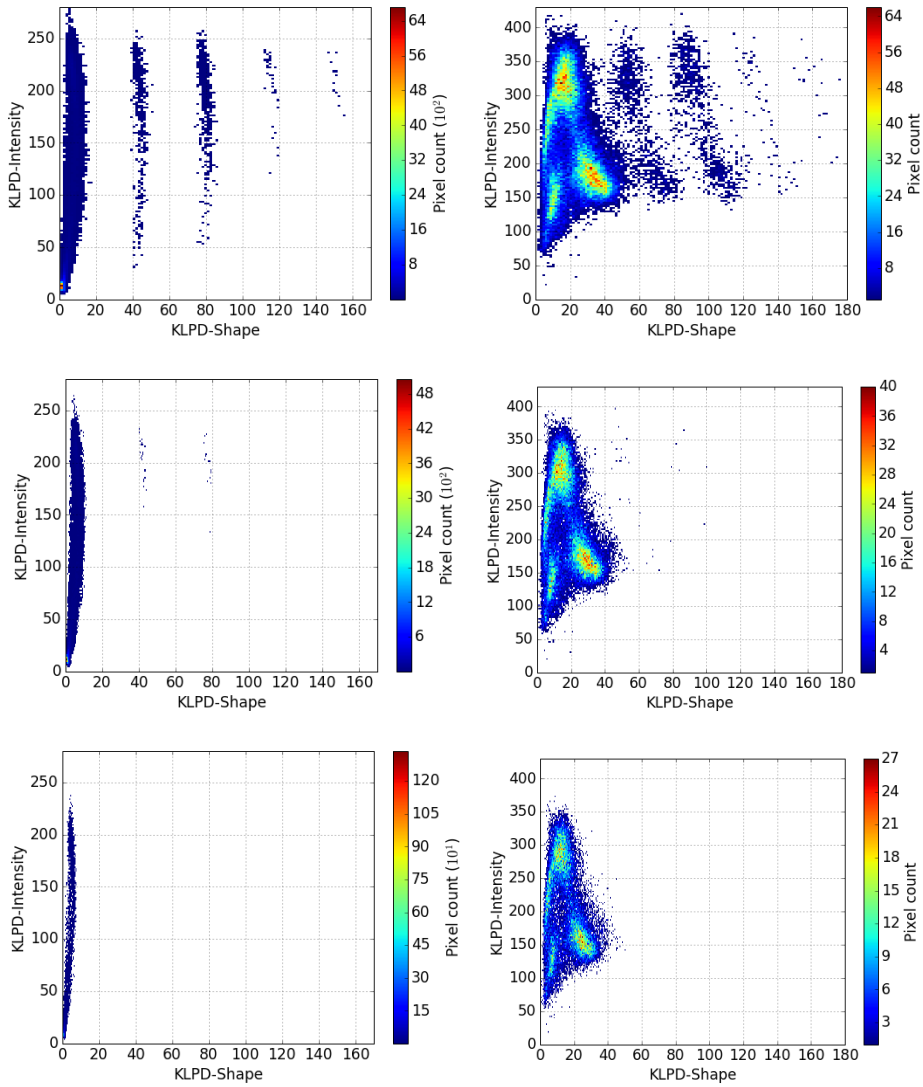

(a) BHSDs of image NP2

(b) BHSDs of image SCC01-1

Figure 5.24 – Three BHSDs for each image NP2 and SCC01-1, obtained using KLPD function, S_{Wh} as spectral reference, ε=10^{-32}, and 3 different band cutoffs. From top to bottom the band cutoffs are 0, 5, and 10. The periodic waves disappear when spectral bands at the extremities are removed.

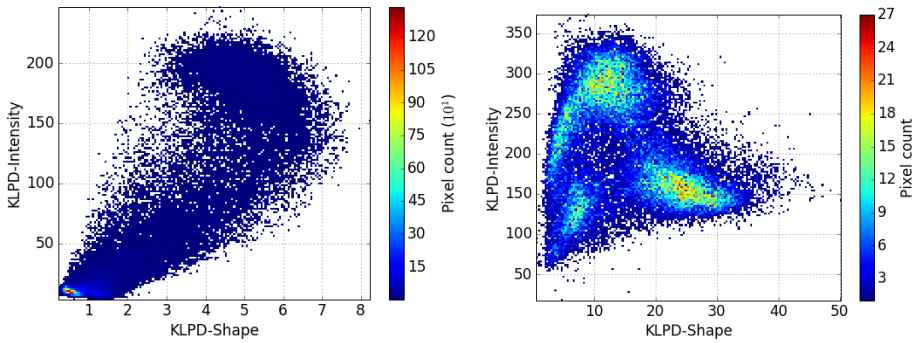

(a) BHSD of image NP2

(b) BHSD of image SCC01-1

Figure 5.25 – BHSDs of denoised image NP2 and SCC01-1 previously shown in Fig. 5.24a and 5.24b, for band cutoff of 10, given in the scale of their respective dynamic ranges.

5.6 Conclusions

Spectral distance enables many advanced image processing and analysis tools. However, a spectral distance in itself is an analysis tool useful for various applications tasks. It has been demonstrated that by solely using different graphical representations of spectral differences, an understanding of a given image by means of its value distribution can be obtained. This distribution of pixel values will, in turn, serve as an aid in deciding an algorithm or parameters in a classification task.

The question of reference is central in the context of spectral distance. It has a significant impact in the calculation of spectral differences, and it can be demonstrated using the aforementioned graphical representations. Thus, in this chapter it has been formulated how an optimal spectral reference should be selected. After criteria were proposed, their usefulness was also validated using a cutout of a painting in which several groups of color pigments could be identified. This experiment has shown that by only selecting an optimal spectral reference, a more advanced classification algorithm might not be needed. And it is because in the spectral difference dimension, good discrimination of spectral content can already be obtained.

While in this chapter the use of spectral difference has only been demonstrated for bi- and tri-dimensional histograms of spectral differences, its potential does not stop there. To recall, in the bidimensional case, only one spectral reference is required. In the tridimensional one, two references are required but only two shape and one intensity components are employed. And no criteria have been proposed

in how to select which components are to be employed. But rather than limiting spectral differences to the dimensionality of a graphical representation, they could be used as a feature space. By employing n spectral references, a feature vector of $n \times 2$ elements can be obtained for each pixel in an image. In this $n \times 2$ feature vector, there will be n shape and n energy or intensity features, where each pair comes from one spectral reference.

Summary of Contributions.

- ✓ Protocols of spectral reference selection for the use of KLPD function and spectral distance in general, using the notion of convex hull.
- ✓ Demonstrations of the interest of bidimensional histogram of spectral differences (BHSD) which was first proposed in [145], with examples of use in pigment discrimination and noise identification tasks.
- ✓ Extension of BHSD to the n-dimensional space, with application shown in a three-dimensional case, i.e., tridimensional histogram of spectral differences (THSD).
- ✓ Demonstration of spectral reference combination for pigment discrimination task using a THSD.
- ✓ Identification of noisy spectral bands using BHSD.

Chapter 6

Spectral Rank Order Filters

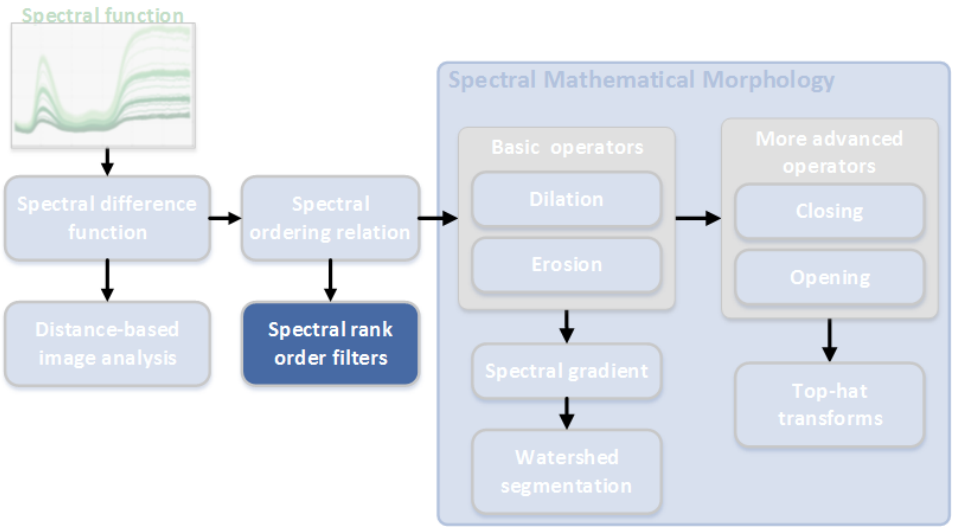

6.1 Introduction

In digital image and signal processing, linear techniques have been extensively used in a variety of applications. Their popularity is mainly due to the fact that they provide simple mathematical expression and implementation. Examples of such techniques are linear filters, whose main limitations are their low-pass characteristics and inability to deal with nonlinearities such as impulse noise filtering, non-linear image degradations, etc. Low-pass characteristic means that the filters tend to remove edges, lines, and fine details in an image. Hence, such filters are not suitable in the case where human vision is involved as it is highly sensitive to high

frequency information [137, 141]. Furthermore, as the linear filters of multivariate images require multidimensional Fourier transform as Clifford-Fourier transform uses hypercomplex number systems [30,38,63], managing data complexity presented in different phase planes is a critical yet difficult task.

The limitations of linear processing techniques are overcome by nonlinear ones, e.g. mathematical morphology, order statistics filters, nonlinear image restoration, etc. Rank order filters (ROF)[1] is a set of filters based on ordering relation. It performs well in the presence of additive white noise and impulse noise. Many of the filters belonging to ROF are also capable of preserving edges. Median filter is the most popular example of ROF. It is known to have good performance with long-tailed noise distribution, which suggests that it is an efficient tool for the removal of impulse noise [137]. Additionally, while removing impulse noise, median filter also preserves edges unlike its linear processing counterpart, i.e., averaging filter.

Scalar ROF have been used in a wide variety of applications [72, 127] and more advanced versions of them are also available [126, 160, 181]. Vector Median Filters (VMF) [18] is a multivariate median filter based on the notion of aggregate distance. Based on VMF, color median filters were constructed varying on the color spaces to use [26] and distance functions to employ [17, 18, 40]. As for the hyperspectral domain, no ROF has been specifically designed for it, i.e., one which considers both the mathematical and physical aspects of hyperspectral data.

Having identified the most suitable difference function and ordering relation for spectral data in Chapter 3 and 4, respectively, a distance-based spectral ROF can be obtained directly. However, metrological aspects of an image processing tool must be enabled and validated at each level of processing. This means that the validity of spectral difference function and spectral ordering relation does not imply the validity of the obtained spectral nonlinear filters. At this level, metrology must be enabled considering properties of the filters. Therefore, evaluation criteria must be developed, which in turn would allow assessing the quality of a constructed spectral nonlinear filter, or any image processing tool in general.

The chapter is organized as follows. A distance-based extension of ROF to the spectral domain can be found in Section 6.2. Then, as mentioned previously, metrology demands quality assessment at each level of processing. Considering two well-known properties of nonlinear filters, i.e., impulse noise suppression and edge preservation, image quality assessment protocols are developed in Section 6.3. The use of this quality assessment protocol are given in Section 6.4 for assessing the quality of distance-based spectral median filters. The same section also provides

[1] Also known as order statistics or percentile filters [159].

discussion regarding the complexity analysis of the spectral median filters. Finally, the chapter is concluded in Section 6.5.

6.2 Spectral Rank Order Filters

6.2.1 Definition

Rank order filters (ROF) is a set of filters based on ordering relation. An ROF works by iteratively sliding a filter window over the entire spatial dimension of an image, each time replacing value at the origin with one that is associated with rank r. Mathematically, ROF can be expressed as in Eq. 6.1 where the notion of rank r is linked to *cardinality* $\mathfrak{c}_v$, see also illustration in Fig. 6.1.

$$\begin{aligned} F_{W,r,g}(S_x) &= \bigvee \{S_v \colon \mathfrak{c}_v \leq r-1,\ S_v \in \mathcal{S}_W\}, \\ \mathfrak{c}_v &= \#\{S_i \colon g(S_i) \leq g(S_v),\ \forall S_i \in \mathcal{S}_W\}, \\ \mathcal{S}_W &= \{Si = I(x+b),\ \forall b \in W\} \end{aligned} \tag{6.1}$$

Interpretation. A rank order filter F, with defined filter window W, rank r, and ordering relation g, takes spectral function at the origin S_x as input. Then, it finds as its output a spectral function S_v from within the neighborhood W, whose *cardinality* $\mathfrak{c}_v$ is less than or equal to the required rank r. Cardinality $\mathfrak{c}_v$ of a spectral function S_v is the number of neighboring spectral functions which, according to g, is less than or equal to S_v. In other words, spectral function associated with rank r is one that has at most $r-1$ 'smaller' spectral functions in the neighborhood.

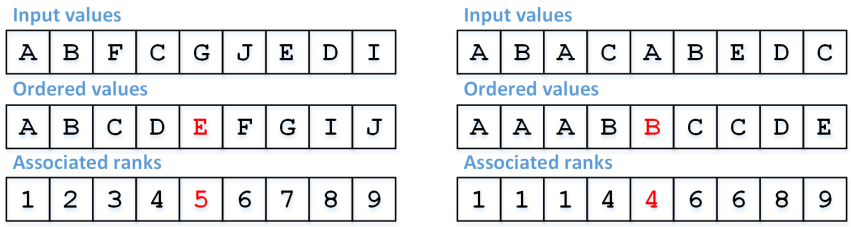

(a) (b)

Figure 6.1 – Two ordered lists of values illustrating the relation between rank r and cardinality $\mathfrak{c}_v$ as described in Eq. 6.1. Value associated with rank $r = 5$ is one that has at most $r - 1 = 4$ smaller values within the neighborhood, and whose $\mathfrak{c}_v$ is maximum among the qualified ones.

By varying the rank r in Eq. 6.1, the following filters can be obtained.

Median filter The objective of this filter is to find in a set of values the closest value to the average position of the set when its values are ordered, i.e. *median*. Conceptually, median is the value at the middle position when the set of data is an ordered list. The rank of this filter is $r = \frac{n_W - 1}{2}$. Grayscale median filter is known for its capability to remove impulse noise while still retaining edges sharp.

Minimum filter A minimum filter replaces the image value at the origin of filter window with that of rank $r = 0$. It is closely related to morphological erosion [115, 116].

Maximum filter This filter replaces image value at the origin of filter window with an image value of rank $r = n_W - 1$. It is closely related to morphological dilation [115, 116].

6.2.2 Extension to The Spectral Domain

From the mathematical expression of ROF shown in Eq. 6.1, it is evident that the difference between ROF in the grayscale or any multivariate domain only lies in the definition of ordering relation g. In the grayscale domain,

$$g(x) = x,\ \forall x \in \mathbb{R}.$$

In the multivariate domain, there are numerous existing multivariate ordering relations [12, 23]. As a consequence, there will be numerous different ways to define, for instance, a multivariate median filter. Specifically talking about the spectral domain, it has been concluded in Chapter 4 that conditional ratio and angular distance ordering relation (CRA) is the most suitable ordering relation. Thus, we can construct a CRA-based ROF for spectral images.

Vector Median Filters (VMF) by Astola *et al*. [18] is a multivariate median filter which employs a cumulative distance ordering relation in Eq. 6.2. However, by construction it is a minimum filter since what is considered as a median is actually a spectral function which corresponds to $r = 0$. Nevertheless, VMF can be directly employed to process spectral images. In a later section, the performance of VMF will be compared to that of CRA-based spectral median filter (CRA-SMF).

$$g_{CumDist}(S) = \sum d(S, S_i),\ \forall S_i \in \mathcal{S}_W \tag{6.2}$$

6.2.3 Properties of Rank Order Filters

One of the main advantages of nonlinear filters is their capability to deal with nonlinearities which occur in an image. As for ROF, in the following are properties of nonlinear filters it can potentially achieve. It is a potential since the properties of nonlinear filters are not obtained automatically. On the contrary, they must be enabled and validated.

6.2.3.1 Edge preservation

In a one-dimensional space, an edge is a simple step function defined by a threshold T, see Fig. 6.2a. In the two-dimensional case, an edge means that within a neighborhood W, on one side of W all pixels have common values a and the rest of the pixels on the other side have common values b, $a \neq b$, see Fig. 6.2b.

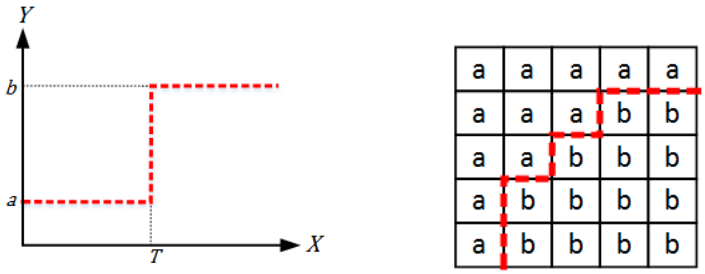

Figure 6.2 – Illustrations of the concept of edge in one- and two-dimensional cases.

The reason to why edge preservation capability is not automatically obtained by an ROF is because it is not induced by the employed ordering relation. Take median filter as an example. For it to be edge-preserving, there are certain constraints to be satisfied. Given a filter window W centered at its origin x, any edges found within W will be preserved if W is symmetric and x is included in the computation of median [88, 172].

6.2.3.2 Impulse noise suppression

Impulse noise is characterized by randomly distributed values which disturbs a signal, resulting in speckled images. It has a uniform probability density function, i.e., the noise random variable is independent and identically distributed over the image. In *salt-and-pepper* noise, the impulse noise corresponds to very large positive and negative values, respectively. And due to this, the noise appears to be white and black spots, hence the name salt-and-pepper. An example of a grayscale image which is disturbed by salt-and-pepper noise and the removal of this noise by median filter can be observed in Fig. 6.3.

(a) Original image (b) Noisy image (c) Median filtered image

Figure 6.3 – Illustration of a grayscale image which is disturbed by salt-and-pepper noise and the removal of this noise by a median filter.

Minimum filter can effectively remove salt noise in an image, but it tends to enhance the pepper noise. On the contrary, a maximum filter removes pepper noise but at the same time worsen the salt noise. Median filter is known to be effective in reducing both salt and pepper noise. Given a filter window W consisting of n_W pixels, median filter will considerably reduce impulse noise if the count of pixels disturbed by this noise is less than or equal to $(n_W - 1)/2$. Performance of a rank order filter can potentially be improved by increasing n_W, at the cost of increasing signal distortion [79, 88].

6.2.3.3 Performance in the presence of white noise

In addition to impulse noise, median filter is also known as a tool to suppress white noise. The performance of median filter in removing several noise distributions can be found in [88]. Noise distributions mentioned in the work are, i.e., uniform, normal, and double exponential distributions.

6.3 Quality Assessment Protocol of Spectral Rank Order Filters

The quality of an image processing tool can be assessed through its resulting images. By knowing the expected properties and behaviors of an image processing tool, a set of images of known properties can be employed as target. Fig. 6.4 provides two levels of quality assessment for spectral rank order filters, i.e., metrological validation and application. Aiming to assess noise suppression performance, images disturbed by theoretical noise signals can be generated and employed as assessment target. At the level closer to the real case, edge preservation capability can be assessed by employing images which comes with references or ground truths. At the highest application level, image processing quality assessment can

be carried out aiming to reach a certain application goal, e.g., classification, etc. At this level, however, ground truth images do not exist. In the following, two protocols for performance analysis of spectral rank order filters in noise suppression and edge preservation tasks will be developed.

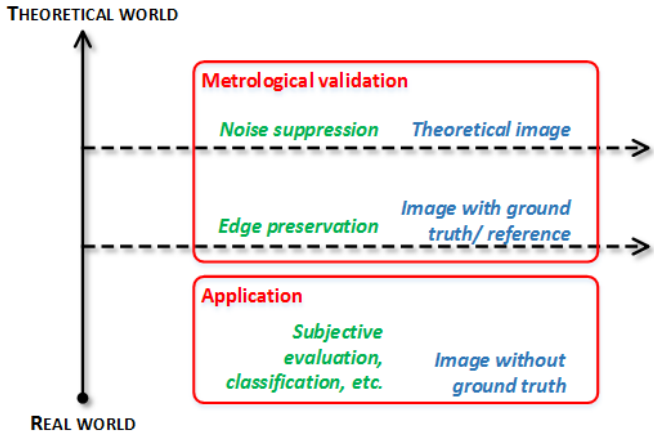

Figure 6.4 – Different levels of quality assessment for spectral rank order filters.

6.3.1 Performance Assessment in Impulse Noise Suppression

Image denoising or frequency-band decomposition are often employed to evaluate the performance of filtering algorithms. In the case of nonlinear filters, the relationship between spatial frequency and filter parameters are not straightforward. And due to that, given a certain model, the performance of nonlinear filters should be assessed in the context of image denoising. Among the existing noise models, impulse noise is one of the most often employed noise type [6,40,92]. It models or approximates malfunctioning pixels in the sensor of a camera, transmission problems over a noisy channel, or faulty memory locations in data storage [41]. Furthermore, despite the assumption of a calibrated imaging system, impulse noise is said to be ubiquitous in spectral images [130]. In order develop a protocol for the performance assessment of spectral nonlinear filters in image denoising, impulse noise model must be extended to the spectral domain.

A simple additive noise model is given in Eq. 6.3, where a noise signal $\mathcal{N}$ is disturbing an ideal image $I_g(x)$, resulting in a noisy image $\tilde{I}(x)$.

$$\tilde{I}(x) = I_g(x) + \mathcal{N} \tag{6.3}$$

In the case of impulse noise, the previous model can be rewritten as in Eq. 6.4, where p is the probability of a pixel to be disturbed by impulse noise signals $\mathcal{N}_1$

and $\mathcal{N}_2$ with $T \in [0,1]$. Probability density function of the noise signal is as illustrated in Fig. 6.5. Then, depending on how the noise signals $\mathcal{N}_i,\ i = 1, \cdots, n$ are obtained, varying types of spectral impulse noise can be obtained.

$$\tilde{I}(x) = I_g(x) + \mathcal{H}(T-p)\Big(\mathcal{N}_1 - I_g(x)\Big) + \mathcal{H}(p-1+T)\Big(\mathcal{N}_2 - I_g(x)\Big) \quad (6.4)$$

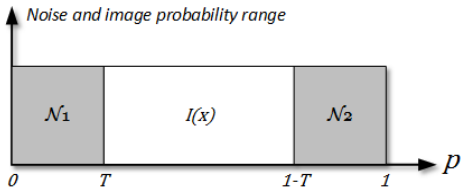

Figure 6.5 – Probability range of an image value being disturbed by fixed impulse noise signals $\mathcal{N}_1$ and $\mathcal{N}_2$.

6.3.1.1 Salt-and-pepper noise

In the grayscale domain, salt-and-pepper noise is characterized by its black and white dots appearance. Extending salt-and-pepper noise from its initial sense, the noise signals $\mathcal{N}_1$ and $\mathcal{N}_2$ can be represented by S_{Bk} and S_{Wh} in the reflectance space, respectively. In Fig. 6.6, several images from Pigment-56 dataset which are disturbed by spectral salt-and-pepper noise can be observed.

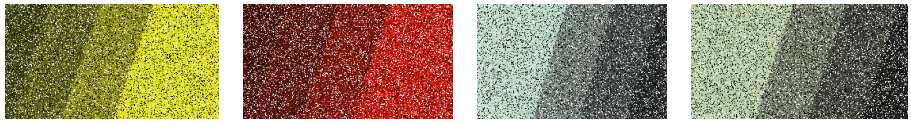

(a) (b) (c) (d)

Figure 6.6 – Several images from Pigment-56 dataset which are disturbed by salt-and-pepper noise, with noise probability threshold $T = 0.3$. Shown images are generated by FIXED visualization method.

6.3.1.2 Randomized impulse noise

The grayscale impulse noise model has been extended to the color domain by a marginal approach [21, 125]. In other words, the impulse value is generated at random and independently for each image channel, resulting in images being disturbed by random colors. Extending this approach to the spectral domain is straightforward since the only difference lies in the numbers of channels. This randomized impulse noise model can be rewritten as in Eq. 6.5, with the noise

signal $\mathcal{N}$ given in Eq. 6.6 for the spectral reflectance space. Examples of pigment images disturbed with this impulse noise type can be observed in Fig. 6.7.

$$\tilde{I}(x) = I_g(x) + p \cdot (\mathcal{N} - I_g(x)) \tag{6.5}$$

$$\mathcal{N} = \{s(\lambda) = y,\ y \in [0, 1]\} \tag{6.6}$$

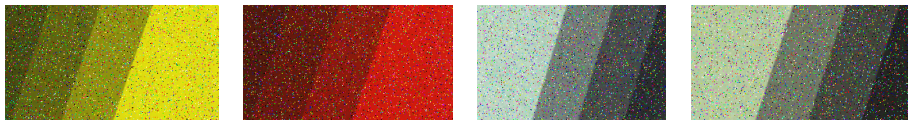

(a) (b) (c) (d)

Figure 6.7 – Several images from Pigment-56 dataset which are disturbed by spectral randomized impulse noise, with noise probability threshold $T = 0.3$. Shown color images are generated by FIXED visualization method.

6.3.1.3 Performance assessment protocol

Having previously defined several impulse noise models, performance assessment protocol of spectral nonlinear filters in removing impulse noise is constructed, see Fig. 6.8. Images from Pigment-56 dataset (Appendix B) will be employed as the target images. Both spectral salt-and-pepper and randomized impulse noise types will be applied to the pigment images to obtained the noisy image datasets. Noise probability threshold $T = 0.3$ are chosen for both noise types. Noisy image datasets corresponding to those disturbed by salt-and-pepper and randomized impulse noise will be referred to as SP-30 and RC-30, respectively. For the final performance assessment which is shown in the red box in Fig. 6.8, average spectral Kullback-Leibler pseudo-divergence (KLPD) in Eq. 6.7 will be employed as the image difference measure, where n_I is the number of pixels in an image. A better performing filter will yield lower image difference.

$$\text{Noise removal performance} = \frac{1}{n_I} \sum_{x=0}^{n_I - 1} div_{KL'}(I_1(x), I_2(x)) \tag{6.7}$$

6.3.2 Performance Assessment in Edge Preservation

The protocol for edge preservation performance assessment of spectral nonlinear filters is as depicted in Fig. 6.9, given for the case of spectral median filters. For every case of nonlinear filters to be evaluated, a corresponding reference or benchmark filter needs to be identified. For the multivariate domain in general, Vector Median Filters (VMF) [18] is known to be the most statistically robust estimator

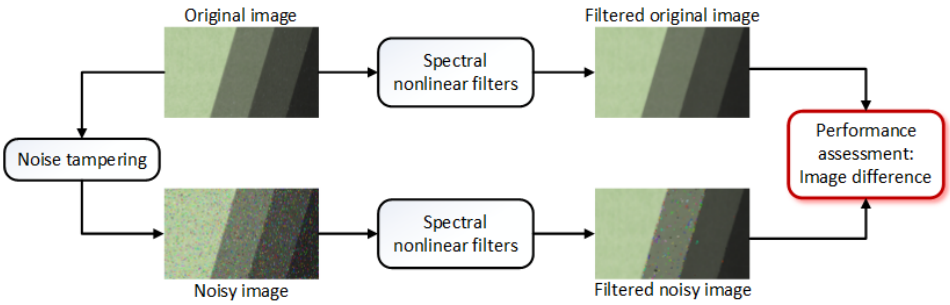

Figure 6.8 – Performance assessment protocol for spectral rank order filters in impulse noise suppression task.

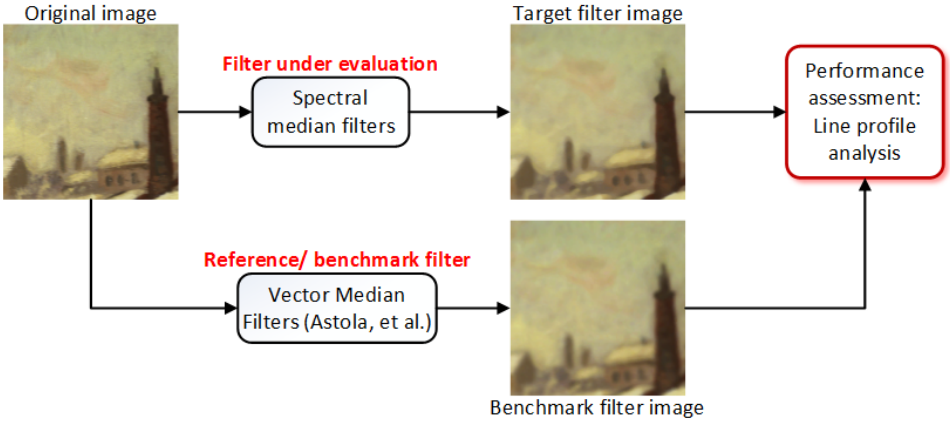

Figure 6.9 – Performance assessment protocol for spectral rank order filters in edge preservation task, shown for the case of spectral median filters.

of multivariate median. Therefore, this filter will be employed as the benchmark for spectral median filters performance assessment. Then, any arbitrary image where edges are relatively prominent can be employed as target. Most hyperspectral images used throughout this study, see Appendix B, can be employed except for texture images such as PN1 and PN2 from Subsets-250 dataset.

To illustrate the line profile analysis shown in the red box of Fig. 6.9, a pigment image is used as target for the assessment of spectral median filters. After performing the protocol, 3 images are obtained, i.e., original image (OI), an image filtered by the benchmark filter (BFI), and an image filtered by the filter under evaluation (FI). For each of the three images, a line profile will be extracted, i.e., distance between pixels under the green line shown in Fig. 6.10a and an arbitrary refer-

ence. In Fig. 6.10b, S_{Wh} is employed as reference to obtain line profiles from OI, BFI, and FI. The filter under evaluation is said to be well-performing if it is able to approximate the performance of benchmark filter. Note that this performance assessment protocol has also been employed as a trueness in rank ordering test in Chapter 4.

(a) Spatial coordinate or pixel location where a line profile is extracted from

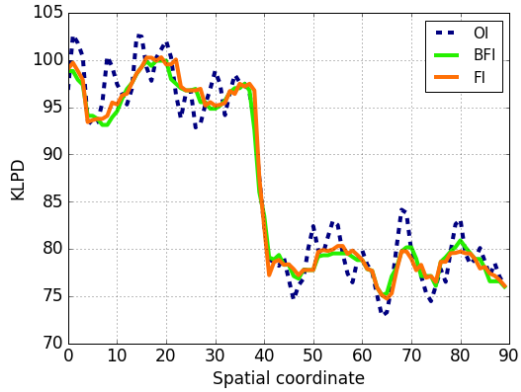

(b) Line profiles obtained from the original image shown in (a) and two of its corresponding filtered images. S_{Wh} is employed as reference.

Figure 6.10 – Illustration of line profile extraction in the assessment of spectral median filters performances in edge preservation task. Lines profiles are given for original image (OI), image filtered by the benchmark filter (BFI), and image filtered by the filter under evaluation (FI).

6.4 Quality Assessment of Spectral Median Filters

In order to demonstrate the use of assessment protocols which have been defined in Section 6.3, in the following are quality assessments of spectral median filters. Furthermore, note that the aim of this section is not to construct the most efficient median filters, *per se*.

6.4.1 Performance in Impulse Noise Suppression

6.4.1.1 The impact of spectral difference function in salt-and-pepper noise removal

To assess the impact of spectral difference function choice in CRA-based spectral median filter (CRA-SMF) construction, several spectral difference functions are to be evaluated, i.e., spectral angle (further on, will be referred to as SAM), Euclidean distance, Euclidean distance of cumulative spectrum (ECS), and spectral

Kullback-Leibler pseudo-divergence (KLPD). Then, S_{Bk} and S_{Wh} will be employed as references for the ordering relation.

The performances of 5×5 CRA-SMF with varying spectral difference functions in suppressing salt-and-pepper noise in SP-30 dataset can be observed in Fig. 6.11, where dynamic ranges of each function are not identical. According to this statistical performance measure, the best performing spectral difference functions are Euclidean and ECS distances, which provide identical performances. The two are consecutively followed by SAM and KLPD function.

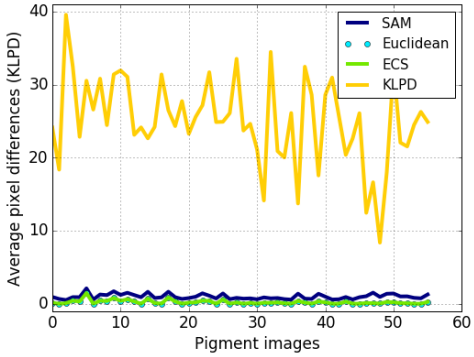

Figure 6.11 – The impact of spectral difference function choice in the performance of CRA-SMF in suppressing salt-and-pepper noise. S_{Bk} and S_{Wh} are employed as references and filter window is of size 5×5 pixels.

To better understand the previous statistical performance, filtered pigment images from the employed dataset are also shown in Fig. 6.12. Observing these results, it becomes more evident that indeed Euclidean and ECS distances are the most performing ones compared to the other spectral difference functions, since both of them manage to almost completely remove the salt-and-pepper noise. On the other, SAM and KLPD functions retain some of the salt and pepper noises, respectively.

A 5×5 window from the unfiltered yellow pigment image previously shown in Fig. 6.12 can be observed in Fig. 6.13. With a total of 25 pixels within the window, it can be observed that there are 5 black pixels and 8 white pixels, each correspond to pepper and salt noises. This makes the total number of noisy pixels exceeds half of the window size, causing the median filter to reach its limit, which is also illustrated in Fig. 6.14. In the case of SAM and KLPD function, the median computation encounters the case illustrated in Fig. 6.14a, i.e., both salt and pepper noises are given the lowest ranks. One part of the reason is because the reference pair and the noise signals are identical, i.e., S_{Bk} and S_{Wh}. Then, since SAM is a measure of shape differences, the difference between S_{Bk} and S_{Wh} is 0 since they

are both equi-energetic. For KLPD function, which measures both intensity and shape differences, the zero shape difference between S_{Bk} and S_{Wh} is considered as significant in the overall differences. Hence, the low ranks of the salt and pepper noises. On the other hand, Euclidean and ECS distances are able to reach the case shown in Fig. 6.14b, since the noise signals have minimum and maximum intensities. To recall from Chapter 3, Euclidean distance is a measure of intensity differences and ECS distance is more sensitive to intensity than shape differences.

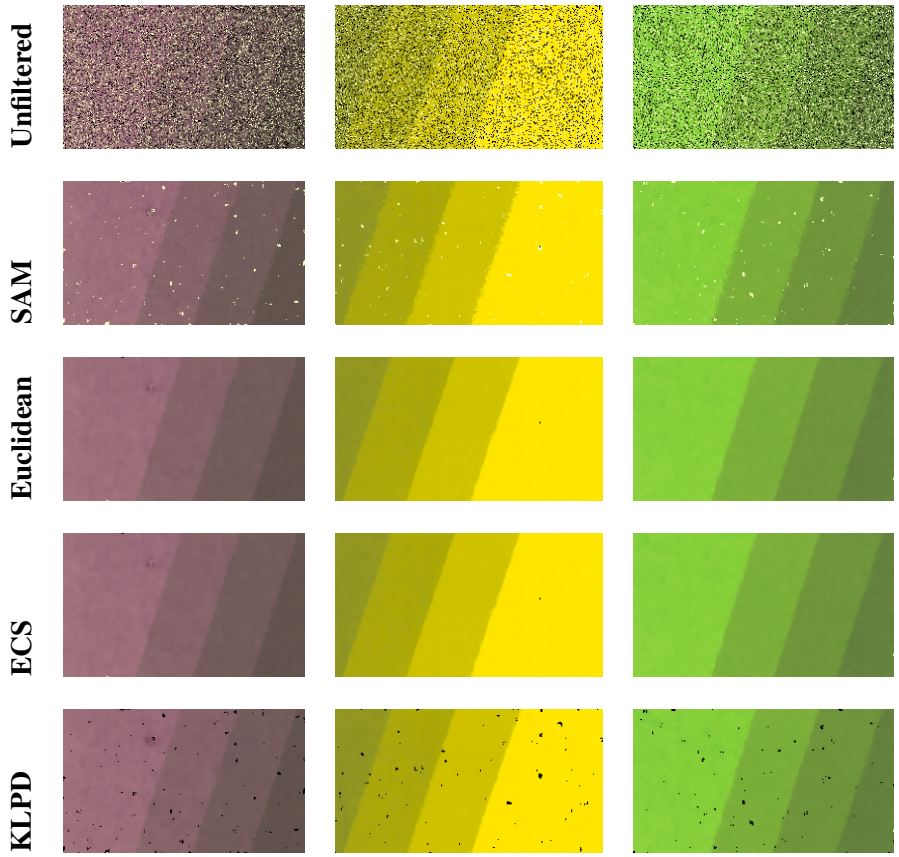

Figure 6.12 – The impact of various spectral difference functions on the performance of CRA-SMF in salt-and-pepper noise suppression task, where the probability of a pixel being disturbed by noise is $T = 0.3$. Shown color images are generated using CLTR visualization method.

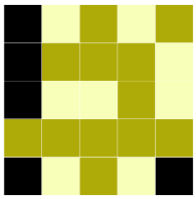

Figure 6.13 – A 5×5 window of a yellow pigment image where CRA-SMF using SAM and KLPD functions were not able to remove the salt-and-pepper noise (the black and white pixels). With the total number of salt and pepper noises exceeding half of the total number of pixels within the window, median filter reaches its limit.

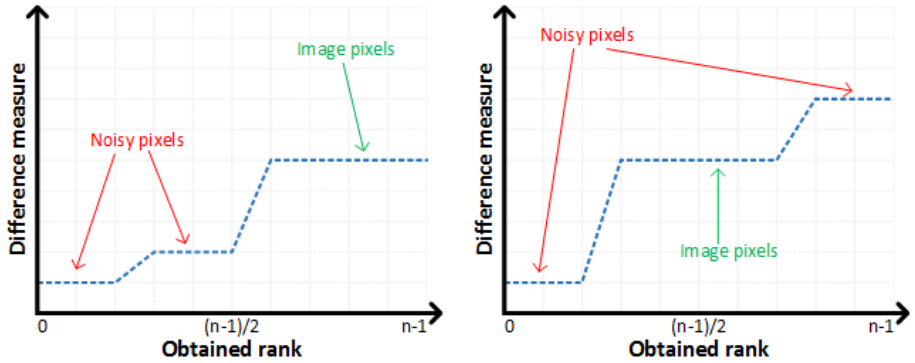

(a) All noisy pixels are given the lower ranks (or the higher ones)

(b) Noisy pixels are given ranks at the extremeties

Figure 6.14 – Illustrations of two cases of median computation when the total amount of salt-and-pepper noise exceeds half of the total numbers of pixels within the filter window.

6.4.1.2 The impact of spectral difference function in randomized impulse noise removal

In the previous evaluation where salt-and-pepper noise are to be removed from the target images, Euclidean and ECS distances performed better than SAM and KLPD functions despite the limitation of median computation. In the following, performances of the same spectral difference functions will be further assessed by employed randomized impulse signals, S_{Bk} and S_{Wh} are again employed as references. Several of the noisy images have been shown in Fig. 6.7.

The performances of 5×5 CRA-SMF with varying spectral difference functions in suppressing randomized impulse noise in RC-30 dataset can be observed in

Fig. 6.15. From this figure, it can be observed that none of the difference functions except for KLPD function is able to remove the randomized impulse noise. The results for three pigment images can also be observed in Fig. 6.17. Among the 4 spectral difference functions, SAM is the least performing one. As for Euclidean and ECS distances, they retain the impulse noises only certain color shades in each of the pigment images.

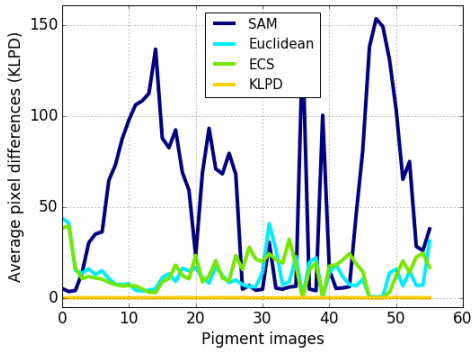

Figure 6.15 – The impact of spectral difference function choice in the performance of CRA-SMF in suppressing randomized impulse noise. The employed filter window is of size 5×5 pixels.

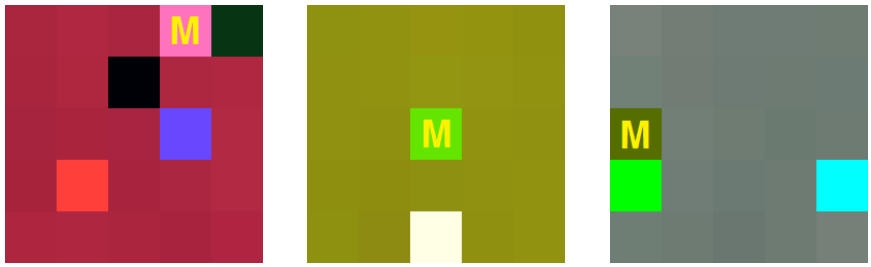

(a) SAM (b) Euclidean distance (c) ECS distance

Figure 6.16 – Three instances from unfiltered images shown in Fig. 6.17, where CRA-SMF embedding the corresponding function failed to remove the impulse noise. Medians selected by each function are marked by the letter 'M'.

To have a closer observation of the impact of spectral difference functions, 5×5 window regions are extracted from three pigment images previously shown in Fig. 6.17. The localized regions can be observed in Fig. 6.16, where the selected medians are marked with the letter 'M' in each image. As observed, in all the shown examples, the number of noisy pixels does not reach half of the total pixels

in the window. Thus, in these cases, the median filters are expected to select pixels which are undisturbed by noise. The failure of SAM is attributed to the use S_{Bk} and S_{Wh} as references, which are identical in shape. Due to this, the values obtained by CRA ordering relation for any arbitrary spectral functions S_i will always be unitary since

$$g_R^-(S_i) = \frac{d(S_i, S_{Wh})}{d(S_i, S_{Bk})} = \frac{y}{y} = 1.$$

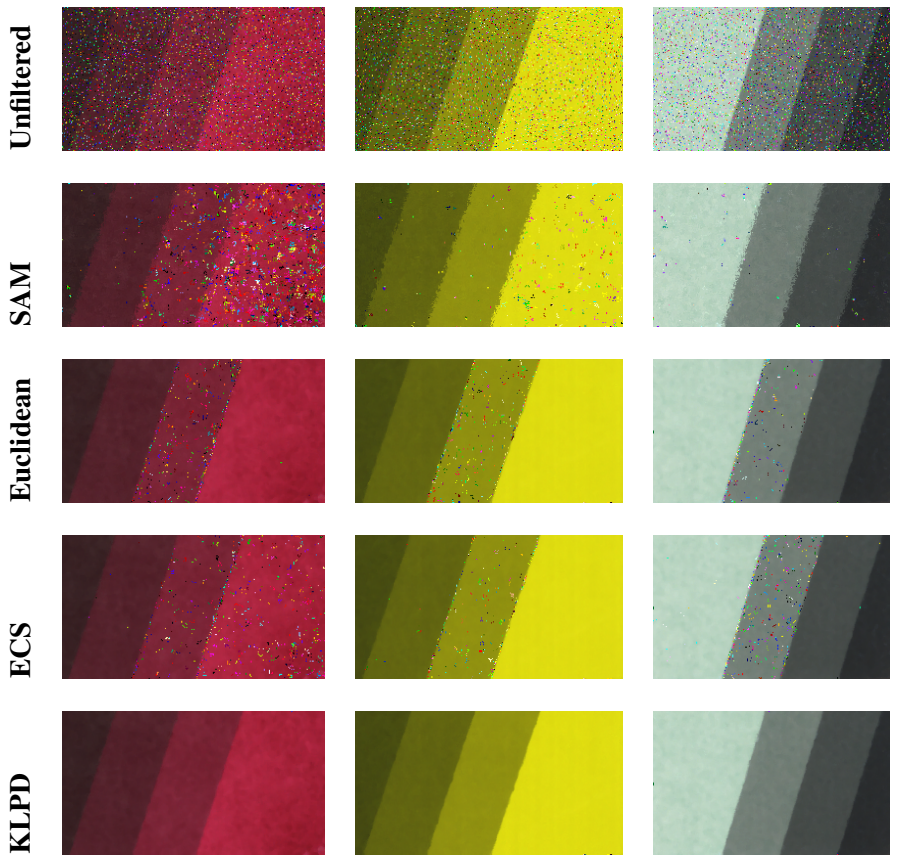

Figure 6.17 – The impact of various spectral difference functions on the performance of CRA-SMF in randomized impulse noise suppression task, where the probability of a pixel being disturbed by noise is $T = 0.3$. Shown color images are generated using FIXED visualization method.

For Euclidean and ECS distances, the choice of S_{Bk} and S_{Wh} references will cause them to fail at the color shades whose intensity values are around half of

the dynamic range of the value space. This is because the intensity differences between the spectral functions to each of the references will be approximately the same. Spectral functions which correspond to the localized filter windows shown in Fig. 6.16b and 6.16c can be observed in Fig. 6.18a and 6.18b, respectively. The impulse signals shown in the figures are clearly distinguishable in shape from the image content. But since Euclidean distance is a measure of intensity differences, the significant shape differences are not considered in the computation of median. ECS, due to its cumulative spectrum approach, gives significantly more importance to intensity rather than shape differences. And finally, ECS demonstrates similar behavior than that of the Euclidean distance.

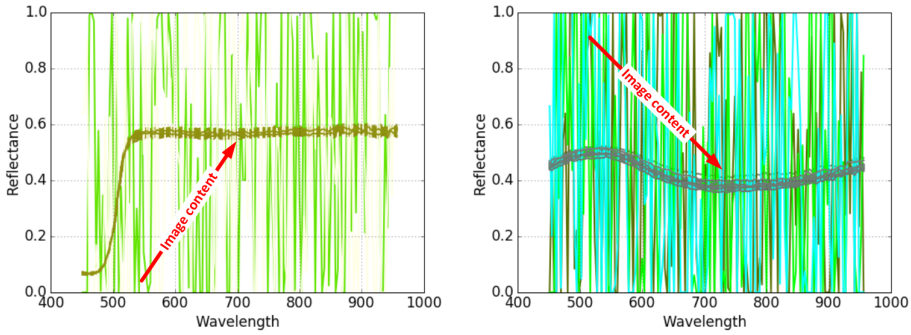

(a) Spectral functions from Fig. 6.16b (b) Spectral functions from Fig. 6.16c

Figure 6.18 – Spectral functions of two localized filter windows shown in Fig. 6.16, where the impulse signals are distinguishable in terms of shape from the original image content.

To summarize, among the 4 spectral difference functions, KLPD function gives the best performance due to its sensitivity to both shape and intensity differences. In the previous evaluation where salt-and-pepper noise model was employed, SAM and KLPD functions were found to be unable to remove some of the salt and pepper noises, respectively. The observed performance was however due to the limit of median computation rather than the spectral difference functions themselves. The actual performances of the functions become evident when randomized impulse noise model was employed. SAM and Euclidean distance which are exclusively measures of shape and intensity differences, respectively, were not able to remove the randomized impulse noise. And so does ECS distance even though it is a measure of both shape and intensity differences. Its limitation was reached due to its prioritization for intensity differences, as a cause of cumulative spectrum approach. Finally, the best performance was delivered by KLPD function which is equally sensitive to both shape and intensity differences.

6.4.1.3 The impact of spectral ordering relation in randomized impulse noise removal

VMF is a statistically robust multivariate median filter due to its aggregate distance ordering. With this approach, a median is considered as the pixel having minimum total distance to the other pixels within the filter window, which makes it essentially a minimum filter. On the other hand, in CRA-SMF a median is identified relative to the pair of references. Comparing the performance of the two different approaches of multivariate median filters, RC-30 image dataset from the previous subsection will be employed as target. Then, as KLPD has been found to be the most performing spectral difference function, it will be embedded in both VMF and CRA-SMF. S_{Bk} and S_{Wh} are employed as references for CRA-SMF, and filter window size to use is 5×5 pixels.

The performance of VMF and CRA-SMF in suppressing randomized impulse noise from RC-30 dataset can be observed in Fig. 6.19. Comparing the dynamic range of this figure with the previous ones in Fig. 6.15, it can be said the performances of the two approaches do not differ significantly, with CRA-SMF performs slightly better. And as can be observed through Fig. 6.20, both median filters are able to completely remove the impulse noise signals. Finally, it can be observed that differences depicted in Fig. 6.19 are mainly due to different medians being selected from the image content, rather than different ability to remove impulse noises.

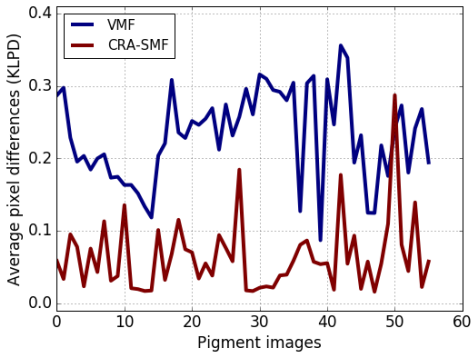

Figure 6.19 – The impact of spectral ordering relation choice in the suppression of randomized impulse noise. The employed filter window is of size 5×5 pixels.

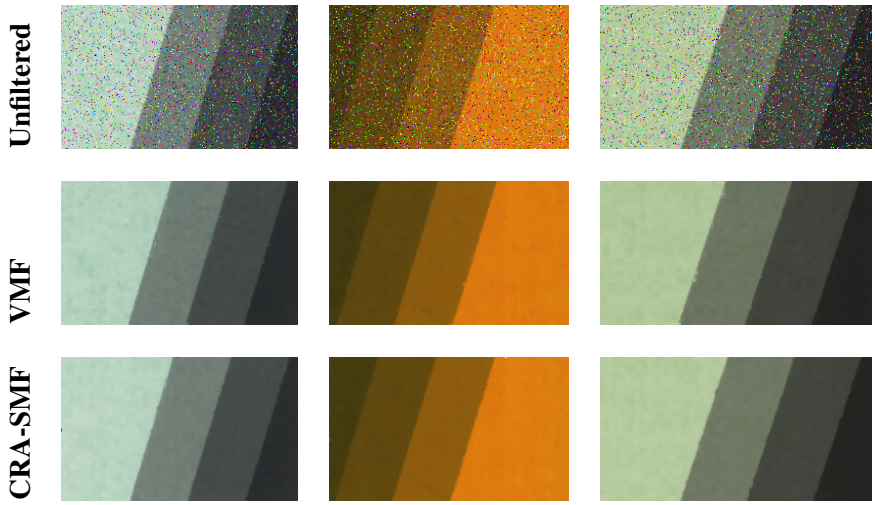

Figure 6.20 – The impact of spectral ordering relation choice in the suppression of randomized impulse noise, where the probability of a pixel being disturbed by noise is $T = 0.3$. Shown images are generated using FIXED visualization method.

6.4.2 Performance in Edge Preservation

In the following, the performance of CRA-SMF in edge preservation task will be evaluated relative to the performance of VMF. Both median filters embed KLPD function as their spectral difference functions and employ 7×7 filter window size. Then, S_{Bk} and S_{Wh} are employed as references for CRA-SMF.

A pigment image from Pigment-56 dataset (Appendix B) is employed as filtering target in Fig. 6.21, where the results of VMF and CRA-SMF are also provided. By visual comparing Fig. 6.21c and 6.21d, CRA-SMF filtered image seems to have sharper edges than the one filtered by VMF. To confirm the visual observation, line profiles from the original and filtered images are provided in Fig. 6.21a. And through this figure it becomes clearer that indeed VMF blurs the original image more than CRA-SMF. The edge produced by CRA-SMF can approximate the original edge, while one produced by VMF is more inclined.

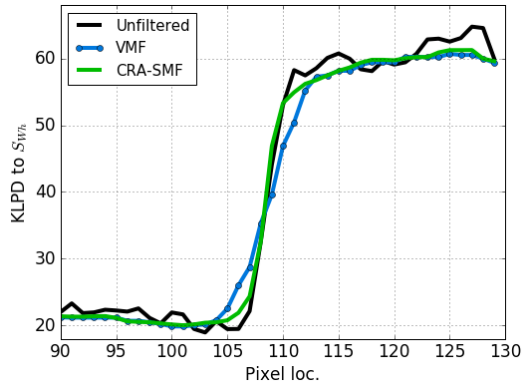

(a) Line profiles obtained from pixels located under the red line shown in (b) for all pigment images below

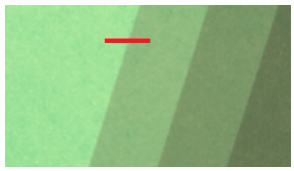

(b) Original image

(c) VMF filtered image

(d) CRA-SMF filtered image, S_{Bk} and S_{Wh} as references

Figure 6.21 – The impact of VMF and CRA-SMF, both embedding KLPD function and of filter window size 7×7 pixels, in the edge preservation of a green pigment image. The line profiles are obtained by computing spectral differences to S_{Wh} using KLPD function. CRA-SMF yields sharper edges compared to VMF.

The pigment image used previously does not have a complex structure since it consists of only 4 homogeneous regions separated by 3 edges. In Fig. 6.22, the results of applying VMF and CRA-SMF to two images from Subsets-250 dataset (Appendix B) are given. The two images can be considered as images which consist of background and foreground parts. The background can be considered as homogeneous regions where no edges are present. Image structures become important in the foreground regions. With this type of images, the result comparison of VMF and CRA-SMF still agree with the previous result employing a simple pigment image. Filtered images obtained by VMF are generally blurrier than those obtained by CRA-SMF.

Performance of the two median filters is further assessed using an image with an even more complex structure. In image FN2 from Subsets-250 dataset, various different objects compose the image and there is no region which can be considered

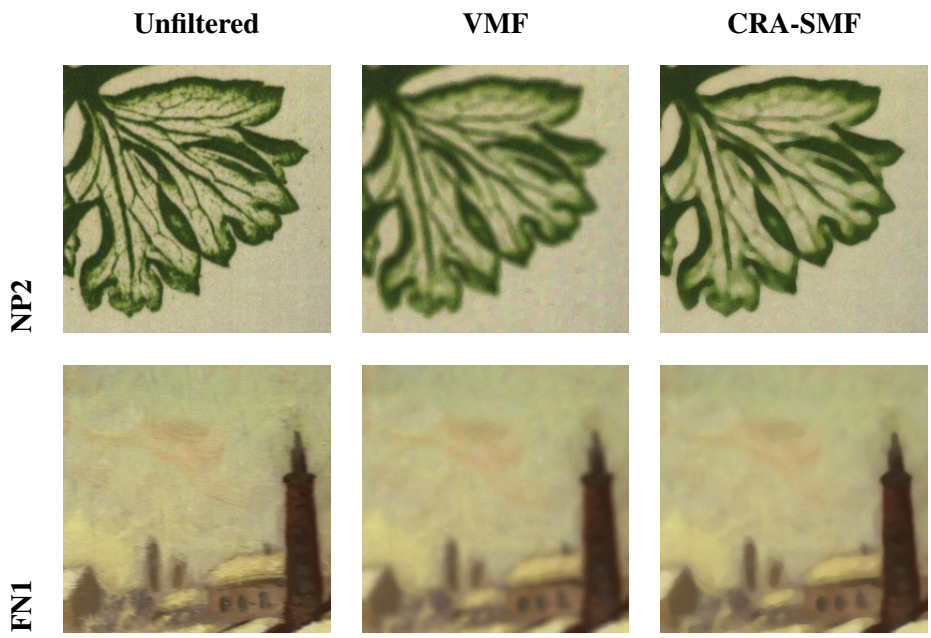

Figure 6.22 – The impact of VMF and CRA-SMF, both embedding KLPD function and of filter window size 7×7 pixels, in preserving edges in two images from Subsets-250 dataset (Appendix B). Results obtained by VMF are blurrier than those obtained by CRA-SMF.

as background. Results obtained after applying 7×7 VMF and CRA-SMF can be observed in Fig. 6.23, where the first and second rows give the full images and a portion of them, respectively. From the full view of the images, again, the performance of CRA-SMF is better as it generates sharper images than VMF. However, observing the images in smaller details through what are shown in the second row, VMF filtered image does not suffer from grainy artifacts. In Fig. 6.24 we provide an even closer zoom of image FN2, i.e., from the head region as indicated by the blue arrow in Fig. 6.23. And it is in this region that we can observe an example of where grainy artifacts are generated by CRA-SMF while VMF gives a blurry effect without the artifacts. If we further observe the modified bidimensional histogram of spectral differences (BHSD) of this image subset by using S_{Wh} as reference, we know that distribution of spectral variation within this particular region is multimodal, see Fig. 6.24. In this case the computation of median reaches its limit and nothing ensures the stability of VMF. Thus, at this point we are not able to determine which of VMF or CRA-SMF provides a better performance.

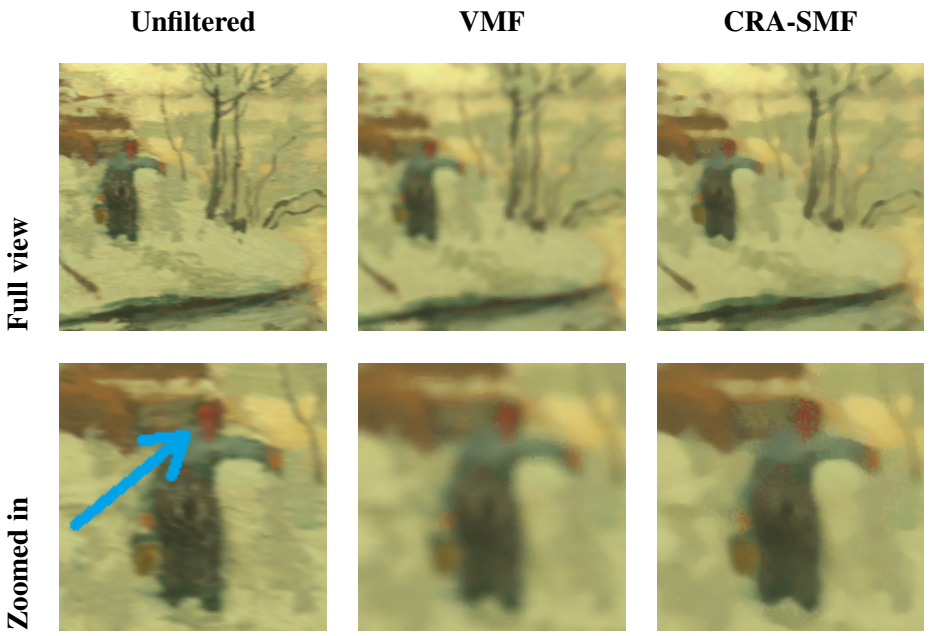

Figure 6.23 – Comparison of the impact of VMF and CRA-SMF in the smaller details of a portion of image FN2. Even though the image obtained by VMF is generally blurrier than the one obtained by CRA-SMF, it does not suffer from grainy artifacts as CRA-SMF filtered image does. A further zoom of location indicated by the blue arrow can be seen in Fig. 6.24.

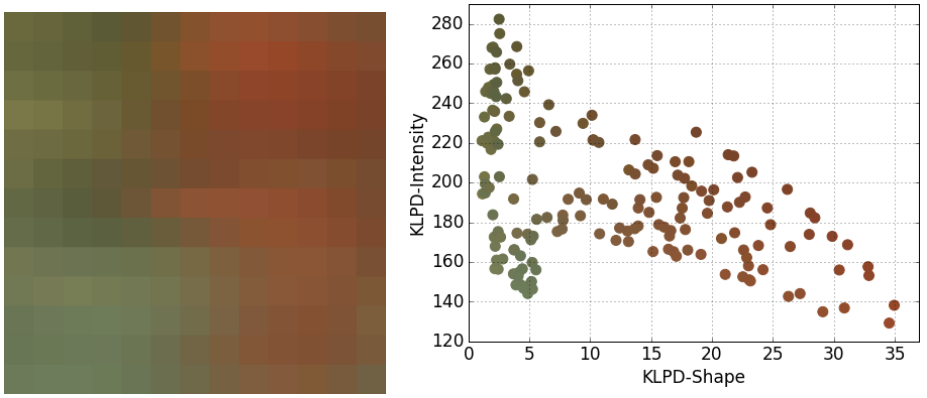

(a) A subset of FN2

(b) Spectral variation of image in (a)

Figure 6.24 – Subset of image FN2 as indicated by the blue arrow in Fig. 6.23 and its modified BHSD obtained using S_{Wh} as reference. Distribution of spectral variation is multimodal, which is the limit of median computation.

6.4.3 Complexity Analysis

VMF has been considered as the benchmark for multivariate median filter due to its stability and robustness which is induced by the cumulative distance ordering [18, 88, 172]. However, its robustness comes with a great computational complexity which has been analyzed in [25]. If it is to be compared to CRA-SMF, a significant improvement of the complexity can be achieved.

A hyperspectral image consists of hundreds of spectral bands. With the same spatial dimension as its color counterpart, a hyperspectral image will require a significantly larger amount of memory due to its spectral dimension. Therefore, when designing a median filter algorithm for a hyperspectral image, the trade-offs are between memory or space and time. In the following, the computational cost of both VMF and CRA-SMF will be analyzed for the two cases, i.e. space and time complexity. Space complexity is relevant when memory is limited, while time complexity is the case where memory is abundant and computation time matters.

6.4.3.1 Space complexity

Both VMF and CRA-SMF apply the median filter through a distance map that is obtained from an input image. If there is sufficient memory available, computation time that is required by either VMF and CRA-SMF will be significantly lower since the computation of distance map can be done globally before the filtering iteration. The space complexity for VMF and CRA-SMF are as shown in Table 6.1, where $n_I \times n_\lambda$ is the spatial and spectral dimensions of an image, n_W is the size of the filter window, and p is the number of basic arithmetic operations required by the distance function used. The complexity of VMF is larger by a factor of n_W^2 since the distance of a pixel to all its neighbors within the filter window has to be computed. On the other hand, CRA-SMF only needs to compute the distance of each pixel to two references. As an illustration, if a single value requires 4 bytes of memory, an image of $n_I = 1000 \times 1000$ and $n_\lambda = 100$, $p = 4$, and a filter window of $n_W = 3 \times 3$, VMF would require 129.6 GB of memory while CRA-SMF only 3.2 GB.

6.4.3.2 Time complexity

For a hyperspectral image with several hundreds of rows and columns, memory availability is already a great challenge, as the numbers above have illustrated. Therefore, each of the operations from loading the image pixels to sorting the distance values needs to be carried out locally at each filter window iteration. Table 6.2 provides the analysis of time complexity for VMF and CRA-SMF when we face a lack of memory. CRA-SMF outperforms VMF by a factor of filter window size n_W through its direct distance computation. If, as previously, we have an

image of $n_I = 1000 \times 1000$ and $B = 100$, $n_W = 3 \times 3$, $p = 4$, and that a single element operation requires in average 1 µs, VMF would need 9 hours to process while CRA-SMF only an hour. However, note that for the spatial dimension n_I that is thousands by thousands of pixels, we generally cannot use a small n_W as it has to grow together with n_I in order to be able to work with the details in the image. If for the same image size we have a filter window of size $n_W = 20 \times 20$, the time required to process VMF would be around 740 days, while only less than 2 days for CRA-SMF. Certainly there is scope for optimization for both VMF and CRA-SMF. But by comparing the two of them in this manner, i.e. using the same distance function, we are allowed to see how big is the differences in time, as well as memory, complexity of the two filters.

Table 6.1 – Space complexity analysis of VMF and CRA-SMF. $n_I \times n_\lambda$, n_W, and p are the spatial and spectral sizes of image input, the size of filter window, and the number of basic arithmetic operations required by the selected distance function, respectively.

Operations	**# of elements**	
	VMF	**CRA-SMF**
Image load	$n_I \times n_\lambda$	$n_I \times n_\lambda$
Filter window	n_W	n_W
Distance map	$n_I \times n_W^2 \times n_\lambda \times p$	$n_I \times n_\lambda \times p \times 2$
Cumulative distance	$n_I \times n_\lambda$	-
Ratio & angular distance (CRA)	-	$n_I \times n_\lambda \times 2$
Quicksort (space complexity)	$\log n_W$	$\log n_W$
Complexity	$O(n_I \cdot n_W^2 \cdot n_\lambda \cdot p)$	$O(n_I \cdot n_\lambda \cdot p)$

Table 6.2 – Time complexity analysis of VMF and CRA-SMF.

Operations	**# of elements per window iteration**	
	VMF	**CRA-SMF**
Image load	$n_W \times n_\lambda$	$n_W \times n_\lambda$
Distance map	$n_W^2 \times n_\lambda \times p$	$n_W \times n_\lambda \times p$
Cumulative distance	$n_W \times n_\lambda$	-
Ratio & angular distance (CRA)	-	$n_W \times 2$
Quicksort (time complexity)	$n_W \log n_W$	$n_W \log n_W$
Complexity	$O(n_I \cdot n_W^2 \cdot n_\lambda \cdot p)$	$O(n_I \cdot n_W \cdot n_\lambda \cdot p)$

6.5 Conclusion

In this chapter, we have designed our first metrological image processing tools for spectral images, i.e., spectral rank order filters (ROF). Comparing it with the state of the art multivariate median filters, i.e., Vector Median Filters (VMF) by Astola *et al*. [18], we have shown that our spectral median filters construction using conditional ratio and angular distance ordering relation (CRA) is significantly more efficient in time and memory. In turn, this will give a more attractive solution for more advanced spectral nonlinear filters.

In designing the metrological validation for spectral ROF, we encountered a difficulty in defining a realistic spectral noise model useful for performance assessment in noise removal. Our first approach was by using the salt-and-pepper noise, where the salt and pepper signals are replaced by equi-energetic black and white spectral functions. In the second approach, where the noise model is not significantly better, we use impulse noise model with randomized spectral function as the noise signal. Nevertheless, using the two noise models we have been able to show the limit and advantage of our construction of spectral ROF using CRA ordering relation and spectral Kullback-Leibler pseudo-divergence (KLPD) function. The second metrological validation was developed with VMF as reference. However, in the real case using complex images we have shown that our CRA-based spectral median filter (CRA-SMF) provides better edge preservation capability. While VMF generally blurs the input image, edges in CRA-SMF filtered images remain sharp. On the other hand, CRA-SMF also generates grainy artifacts, which do not appear in the blurrier VMF-filtered images.

Summary of Contributions.

- ✓ Extension of rank order filters (ROF) to the spectral domain by means of a distance based ordering relation, i.e., conditional ratio and angular distance ordering relation (CRA).
- ✓ Quality assessment protocols for spectral rank order filters and the performance assessment itself for spectral median filters.
- ✓ Application and performance comparison of Vector Median Filters (VMF) and CRA-based spectral median filter (CRA-SMF) to hyperspectral images.
- ✓ Time and space complexity analyses of VMF and CRA-SMF.

Chapter 7

First Levels of Spectral Mathematical Morphology

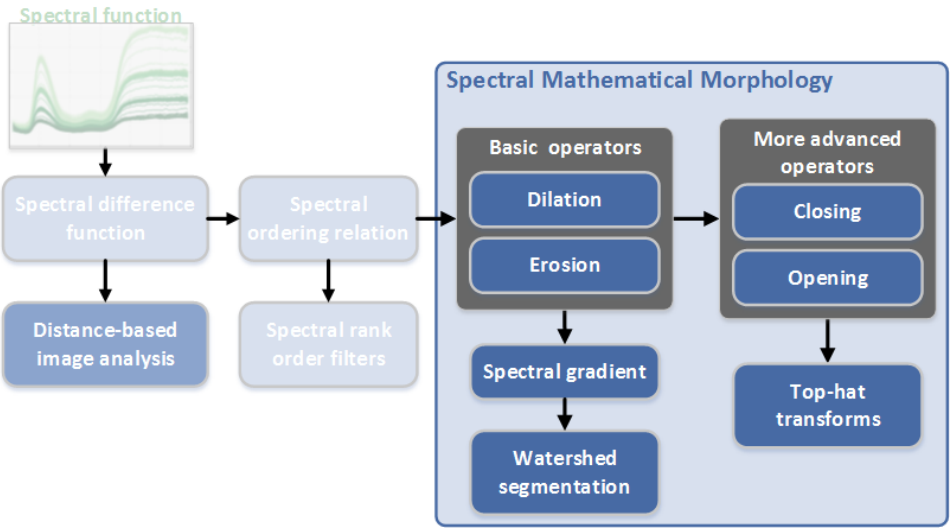

7.1 Introduction

In the previous chapters, a significant amount of work has been carried out at the theoretical level. Various distance functions have been studied, evaluated, and validated in the pursuit of finding the most suitable one for spectral data in Chapter 3. It was then followed by an entire chapter dedicated to the study of multivariate ordering relation in Chapter 4, again in the pursuit of finding the most suitable one for spectral image processing. In both chapters, the focus has been theoretical val-

idation using artificial datasets or ones derived from a real dataset but nevertheless were in a controlled condition. But one might wonder if such extensive efforts are needed to construct a spectral image processing framework. And eventually, what will be the gain of it in the real case, where theoretical assumptions are rarely met or satisfied.

Theoretical validation ensures a stable performance. And thus, being able to assess the theoretical properties of image processing tools will, in turn, allow predicting and understanding the image processing results. Furthermore, with the added metrological constraints, the obtained functions and/ or operations will be able to manage accuracy, uncertainty, and bias throughout the following image processing chain. Looking at the above diagram, it is evident that after having defined spectral distance function and ordering relation, spectral mathematical morphology framework is what follows. And thus, in this chapter, it will be shown how the framework and its components can be developed and used for real images.

The rest of the chapter is organized as follows. The definition and extension of erosion, dilation and Beucher's gradient to the spectral domain will be provided in Section 7.2. In the same section, the extended operators will be applied to several hyperspectral images and results will be explained and discussed. Having defined Beucher's gradient, watershed segmentation algorithm can be developed and it will be given in Section 7.3. Having opening and closing operators allow defining an entire class of morphological filters. Grayscale opening and closing are extended to the spectral domain in Section 7.4 and they will be employed to construct a morphological filter, i.e., top-hat transforms. Finally, this chapter will be concluded in Section 7.5.

7.2 Erosion, Dilation, and Beucher's Gradient

7.2.1 Definition

Definitions and mathematical expressions provided in the following are of the grayscale domain and taken from Soille [159].

7.2.1.1 Structuring element

Mathematical morphology (MM) analyses and processes the structure of a given image by probing the said image with a structuring element (SE) of a certain shape and size. An SE is realized by a small image whose values can be binary, grayscale, or n-dimensional. Throughout this chapter, only binary (or flat) SE will be considered. Example of possible SEs of radius 1 pixel are provided in Fig. 7.1, where all SE has its origin at the center of the 3×3 pixels region. Origin of an SE

allows the positioning of this SE at a particular location in the given image. If an SE is said to be at location $\mathbf{x}$, it means its origin coincides with $\mathbf{x}$.

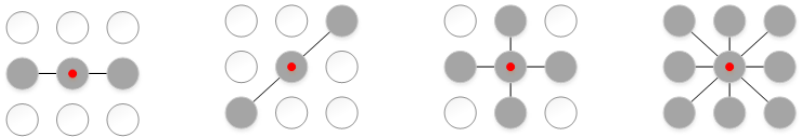

(a) 0°line (b) 45°line (c) Cross (d) Square

Figure 7.1 – Several possible SEs of radius 1 pixel or of size 3×3 pixels, each having its origin at the center.

The shape and size of an SE must be chosen such that it matches the relevant structure within the given image. For example, horizontal line SE is suitable to detect horizontal lines. In the rest of this chapter, SE having a shape of a disk will be used. Digital approximations of this particular shape are shown in Fig. 7.2 for 4 different radii.

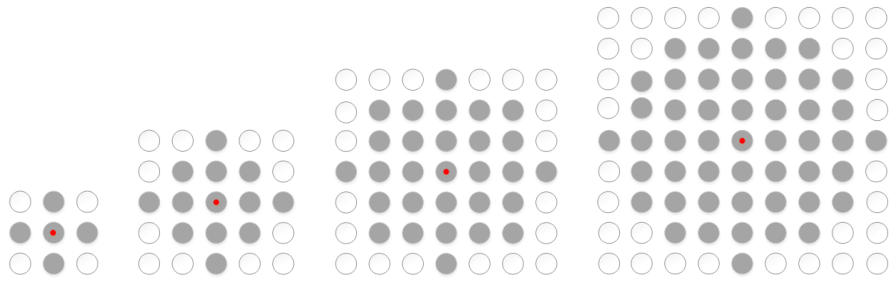

(a) 1 pixel (b) 2 pixels (c) 3 pixels (d) 4 pixels

Figure 7.2 – Digital approximations of disk SEs with various radii.

7.2.1.2 Erosion and dilation

Eroding an image with an SE can be regarded as trying to find where this particular shape of the SE would fit into structures which exist in the image. As for dilation, it will find structures in the image where the origin of the SE would always hit. Illustration of erosion and dilation with disk SE is provided in Fig. 7.3, where both target image and SE are considered as sets. This set erosion ϵ and dilation δ can also be expressed as in Eq. 7.1.

$$\epsilon_B(I) = \bigcap_{\mathbf{b}\in B} I_{-\mathbf{b}},\ \delta_B(I) = \bigcup_{\mathbf{b}\in B} I_{-\mathbf{b}} \tag{7.1}$$

Extending the set definition to work for binary and grayscale images, the aforementioned expressions are modified into Eq. 7.2.

$$\epsilon_B(I) = \bigwedge_{\mathbf{b}\in B} I_{-\mathbf{b}},\ \delta_B(I) = \bigvee_{\mathbf{b}\in B} I_{-\mathbf{b}} \tag{7.2}$$

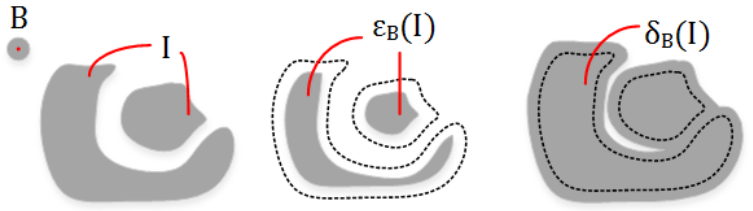

Figure 7.3 – Illustrations of erosion and dilation of a set I by an SE . Erosion reduces the initial set into $\epsilon_B(I)$ while dilation connects the initially separate objects into $\delta_B(I)$.

7.2.1.3 Beucher's gradient

The basic gradient operator of the MM framework is called *Beucher's gradient* [146]. It is defined as the arithmetic difference between the dilation and erosion of the input image, or as expressed in Eq. 7.3.

$$\varrho_B = \delta_B - \epsilon_B \tag{7.3}$$

Note that, by definition, morphological gradients are non-negative. But this can only be guaranteed if the dilation and erosion are extensive and anti-extensive, respectively, see Eq. 7.4. Also note that the non-negativity of morphological gradients demands the use of symmetrical structuring elements.

$$\begin{aligned} \delta \text{ is extensive} &\Leftrightarrow \mathbf{id} \leq \delta \\ \epsilon \text{ is anti-extensive} &\Leftrightarrow \epsilon \leq \mathbf{id} \end{aligned} \tag{7.4}$$

Finally, Fig. 7.4 is provided to allow readers to see the impact of applying the aforementioned morphological operators to a grayscale image. Eroding and dilating a grayscale image will cause the dark and bright regions, respectively, to expand. Using a Beucher's gradient, edges found in the original image are extracted.

(a) Original image

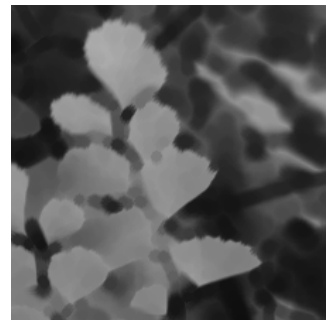

(b) Eroded image

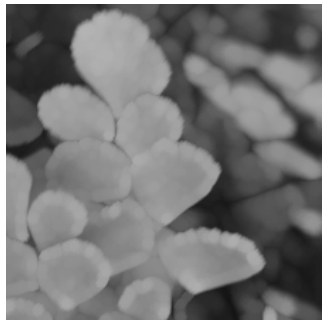

(c) Dilated image

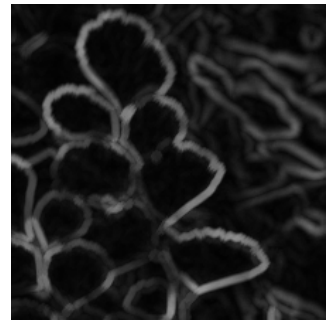

(d) Beucher's gradient

Figure 7.4 – The impact of basic grayscale morphological operators to an input image, using 3 pixels radius disk SE. Erosion and dilation expand dark and bright regions, respectively. Beucher's gradient extracts edges from the original image.

7.2.2 Extension to the Spectral Domain

The mathematical expressions of grayscale erosion and dilation do not need an explicit definition of ordering relation. This is because in the scalar domain, the notion of ordering is automatically obtained. Thus, extending the grayscale operators to the spectral domain requires rewriting them by including the spectral ordering relation. From Chapter 4, conditional ratio and angular distance ordering relation (CRA) has been concluded to be the most suitable spectral ordering relation. To recall, it is a distance-based function, hence requiring to define a suitable spectral distance function. As a conclusion of Chapter 3, spectral Kullback-Leibler pseudo-divergence (KLPD) was said to be the most suitable spectral difference function which consists of two independent components measuring shape and intensity differences. With these spectral ordering relation and spectral difference function, the mathematical definitions of erosion ϵ, dilation δ, and Beucher's gradient ϱ are

expressed as in Eq. 7.5.

$$\begin{aligned} \epsilon_B(I) &= \bigwedge_{\mathbf{b}\in B} g_{CRA}(I_{-\mathbf{b}}), \\ \delta_B(I) &= \bigvee_{\mathbf{b}\in B} g_{CRA}(I_{-\mathbf{b}}), \\ \varrho_B(I) &= d_{KLPD}(\delta_B(I), \epsilon_B(I)) \end{aligned} \tag{7.5}$$

7.2.3 Subjective Assessment of Ordering Relation Impact

Aiming to subjectively assess the impact of ordering relation to basic morphological operators, image FN1 from Subsets-250 dataset (Appendix B) is employed as target image. Three objects as depicted in Fig. 7.5 are chosen as ROIs, i.e., tower, roof, and the three windows. In the following, in addition to CRA, the impact of lexicographic and marginal ordering relations will also be evaluated. To recall, it has been concluded in Chapter 4 that CRA is currently the most suitable ordering relation for spectral image processing. Read the chapter for evaluation and discussion surrounding other multivariate ordering relations. Then, as CRA is a distance-based approach, it follows that a spectral distance function must be embedded. From Chapter 3, KLPD has been concluded as the most suitable one to date. Thus, in the following, it is KLPD function which will be embedded by CRA. It is also employed as the difference function in Beucher's gradient computation.

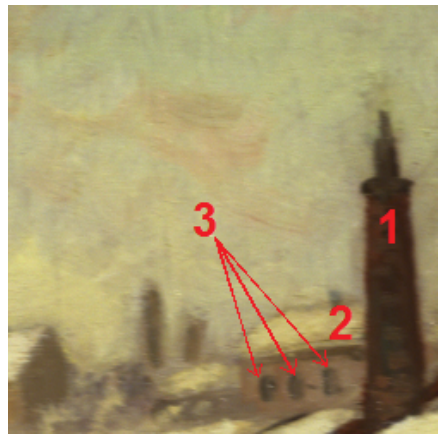

Figure 7.5 – Image FN1 an input for spectral erosion, dilation, and Beucher's gradient. The relevant ROIs are (1) tower, (2) roof, and (3) three windows.

With a disk SE of 2 pixel radius, CRA-based morphological operators are applied to image FN1. In this experiment, CRA employs spectral references S_{Bk} and S_{Wh}.

All resulting images can be observed in Fig. 7.6. In the grayscale domain, erosion will expand image regions having lower intensity values. While for dilation, it is the higher intensity regions that will be expanded. Due to the use of S_{Bk} and S_{Wh} as references in CRA, similar behavior to that of grayscale morphology are obtained. As an example, the tower object whose spectral functions are of lower intensity has its region expanded. And so have the three windows located next to the tower. These objects then shrink when image FN1 is dilated. And the shrinking of lower-intensity regions occurs together with the expansion of higher-intensity ones, e.g., roof. If eroded and dilated images are compared, it can be observed that background of the dilated image is generally of higher intensity than that of the eroded image. This also agrees with the behavior of grayscale erosion and dilation, but particularly so due to the chosen spectral references. Dilation with CRA would cause spectral functions which are 'closer' to S_{Wh} to remain in the dilated image. And since S_{Wh} is equi-energetic, spectral functions with higher intensity would be chosen as the maximum, regardless of their shapes. The use of an equi-energetic spectral reference would reduce the impact of shape differences in distance computation. The obtained Beucher's gradient image is as expected, i.e., showing region boundaries within FN1.

Lexicographic and marginal ordering relations do not respect the physical properties of spectral data, making them unsuitable choices for spectral image processing. And this is despite them being full-band approaches, see complete discussion in Chapter 4. But in Fig. 7.7 their impact on erosion, dilation, and Beucher's gradient can be observed through image FN1. The used SE is disk of size 3×3 pixels. Observing the eroded and dilated images, the global impacts remain the same. Erosion expands darker objects, i.e., tower and windows, and dilation shrinks them. In the dilated images, roof objects are expanded and the background is also of higher intensity than in the eroded images. Comparing the results of lexicographic- and marginal-based morphological operations, images yield by lexicographic ordering relation seem to suffer from grainy artifacts.

Original image

Eroded image

Dilated image

Beucher's gradient image

Figure 7.6 – Image FN1, eroded and dilated with disk SE of 2 pixel radius. CRA ordering relation is employed, embedding KLPD function and spectral references S_{Bk} and S_{Wh}. Beucher's gradient image is obtained using KLPD function.

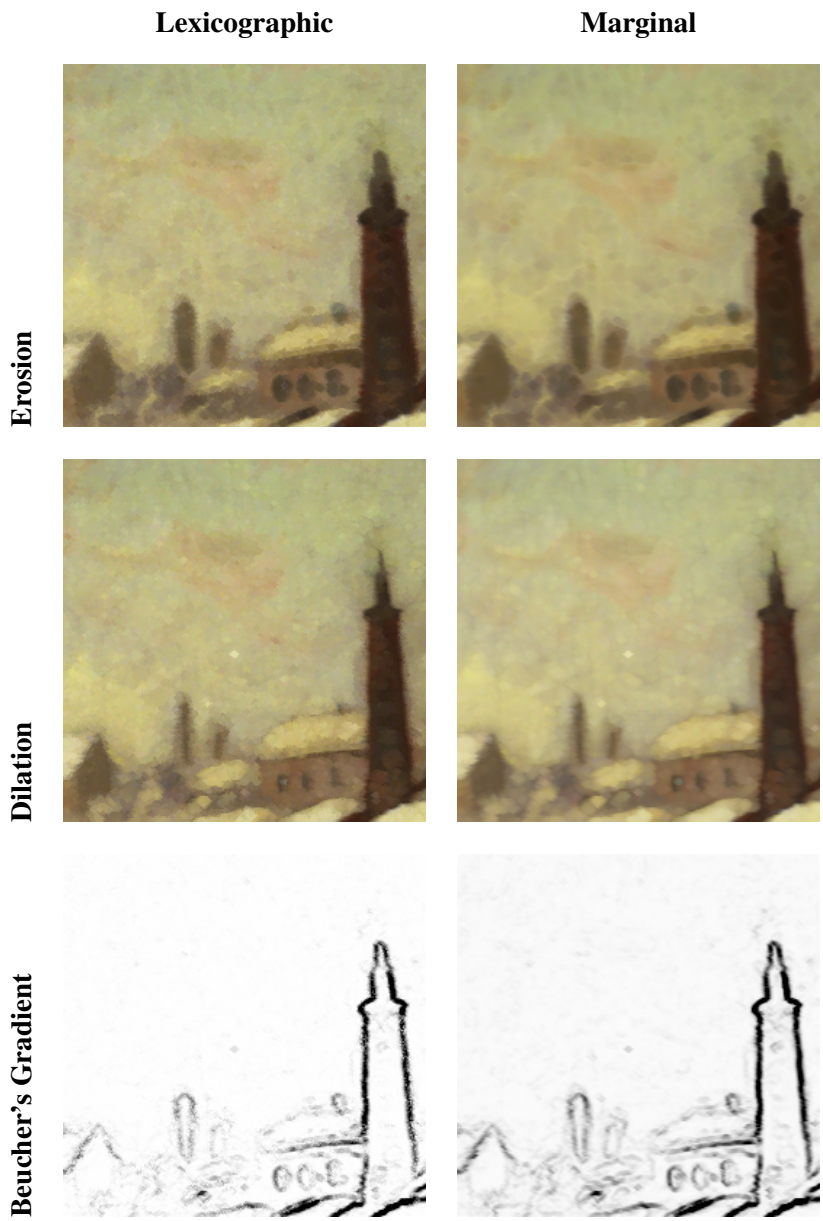

Figure 7.7 – Comparison of the impact of lexicographic and marginal ordering relations in erosion, dilation, and Beucher's gradient. The input is image FN1, SE is disk of radius 2 pixels, and subtraction operation in the gradient computation is replaced by KLPD function. Images generated by lexicographic ordering based morphological operators suffer from grainy artifacts, which is also emphasized by the gradient image. Marginal ordering relation produces smoother images.

The choice of SE size 3×3 pixels induces that the differences of ordering relation impact would be more evident in small details of the image, especially in the presence of edges. Detailed portions of eroded, dilated, and gradient images previously shown in Fig. 7.6 and 7.7 are now shown in Fig. 7.8, allowing a closer observation. Among the three ordering relations, lexicographic approach is the least performing one. Edges in its dilated and eroded images are not maintained, unlike those in CRA- and marginal-based operations. A clearer demonstration of the limitation of lexicographic approach in presence of edges can be observed through the gradient images. Edges obtained by CRA and marginal ordering relations are more solid than that of lexicographic one which suffer from grainy artifacts.

Comparing performances of CRA- and marginal-based operations, there are perceptible differences in the resulting images, see Fig. 7.8. But none of the approaches seem to be completely superior than other. Edges shown in the gradient images are also not significantly different.

To recall, marginal ordering relation is an unsuitable choice for spectral image processing since it suffers from false spectral function problem, see illustration in Fig. 4.18 in Chapter 4. In other words, marginal processing will generate spectral functions which do not exist in the initial spectral set. In a small SE, this problem might be less severe since there is a higher chance of the region being homogeneous. Increasing the size of SE into 7 pixel radius, results of CRA- and marginal-based erosion and dilation using FN1 as target can be observed in Fig. 7.9. Even though the SE has been increased in size so as to have sufficiently non-uniform region, marginal approach still seem to be a well-performing ordering relation. But this behavior is not unexpected. First of all, reducing a spectral image to a color domain reduces the ability to perceive differences. Thus, rather than assessing ordering relations in the color domain, they must be assessed in the spectral domain. Secondly, the good performance of marginal ordering relation must be attributed to the employed image target rather than the ordering relation itself. False spectral function problem still exist in this image, but nevertheless are significantly reduced. On the other hand, the problem will become evident when a texture image is considered. Performance assessment using a texture image can be found later in Section 7.2.4.

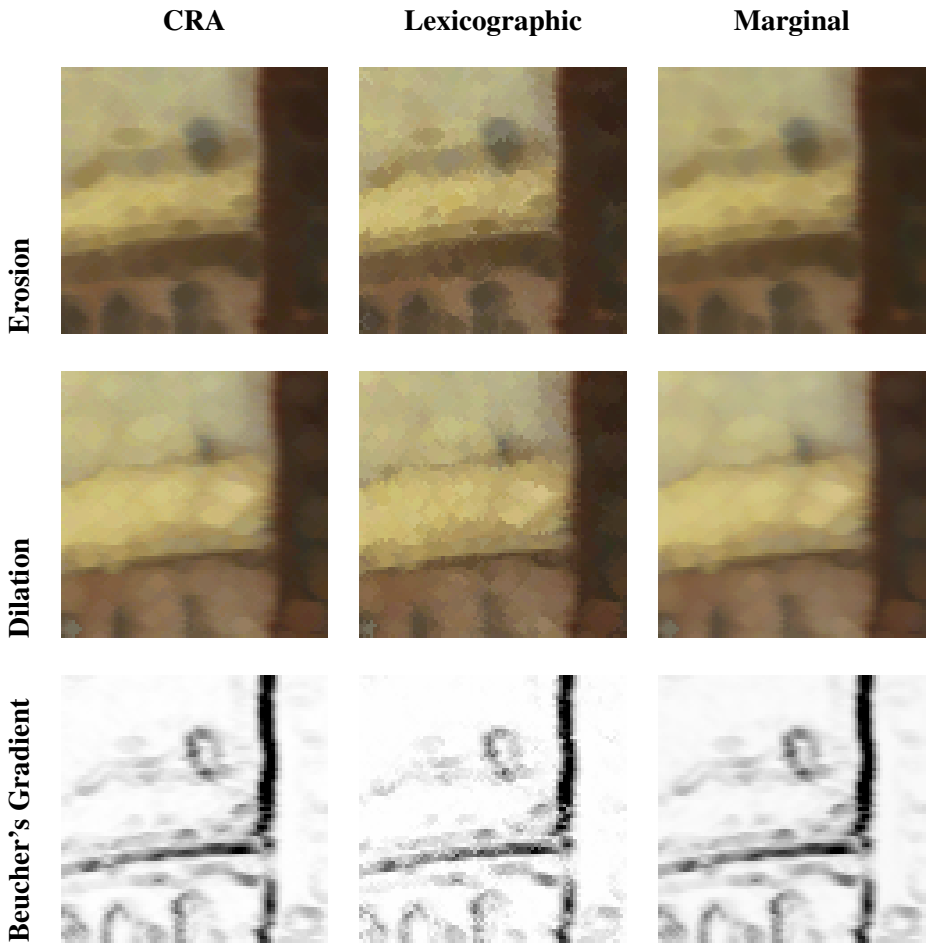

Figure 7.8 – Performances of CRA, lexicographic, and marginal ordering relations in erosion, dilation, and Beucher's gradient shown for a smaller portion of image FN1. Differences in ordering relation impact are better emphasized in the gradient images. Compared to CRA and marginal ordering relations, the lexicographic one produces images with grainy artifacts and a gradient image of less solid edges.

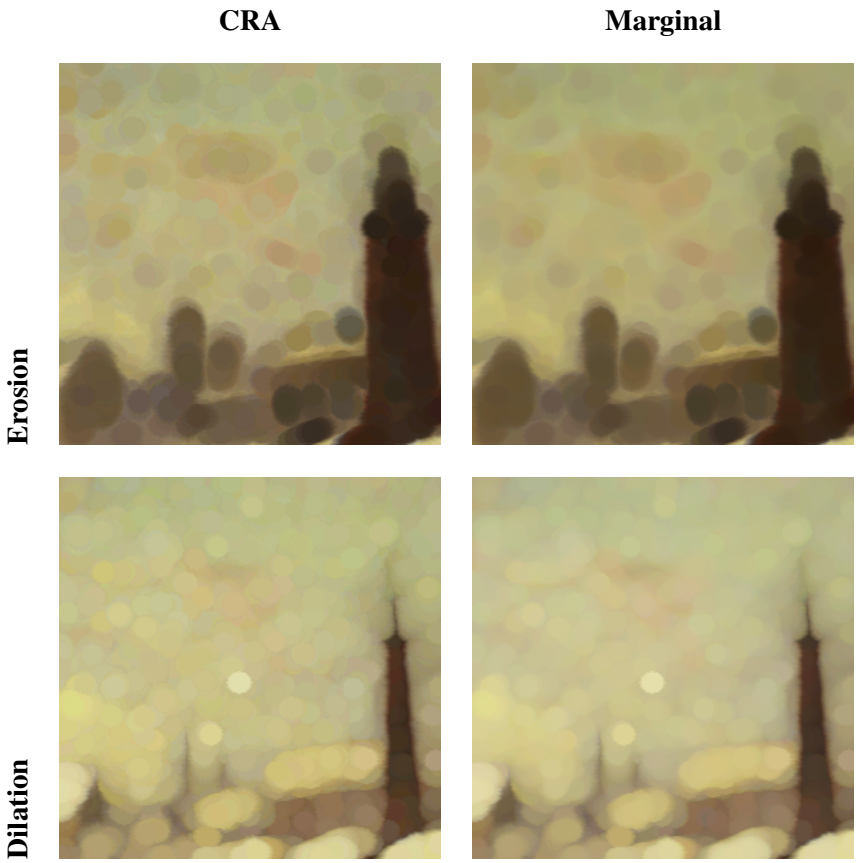

Figure 7.9 – Comparison of the performance of CRA and marginal ordering relations in the erosion and dilation of image FN1 from Subsets-250 dataset, with a disk SE of radius 7 pixels. No significant differences are perceived in the results.

7.2.4 Metrological Assessment of Ordering Relation Impact

Aiming to develop a metrological image processing framework demands for the performance evaluation to be carried out metrologically. Within this context, the use of visual observation in the previous subsection is found to be very limiting. Thus, in the following, assessment will be carried out statistically showing distribution of spectral functions within an image and spectrally through showing the resulting spectral functions. In addition, a texture image will be employed as target in order to better demonstrate the impact of marginal ordering relation.

7.2.4.1 Understanding the results

CRA and marginal ordering relations will be used to construct erosion and dilation, which will be applied to a texture image from Subsets-250 dataset, see Fig. 7.10. Using a disk SE of 7 pixel radius, the impact of erosion and dilation will be observed with a focus on region within the red square. However, note that this particular region is not only impacted by pixels within itself but also its surrounding neighbors depending on the SE size. Neighboring pixels which will contribute to the result of erosion and dilation within the red square includes those located within the blue square.

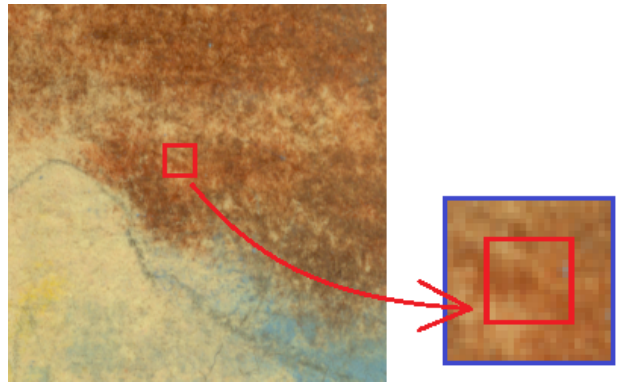

Figure 7.10 – Image PN1 from Subsets-250 dataset and its subset, as marked in red, where impact of CRA and marginal ordering relation would be observed. Note that due to the SE size, all pixels within the blue square will affect results of erosion and dilation within the red square region.

The impact of ordering relation within the said region will be assessed by means of spectral value distribution using bidimensional histogram of spectral differences (BHSD). But rather than using BHSD in its original form, each dot in the plot corresponds to one spectral function within the considered image region. Spectral value distribution within the blue square shown in Fig. 7.10 can be observed

in Fig. 7.11. This BHSD was computed with S_{Wh} as the spectral reference. In addition to evaluating through spectral value distribution, evaluation will also be carried out showing the impact of ordering relation at an obtained maximum/ minimum spectral function.

7.2.4.2 Expected results of erosion and dilation

Erosion and dilation will replace spectral function at the origin with the minimum and maximum spectral functions, respectively, of pixels within the used SE. As a consequence, distribution of spectral values in the eroded and dilated images would converge towards $-\infty$ and $+\infty$, respectively. In marginal ordering relation, these convergence coordinates are assumed to be S_{Bk} and S_{Wh} for spectral reflectance space. In case of spectral radiance space, S_{Wh} would be replaced by a spectral function having maximum possible energy at each wavelength. Using spectral value distribution shown in Fig. 7.11, the convergence direction of marginal ordering relation is as depicted in Fig. 7.12a. In CRA ordering relation, the pair of convergence coordinates must be defined explicitly through the choice of spectral references. Due to this, the convergence of CRA-based erosion and dilation could be any of any arbitrary direction. Three different directions of convergence for CRA are illustrated in Fig. 7.12b.

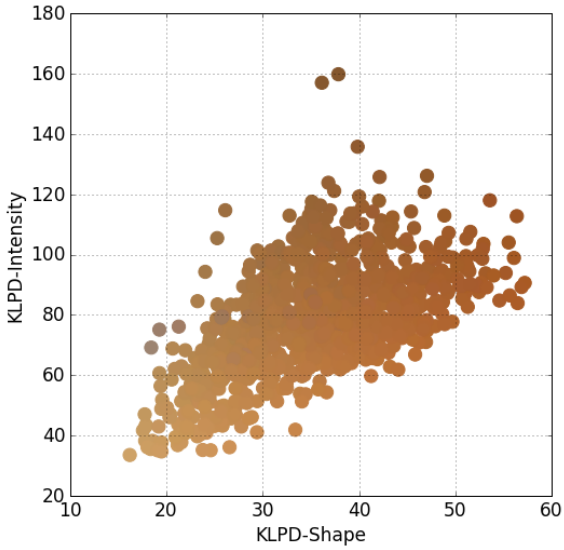

Figure 7.11 – Spectral value distribution of all pixels within the blue square region indicated in Fig. 7.10, obtained with S_{Wh} as reference. Color of each dot in the figure corresponds to color of the spectral function, as obtained by CLTR visualization method.

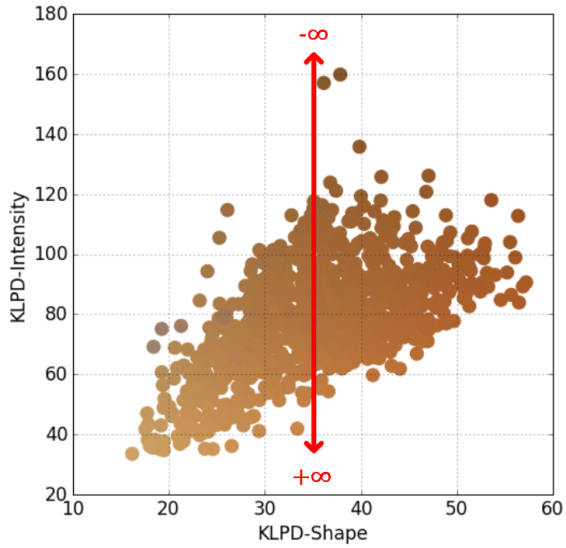

(a) Fixed pair of convergence coordinates in marginal ordering relation

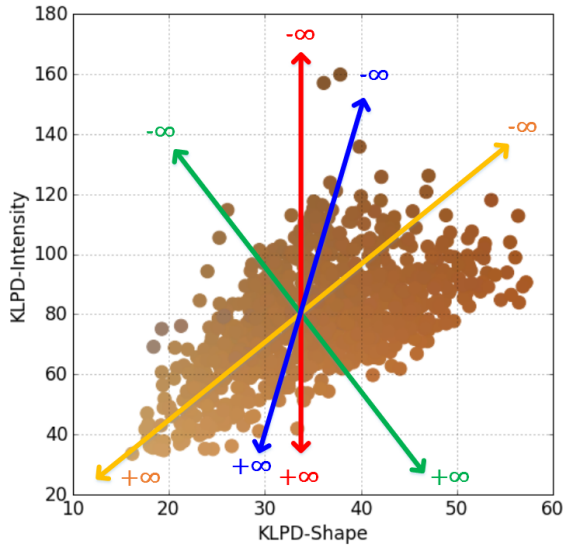

(b) Variable pairs of convergence coordinates in CRA ordering relation

Figure 7.12 – Illustrations of the convergence coordinates of marginal and CRA ordering relations. Shown BHSDs are obtained using S_{Wh} as reference. Marginal ordering relation implicitly assumes a pair of convergence coordinates, i.e., S_{Bk} and S_{Wh} for the reflectance space. On the other hand, with CRA ordering relation, we are required to explicitly define a pair of convergence coordinates by selecting two spectral functions.

7.2.4.3 Performance assessment of erosion and dilation

The impact of CRA- and marginal-based erosion and dilation on image PN1 can be observed in Fig. 7.13, where there is no evident differences between the two approaches. Differences start to become perceptible in Fig. 7.14, when observation is carried out for subset of PN1 which was depicted in Fig. 7.10. Especially for dilation result, marginal ordering relation generates purplish colors which do not exist in the initial spectral set.

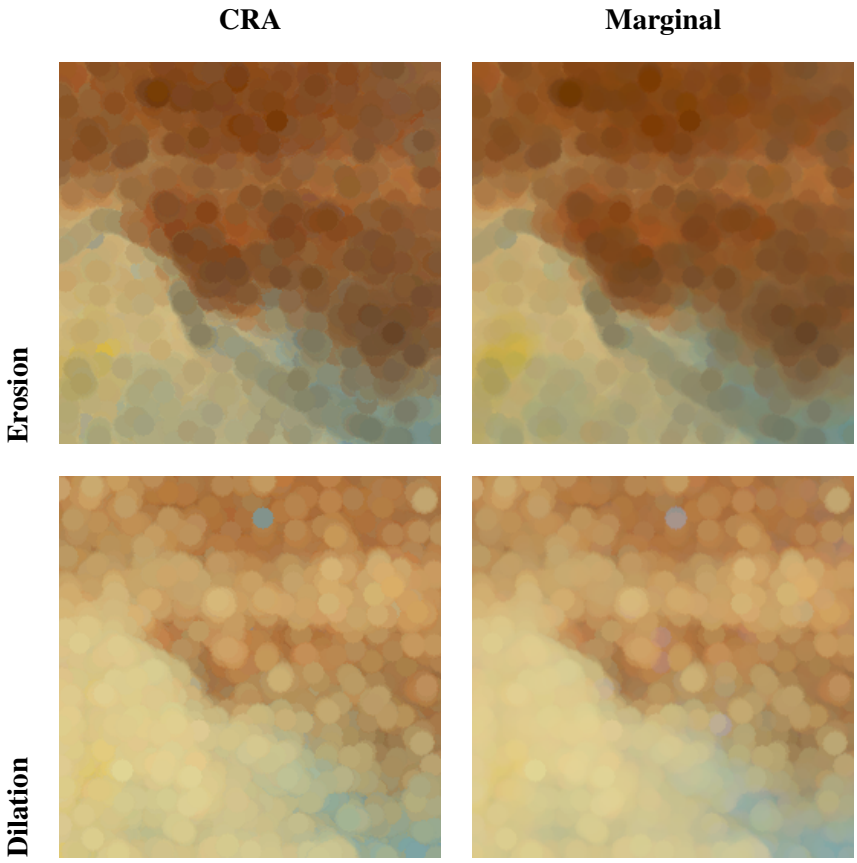

Figure 7.13 – Image PN1, dilated and eroded with disk SE of 7 pixel radius. Both operators are constructed based on CRA and marginal ordering relations.

False spectral function generated by marginal processing can be described as due to marginal mixing procedure. A 3×3 pixel region is obtained from image PN1 where two main colors exist, i.e., brownish and bluish ones. Spectral functions from the said region are plotted in Fig. 7.15a. Given a task to obtain a maximum spectral function from this initial set, marginal ordering relation takes maximum

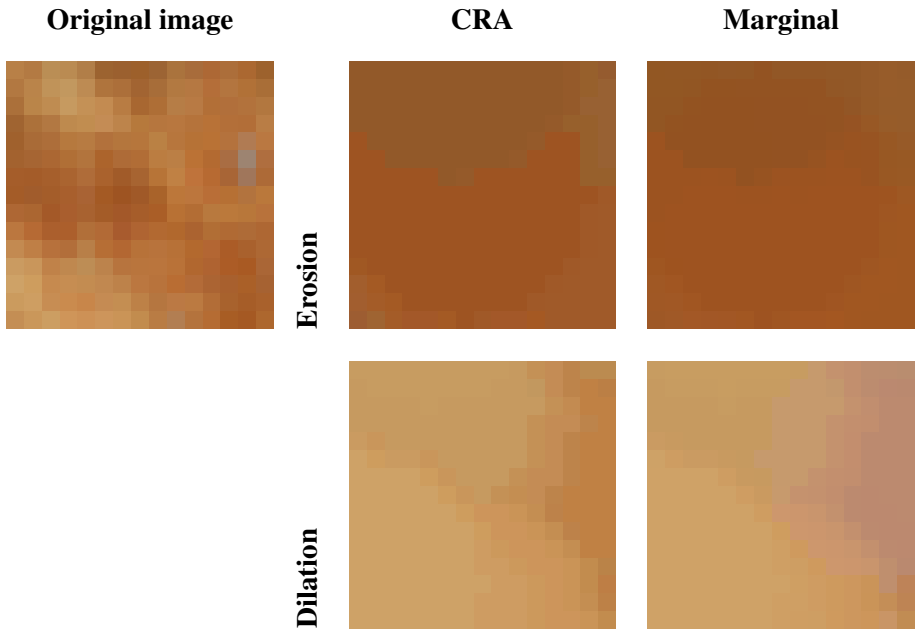

Figure 7.14 – The impact of CRA- and marginal-based erosion and dilation on subset of PN1, as compared to original image prior to processing. False spectral function issue suffered by marginal processing is evident in its dilated image. Purplish colors which do not exist originally appear in the dilated image.

value at each wavelength resulting in a spectral function shown in Fig. 7.15b. The obtained marginal maximum is shown in boxes. Each box corresponds to spectral function of the same color in the initial set where the portion is taken from. And thus, this procedure can be seen as a mixing procedure. But neither optical nor chemical mixing proceeds in this regard. Therefore, the obtained maximum spectral function does not have a physical sense and, ultimately, violates the metrological constraint imposed on the image processing framework.

To further demonstrate the unsuitability of marginal ordering relation, in the following analysis will be carried out with regards to spectral value distribution within subset of PN1 which was depicted in Fig. 7.10. The impact of CRA- and marginal-based erosion to spectral value distribution can be observed in Fig. 7.16, where the BHSD is obtained using S_{Wh} as reference. Note that distribution of the initial spectral set, which was previously shown in color in Fig. 7.11, are now represented by the white circles. CRA and marginally obtained spectral functions are represented by blue and red dots, respectively. As observed, marginal ordering relation converges faster than CRA. But in a closer observation, it is shown that none

of the marginally obtained spectral functions originate from the initial set, unlike those obtained by CRA. Finally, this explains the convergence speed of marginal ordering relation. In a local neighborhood of n pixels, CRA only has n potential solutions. On the other hand, marginal ordering relation is not limited by this number since it considers the solution separately for each wavelength. Hence, the false spectral functions. Spectral value distribution prior to and post-dilation operation can also be observed in Fig. 7.17. Similar behavior is obtained for both CRA and marginal ordering relations. CRA-obtained maximum does exist in the initial spectral set, but not in the case of marginally obtained maximum spectral functions. Finally, these plots show the risk and danger of using marginal ordering relation for spectral image processing. If a spectral image is processed marginally, its result will only be digital results without any physical meaning. And since metrological aspects of the data cannot be ensured, neither results analysis nor interpretation will be accurate and of high relevance.

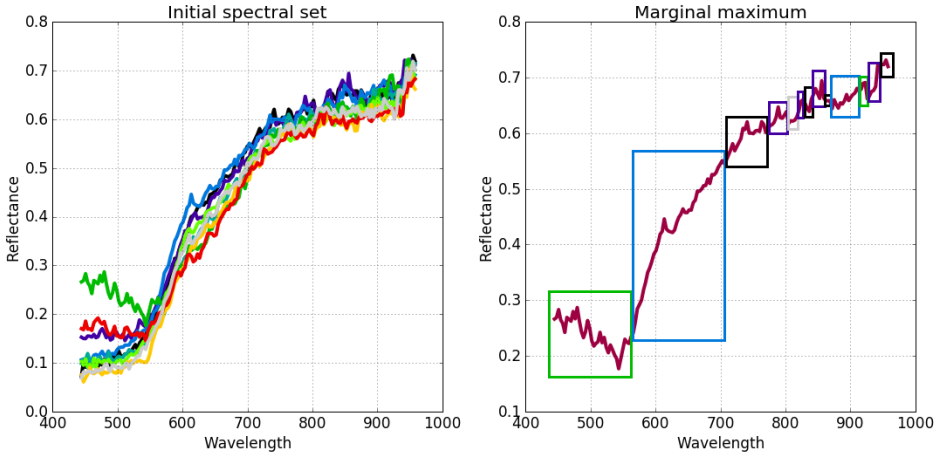

Figure 7.15 – Initial spectral set from a 3×3 pixels region and its corresponding maximum spectral function obtained by marginal ordering relation. Marginal ordering relation computes maximum value independently for each channel. As a consequence, parts of the marginal maximum is taken from different spectral functions. The origin of these parts are spectral functions having the same color coding with the colors of the square.

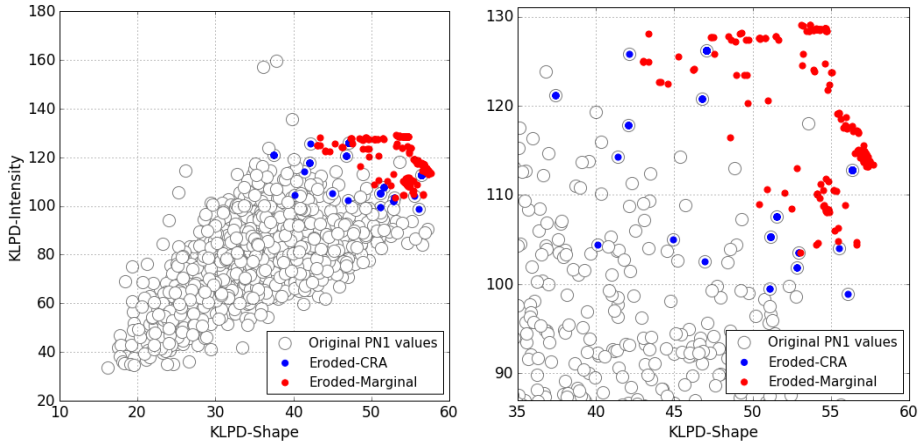

(a) Full view of spectral distribution (b) A zoom of distribution in (a)

Figure 7.16 – Spectral value distribution of a subset of image PN1 which was shown in Fig. 7.10, for before and after erosion operation. Distribution of spectral values prior to erosion is represented by white circles. Red and blue circles are used to represent spectral values post-erosion. Marginally generated values do not exist in the original image since they are not encircled by the white ones.

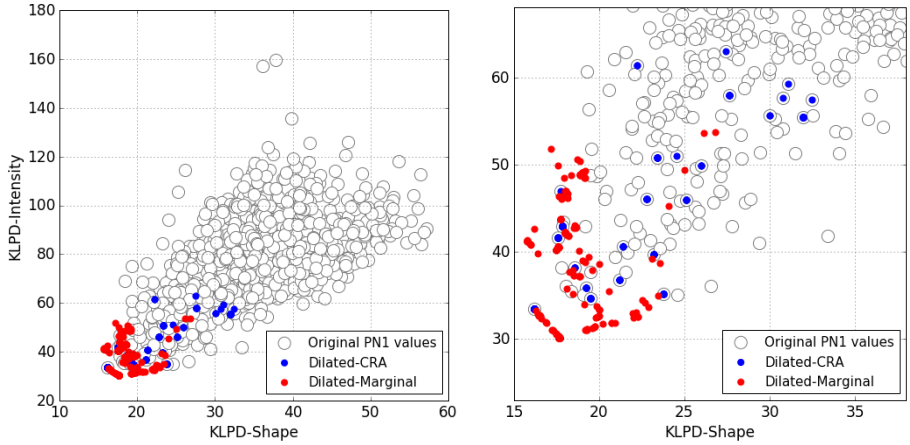

(a) Full view of distribution (b) A zoom of distribution in (a)

Figure 7.17 – Spectral value distribution of a subset of image PN1 which was shown in Fig. 7.10, for before and after dilation operation. Distribution of spectral values prior to dilation is represented by white circles. Red and blue circles are used to represent spectral values post-dilation. Marginally generated values do not exist in the original image since they are not encircled by the white ones.

7.2.5 The Impact of Spectral Reference Selection

In the previous subsection, a black and white spectral functions S_{Bk}, S_{Wh} have been employed as references, which is analogous to the implicit convergence coordinates of the grayscale domain. But CRA ordering relation is not limited to this choice. Reference selection can be made according to application goal at hand. And this choice will, in turn, allows controlling the convergence of erosion and dilation operators.

As a first demonstration, image NP1 from Subsets-250 dataset (Appendix B) will be employed as target. The said image target is shown in two different color visualizations in Fig. 7.18. Five main colors can be observed in this image target. According to their numbers, the colors are (1) dark green of the flower stem, (2) white of the background, and (3-5) different shades of red of the flower petals and pollen. Spectral reflectance functions for each color are obtained from 3×3 homogeneous pixel regions and can be observed in Fig. 7.19. Spectral value distribution of the initial spectral set of image NP1 can also be observed in Fig. 7.20, where S_{Wh} is employed as reference in the KLPD function computation. Note that this particular image is processed with zero replacement value of 10^{-6}, see Section 5.5.1.

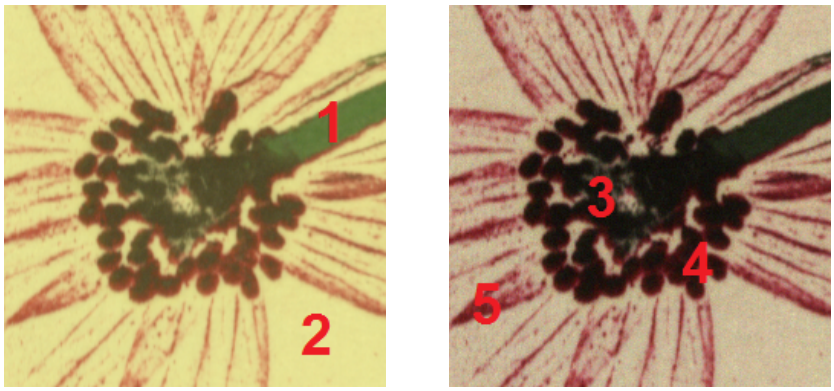

(a) ROIs 1 and 2, in CLTR visualization (b) ROIs 3–5, in FIXED visualization

Figure 7.18 – Image NP1 from Subsets-250 dataset and its two color visualizations, where the relevant ROIs are marked.

Given an image whose spectral values can be described as a convex hull, any arbitrary spectral function is said to be an optimal spectral reference if it lies outside the convex hull of the initial spectral set, see Section 5.3. Additionally, it should not lie too far from the periphery of the convex hull. As for image NP1, its convex

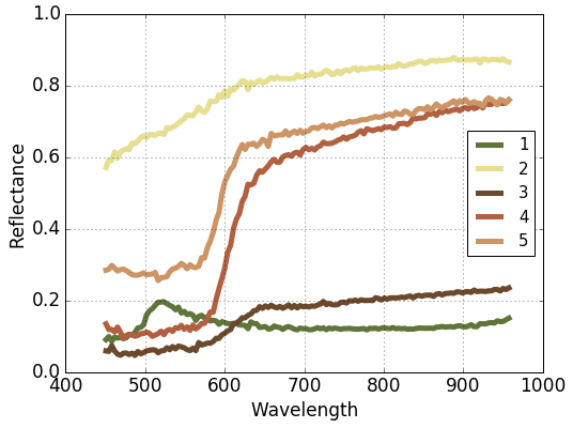

Figure 7.19 – Spectral reflectance functions for each ROI shown in Fig. 7.18, obtained by averaging 3×3 homogeneous pixel region from each ROI. Colors for each spectral function are obtained by CLTR visualization.

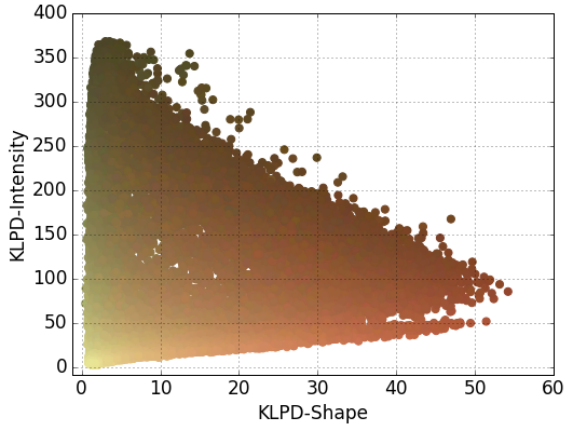

Figure 7.20 – Spectral value distribution of image NP1, obtained using KLPD function and S_{Wh} as reference.

hull can be described through BHSD shown in Fig. 7.20. As observed, in NP1, hue differences hold more importance than intensity differences. In fact, intensity differences are mainly due to the shades of red coming from regions numbered 3 to 5, see Fig. 7.18. Based on these observations, in the following are two application goals and their corresponding reference choices.

S_{Bk}–S_{Wh} **reference pair** Both S_{Bk} and S_{Wh} are equi-energetic spectral functions. Selecting the two as references entail that the convergence of erosion

and dilation will lie at both ends of the intensity axis. Or in the case of BHSD using KLPD function, erosion and dilation will move towards either ends of KLPD-Intensity axis. Due to this, erosion will expand regions corresponding to those numbered with 1, 3, and 4, since they are of lower intensity values. On the other hand, dilation will expand regions with the lighter red color and also the background.

Simulated red (SR) and green (SG) reference pair The pair is selected aiming to control the convergence of erosion and dilation along the shape axis. See the two spectral functions in Fig. 7.21a. SG is chosen knowing that most likely there is only one type of green within image NP1. This selection will allow distinguishing green with other colors in the image. Then, the intensity of SG must be considerably different than the greens which actually exist within the image, such that SG does not fall inside the convex hull of NP1. SR spectral function is selected through observing the convex hull of NP1 obtained by using SG as reference, see Fig. 7.21b. Intensities of the two spectral functions should be rather similar such that intensity differences do not have a significant impact on the convergence of erosion and dilation.

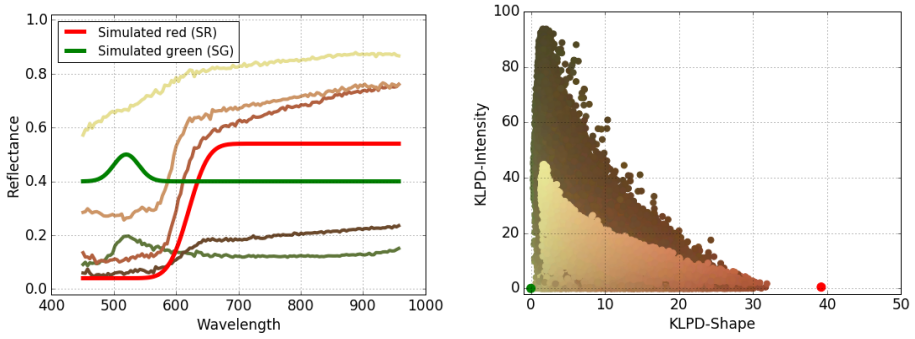

(a) Selected spectral references with respect to samples from the initial spectral set

(b) Spectral value distribution of the initial set, with respect to SG shown in (a)

Figure 7.21 – Spectral variation of the chosen spectral references with respect to variation within the initial spectral set of image NP1. Shown BHSD is generated KLPD function, with simulated green (SG) as reference.

Erosion and dilation results of NP1 using the two aforementioned pairs of spectral references can be observed in Fig. 7.22, disk SE of radius 7 pixels (or of size 15×15) is employed. S_{Bk} causes erosion to converge towards darker spectral functions. And as a consequence, erosion operator will be in favor of spectral functions with lower intensity values, hence the expansion of regions corresponding to stem

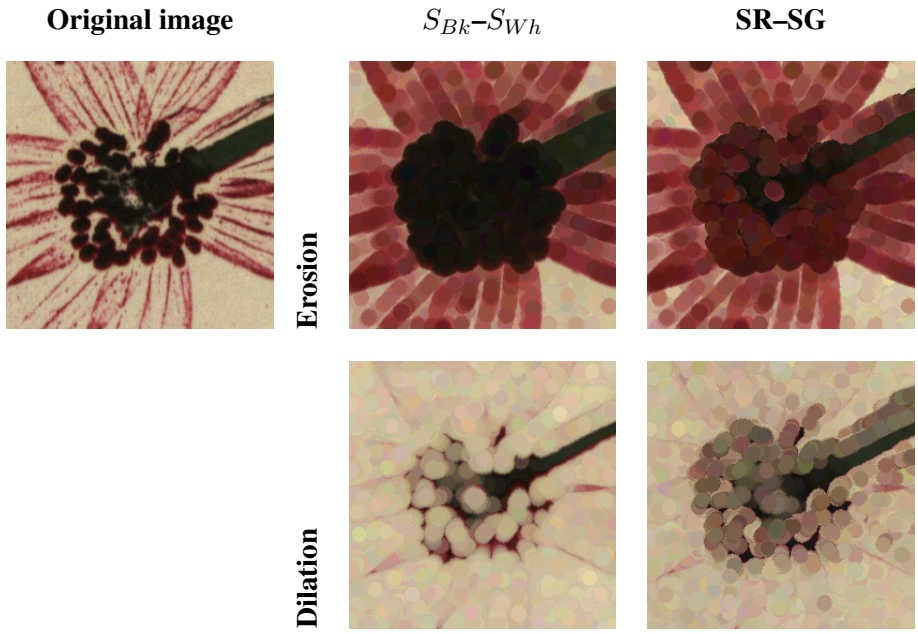

Figure 7.22 – Erosion and dilation results of image NP1 (in FIXED visualization), obtained with two different pairs of spectral references, i.e., S_{Bk}–S_{Wh} and simulated red (SR)–simulated green (SG). Disk SE of radius 7 pixels is employed. S_{Bk} causes erosion to converge toward darker spectral functions and SR toward the reddish ones. The different impacts are especially evident in ROI 3. S_{Wh} causes dilation to enlarge regions having higher intensities, while SG causes dilation to favor greenish spectral functions. Differences can be perceived in ROIs 1 and 3.

and pollen of the flower. Regarding regions which correspond to flower petals, in each local neighborhood of size 15×15 pixels, most likely there will only be spectral functions of the white background and the lighter and darker red of the petals. In such a case, evidently spectral functions of darker red ones will be replacing the other two. Therefore, edges of the flower petals are now more defined and comes with darker red color. In the case of dilation which converges toward S_{Wh}, the result is also as expected. Darker regions such as those corresponding to the stem and pollen of the flowers are shrinking. Then, at the same time, the effect is almost like removing flower petals from the image. This is because dilation will be in favor of those of more similar intensity than S_{Wh}, hence the domination of spectral functions corresponding to the background region. Erosion operator which converges toward SR, see Fig. 7.21a, will cause regions initially having the reddish hue to be expanded. Then, since SR is of lower intensity value, erosion will be favoring brighter than the darker spectral functions. As a consequence, regions in

the image corresponding to pollen of the flower will become brighter compared to the image prior to dilation. Lastly, dilation which converges to SG will tend to remove the reddish spectral functions. This is because shapes of SG and SR are located at the extreme ends of the initial convex hull, see Fig. 7.21b. On the other hand, spectral functions of the background are more similar to SG in terms of their shapes. Hence, the reddish regions are replaced with spectral functions originating from the background. Despite having SG as maximum convergence coordinate, greenish regions are shrinking instead of expanding in the dilated image. This is, however, not surprising. It is caused by the different intensity levels of SG and the greens of the original image. If we observe Fig. 7.21b, dynamic ranges of KLPD-Intensity of the green spectral functions are almost twice of those corresponding to the beige colors of the background. The greens go from 0 to almost 100, while the beige ones roughly from 0 to almost 50. Due to this, if a dark green is competing against ones coming from the background, dilation will always select the latter. This decision is made based on intensity variations because shape differences between the greenish and beige spectral functions are very reduced, see Fig. 7.21b.

The impact of reference selection to erosion and dilation is also observed through employing a texture image, i.e., image PN1 shown in Fig. 7.23. Five ROIs are determined within PN1, numbered from 1 to 5. Their corresponding colors/ regions are (1) blue, (2) yellow, (3) dark grayish outline, (4) brown, and (5) beige color, possibly of paper. Spectral reflectance functions representing each color group are obtained by averaging 3×3 considerably homogeneous regions, see Fig. 7.24a. Using S_{Wh} as reference, spectral value distribution of PN1 can also be observed in Fig. 7.24b. And as seen in the distribution, despite being dominated by brown colors, there are also some blue, yellow, dark grayish color, and beige.

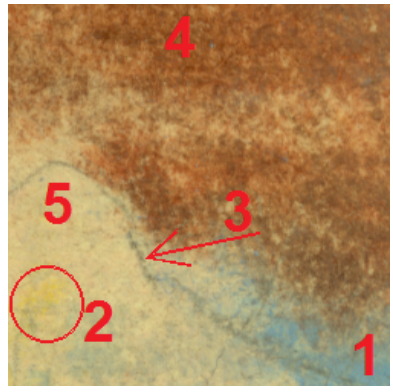

Figure 7.23 – Image PN1 (in CLTR visualization) and its relevant ROIs.

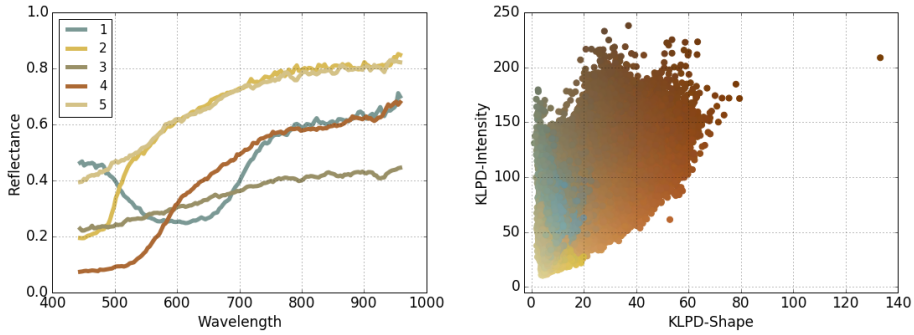

(a) Spectral functions of the 5 ROIs in Fig. 7.23 (b) Spectral value distribution using BHSD

Figure 7.24 – Spectral reflectance functions and value distribution of image PN1. Spectral reflectance functions are obtained by averaging 3×3 homogeneous regions in each ROI. Spectral value distribution is obtained using S_{Wh} as reference.

Upon observing the content of the initial spectral set of PN1, in the following are two pairs of spectral references and the application goal they were considered for.

Simulated yellow (SY) and blue (SB) First of all, this pair was selected such that the convergence of erosion and dilation moves along the intensity axis. However, instead of completely ignoring shape differences like S_{Bk}–S_{Wh} choice, the minimum and maximum convergence are to have different spectral shape, see Fig. 7.25a. Spectral value distribution of the initial spectral set of PN1 obtained using SB as reference is also provided in Fig. 7.25b. As observed, dynamic range of the intensity axis is almost three times that of the shape axis. It can also be observed that variations within the blue and yellow colors are almost exclusively dominated by intensity and shape differences, respectively. Due to this, despite erosion being controlled by a dark yellow convergence coordinate, erosion will be in favor of dark blue spectral functions since the yellow spectral functions are of considerably highter intensity values. As for dilation, the dilated image will generally be of higher intensity values than that of the eroded one. Additionally, darker blue ones will be favored than other dark colors such as brown.

Simulated brown (SBr) and yellow-2 (SY2) This second pair is chosen such that shape differences will have greater impact to erosion and dilation than if the previous reference pair is employed. As seen in Fig. 7.26a, intensity differences between SBr and SY2 are not significant. And if they are observed within the context of spectral value distribution of the initial spectral set, see

Fig. 7.26b, differences in dynamic ranges of shape and intensity axes have become reduced. Then, the yellow and beige colors are now equally distributed along the origin of both axes. Blue colors can be seen as having higher intensity and shape differences relative to SY2. With this reference pair, eroded images will still be darker than the dilated ones. However, due to the spectral value distribution it generates, beige colored spectral functions will be selected when there is a competition with the blue ones.

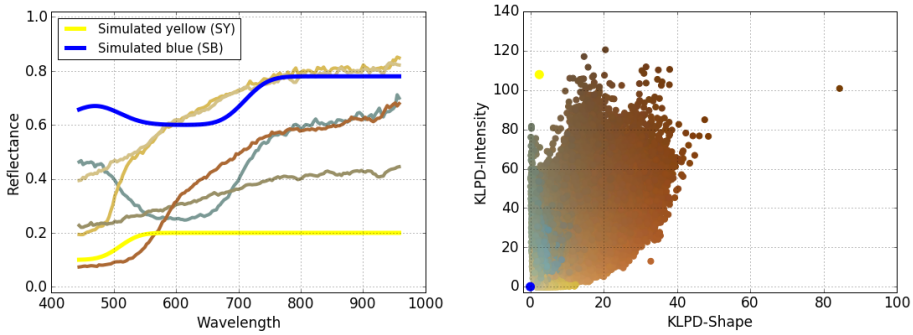

(a) Spectral reflectance plot (b) Spectral value distribution using BHSD

Figure 7.25 – Spectral variation of spectral reference pair simulated yellow (SY) and simulated blue (SB) with respect to variation within the initial spectral set of image PN1. Spectral value distribution is generated using SB as reference.

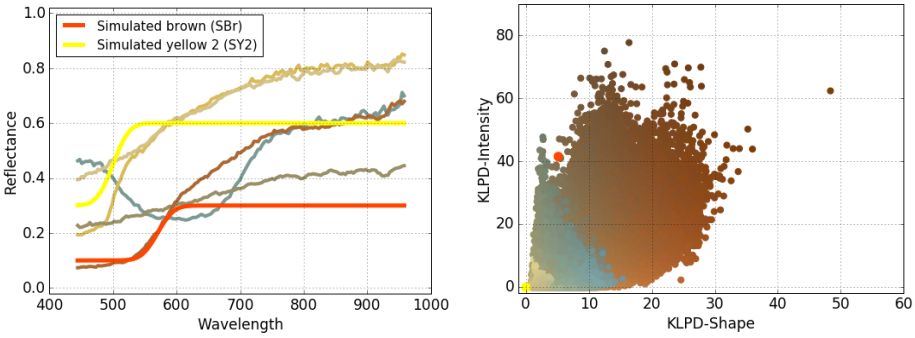

(a) Spectral reference plot (b) Spectral value distribution using BHSD

Figure 7.26 – Spectral variation of reference pair simulated brown (SBr) and simulated yellow-2 (SY2) with respect to variation within the initial spectral set of image PN1. Spectral value distribution is generated using SY2 as reference.

Erosion and dilation results of image PN1 using the two different pairs of spectral references can be observed in Fig. 7.27. As expected, intensities of pixels belonging to ROI 4 previously described in Fig. 7.23 have now become lower and higher for erosion and dilation, respectively. The same can be observed not only for the pair SY–SB, but also SBr–SY2. For ROIs 1 and 3, slight differences are obtained by the different reference pairs. Significant differences can be observed in the eroded images of ROIs 2 and 5. For SY–SB pair, since intensity differences between the references are important, the erosion operator will tend to select darker spectral functions in the local neighborhood. On the other hand, it will not be the case for the latter reference pair, since the intensity difference between SBr and SY2 are reduced. This will allow the erosion operation to consider the minimum spectral function not only in terms of intensity but also shape differences. As a result, the erosion will not necessarily select a darker spectral function. And as observed in the figure, erosion using SBr–SY2 reference pair selects lighter spectral functions as being the minima in ROI 5. The light beige color spectral functions are selected over the darker blue or gray colored ones, unlike eroded images obtained by the previous reference pair which selects the latter.

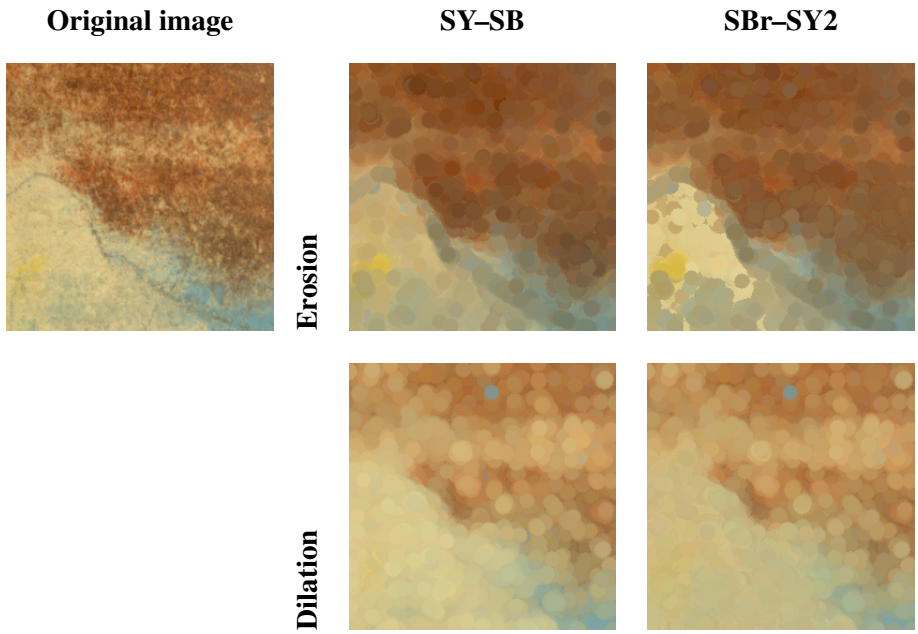

Figure 7.27 – Erosion and dilation results of image PN1, obtained with two different pairs of spectral references, i.e., SY–SB and SBr–SY2 pairs. Disk SE of radius 7 pixels was employed. Images are visualized using CLTR method.

7.3 Watershed Transformation

7.3.1 Brief Introduction of Segmentation Using Watershed

Image segmentation is the partition of an image into regions, each having certain properties [159]. By representing an image by groups of pixels forming objects, more advanced processing and understanding of the image are made possible. Within the context of grayscale segmentation, an image is assumed as connected regions which have small grayscale variations. Consequently, when two adjacent pixels have significant grayscale differences, it means that they belong to different regions or objects. When the image at hand is a color image, more information is available allowing to quantify the variations not only in terms of intensity but also color, e.g., hue and saturation. As a result, the segmentation result can be more accurate. A significant gain in accuracy can be obtained in the spectral domain, since spectral resolution of the data is significantly higher and different materials may greatly differ in their spectral properties. But the desired level of accuracy cannot be obtained automatically. A full-band segmentation which will be able to extract meaningful information from the big amount of data is required. And in Chapter 5, it has been demonstrated how spectral variations within an image can be described by means of spectral differences.

Watershed transformation is a morphological approach to image segmentation. In the concept of watershed, an image is regarded as a topographic surface. For a two-dimensional grayscale image, in addition to its spatial dimension, its intensity values will be considered as another dimension which represents the depth of the topographic surface. In this regard, the segmentation approach can be described using the analogy of flooding simulation. If the surface is slowly immerged into water, catchment basins will be filled with water. Then, as the flooding progresses, smaller water dams (which correspond to local minima) will be merged into a single dam. The watershed itself corresponds to the entire set of the obtained dams, which provide the partitions of an image into its catchment basins [159]. More detailed explanation regarding the theoretical foundation and computation of morphological watershed can be found in [79, 159].

7.3.2 Spectral Gradient: Shape, Intensity, and Total Differences

Watershed transformation takes a gradient image as input. In the previous section, Beucher's gradient for a spectral image has been defined as the spectral differences between its dilated and eroded images, computed using KLPD function. However, depending on the composition of a spectral image, one spectral variation might be of more importance than another. Thus, in order to obtain an optimal result,

the selection of spectral difference function must take into consideration which spectral variation is more prominent in a given image.

KLPD function itself is composed of two independent components, i.e., one measure of shape differences and one of intensity differences. Due to this, KLPD function allows to determine which spectral variation holds more importance in a given image, whether shape, intensity, or both are equally important. As a consequence for spectral Beucher's gradient, its difference function can be adjusted depending on which spectral variation is of greater importance. The gradients will further be addressed as total, shape, and intensity gradients if the used functions are KLPD, KLPD-Shape, and KLPD-Intensity, respectively.

7.3.2.1 Understanding the results

In the following, spectral gradient of several images from Subsets-250 dataset (Appendix B) will be presented. Erosion and dilation of these images are implemented with CRA ordering relation embedding KLPD function, disk SE of radius 4 pixels, and spectral references S_{Bk} and S_{Wh}. Total and intensity gradient images will be shown in inverted grayscale values, see Fig. 7.28a. Shape gradient images will be presented using the color map shown in Fig. 7.28b. In this color map, the significance of a shape difference increases from left to right. Homogeneous region will be color coded with purplish white. Slight shape variations will be colored by shades of purple, and as shape variations increase the color code will go from red to dark blue as depicted in the color map.

(a) Color map for total and intensity gradients

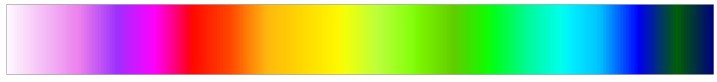

(b) Color map for shape gradient

Figure 7.28 – Color maps employed to visualize the different spectral gradient images. From left to right are low to high gradient values.

7.3.2.2 Performance assessment of spectral gradients

Gradient images of NP1, FN1, and PN2 are computed and shown in Fig. 7.29. If variations within a given spectral image are dominated by intensity differences, the resulting intensity and total gradient images will be highly similar. And among the three target images, this can be observed for image FN1. Faint shape gradient image of FN1 suggests that shape differences have limited importance in the image. Image structures extracted by the shape gradient also present in the intensity gradient, albeit in a significantly lesser magnitude. This can also be interpreted as the image being composed of few color pigments. In case of image NP1, it can be observed that both shape and intensity differences have a considerable contribution to the total gradient image. Significant intensity changes can be found among the stem and pollen objects. This intensity gradient image allows to deduce that spectral functions belonging to these regions are significantly lower in intensity than those originating from the background or petals of the flower. Then, compared to the high intensity differences found within the previous objects, intensity differences between the background and flower petals becomes insignificant. But by observing the shape gradient image, it becomes evident that it is shape differences which are the more prominent spectral variations.

The notion of gradient has limited use in case of texture images, e.g., image PN2 in Fig. 7.29. This is because the assumption of reduced local variations are generally not met. In a texture image, local variations could potentially be higher than variations occurring at region boundaries. In fact, there might not even be clear region boundaries within the image. Nevertheless, gradient images of PN2 can still provide a useful information. Observing the intensity and total gradient images of PN2, it can be said that they are not significantly different. The total gradient is only slightly darker than the intensity one. However, contribution of the shape gradient image to the total one cannot be ignored. This is because different details of the image are found by the shape gradient, which are not evident neither in intensity nor total gradient images. See red dots in the shape gradient image which correspond to yellow strokes in the original image of PN2. Finally, despite PN2 being composed of seemingly homogeneous regions of very few colors, the gradient images suggest that this image is in fact highly textured. Moreover, there might be four different colors that exist within the image according to structures extracted by the individual gradient images.

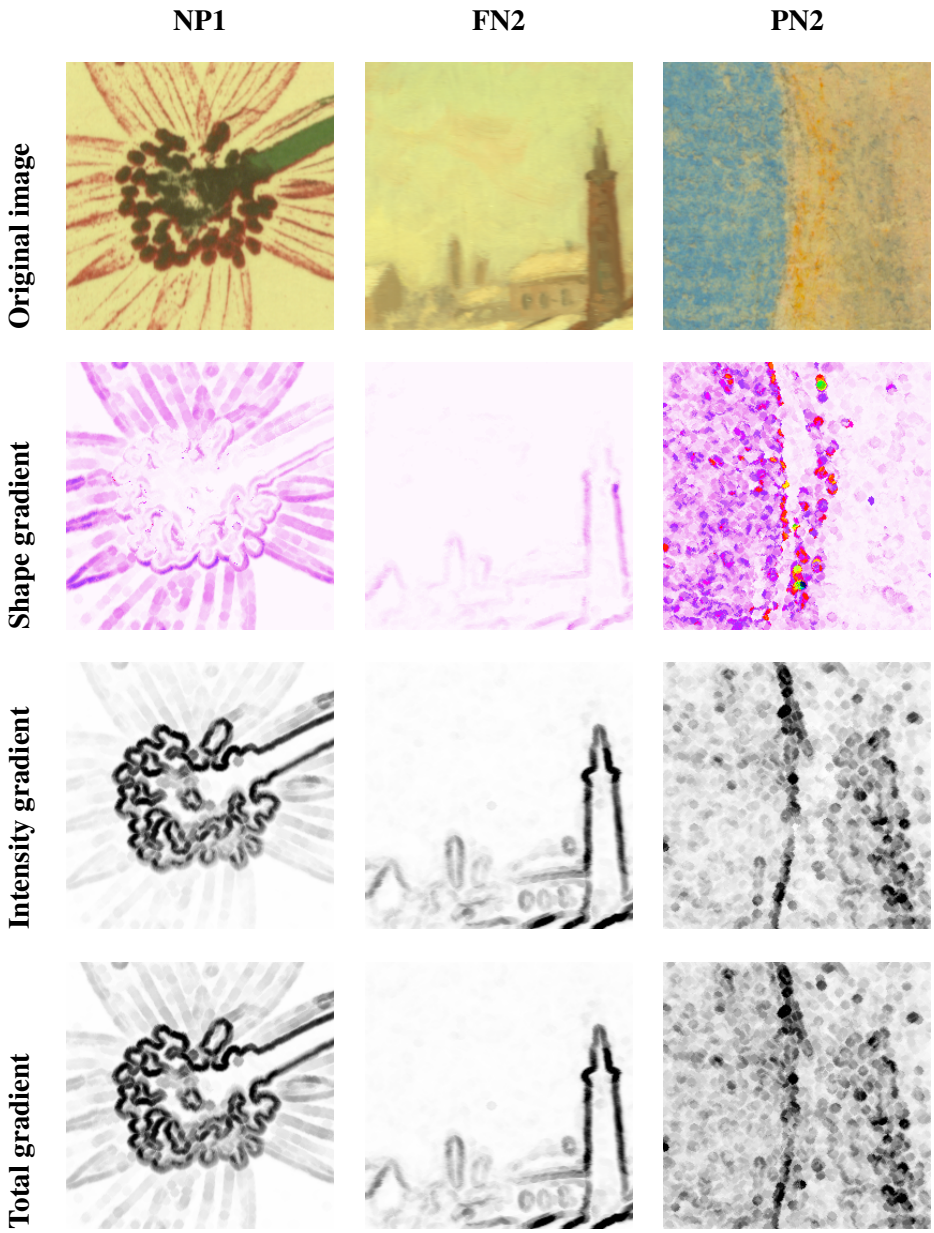

Figure 7.29 – Gradient images of NP1, FN1, and PN2 from Subsets-250 dataset, as obtained by disk SE of 4 pixel radius. Shape and intensity gradient images are obtained by the individual components of KLPD function, while the total one is by KLPD function as a whole.

7.3.3 Marker-Controlled Watershed using Spectral Gradients

Gradient is particularly useful for segmentation and texture analysis. We have previously defined three spectral morphological gradients. In the following, we will use them in spectral image segmentation using marker-controlled watershed (MCW) [121]. Further explanations and details can be read in [28, 159].

Image processing steps required to reach MCW are depicted in Fig. 7.30. Parameter choice at the level of erosion and dilation steps are provided in Table 7.1. As seen in the figure, MCW takes two images as input, i.e., local gradient and marker images. Local gradient image should be able to capture structures and fine details in the original image. Hence, a small size SE is employed. Marker image is required at the initialization of watershed transformation, acting as local minima where flooding process of the catchment basins starts from. Representing homogeneous regions, the local minima are gradient of low magnitudes. Then, in order to reduce the impact of noise and small variations within a local neighborhood, generally a larger SE is employed to obtain the marker image. After gradient computation, marker image is obtained by thresholding and labeling the previously obtained gradient. Final segmentation results will also depend on selected marker threshold T.

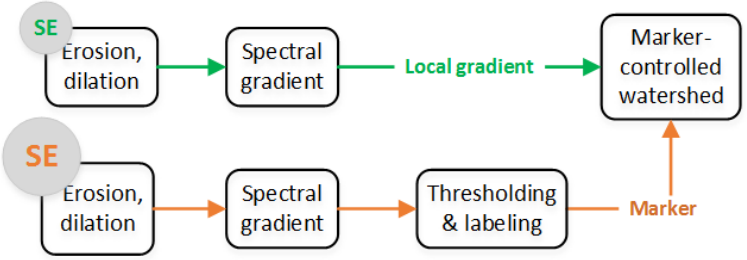

Figure 7.30 – Image processing steps required to reach segmentation using marker-controlled watershed (MCW) transformation. Note that SE size required to compute marker image is larger than that of local gradient image.

Table 7.1 – Parameter choice for erosion and dilation steps in the context of MCW shown in Fig. 7.30. Local gradient and marker images are obtained using disk SE of radius 2 and 4 pixels, respectively.

Use of gradient in watershed	**Erosion and dilation parameters**			
	Ord. relation	**Diff. function**	**Ref. pair**	**SE radius**
Local gradient	CRA	KLPD	S_{Bk}, S_{Wh}	2
Marker				4

7.3.3.1 Observing the impact of spectral gradients

From Fig. 7.29, it can be observed that both intensity and shape gradients of image NP1 contribute to the total one. Aiming to observe the impact of different spectral gradients on the results of MCW, the three gradients of image NP1 are employed to segment the image, whose relevant ROIs are marked in Fig. 7.31. The results of MCW where identical marker threshold $T = 1$ is employed can be observed in Fig. 7.32. Among the three results, better segmentation result for ROI 1 is obtained by the shape gradient, where the stem region is segmented as a single region. Using the two other spectral gradients, ROI 1 is segmented into smaller different parts. Shape gradient also provides better separation between ROIs 3 and 4, compared to intensity and total gradients. But this is as expected since spectral variations within these regions are dominated by shape differences, see Fig. 7.29. On the other hand, intensity gradient captures more information from ROI 2. Consequently, it better segments this ROI. The contours of segmented pollen regions are more similar to those in the original image. Then, when total gradient is employed to segment image NP1, the result cannot be considered as superior from the two previous results. This is despite total gradient being the total sum of shape and intensity differences. It can be observed that separation between ROIs 3 and 4 are not as optimal compared to when shape gradient is used. Segmentation of ROI is also not as good compared to when intensity gradient is used. This, however, is as expected. Combining both shape and intensity differences through a sum operation may reduce the sensitivity of gradient compared to when used individually. Finally, these results have demonstrated that the choice of spectral gradient should consider the relevant spectral variations in an image. Then, decisions can be made according to a specific application goal. For example, if we are interested in segmenting the pollens in image PN1, then intensity gradient should be selected among others.

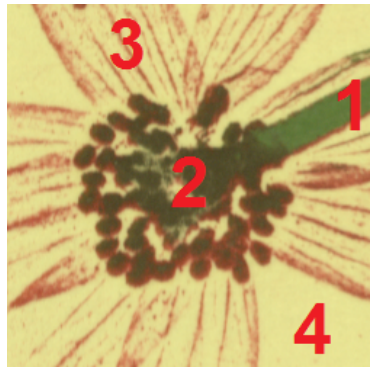

Figure 7.31 – Image NP1 and its relevant ROIs, i.e., (1) stem, (2) pollens, (3) petals, and (4) background parts. Shown image is produced using CLTR method.

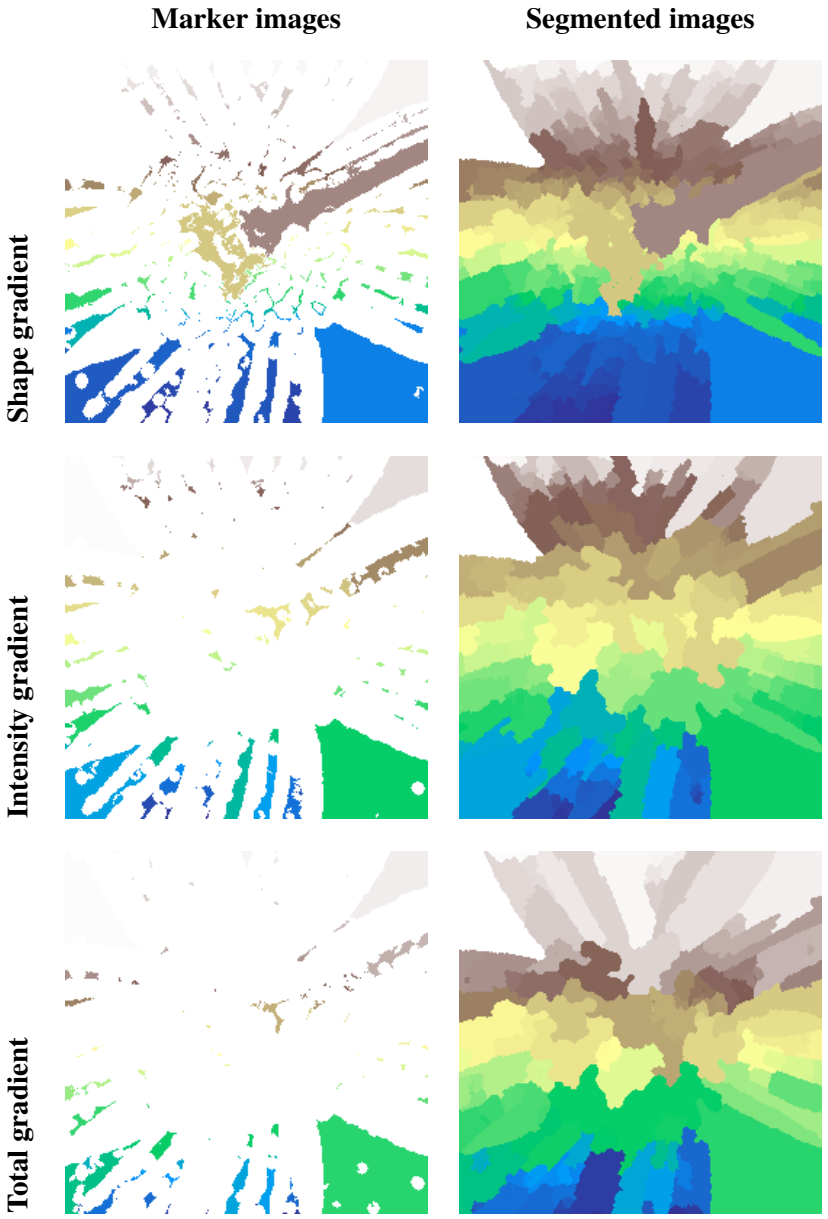

Figure 7.32 – Results of marker-controlled watershed segmentation (MCW) applied on image NP1, using three different spectral gradients, i.e., shape, intensity, and total. For each of them identical marker threshold is employed, i.e., $T = 1$. Parameters required by operations preceding MCW are provided in Table 7.1.

7.3.3.2 Observing the impact of marker threshold

Another parameter which impact the result of MCW segmentation is the marker threshold T. To observe its impact, MCW is applied to image FN1, whose ROIs are marked in Fig. 7.33a. According to Fig. 7.29, intensity differences is the prominent spectral variation in this image. Then, since the intensity and total gradient images are almost identical, total gradient using KLPD function is chosen to segment image FN1, see Fig. 7.33b. Three segmentation results obtained by varying the marker threshold $T = \{2, 4, 5\}$ can be observed in Fig. 7.34. Starting with marker threshold $T = 2$, the total gradient can already separate foreground objects in the image from the background. Several objects are also well-segmented, e.g., ROI 1. Increasing the threshold to 4, segmentation for ROIs 2 and 3 is improving. Especially for ROI 3, the two trees are now separated by background pixels. With marker threshold $T = 5$, two out of three windows from ROI 4 are recognized. Nevertheless, it can be observed that giving a low T may lead to oversegmentation. On the other hand, when T value is increased, it also increases the chance for regions to be merged. Then, at a certain T value, the algorithm will not be able to detect regions anymore and instead considering the entire image as a single object.

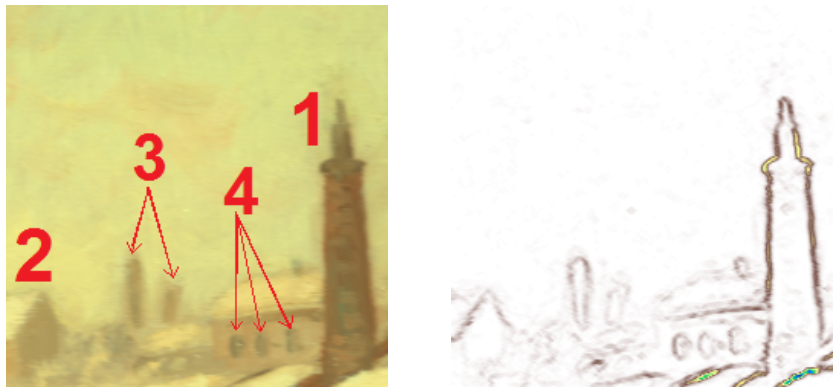

Figure 7.33 – The relevant ROIs and local gradient of image FN1. The ROIs correspond to (1) tower, (2) house, (3) two trees, and (4) three windows. The local gradient is obtained using total gradient.

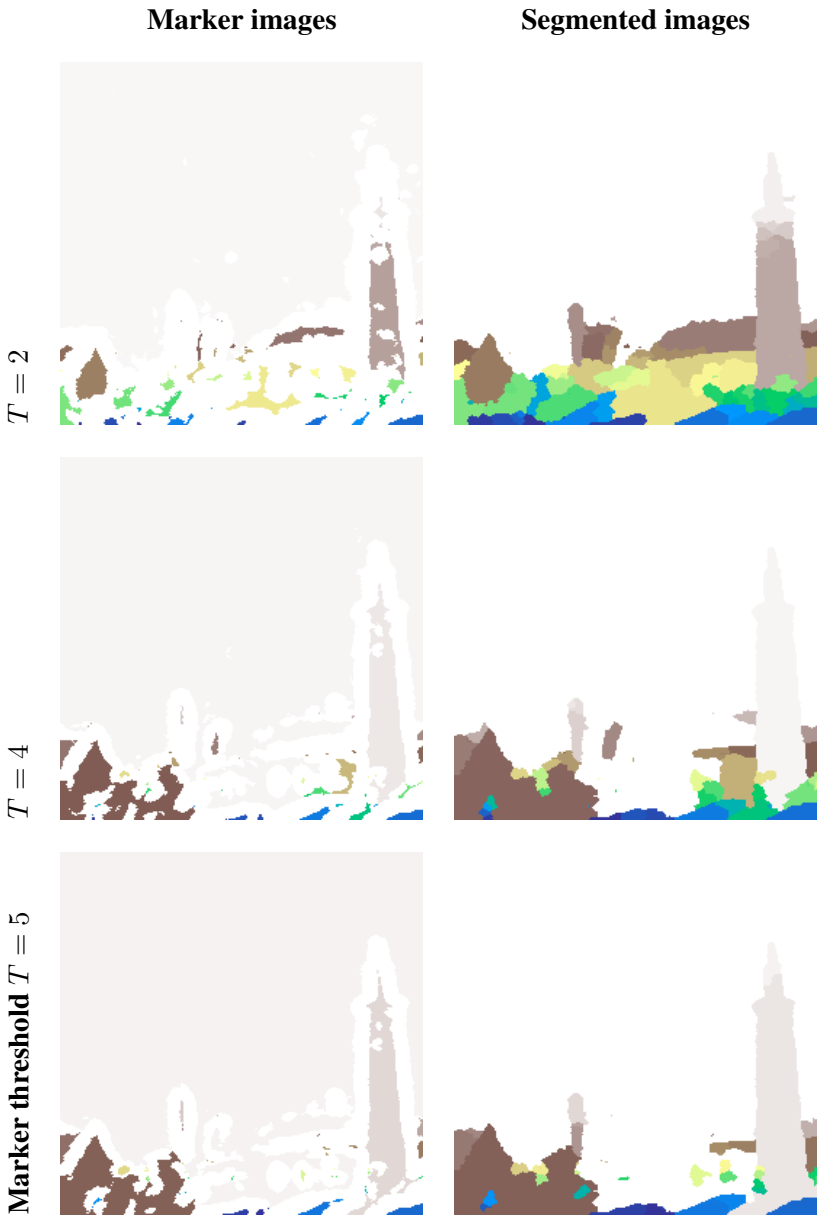

Figure 7.34 – Results of marker-controlled watershed (MCW) segmentation applied on image FN1, shown for 3 different marker thresholds. Parameters required by operations preceding MCW can be seen in Table 7.1.

7.3.4 Quality Assessment of Spectral Gradients in Watershed, A Preliminary Development

In the previous section, MCW has been employed to segment several real images, allowing to observe the impact of its parameters. However, those examples only demonstrate that MCW using the proposed spectral gradients can provide a sensible segmentation results. In order to obtain a segmentation algorithm which respect the constraints of metrology, a protocol for its quality assessment must be developed. Aiming to do so, in the following is a preliminary stage of the assessment protocol development.

In each pigment image coming from Pigment-56 dataset (Appendix B), there are 4 stripes of homogeneous color shades. Therefore, by using these images as the segmentation target, the number of expected segments N_O are known. In turn, use of the said images will allow assessing the stability of spectral gradients within the context of MCW segmentation, see Fig. 7.35. Small variations which exist within a homogeneous area may lead to detections of smaller regions by MCW. Therefore, to avoid counting all the obtained segments, in this evaluation only the major ones will be counted, see Eq. 7.6. The number of major segments N_L are obtained by counting the number of labels in the labeled image $L(x)$ which has certain minimum numbers of pixels belonging to it. And in the case of these pigment images it is chosen to be 10% of the total numbers of pixels in the image, i.e., $c \cdot n_I = 0.1 \cdot n_I$.

$$N_L = \#\{y_i \colon \#\{L(x) = y_i\} \geq (c \cdot n_I),\ \forall y \in \mathbb{Z}\} \tag{7.6}$$

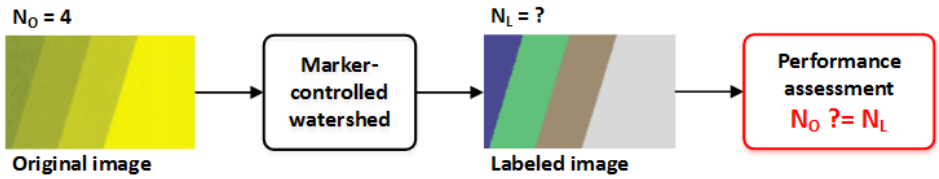

Figure 7.35 – Preliminary assessment protocol of the stability of spectral gradients in watershed segmentation.

As a first experiment, 5 pigment images from the dataset are employed as target where total gradient is employed to compute the local gradient and marker images. Parameters of the erosion and dilation operations which precede MCW can be found in Table 7.1. Results of three of the pigment images are shown in Fig. 7.36, where marker threshold $T = 2$ is employed. As observed in the local

gradient images, there are variations within each homogeneous regions of a pigment image. The presence of these small variations is more evident in the brown and blue pigment images. Nevertheless, by arbitrarily choosing $T = 2$, all of the shown pigment images are correctly segmented into 4 regions.

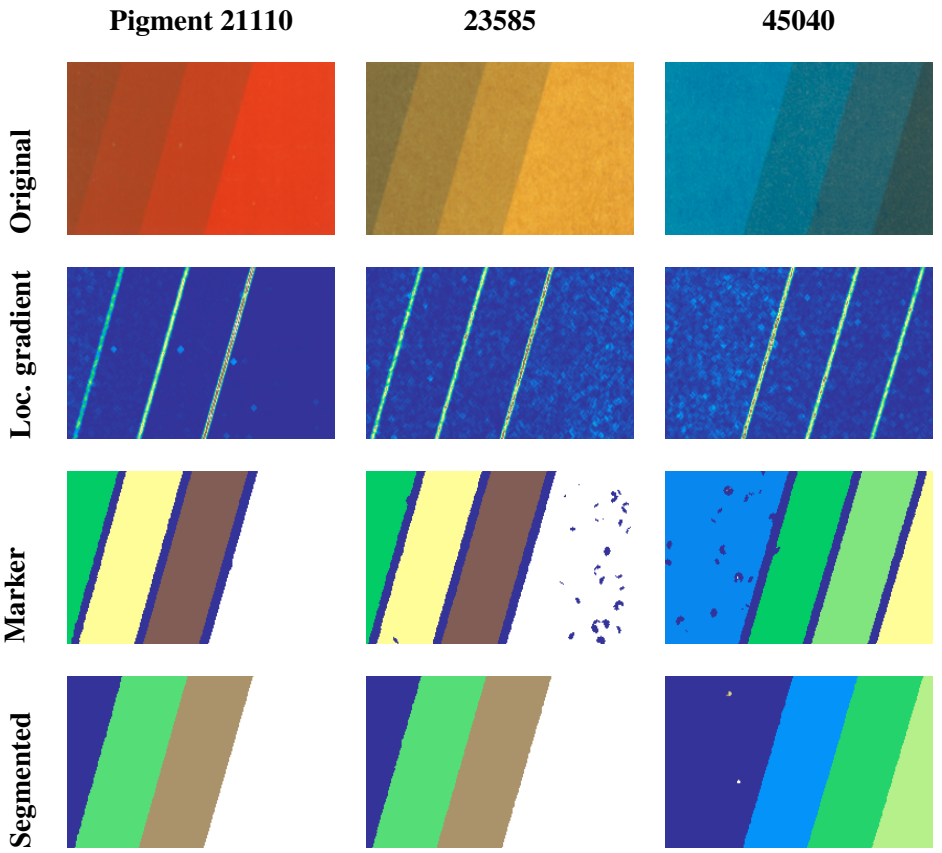

Figure 7.36 – MCW results of 3 pigment images, with marker threshold $T = 2$ and total gradient to compute the local gradient and marker images. Parameters of erosion and dilation preceding MCW can be found in Table 7.1.

The performance of total gradient in MCW with varying marker thresholds T are provided in Table 7.2. Marker threshold $T = 2$ is found to be the optimal threshold for all 5 pigment images. Then, as T is increased, the number of major segments decreases until MCW is finally unable to differentiate homogeneous regions in all pigment images at $T = 12$. From this table, it also becomes evident that the threshold must be adapted for individual images. To investigate how T impacts the watershed results, line profiles of marker images of pigment 21110 and 44450 are

plotted in Fig. 7.37. From each line profile three significant peaks can be observed, which correspond to edges between the homogeneous regions. For pigment 21110, whose N_L declines the fastest in Table 7.2, it can be observed that the difference between regions on the left and right of gradient 1 in Fig. 7.37a is not significant. In fact, the magnitude of gradient 1 which is just above 4 also corresponds to 8.06 CIELAB color difference. Color differences for gradient 2 and 3 are 10.60 and 15.19, respectively. This is why when $T = 4$, the two regions merge resulting in $N_L = 3$. As for pigment 44450, differences between two adjacent homogeneous regions are almost equally significant, see Fig. 7.37b. Its gradients from 1 to 3 correspond to color differences of 16.27, 14.92, and 14.67. Due to this, it is only when $T = 8$ that the N_L of pigment 44450 starts to decline.

To summarize, in this section we have addressed one of the most complex question in image processing, i.e., segmentation. Our purpose was to assess the quality of our spectral gradients within this context using the watershed approach. First, we have shown that without pre- and post-processing steps, the results were highly encouraging. Then, we have shown that the segmentation parameter choice, i.e., marker threshold, is directly related to the gradient magnitude. Finally, just as in the previous sections and chapters, the results we obtain also depend on the reference selection. But, in this case, selecting a more suitable spectral reference will be a chance to improve the final segmentation results.

Table 7.2 – The number of major segments N_L in 5 pigment images as obtained by MCW of varying marker thresholds T. Expected number of segments is $N_O = 4$, correct segmentation results are marked in green. Total gradient images were employed to obtain the watershed results.

Pigment image	**Marker threshold (T)**					
	2	**4**	**6**	**8**	**10**	**12**
21110	4	3	3	2	2	1
23585	4	4	4	2	1	1
23610	4	4	4	3	2	1
44450	4	4	4	4	2	1
45040	4	4	4	2	1	1

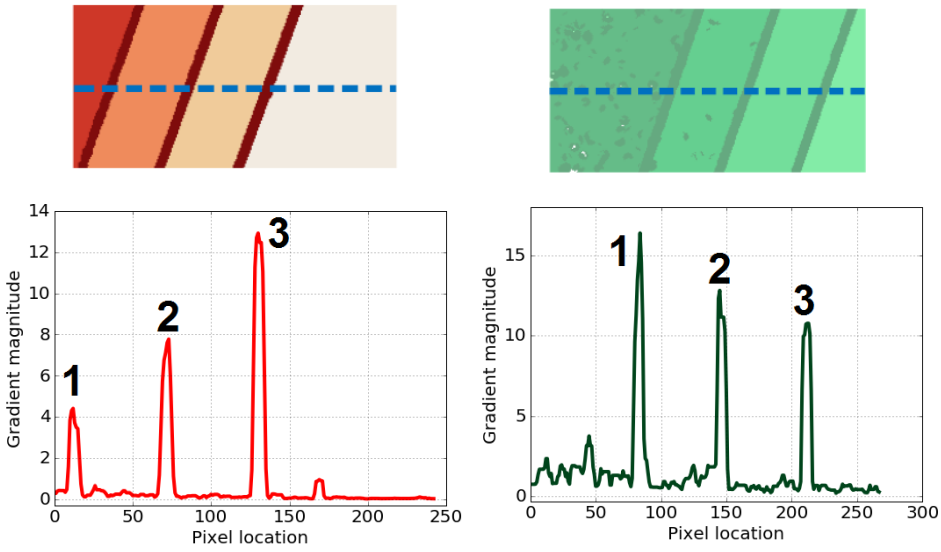

(a) Pigment 21110

(b) Pigment 44450

Figure 7.37 – **(Top)** Marker images and **(bottom)** their corresponding line profiles obtained from locations under the dashed blue lines. Parameters used to obtain the marker images can be seen in Table 7.1. Three peaks are obtained, each corresponding to the edge between two adjacent homogeneous regions in the image.

7.4 Towards Spectral Morphological Filters

Morphological filters are useful for noise filtering and selective removal of image objects [159]. They can be obtained by combining elementary morphological filters, i.e., openings and closings. First results of spectral morphological opening and closing are provided in the following. Then, an advanced morphological transform will also be extended to the spectral domain.

7.4.1 Opening and Closing

7.4.1.1 Definition and extension to the spectral domain

Morphological opening is defined by applying erosion followed by dilation operations to an image, see Eq. 7.7. In the grayscale domain, opening impacts an image in the way it smooths object contours, breaks narrow straits, and removes thin protrusions. Morphological closing, which is defined by dilation followed by erosion (Eq. 7.8), also tends to smooth object contours. However, as opposed to opening, it will also fill gaps, merge narrow breaks and long thin gulfs, and remove small holes. The impact of opening and closing to a grayscale image is demonstrated

in Fig. 7.38. More detailed explanation and illustration of grayscale opening and closing can be found in [79, 159].

$$\gamma_B(I) = \delta_B(\epsilon_B(I)) \tag{7.7}$$
$$\phi_B(I) = \epsilon_B(\delta_B(I)) \tag{7.8}$$

Since opening and closing are defined by consecutive erosion-dilation and dilation-erosion, respectively, their extensions to the spectral domain only require spectral erosion and dilation. And in Section 7.2.2, the two have been obtained by means of defining a spectral ordering relation, i.e., CRA ordering relation.

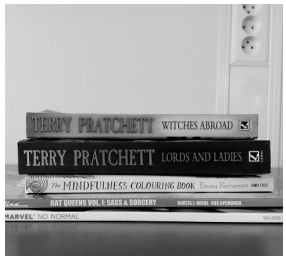

(a) Original image

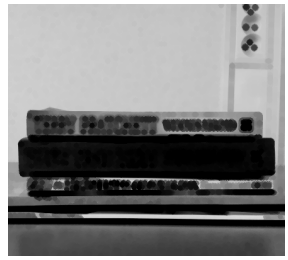

(b) Eroded image

(c) Dilated image

(d) Opened image

(e) Closed image

Figure 7.38 – The impact of grayscale morphological opening and closing to an input image, with a disk SE of radius 4 pixels. Opening removes the bright letters. It also expands and merges regions of the dark letters. Closing operation has the opposite impact of opening. In addition, 6 black dots originally located at the top right of the original image are eliminated.

7.4.1.2 On the idempotency of CRA ordering relation

Morphological opening and closing are required to satisfy the idempotency property, see Eq. 7.9. If it is satisfied, further application of the same operation will not further modify the image target. Idempotency is a necessary property allowing to enable the whole class of morphological filters.

$$\gamma(I) = \gamma(\gamma(I)),\ \phi(I) = \phi(\phi(I)) \tag{7.9}$$

Idempotency can be reached if the behavior of erosion and dilation are as illustrated in Fig. 7.39, i.e., the local extrema are always switched between two values. In other words, the local minimum and maximum obtained by ordering functions employed for dilation and erosion are identical. In the grayscale domain, idempotency property is automatically obtained because the scalar values are naturally ordered. The minima obtained by ordering relation $\leq$ and $\geq$ are always identical, and so are the maxima they obtain.

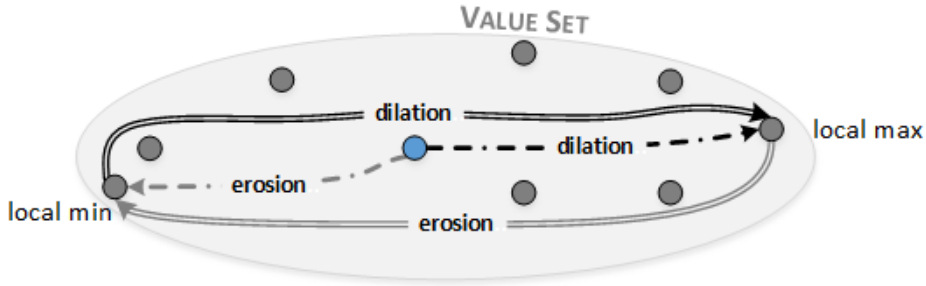

Figure 7.39 – Illustration of the behavior of idempotent opening and closing in the value set of a local neighborhood. If the blue dot represents value at the origin of an SE, erosion and dilation will replace this value with the local minimum and maximum, respectively. Thus, in an opening, the blue dot will first get replaced by the local minimum and then local maximum, and vice versa for closing operation. If an opening is applied one more time, the current value at the origin will not change and remain to be the local maximum.

In the multivariate domain, idempotency property must be enabled. The ordering relation of Convergent Color Mathematical Morphology (CCMM) [106] which can be directly extended to the spectral domain, see Eq. 7.10, is not idempotent. The ordering functions it uses to obtain minimum and maximum are not related because they employ different reference points. Consequently, the case illustrated in Fig. 7.40 will occur, i.e., different local extrema are obtained by g^{-}_{CCMM} and g^{+}_{CCMM}.

$$g^{-}_{CCMM}(S) = d(S, S^{-\infty}),\ g^{+}_{CCMM}(S) = d(S, S^{+\infty}) \tag{7.10}$$

On the other hand, given a local value set, CRA ordering relation computes minimum and maximum values relative to both of the reference points, see Eq. 7.11. The relationship between g_R^- and g_R^+ ensures that the local extrema obtained by both functions are identical.

$$g_R^-(S) = \frac{1}{g_R^+(S)},\ g_R^+(S) = \frac{d(S, S^{-\infty})}{d(S, S^{+\infty})} \tag{7.11}$$

As a numerical demonstration, we have tested whether the results of applying opening once and twice to images from the Subsets-250 dataset (Appendix B) give identical results. The same test is also carried out in the case of closing operation and the results are provided in Table 7.3.

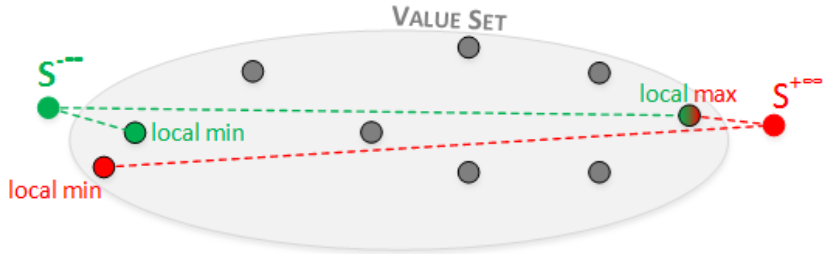

Figure 7.40 – Illustration of the impact of spectral ordering relation which is directly extended from the CCMM construction in [106]. Since the functions which are employed to obtain minimum and maximum use different reference points, the idempotency property is not satisfied. Local minima obtained by $S^{-\infty}$ and $S^{+\infty}$ are not identical.

Table 7.3 – Idempotency test applied to images from Subsets-250 dataset (Appendix B) using a 2 pixel radius disk SE. In all cases, idempotency property are reached, i.e., resulting images obtained after applying an opening once and twice are identical. Identical resulting images are also obtained in the case of closing.

Image	Idempotency	Image	Idempotency
FN1	✓	PN1	✓
FN2	✓	PN2	✓
NP1	✓	SC1	✓
NP2	✓	SC2	✓

7.4.2 First Results of Spectral Opening and Closing

Image NP1 from Subsets-250 dataset, see Appendix B, is employed as target for CRA-based openings and closings. The relevant ROIs which will be our observation focus can be seen in Fig. 7.41. ROI 1 corresponds to purple structures which

make up the petals of the flower. ROI 2 corresponds to the dark circles in the center of the image, which will also be referred to as the pollens.

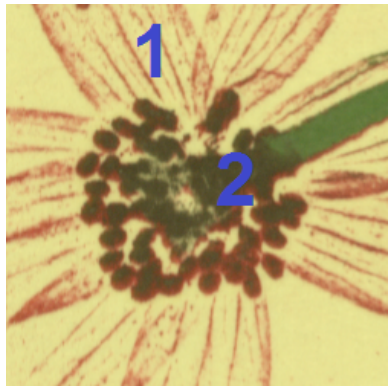

Figure 7.41 – Image NP1 as target for CRA-based opening and closing. Relevant ROIs, i.e., flower petals and pollens, are respectively numbered 1 and 2. Shown image and its latter processing results are visualized using CMF method.

Resulting images of applying CRA-based openings and closings of increasing disk SE size can be observed in Fig. 7.42. These results are obtained using S_{Bk} and S_{Wh} as references, and KLPD function as the embedded spectral difference measure. As observed, with the increasing radius of SE, opening gradually fills bright gaps within the dark circles in ROI 2. Fine structures of the flower petals in ROI 1 are also gradually connected as the SE radius grows. For closing, the opposite effects are obtained. Dark colored structures whose sizes are smaller than the employed SE are gradually removed, e.g., flower petals corresponding to ROI 1. As for structures found in ROI 2, they are retained but their colors are getting lighter as brighter spectral functions are replacing darker ones.

With the reference pair previously used in erosion and dilation, see Fig. 7.21a, opening and closing are applied to the same target image. Results obtained by varying the radius of disk SE can be observed in Fig. 7.43. Due to the use of a simulated red (SR) spectral function as the minimum convergence coordinate, erosion will favor reddish spectral functions than other colors despite their intensity differences. As a consequence, it can be observed in the figure that reddish spectral functions originating from ROI 1 start to dominate the image as SE radius increases. Due to the use of a simulated green spectral function (SG), any greenish structures in the image will remain. On the other hand, other colors will be replaced with spectral functions which are more similar to SG.

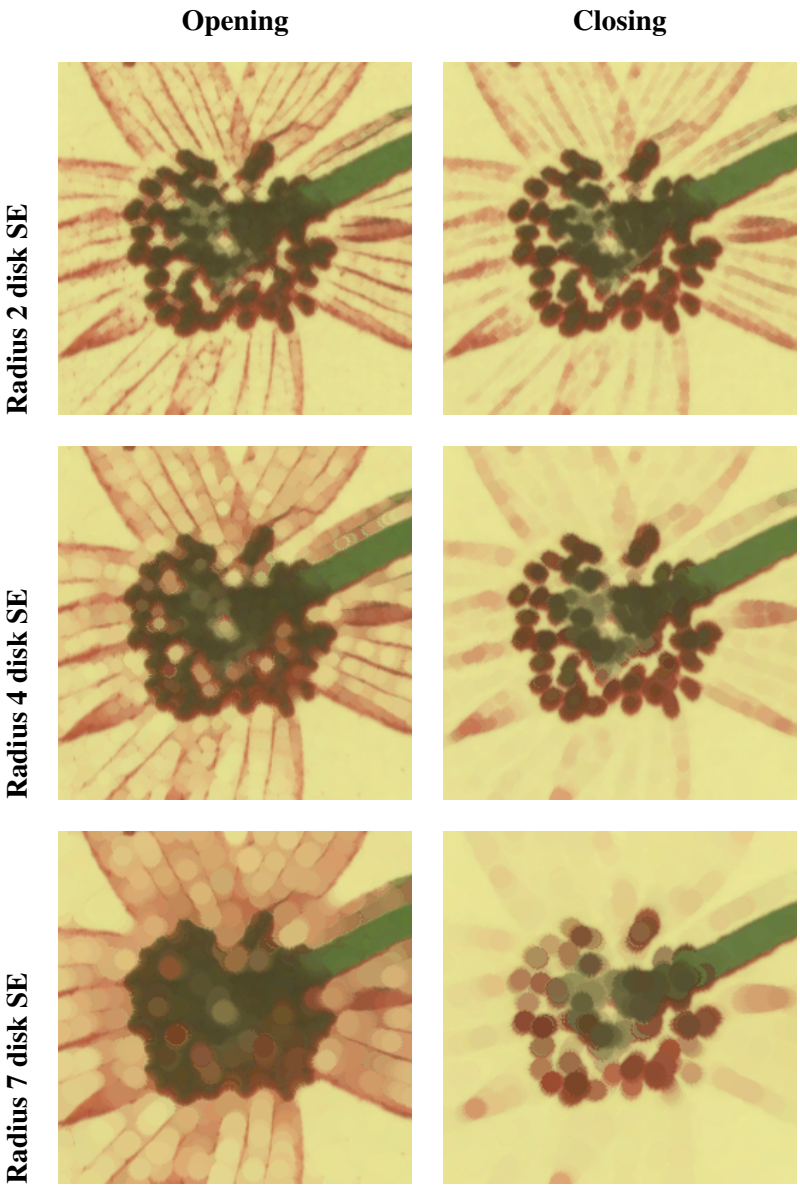

Figure 7.42 – The impact of CRA-based openings and closings of increasing disk SE radius to image shown in Fig. 7.41. S_{Bk} and S_{Wh} are employed as references and KLPD as spectral difference function. Opening is expected to connect and fill the gaps in ROIs 1 and 2 whose size is smaller than the SE. Closing is seen as gradually removing objects which correspond to ROI 1. For objects in ROI 2, their sizes are larger than the employed SEs. Consequently, most of them are retained but with lighter colors.

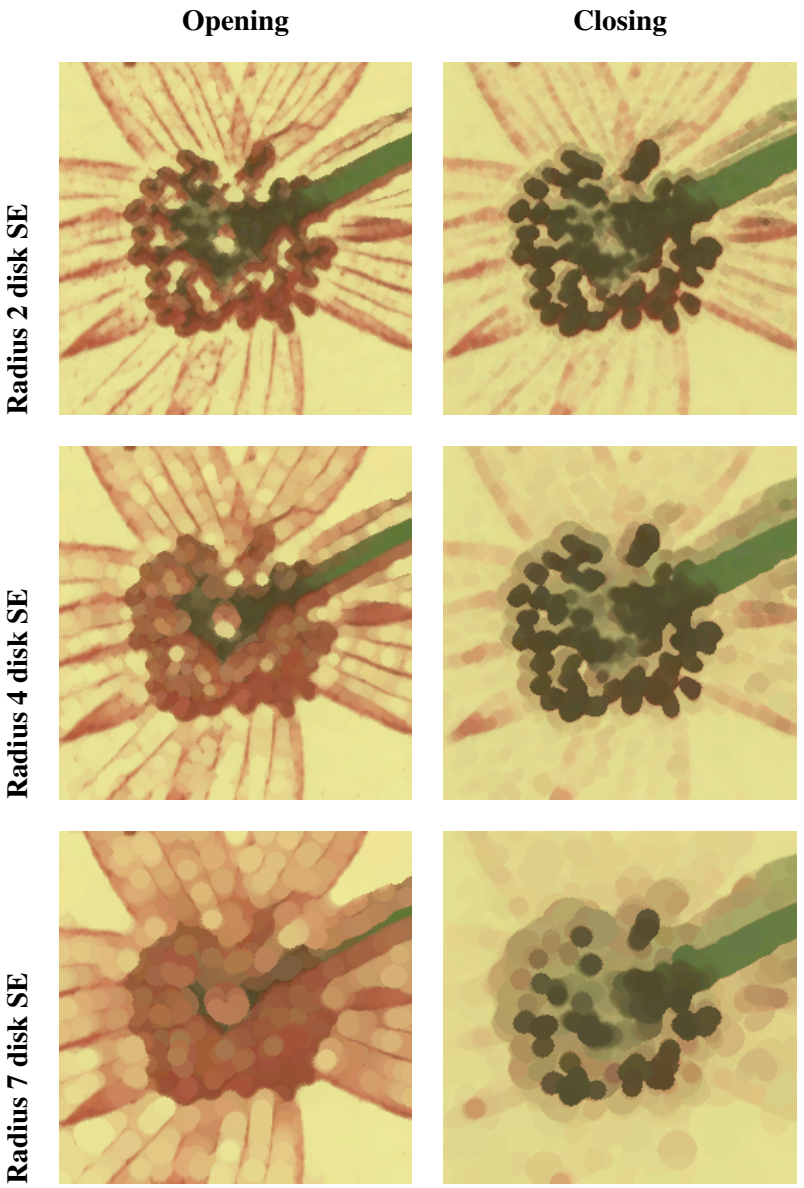

Figure 7.43 – The impact of CRA-based openings and closings of increasing disk SE radius to image NP1. Simulated red (SR) and green (SG) from Fig. 7.21a are employed as references for KLPD function. Since SR is employed as the minimum convergence, opening the image with an increasing radius causes the reddish spectral functions originating from ROI 1 to dominate the image. With SG as the maximum convergence, existing green spectral functions remain in the image, while other colors get replaced depending on their differences to SG.

7.4.3 Top-Hat Transformations

7.4.3.1 Definition

Top-hat transformations consist of two operations, i.e., black and white top-hats[1]. The black top-hat is defined by subtracting the result of closing an image by its original image, see Eq. 7.12. As for the white top-hat, it subtracts the original image by its opening result, see Eq. 7.13.

$$BTH(I) = \phi(I) - I \tag{7.12}$$

$$WTH(I) = I - \gamma(I) \tag{7.13}$$

In opening and closing, objects whose shape do not match the SE shape and size will be removed. The interest of top-hat is in recovering the removed objects. White top-hat will recover objects with bright contrasts, i.e., bright objects on a dark background. As for black top-hat, it recovers objects with dark contrasts, i.e., dark objects on a bright background. Fig. 7.44 is given to demonstrate the impact of both top-hat transforms on the grayscale image previously shown in Fig. 7.38a. Black top-hat extracts dark letters whose surrounding are of higher intensities, e.g., 'COLORING BOOK' and 'WITCHES ABROAD'. In addition, it also obtains the periphery of letters having higher intensities, e.g., 'LORDS AND LADIES'. On the other hand, letters having bright contrasts are recovered by white top-hat, e.g., 'SASS & SORCERY'. Then, the transform also recovers the periphery of letters having lower intensity values, e.g., 'MINDFULNESS'.

7.4.3.2 Extension to the spectral domain

As seen from Eq. 7.12 and 7.13, top-hat transforms require opening, closing, and subtraction operation. From Section 7.4.1, spectral opening and closing have been obtained. In order to adapt the scalar subtraction to the spectral domain, the image difference will be carried out by means of spectral difference measures, i.e., KLPD function. Then, the notions of 'black' and 'white' top-hat transforms were originally given for their uses in retaining dark/ bright objects on bright/ dark backgrounds, respectively. In the spectral domain, referring to them with the notion of 'black' and 'white' has a very limited sense. This is because the grayscale black and white top-hat transforms are analogous to CRA-based top-hat transforms when S_{Bk} and S_{Wh} are employed as references. And as we know, in CRA ordering relation, the reference pair can be chosen arbitrarily. Thus, the black and white top-hat transforms are now denoted by TH^- and TH^+, respectively. The spectral top-hat TH^- and TH^+ will retain objects whose spectral functions converge toward the

[1] In other works, e.g., in [79], top-hat transform is used to specifically refer to white top-hat transform. In this case, black top-hat transform will be referred to as bottom-hat transform.

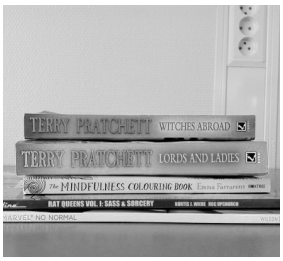

(a) Original image

(b) Opened image

(c) Closed image

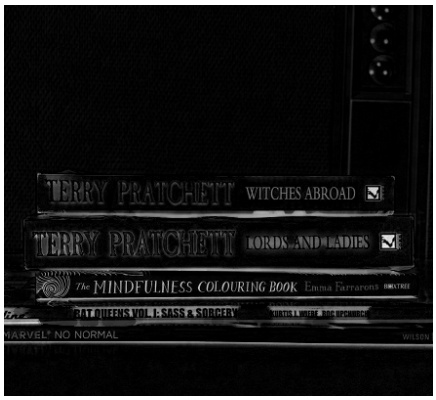

(d) Black top-hat image

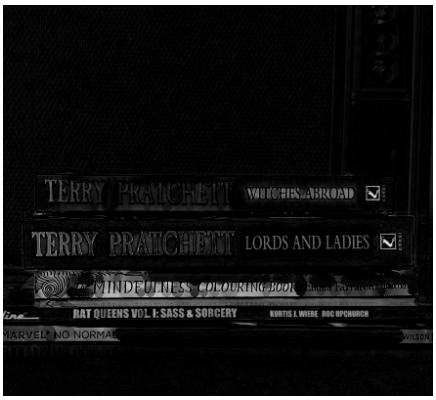

(e) White top-hat image

Figure 7.44 – The impact of applying top-hat transforms to a grayscale image, with a 4 pixels radius disk SE. Black top-hat obtains dark letters and peripheries of the bright ones. White top-hat extracts bright letters and peripheries of the dark ones.

minimum and maximum convergence coordinates, respectively. Their final mathematical expressions are provided in Eq. 7.14 and 7.15.

$$TH^{-} = d_{KLPD}(\phi(I), I) \tag{7.14}$$

$$TH^{+} = d_{KLPD}(I, \gamma(I)) \tag{7.15}$$

The impact of applying the two top-hat transforms using a 2 pixel radius disk SE to images NP1 and NP2 from Subsets-250 dataset (Appendix B) can be observed in Fig. 7.45. And as observed they detect different edge structures from the original images. More complete application of the spectral top-hat transforms will be given in Chapter 8. In the chapter, focus will be given to the application task rather than the morphological tool itself.

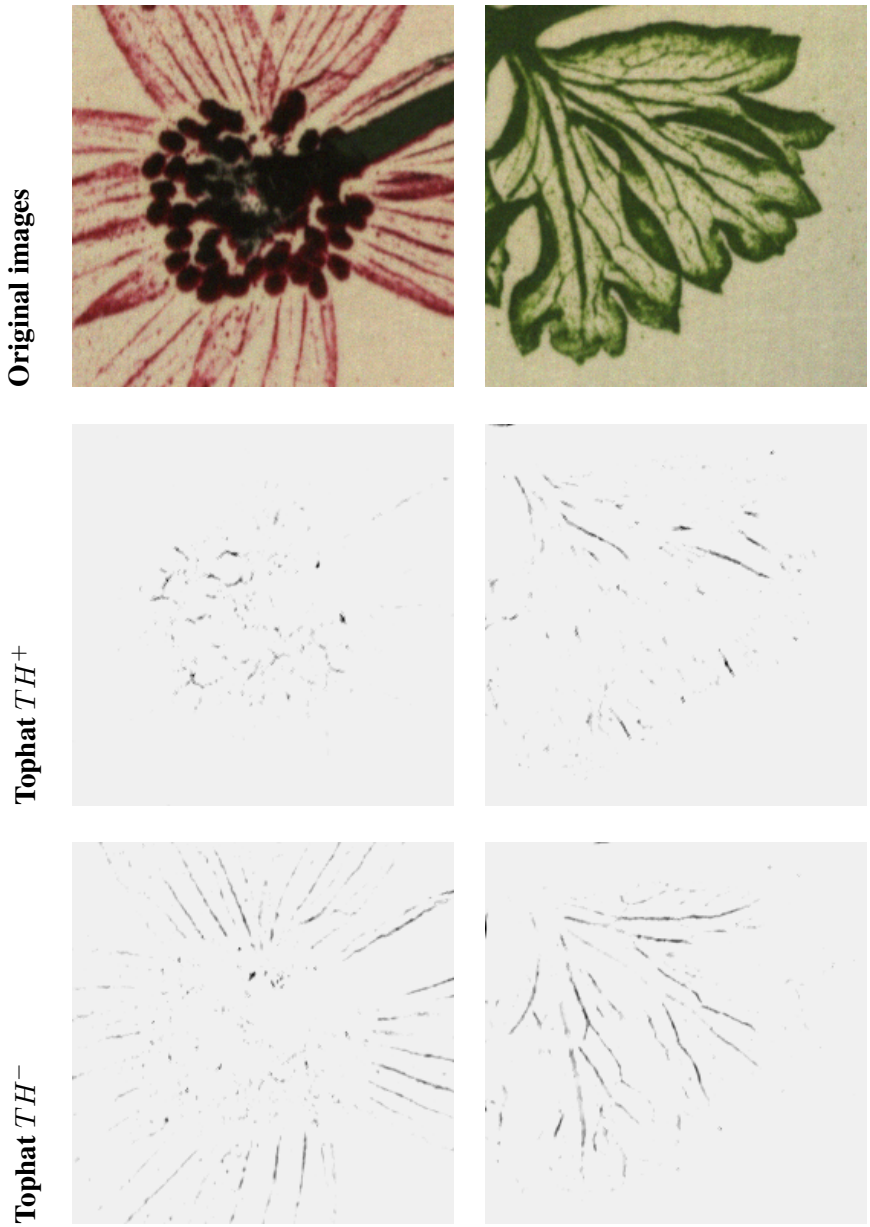

Figure 7.45 – The impact of applying CRA-based top-hat transforms of 2 pixel radius disk SE to images NP1 and NP2 from Subsets-250 dataset. KLPD function embedded in CRA employs S_{Bk} and S_{Wh} as references. The two top-hat transforms detect different edge structures from the original images.

7.5 Conclusion

Based on the spectral difference function and spectral ordering relation obtained in Chapter 3 and 4, the extension of elementary morphological operators and tools to the spectral domain have been provided in this chapter. These operators and tools are erosion, dilation, gradient, opening, closing, and top-hat transforms. In addition to the extension using KLPD function and CRA ordering relation, various protocols for the quality assessment of these morphological tools have also been developed.

But more than merely extending the operators to the spectral domain, in this chapter we have proven the interest of our full-band spectral approach. In particular, we have extensively used the bidimensional histogram of spectral differences (BHSD) previously introduced in Chapter 5 to analyze the distribution of spectral variations within an image; a modified BHSD has also been introduced. And through this BHSD we have been able to assess the performances of our morphological tools. Then, given a specific application goal, we have also demonstrated the selection of spectral references and their impacts in the case of erosion, dilation, opening, and closing.

One of the novelties which can be found in this chapter is the construction of new spectral morphological gradients using spectral Kullback-Leibler pseudo-divergence (KLPD) function, i.e., shape, intensity, and total gradients. Then, to show the interest and usefulness of these new gradients, we have used them for spectral image segmentation using morphological watershed approach. Along the way, we have also provided the elements useful for choosing the proper spectral gradient given a certain spectral variation in an image. Even though we have not fully developed a metrological assessment protocol for the tools, we have shown that without any pre- or post-processing steps we were able to obtain highly encouraging results.

Summary of Contributions.

- ✓ Extension of elementary morphological operators and tools to the spectral domain, i.e., erosion, dilation, gradient, opening, closing, and top-hat transforms.
- ✓ Proof of interest of full-band processing which respects metrological constraints. In particular, the use of bidimensional histogram of spectral differences (BHSD) to explore the spectral distribution of an image.
- ✓ Proof of validity of metrological processing, that it does not produce false colors even when given a real image coming from spectral acquisitions.
- ✓ Protocol of how to select spectral reference when given a specific application goal.
- ✓ Definition of new spectral morphological gradients using spectral Kullback-Leibler pseudo-divergence (KLPD) and conditional ratio and angular distance ordering relation (CRA) which have been previously validated under metrological constraints.
- ✓ Proposal of a gradient based segmentation using morphological watershed algorithm

Chapter 8

Crack Detection for Cultural Heritage Paintings

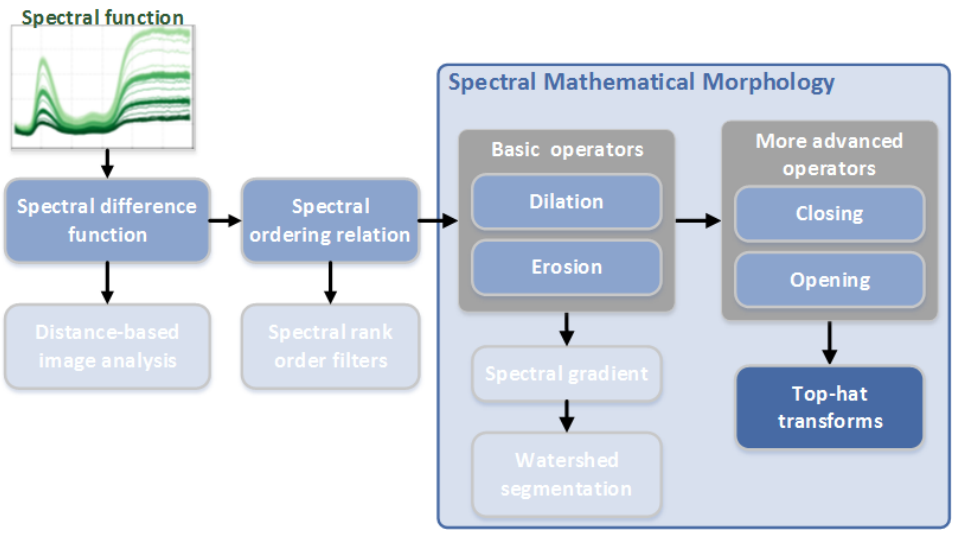

8.1 Introduction

Due to its age, cultural heritage paintings suffer from cracks, i.e., the breaking of the paint or pigment, varnish, or substrate layers of the painting. As a painting ages, the canvas or wood support could suffer non-uniform contraction which in turn stresses the paint layers. In addition to age-induced cracks, other factors that could potentially inflict such damage are drying and mechanical factors. Drying cracks are caused by evaporation of volatile paint components, causing shrinkage

of the paint layer. Cracks could also occur due to vibrations and impacts, e.g., during its transportation [78].

Different opinions exist regarding whether cracks, or also known as craquelure, are undesirable patterns. If they do, then the painting should be restored by filling out the cracks with new paint layers. The other side of the argument, however, says that cracks are part of the painting and are actually considered as adding the age value. One study stated that cracks deteriorate the perceived image quality of a painting [78]. But an even earlier study suggested that human subconsciously filters the cracks, since they are seen as irrelevant with what the artist had intended to depict in his painting [33]. Note that this study was carried out only to cracks that formed slowly by brittle failure of dry paint.

Despite the ongoing discussion and study of the aesthetic value of cracks, there are other motivations supporting the necessity and importance of crack detection. Virtual restoration of cracks can be carried out without altering the original painting, and it can be made possible after a crack detection procedure. A virtually restored painting will, in turn, provide clues to historians, curators, and general public of its initial state, before all the inflicted damages [78]. Cracks can also be considered as the signature of a painting, since no two paintings have identical cracks. Serving its purpose as a signature, it can be employed as, e.g., a mean to judge authenticity in case of forgery. It is also useful for preservation purposes. Given an initial state of the cracks, its current state could provide an indication of certain type of degradation a painting is going through. This knowledge would aid conservators in their decisions. Yet another potential of cracks is as an identification tool for the origin of a painting. Paintings were classified into four categories, i.e., Italian, Flemish, Dutch, and French, based on its photographed crack patterns [34]. This study has shown that each of the categories has its typical crack patterns.

Crack detection task for cultural heritage paintings could be related to similar studies in other fields. For example, crack detection has gained a lot of interest in studies of concrete structures, mainly for its use in automatic structural health monitoring of concrete surfaces [46, 134, 191]. Not only that, its advantages is also perceived in, e.g., egg processing industry [70], steelmaking [102], and glass production [186]. One similar topic is the detection and removal of line scratches and other artifacts from motion picture films [87]. This last topic is, however, not directly applicable to the crack detection of paintings since it relies on information obtained over several adjacent frames.

Spectral imaging has been employed in the acquisitions of cultural heritage paintings since the 1990s [39, 118, 144]. The high cost and complexity of such acquisition are justified due to the significance and importance of these cultural heritage

objects to the society. Unfortunately, the improvement of accuracy in the acquisition stage has not been met with similar level of accuracy in the processing stage. The state of the art of crack detection methods for cultural heritage paintings, as well as from other related fields, is summarized in Table 8.1. And as observed, even though in several cases the inputs are multivariate images, these crack detection methods remain in the scalar domain where grayscale images are used as input to the methods, or by marginal approach.

Table 8.1 – Summary of the state of the art of crack detection algorithms employed in various fields.

Method	**Input image**	**Detailed approach**
Grayscale top-hat transforms, generally followed by thresholding	Grayscale	[64, 70, 191]
	Color	Applied on luminance channel [73,78,162], on one color channel of RGB image providing the highest contrast between cracks and non-cracks [150]
	Multispectral	Applied on each spectral channel, resulting crack maps are superimposed [48]
Crack tracking	Color	Applied on one color channel, traces crack in 8-neighborhood pixels based on an adaptive threshold [24]
Gabor filters	X-radiographs	Multi-oriented, applied on grayscale x-ray images [2]
Sobel edge detector	Grayscale	Followed by morphological processes [46]

Focusing on addressing the task of crack detection for paintings rather than the image processing tools as in the previous chapters, this chapter is organized as follows. Using several multivariate ordering relations, crack detection algorithm is extended to the hyperspectral domain in Section 8.2. Then, protocol for the quality assessment of crack detection methods is developed in Section 8.3. Section 8.4 follows by assessing the quality of previously obtained spectral crack detection methods using the developed protocol. In this section, in addition to selecting the most suitable crack detection approach, optimum parameters for the said approach is also obtained. Having the method and parameters set, application to real data coming from cracking layers of a painting is carried out in Section 8.5. Before to conclude the chapter in Section 8.7, a discussion is provided regarding the computational complexity of the full-band crack detection algorithm in Section 8.6.

8.2 Hyperspectral Crack Detection Approaches

8.2.1 Defining Cracks in Hyperspectral Images

In the context of hyperspectral imaging, image pixels are generally represented in terms of radiance or reflectance. The former representation corresponds to the amount of energy reflected by the object of interest that is captured by the sensor. Thus, in a radiance value, both information from surface and light source are mixed. Reflectance, on the other hand, is a surface property describing the ability to reflect incoming light in the direction of the hyperspectral sensor. In both cases of radiance and reflectance, the spectral values are considered to be continuous over the wavelength range of the sensor, i.e., between $\lambda_{\min}$ and $\lambda_{\max}$. Each pixel in a hyperspectral image associated with spatial coordinate x can therefore be expressed as in Eq. 8.1. Note that in the rest of this chapter, images will be considered in terms of spectral reflectance.

$$I(x) = S = \{s(\lambda),\ \forall\lambda \in [\lambda_{\min}, \lambda_{\max}],\ s(\lambda) \geq 0\} \tag{8.1}$$

In the grayscale or color domain, cracks are generally defined as having elongated structures with, generally, low luminance values [78]. In the hyperspectral domain, these definitions can be improved. When there is a crack in a paint layer, it means a break in the continuity of the spectral reflectance functions of the pigments. Spectral reflectance function of the crack itself could be of low intensity values close to an equi-energetic black S_{Bk} or of any layer beneath the cracking paint layer. In the latter case, a crack pixel might have the reflectance of a pigment or the substrate of the painting.

8.2.2 Hyperspectral Top-Hat Transforms

As summarized in Table 8.1, crack detection is a labeling process employing various image processing techniques, e.g., filtering, morphological tools, etc. The state of the art, however, is grayscale top-hat transforms. Following this direction, the image processing chain of crack detection algorithm is as depicted in Fig. 8.1. Depending on the contrast of the crack pixels, black or white grayscale top-hat transforms should be employed. Black top-hat transform (Eq. 8.2) will detect dark colored cracks surrounded by brighter background, and the converse for white top-hat transform (Eq. 8.3).

$$TH^{-\infty}(I) = \phi_B(I) - I \tag{8.2}$$

$$TH^{+\infty}(I) = I - \gamma_B(I) \tag{8.3}$$

However, the use of grayscale top-hat transforms demands for hyperspectral images, or any multivariate images for that matter, to be reduced to the grayscale

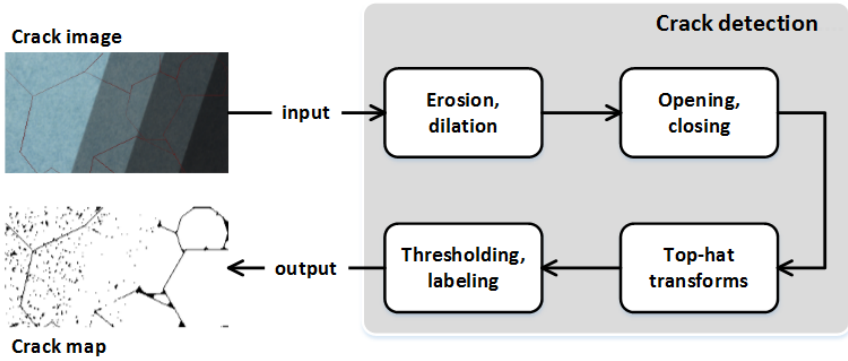

Figure 8.1 – Image processing chain for crack detection algorithm using morphological top-hat transforms.

domain. And in this manner, information and accuracy offered by hyperspectral images will be lost during the reduction process. Thus, it should rather be the top-hat transforms that are extended to the spectral domain.

Extending the grayscale morphological top-hat transforms to the spectral domain requires two things. First, there needs to be a suitable multivariate ordering relation for spectral data. Then, subtraction operation found in the expression of top-hat transforms must also be adapted, such that a grayscale crack map can be obtained. In the following are two possible approaches obtained by directly translating the concept behind the grayscale methods to the hyperspectral domain.

8.2.2.1 Energy-based approach

Grayscale images can be regarded as intensity images. Grayscale top-hat transforms have also been applied to luminance channel when the input are color images. Luminance images can also be regarded as intensity images. In this regard, a hyperspectral ordering relation can be developed based on total amount of energy at every pixel, see Eq. 8.4.

$$g_{esum}(S) = \int_{\lambda_{\min}}^{\lambda_{\max}} s(\lambda)\, d\lambda \tag{8.4}$$

Following the same concept, subtraction operation in top-hat transforms then become the difference of total energy as shown in Eq. 8.5 and 8.6.

$$TH^{-\infty}_{esum}(I) = g_{esum}(\phi_B(I)) - g_{esum}(I) \tag{8.5}$$

$$TH^{+\infty}_{esum}(I) = g_{esum}(I) - g_{esum}(\gamma_B(I)) \tag{8.6}$$

8.2.2.2 Marginal approach

Another strategy allowing to employ grayscale top-hat transforms for multivariate images is by applying them on each image channels separately. Given a spectral image with n channels, n top-hat images will be obtained, which will further be superimposed to create a single top-hat image. This approach can be directly translated to the hyperspectral domain through marginal ordering relation, which computes rank separately at each image channel. The superimposing of different resulting images is expressed through logical operator OR or arithmetic maximum. Mathematical expressions for marginal top-hat transforms are provided in Eq. 8.7 and 8.8.

$$TH^{-\infty}_{marg}(I) = \bigvee_{\lambda} TH^{-\infty}(I_\lambda) \tag{8.7}$$

$$TH^{+\infty}_{marg}(I) = \bigvee_{\lambda} TH^{+\infty}(I_\lambda) \tag{8.8}$$

8.2.3 Proposed Distance-Based Top-Hat Transforms

Based on the conclusion of Chapter 4, conditional ratio and angular distance ordering relation (CRA) is the most suitable ordering relation for spectral data. To recall, its mathematical expressions are provided in Eq. 8.9, where for minimum and maximum extractions Eq. 8.10 and 8.11 shall be employed, respectively.

$$\begin{gathered} g^-_R(S) = \frac{d(S, S^{+\infty})}{d(S, S^{-\infty})}, \quad g^+_R(S) = \frac{d(S, S^{-\infty})}{d(S, S^{+\infty})}, \\ g_A(S) = 2 \cdot \frac{d(S, S^{-\infty})}{d(S^{-\infty}, S^{+\infty})} \end{gathered} \tag{8.9}$$

$$S_1 \preceq_{CRA} S_2 \Leftrightarrow \begin{cases} g^-_R(S_1) > g^-_R(S_2) \text{ or} \\ g^-_R(S_1) = g^-_R(S_2) \text{ and } g_A(S_1) < g_A(S_2) \end{cases} \tag{8.10}$$

Interpretation. Spectral function S_1 precedes S_2 if and only if its ratio of distance according to g^-_R is larger than that of S_2. In case where they are identical, angular ratio of distance g_A of S_1 must be smaller than that of S_2.

$$S_1 \succeq_{CRA} S_2 \Leftrightarrow \begin{cases} g^+_R(S_1) > g^+_R(S_2) \text{ or} \\ g^+_R(S_1) = g^+_R(S_2) \text{ and } g_A(S_1) > g_A(S_2) \end{cases} \tag{8.11}$$

Interpretation. Spectral function S_1 succeeds S_2 if and only if its ratio of distance according to g^+_R is larger than that of S_2. In case where they are identical, angular ratio of distance g_A of S_1 must be greater than that of S_2.

Then, in order to adapt the subtraction operation in top-hat expressions, a distance function will be employed. CRA-based top-hat transforms can therefore be written as in Eq. 8.12 and 8.13.

$$TH^{-\infty}_{CRA}(I) = d(\phi_B(I), I) \tag{8.12}$$
$$TH^{+\infty}_{CRA}(I) = d(I, \gamma_B(I)) \tag{8.13}$$

Since CRA is based on distance function, there is a question of which distance function to use. In the following are four distance and divergence functions to be evaluated within this chapter. Their mathematical expressions can be found in Chapter 3 as well as in Appendix A.

Spectral angle is a similarity function initially developed in remote sensing field [97]. Spectral angle, further on will be referred to as **SAM**, is insensitive to magnitude differences. This induces a capability to suppress the effect of shading in remote sensing data, which is the reason for its popularity in the field.

Euclidean distance is a classical distance function in the Euclidean vector space. It is more sensitive to magnitude differences rather than shape differences.

Euclidean distance of cumulative spectrum (ECS) was originally developed to measure distance between two spectral functions coming from hyperspectral imaging setting where the spectral channels are contiguous, see Section 3.5.3. Unlike SAM and Euclidean distance which are only sensitive to shape and magnitude differences, respectively, ECS detects and incorporates both differences.

Spectral Kullback-Leibler pseudo-divergence (KLPD) was developed for hyperspectral data, considering a spectral function as a series [145]. Based on Kullback-Leibler divergence, KLPD function is composed of two components, i.e., measures of shape and intensity differences. In Chapter 3, KLPD has been concluded as the most suitable spectral difference function.

8.3 Quality Assessment Protocol of Crack Detection Methods

Protocol for the quality assessment of crack detection methods is as provided in Fig. 8.2. Ground truth and target images are obtained by tampering pigment images from Pigment-56 dataset (Appendix B) by artificial crack signals. In the following are details regarding the generation of artificial crack images and the final performance assessment.

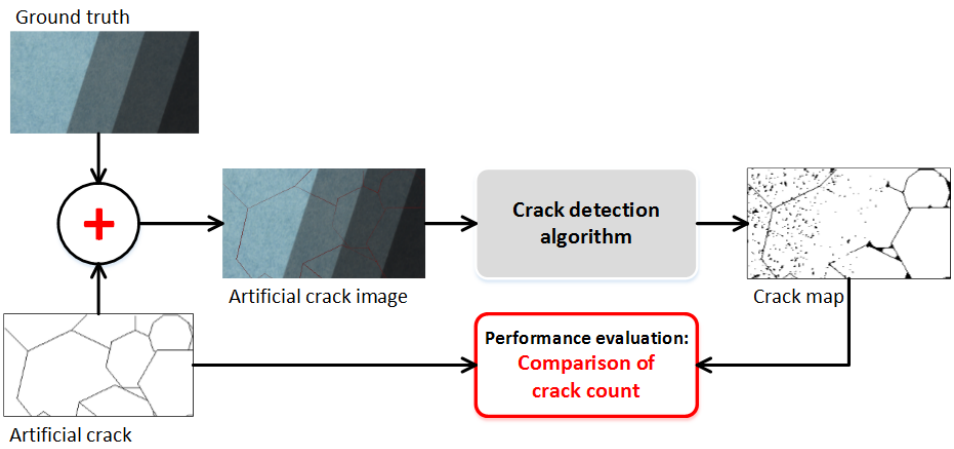

Figure 8.2 – Protocol for the quality assessment of crack detection methods using artificial crack images.

8.3.1 Artificial Crack Images for Accuracy Assessment

Employing 11 images from the Pigment-56 dataset in Appendix B and a crack model shown in Eq. 8.14, a dataset of artificially cracked pigment layer can be generated. Four of the employed pigment images can be observed in Fig. 8.3. Regarding the crack model, there are two parameters to vary, i.e., crack probability α and spectral function associated to the crack $\mathcal{C}$.

$$\tilde{I}(x) = (1 - \alpha) \cdot I_g(x) + \alpha \cdot \mathcal{C} \tag{8.14}$$

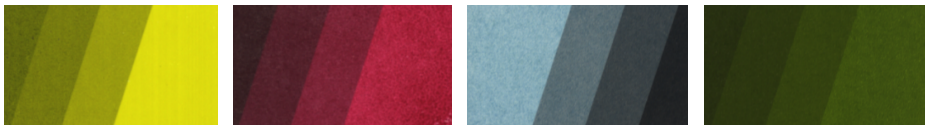

Figure 8.3 – Four instances of pigment images from Pigment-56 dataset used to generate artificial crack dataset. Shown color images are produced using FIXED visualization method.

8.3.1.1 Binary-Black (BB) dataset

To simulate thin cracks, which reflect almost no light, black crack spectral reflectance function is chosen, i.e., $\mathcal{C} = S_{Bk}$. Then, this dark crack is chosen to be identical for the entire image, hence $\alpha \in \{0, 1\}$. Examples of images in this dataset is shown in Fig. 8.4.

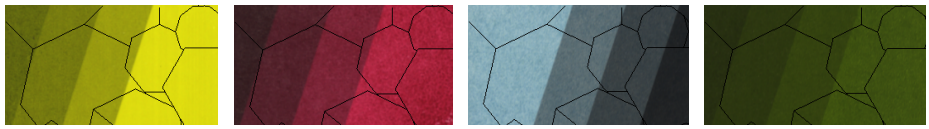

Figure 8.4 – Examples of pigment images in Binary-Black (BB) dataset, with 1 pixel wide crack. Shown color images are generated using FIXED method.

8.3.1.2 Probabilistic-Black (PB) dataset

Binary probability in BB crack dataset is far from realistic case. Therefore, using the same black reflectance function S_{Bk}, α is treated as a probability of having a crack pixel. α is a uniformly distributed random value between $[0, 1]$. With this α, spectral reflectance function of a crack pixel will be a linear mixture between the original reflectance and S_{Bk}. See example images in Fig. 8.5.

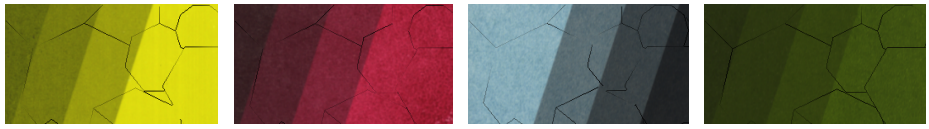

Figure 8.5 – Example of pigment images in Probabilistic-Black (PB) dataset, with 1 pixel wide crack. Shown color images are generated using FIXED method.

8.3.1.3 Probabilistic-Colored (PC) dataset

Considering that a crack does not always appear dark, this dataset serves to simulate cracks which shows layer beneath the cracking one. In reality, revealed layer could be of another paint layer or substrate of the painting. Still using crack probability $\alpha \in [0, 1]$, spectral reflectance functions to be associated with the cracks are chosen randomly from pixels in all pigment images in Pigment-56 dataset, i.e., $\mathcal{C} = \{S_k\}$. With colored crack signal, we are simulating revealed layer being another paint layer. See some of the generated images in Fig. 8.6.

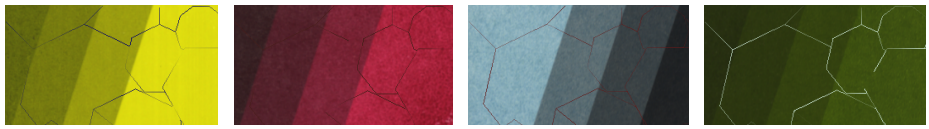

Figure 8.6 – Example of pigment patches in Probabilistic-Colored (PC) dataset, with 1 pixel wide crack. Shown color images are generated using FIXED method.

8.3.2 Evaluation Criteria

The final step of a crack detection method is a thresholding and labeling processes. In a black grayscale top-hat $TH^{-\infty}$, for example, a pixel is determined as crack if the difference between its initial value and after a closing operation is above a certain threshold T. The labeling itself can therefore be modeled as in Eq. 8.15, where $\bullet$ and $\star$ are logical AND and OR operations, respectively.

$$L = \big(I \bullet (TH^{-\infty}(I) \leq T)\big) \star \big(\mathcal{C} \bullet (TH^{-\infty}(I) > T)\big) \tag{8.15}$$

Generated datasets described in the previous subsection allow to have ground truth in the form of pixel count of the cracks n_C, see Eq. 8.16. With this ground truth information, performance of a top-hat transform will be evaluated based on the error of detected crack count E_C, see Eq. 8.17 where Δ is an absolute difference.

$$n_C = \#\{x,\ \Delta(I_g(x), \tilde{I}(x)) > 0\} \tag{8.16}$$

$$E_C = \Delta\Big(n_C,\ \#\{TH^{-\infty}(\tilde{I}) > T\}\Big) \tag{8.17}$$

The various ordering relations generate values in different dynamic ranges. Due to this, the threshold value T cannot be selected independently of the corresponding ordering relation embedded in the crack detection method in question. Hence, T will be adaptively selected for each ordering relation with the criteria of minimizing μE_C, i.e., average crack detection error for all image targets.

8.4 Quality Assessment and Parameter Selection

In the following top-hat transforms based on 6 hyperspectral ordering relations are to be evaluated, i.e., marginal, energy-based, and CRA with 4 spectral difference functions. In order for CRA-based top-hat transforms to be comparable to the marginal and energy-based approach, when relevant black S_{Bk} and white S_{Wh} spectral reflectance functions will be employed as the references, see Eq. 8.18. Then, 3 pixel radius disk structuring element (SE) is selected such that the 1 pixel width crack becomes irrelevant to the opening γ or closing ϕ, allowing top-hat transforms to detect the residual. See also Section 7.4.3.

$$\begin{aligned} S^{-\infty} = S_{Bk} &= \{s(\lambda) = 0,\ \forall\lambda \in [\lambda_{\min}, \lambda_{\max}]\} \\ S^{+\infty} = S_{Wh} &= \{s(\lambda) = 1,\ \forall\lambda \in [\lambda_{\min}, \lambda_{\max}]\} \end{aligned} \tag{8.18}$$

Additionally, performance of combined top-hat transforms CTH will also be evaluated, see Eq. 8.19 where $\star$ is a logical OR operation. This combination allows recovering different image structures which are separately identified by both top-hat transforms.

$$CTH = TH^{-\infty}(\tilde{I})\ \star\ TH^{+\infty}(\tilde{I}) \tag{8.19}$$

8.4.1 Binary-Black (BB) and Probabilistic-Black (PB) Datasets

Using BB and PB datasets, top-hat transforms $TH^{-\infty}$ based on 6 hyperspectral ordering relations are evaluated. Optimum threshold T and its corresponding average crack count error μE_C of each approach can be found in Table 8.2. In case of BB dataset, minimum average crack detection error μE_C of all ordering relations are very reduced, except for CRA ordering relation employing SAM function. First of all, the reduced average error is mainly due to the use of identical black spectral reflectance function throughout the entire image targets. It is also this use of black reflectance which causes CRA-SAM to fail. If we recall, SAM considers shape difference and significantly suppresses magnitude difference. Thus, according to SAM, the employed references S_{Bk}, S_{Wh} and the crack signal S_{Bk} are all identical rendering it to fail at the task.

Table 8.2 – Performance of top-hat transforms $TH^{-\infty}$ employing 6 ordering approaches in BB and PB datasets. S_{Bk} and S_{Wh} are employed as references in the CRA-based top-hat transforms. T is optimum threshold minimizing μE_C, i.e., average crack detection error for all images in each dataset. Best performance in each dataset is highlighted in green.

Ordering approach	**BB dataset**		**PB dataset**	
	T	μE_C	T	μE_C
Marginal	73	5	62	241
Energy	59	5	30	124
CRA-SAM	125	511	125	538
CRA-Euclidean	59	6	29	121
CRA-ECS	57	8	29	114
CRA-KLPD	58	6	3	186

The use of PB dataset allows to evaluate the different top-hat transforms in a more realistic case, where the cracks do not have identical reflectance function. Consequently, the perceived performance is reduced compared to when BB dataset is employed. Observing μE_C obtained for the optimum T of each top-hat transform, the best and worst performance are given by CRA-ECS and CRA-SAM, respectively. See Fig. 8.7 to assess performance of the top-hat transforms in the spatial structure of one target image. All top-hat transforms except for one that is based on CRA-SAM ordering relation performs well. Again, the failure of CRA-SAM is due to the use of S_{Bk} and S_{Wh} as references which reduces its ability to differentiate spectral functions. For other ordering relations, their performances are comparable. False identification of crack does not seem to occur CRA-KLPD, which is obtained at the cost of reduced number of identifications.

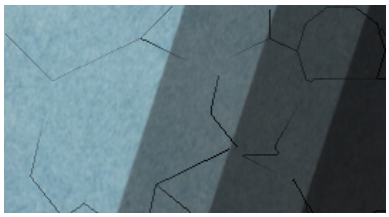

(a) Artificial crack image (PB)

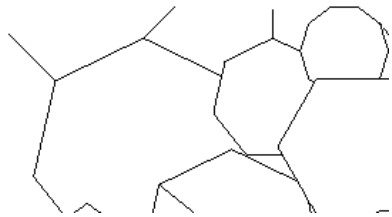

(b) Original crack pattern

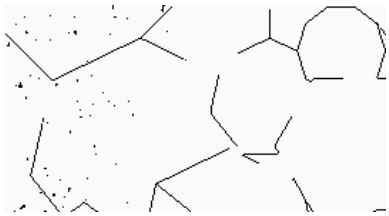

(c) Marginal

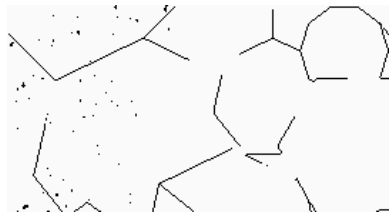

(d) Energy-based

(e) CRA-SAM

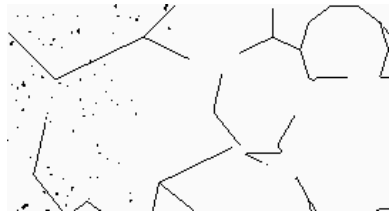

(f) CRA-Euclidean

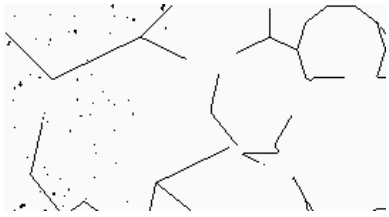

(g) CRA-ECS

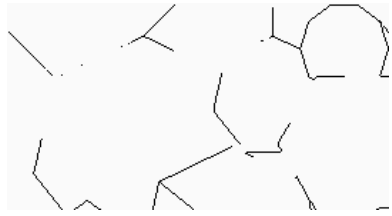

(h) CRA-KLPD

Figure 8.7 – Crack detection results of a pigment patch which are tampered by probabilistic-black crack. This image comes from PB dataset. Shown crack maps are obtained after the thresholding of top-hat transform $TH^{-\infty}$. Among the 6 ordering relations, the least performing one is CRA-SAM as it detects local variations in the image target rather than the crack pattern. The rest of the ordering relations are comparable, with CRA-KLPD being the one which does not falsely recognize local variations in the image as crack pixels, at the cost of reduced numbers of crack pixels that are detected.

8.4.2 Probabilistic-Colored (PC) Dataset with S_{Bk}–S_{Wh} as References

In the previous evaluation, where BB and PB datasets were employed, the contrast of performance between the different top-hat transforms were not significant. It is mainly due to the choice of S_{Bk} as the crack signal, whose shape and intensity differences with the image content are significant. Crack detection becomes more challenging in case of PC dataset where a crack value is chosen randomly from an existing spectral database of pigments. In this case, both magnitude and shape difference between the cracks and initial content of the image might be reduced.

Performances of top-hat transforms of varying spectral ordering relation in the crack detection of PC dataset can be found in Table 8.3. Marginal ordering relation yields the worst and best performances for $TH^{-\infty}$ and $TH^{+\infty}$, respectively. Compared to those based on other ordering relations, differences between the marginal $TH^{-\infty}$ and $TH^{+\infty}$ are highly significant. But it is not surprising since its morphological processes obtain maximum and minimum independently for each channel. This approach is erroneous since neighboring spectral channels are not independent and, thus, are not to be treated separately. On the other hand, top-hat transforms which based on the other 5 ordering relations are more stable, in the sense that μE_C of the $TH^{-\infty}$ and $TH^{+\infty}$ are not significantly different. And such results are due to the full-band approaches of the ordering relations, considering a spectral function as a whole in its entire spectral range. In addition to $TH^{-\infty}$ and $TH^{+\infty}$, Table 8.3 also provides performances of CTH. For this transform, CRA-KLPD ordering relation provides the best performance, although with only slight differences than the other ordering relations.

Table 8.3 – Performance of $TH^{-\infty}$, $TH^{+\infty}$, and CTH employing 6 ordering relations in the crack detection of PC dataset. S_{Bk} and S_{Wh} are employed as references for the CRA-based top-hat transforms. T is optimum threshold minimizing the average crack count error μE_C and is computed independently for each ordering relation. Best performances are highlighted in green.

Ordering approach	$TH^{-\infty}$		$TH^{+\infty}$		CTH	
	T	μE_C	T	μE_C	T	μE_C
Marginal	67	1432	103	206	120	229
Energy	54	457	51	521	61	255
CRA-SAM	65	402	63	415	79	239
CRA-Euclidean	40	335	45	436	56	189
CRA-ECS	45	386	47	471	62	207
CRA-KLPD	7	334	6	357	13	193

CTH-obtained crack maps for artificial crack image using pigment 44450 are also provided in Fig. 8.8 to allow visual observation of the spatial structures of the crack. From this figure, it is evident that marginal approach misses a significant portion of the crack lines. For the energy-based approach, in addition to undetected crack lines, there are a significant number of false detections. CRA-SAM, which failed in the crack detection of BB and PB datasets, now provides a good performance relative to the other CRA ordering relations. But to recall, in the previous datasets, the failures were due to the use of S_{Bk} as both reference and crack signal, which is not the case with PC dataset. Finally, from this visual observation, we have a better idea of performances of the different top-hat transforms. And further on, only CRA-based top-hat transforms will be considered.

8.4.3 Probabilistic-Colored (PC) Dataset with Varying References

The main advantage of CRA-based top-hat transforms lies in the ability to select the references. When the crack signal in an image is known, such flexibility will allow obtaining more accurate crack maps. In this evaluation, the references are selected according to Eq. 8.20.

$$S^{-\infty} = \mathcal{C}, \quad S^{+\infty} = \bigvee \{d(S_k, S_i)\}, \ \forall S_i \in \mathcal{S}_I \tag{8.20}$$

Interpretation. Spectral function associated with the crack signal $\mathcal{C}$ is selected to be reference $S^{-\infty}$. Then, reference $S^{+\infty}$ is one originating from the same crack image, with the biggest differences to reference $S^{-\infty}$.

Performances of the 4 CRA-based top-hat transforms are provided in Table 8.4. As observed, the best performance is given by CRA-KLPD for both $TH^{-\infty}$ and $TH^{+\infty}$, followed by the CRA-Euclidean top-hat transforms. CRA-SAM is the least performing top-hat transforms in all three cases, i.e., $TH^{-\infty}$, $TH^{+\infty}$, and CTH. Then, CTH is found to be improving performances of the individual top-hat transforms $TH^{-\infty}$ and $TH^{+\infty}$, which can be observed for all ordering relations. Best performing CTH is the CRA-Euclidean based transform.

To supplement statistical results shown in Table 8.4, visual observation of the results of CTH can also be carried out through Fig. 8.9. In all cases of CRA ordering relations shown in the figure, obtained crack maps generally overestimate the number of crack pixels, especially at the joint of two or more crack lines. The worst performance is given by CRA-ECS, where spectral variations which exist on the left most color shade of the pigment are considered as crack pixels. Nevertheless, from this visual observation and the previous statistical results given in Table 8.4, none of the CRA variations is entirely superior from the other. Thus, CRA ordering relations with the 4 spectral difference functions will be employed in the coming section to detect cracks in a hyperspectral capture of a painting.

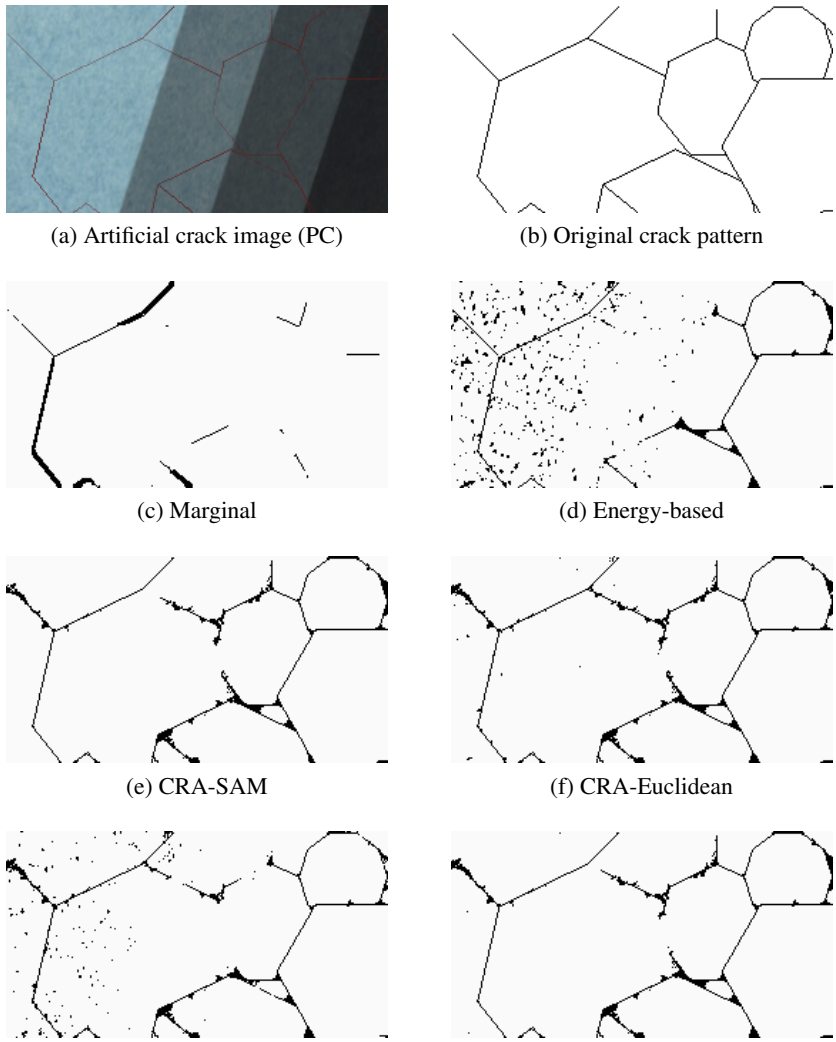

(a) Artificial crack image (PC)
(b) Original crack pattern
(c) Marginal
(d) Energy-based
(e) CRA-SAM
(f) CRA-Euclidean
(g) CRA-ECS
(h) CRA-KLPD

Figure 8.8 – Crack detection results of a pigment patch which are tampered by probabilistic-colored crack. This image comes from PC dataset. Shown crack maps are obtained after the thresholding of combined top-hat transform CTH. Top-hat transform based on marginal ordering relation misses many of the crack lines. The energy-based one is able to detect most of the crack lines, but also with considerable amount of falsely detected crack pixels. CRA-based top-hat transforms of varying spectral difference functions performs well but also with several misidentifications, especially pixels at the joint of several crack lines.

Table 8.4 – Performance of $TH^{-\infty}$, $TH^{+\infty}$, and CTH employing 4 CRA-based ordering relations in the crack detection of PC dataset. Reference selection is made according to criteria shown in Eq. 8.20. Best performances are highlighted in green.

Ordering approach	$TH^{-\infty}$		$TH^{+\infty}$		CTH	
	T	μE_C	T	μE_C	T	μE_C
CRA-SAM	69	339	76	518	84	228
CRA-Euclidean	37	269	38	449	55	160
CRA-ECS	46	337	42	482	58	194
CRA-KLPD	8	247	6	420	14	190

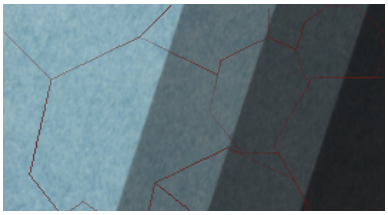

(a) Artificial crack image (PC)

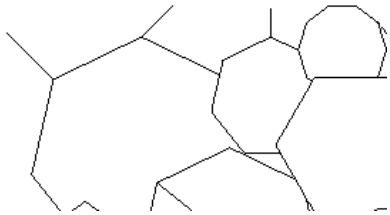

(b) Original crack pattern

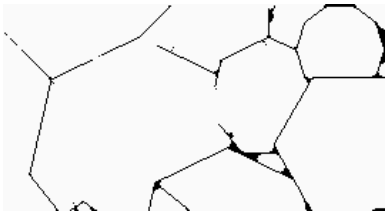

(c) CRA-SAM

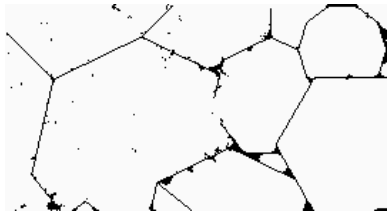

(d) CRA-Euclidean

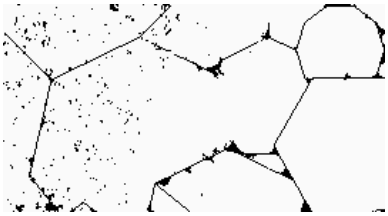

(e) CRA-ECS

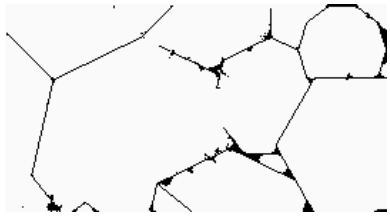

(f) CRA-KLPD

Figure 8.9 – Crack detection results of a pigment patch tampered by probabilistic-colored crack obtained by CTH. The image comes from PC dataset. Relatively cleaner crack map is given by CRA-SAM, followed by CRA-KLPD. In addition to missing several crack lines, CRA-ECS misidentifies local variation in the image as being crack pixels.

8.5 Application to Cracking Layers of A Painting

Based on quality assessment of various hyperspectral top-hat transforms in the previous section, in the following are the applications of the obtained top-hat transforms and their optimum parameters. To summarize, the parameters are provided in Table 8.5. The final crack map is obtained by CTH, which is the superimposing of crack maps obtained by the individual top-hat transforms $TH^{-\infty}$ and $TH^{+\infty}$. Thresholds for each ordering relation will be using the ones provided in Table 8.4.

Table 8.5 – Parameters of hyperspectral crack detection algorithm applied to target images coming Cracks-200 dataset (Appendix B).

Parameter	Value
Ordering relation	CRA
Difference function	SAM, Euclidean, ECS, KLPD
SE shape and size	disk, 5×5 (radius 3 pixels)
Reference pair	S_{Bk} and S_{Wh}
Crack map generation	Combined top-hat (CTH)

8.5.1 Comparison of Spectral Difference Functions

As a first experiment, performances of CRA ordering relation when combined with the 4 spectral difference functions shown in Table 8.5 will be compared. Crack maps obtained for image SCC01-1 for CRA ordering relation of varying spectral difference functions can be observed in Fig. 8.10. Note that shown crack maps are prior to thresholding operation. From these crack maps, we can see that the least performing pair of ordering relation and spectral difference function is CRA-SAM. The crack map it obtains detects the cracks and other structures in the image at relatively the same magnitude, resulting in the crack structures being very faint even compared to other structures in the image. With a quick observation, it could be said that CRA-Euclidean and CRA-ECS have almost identical performances. Then, the two approaches also detect other local variations within the image. As for CRA-KLPD based top-hat transforms, it successfully extracts the main crack lines in image SCC01-1. Additionally, this ordering relation gives more significant differences between the cracks and non-crack structures in the image. Employing thresholds given in CTH column in Table 8.4, final crack maps for the input images is obtained and shown in Fig. 8.11. Since crack map obtained by CRA-SAM is already poor to begin with, there is few the thresholded image can improve on. Comparing CRA-Euclidean and CRA-ECS, crack map obtained by the latter is cleaner but also detects less of the finer cracks, e.g., compare regions circled in red. Then, compared to CRA-ECS, CRA-KLPD is able to extract the main crack lines and also with better contrast between the cracks and non-crack structures.

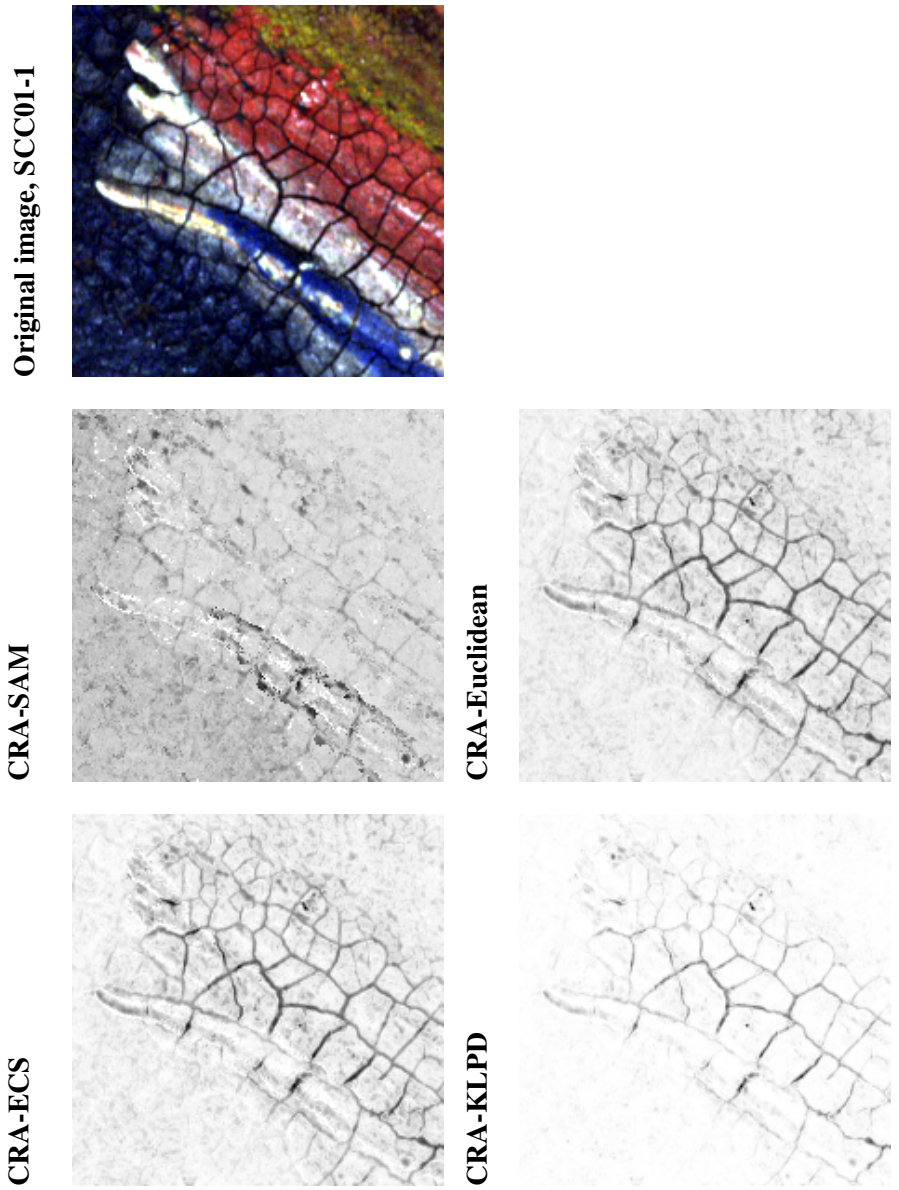

Figure 8.10 – Crack maps obtained by CTH and prior to thresholding. CRA-SAM is the least performing one. Its extracted cracks are very faint compared to the other ones. Result obtained by CRA-Euclidean is almost identical to that of CRA-ECS. The main crack lines are obtained by CRA-KLPD but with more significant differences to other image structures compared to the results of the last two ordering relations.

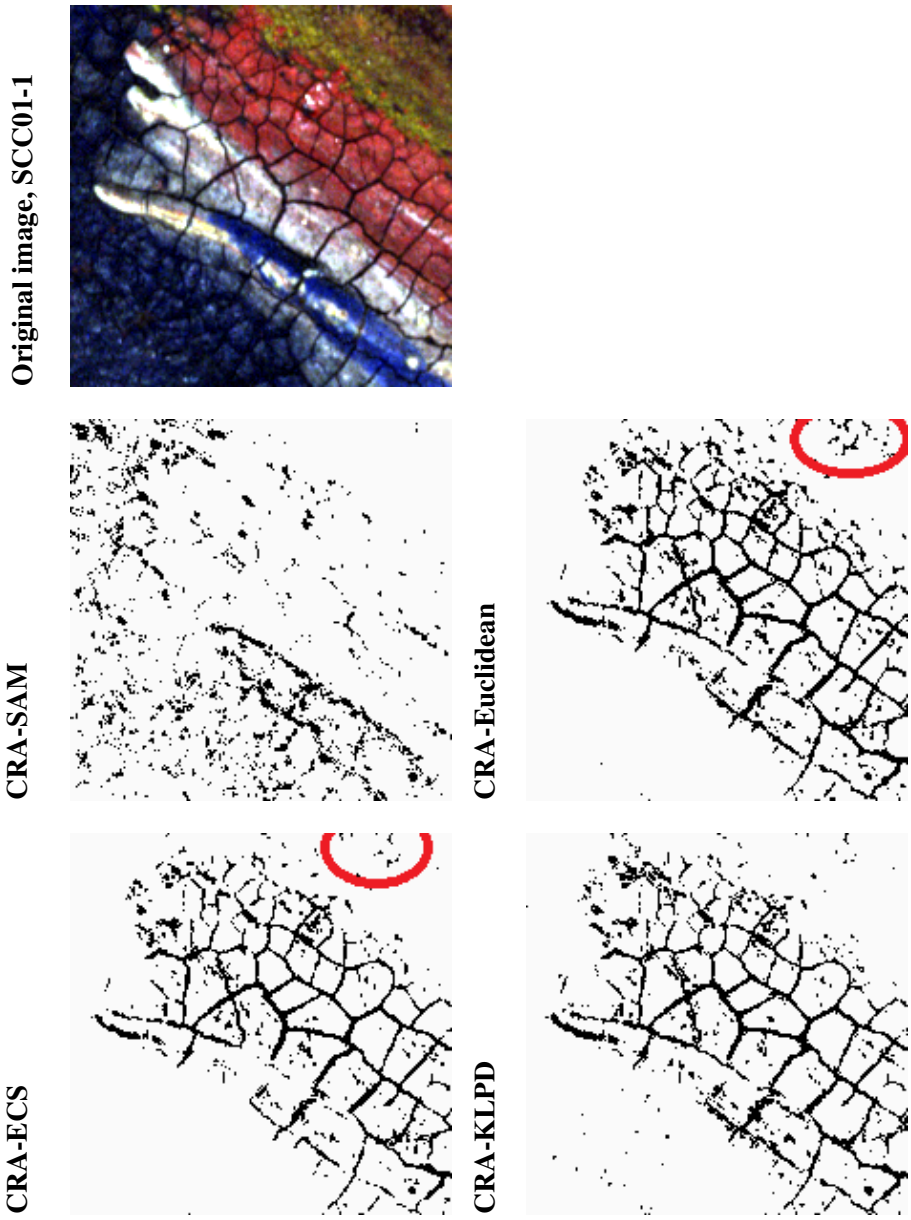

Figure 8.11 – Crack maps obtained after thresholding. Threshold value T for each ordering relation can be found in Table 8.4. CRA-SAM does not extract majority of the crack lines. CRA-ECS provides a cleaner crack map than CRA-Euclidean, but also detects less cracks, e.g., compare regions circled in red. Result of CRA-KLPD is more similar to CRA-ECS.

8.5.2 The Impact of Reference Selection

With the previous image target, i.e., SCC01-1, the cracks are generally wider making it a relatively easier target image to process. Moreover, the crack signals are generally dark and almost black. However, cracking layers in a painting is not always as wide and evident as the cracks in SCC01-1, e.g., in image SCC03-4 also from Cracks-200 dataset. Using this image whose cracks are finer and narrower, we want to compare the performance of CRA ordering relation when paired with Euclidean distance and KLPD function. Euclidean distance is selected based on its ability to detect finer cracks in image SCC01-1. As for KLPD function, it provides more contrast between the cracks and other image structures, see Fig. 8.10.

Crack maps of image SCC03-4 as obtained by CTH, pre- and post-thresholding, can be observed in Fig. 8.12. Comparing crack maps obtained prior to thresholding operation, crack lines extracted by CRA-Euclidean seem to be more prominent than those obtained by CRA-KLPD. However, the crack lines also appear in relatively similar magnitude as other image structures detected by the algorithm. Looking back to the original image, many of the structures seem to be caused by variations of pigments in the paint layer, and not necessarily due to actual cracks. With CRA-KLPD, even though the crack lines are less prominent, better contrast is obtained. Many non-crack structures are not falsely recognized as cracks. To improve visibility of the cracks, thresholding operation is applied on CTH-generated crack maps and the results can be observed in the last row of Fig. 8.12. Between the two thresholded crack maps, no significant difference is perceived.

For this particular image, rather than using S_{Bk} and S_{Wh} as references, we want to adapt the references to the image content. Artificial spectral functions are generated mimicking a dark and vivid blue pigments pointed by the green and red arrows, respectively, in Fig. 8.13. The simulated dark blue (DB) one will act as the minimum convergence coordinate $S^{-\infty}$, and simulated vivid blue (VB) as the maximum one $S^{+\infty}$. Then, the SE radius is also reduced into 2 pixels. The obtained crack maps prior to and post-thresholding operation can be observed in Fig. 8.13. As expected, CRA-KLPD always provide better contrast in the CTH-generated crack map compared to CRA-Euclidean. And due to this, the thresholded map of CRA-KLPD is able to extract crack lines occurring in image SCC03-4, but not CRA-Euclidean.

8.5.3 More Results employing S_{Bk}–S_{Wh} References

Employing the same top-hat parameters as in Table 8.5, more crack maps obtained for other images in Cracks-200 dataset are provided. Brief comments for each result are also provided in the corresponding figure.

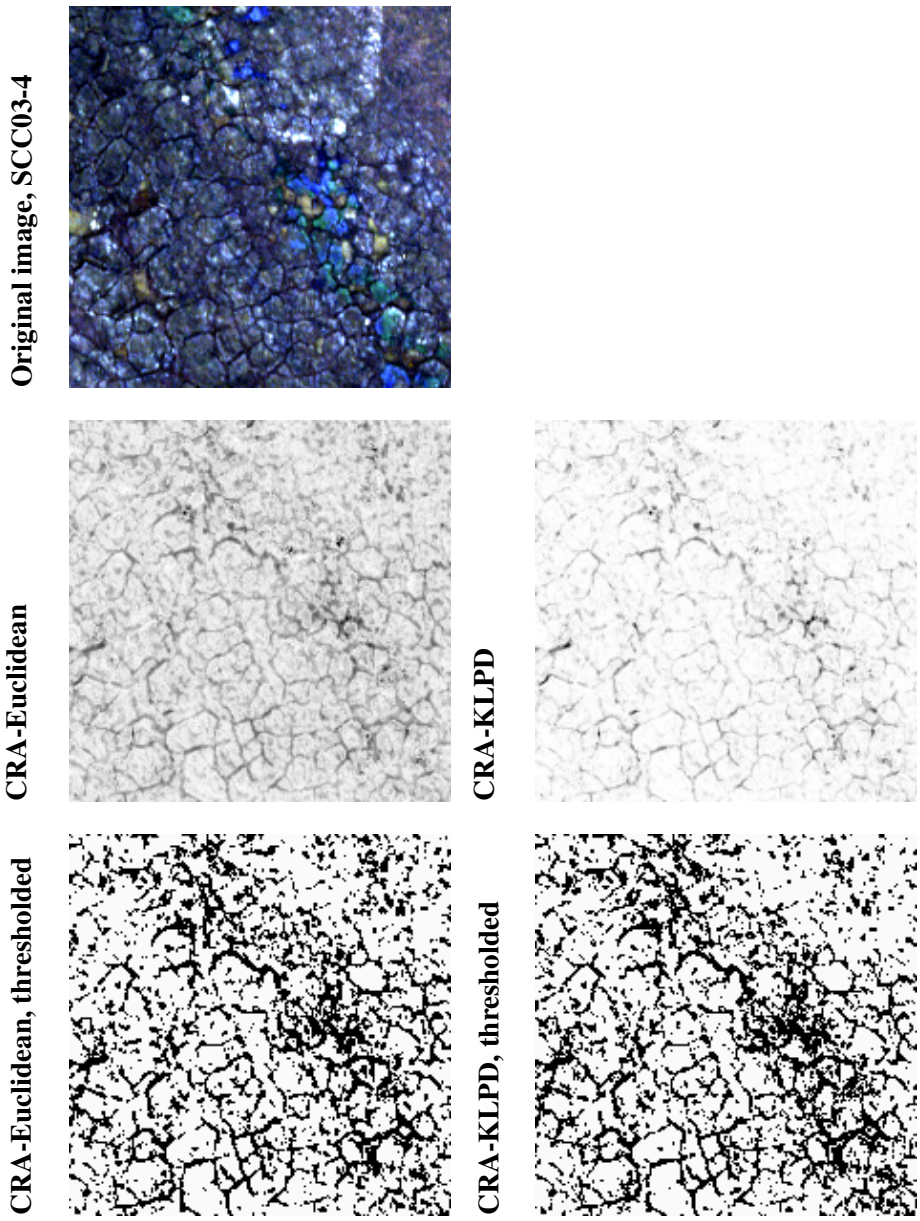

Figure 8.12 – Crack maps of image SCC03-4 from Cracks-200 dataset as obtained by CTH. Crack maps pre- and post-thresholding operation are both provided. Comparing the pre-thresholding maps, crack lines obtained by CRA-ECS seem to be more prominent than those obtained by CRA-KLPD.

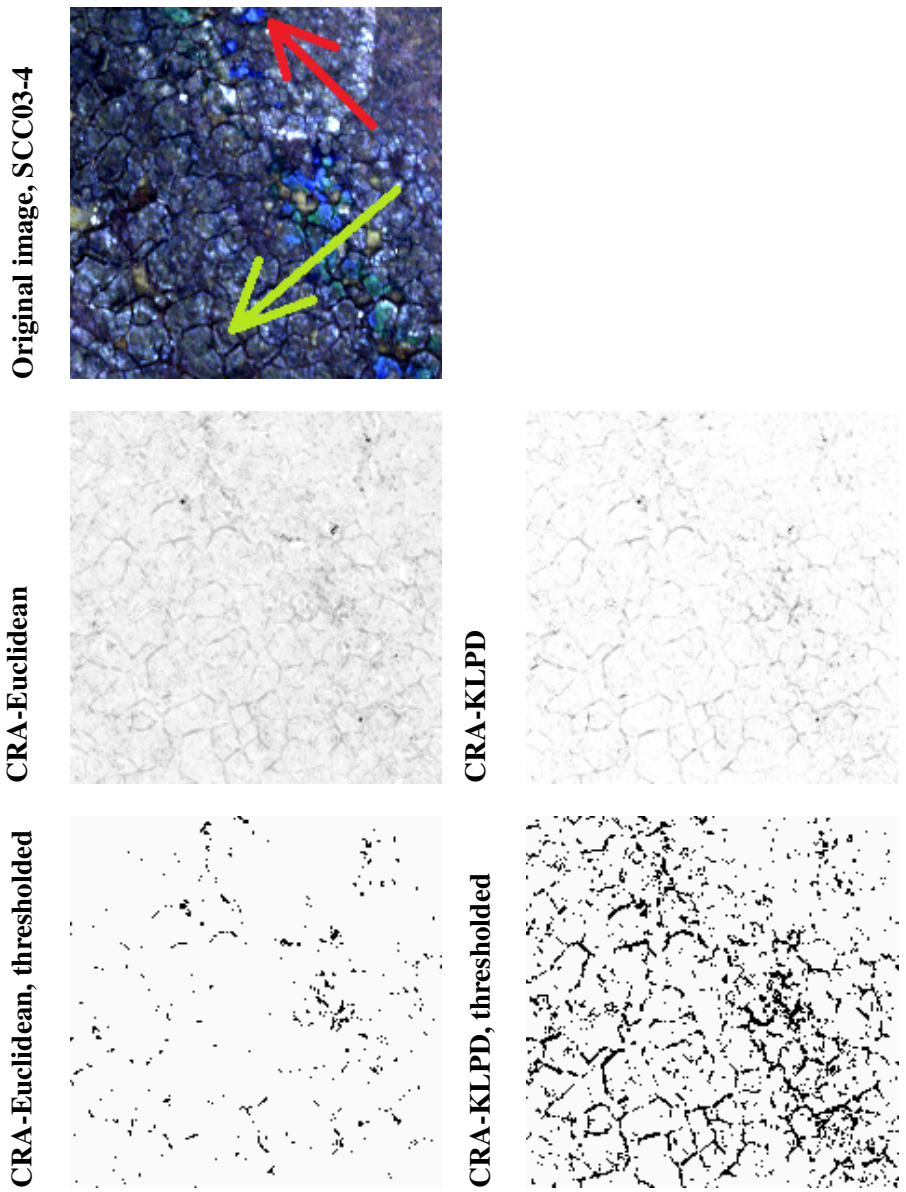

Figure 8.13 – Crack maps of image SCC03-4 from Cracks-200 dataset as obtained by CTH. Artificial spectral functions mimicking dark blue (green arrow) and vivid blue (red arrow) in the original image are employed as references. Using the same threshold as previously, CRA-KLPD successfully extracts most of the cracks unlike CRA-Euclidean. This is due to the high contrast between cracks and non-crack structures provided by CRA-KLPD.

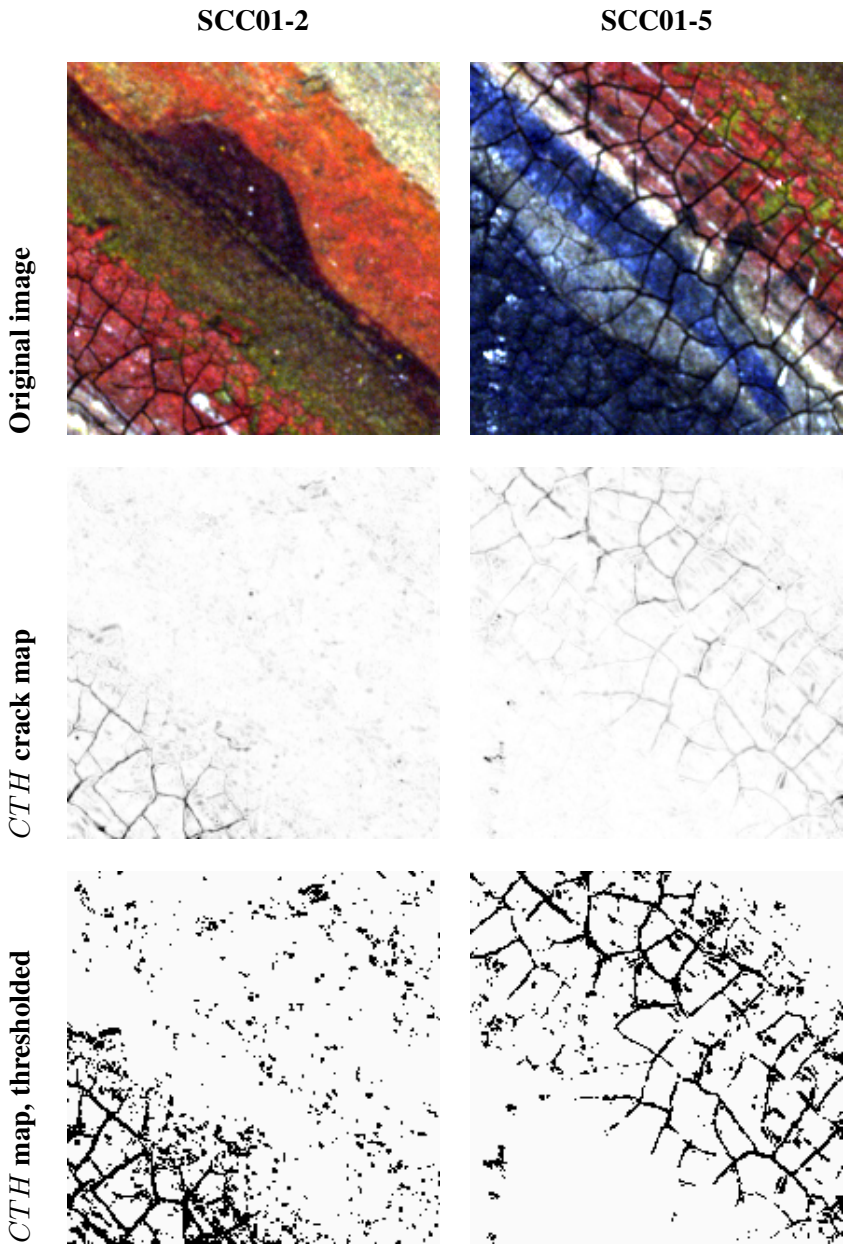

Figure 8.14 – Crack detection results of SCC01-2 and SCC01-5. Wide cracks which appear in each image are detected. Crack maps are obtained by CTH employing CRA-KLPD ordering relation with S_{Bk} and S_{Wh} as references. SE is disk of shape 3×3 pixels and threshold value T is 14. Results shown after this figure are also obtained using the same parameters.

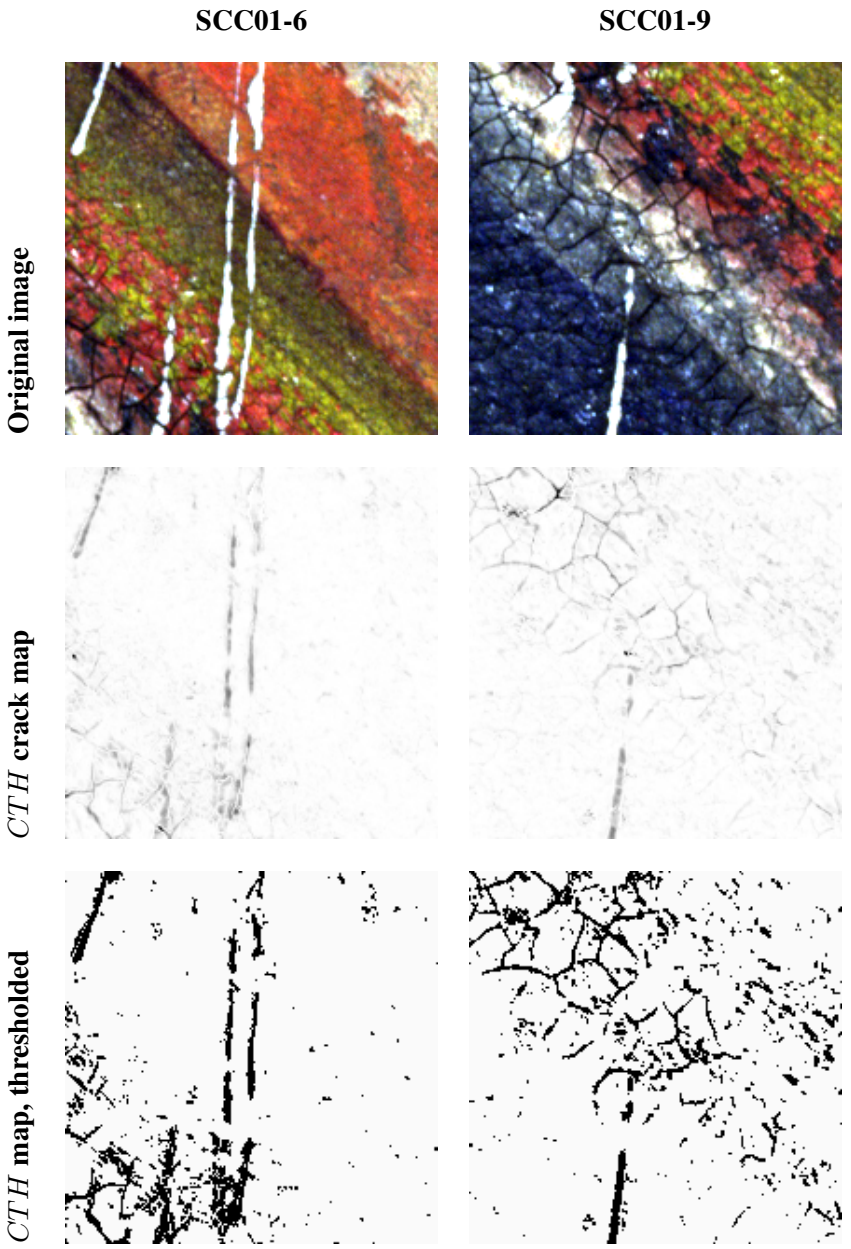

Figure 8.15 – Crack detection results of image SCC01-6 and SCC01-9. Wide cracks in both images are detected. Finer cracks at the lower left corner of SCC01-9 are not detected.

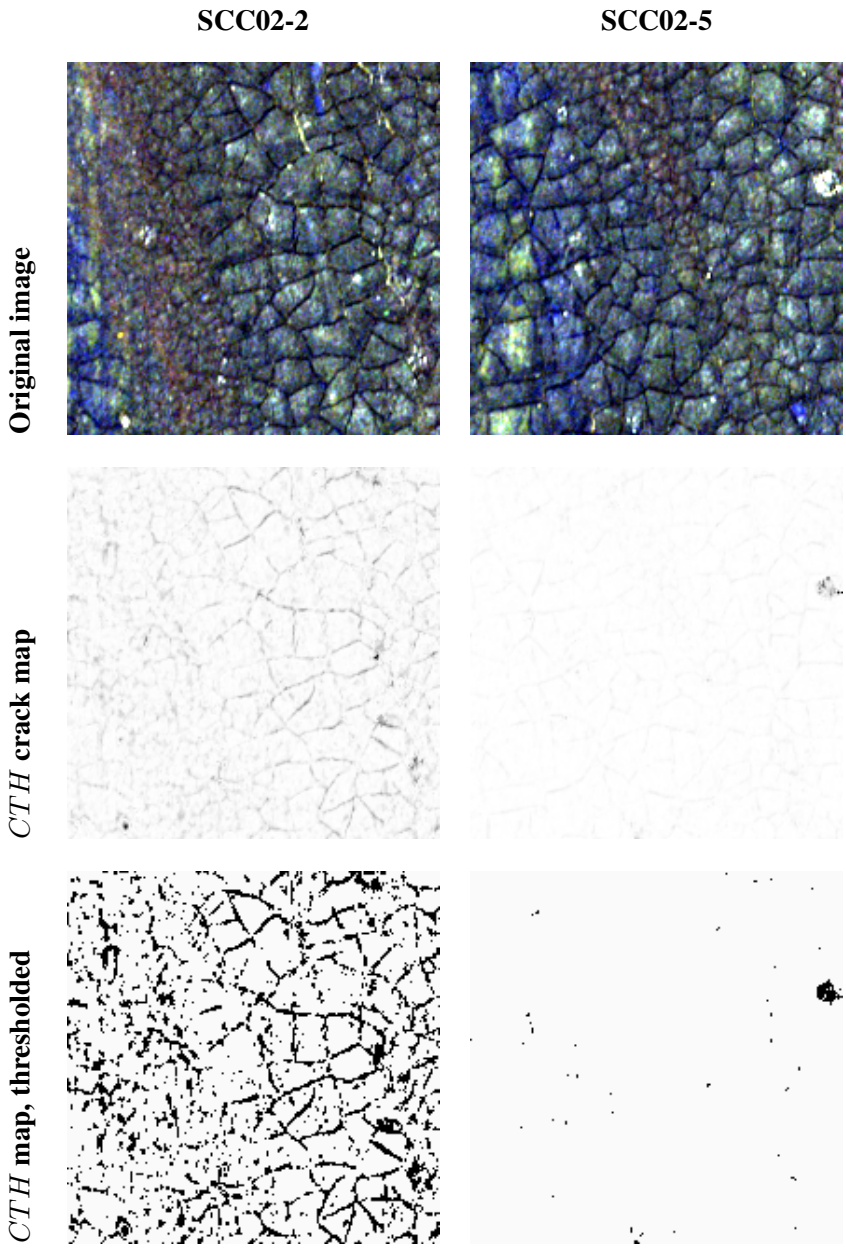

Figure 8.16 – Crack detection results of image SCC02-2 and SCc02-5. Wider cracks in image SCC02-2 are relatively well identified. Cracks in image SCC02-5 are very faint in the pre-thresholding map, due to the contrast of a white splotch at the middle right of the image. As a result, the final crack map obtains no crack line. Further treatment requires suitable reference selection.

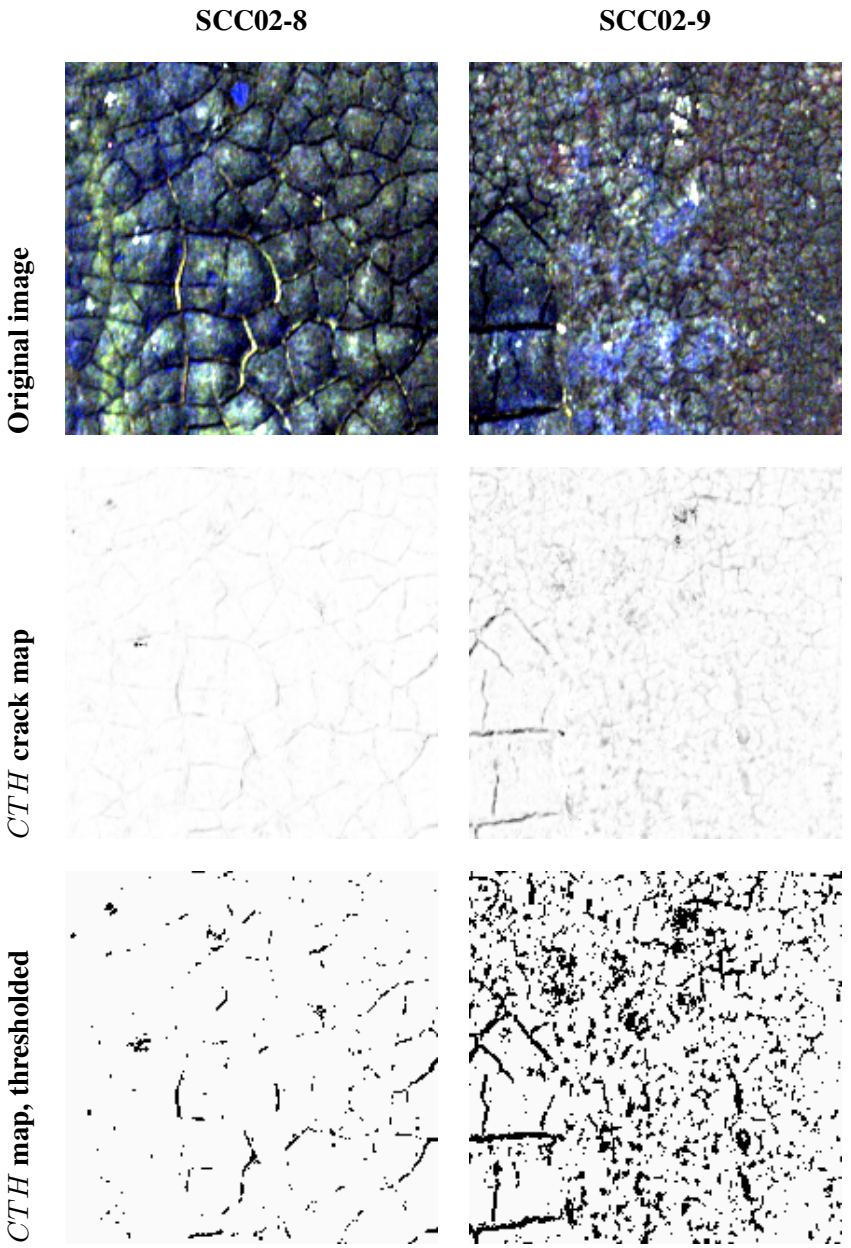

Figure 8.17 – Crack detection results of image SCC02-8 and SCC02-9. Crack lines are found in SCC02-8, but due to the used threshold, these lines are not recovered in the final crack map. The wider cracks in image SCC02-9 are relatively well identified. Finer cracks are also detected, but it is difficult to judge the quality through visual assessment.

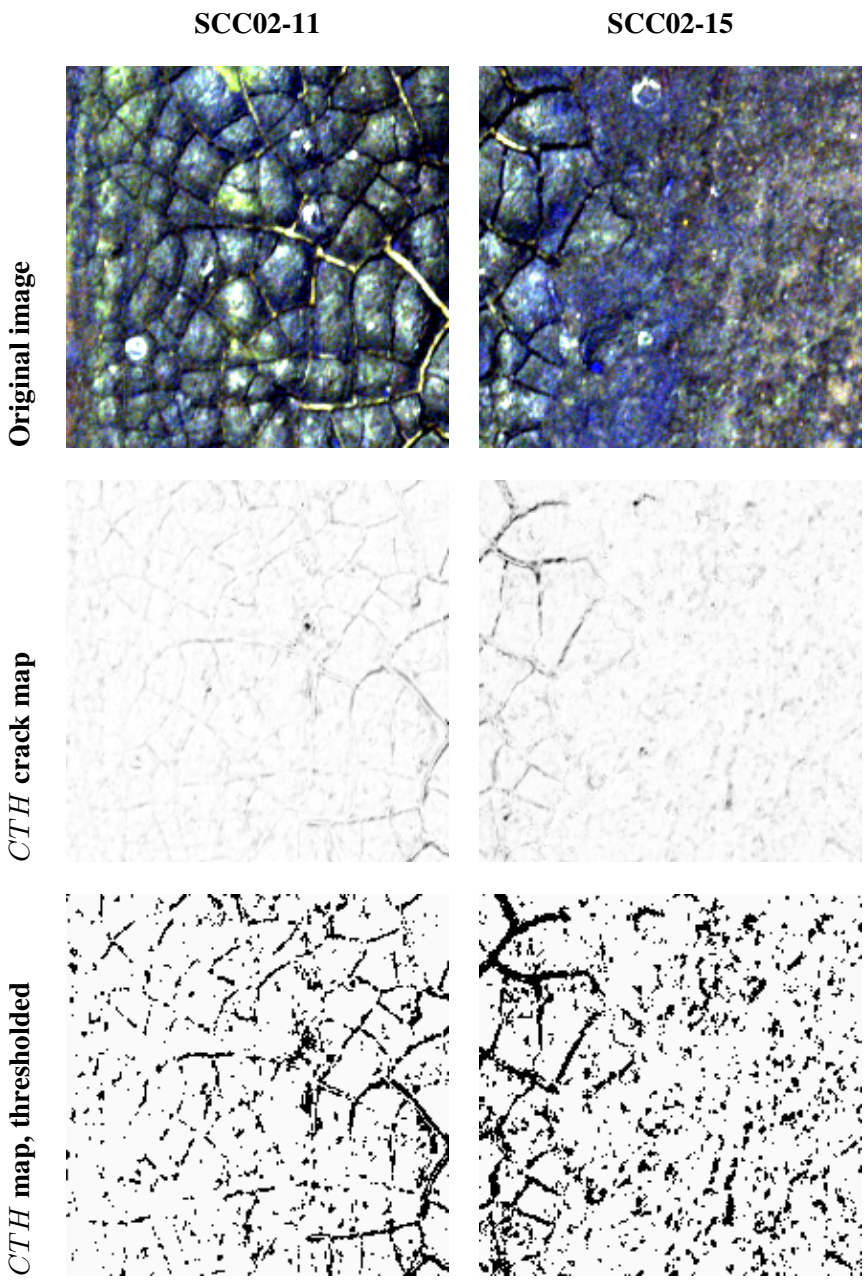

Figure 8.18 – Crack detection results of image SCC02-11 and SCC02-15. Wider cracks in both images, be it black or yellow, are well identified in the crack maps. Improvement can be done for the finer cracks by, e.g., selecting more suitable references.

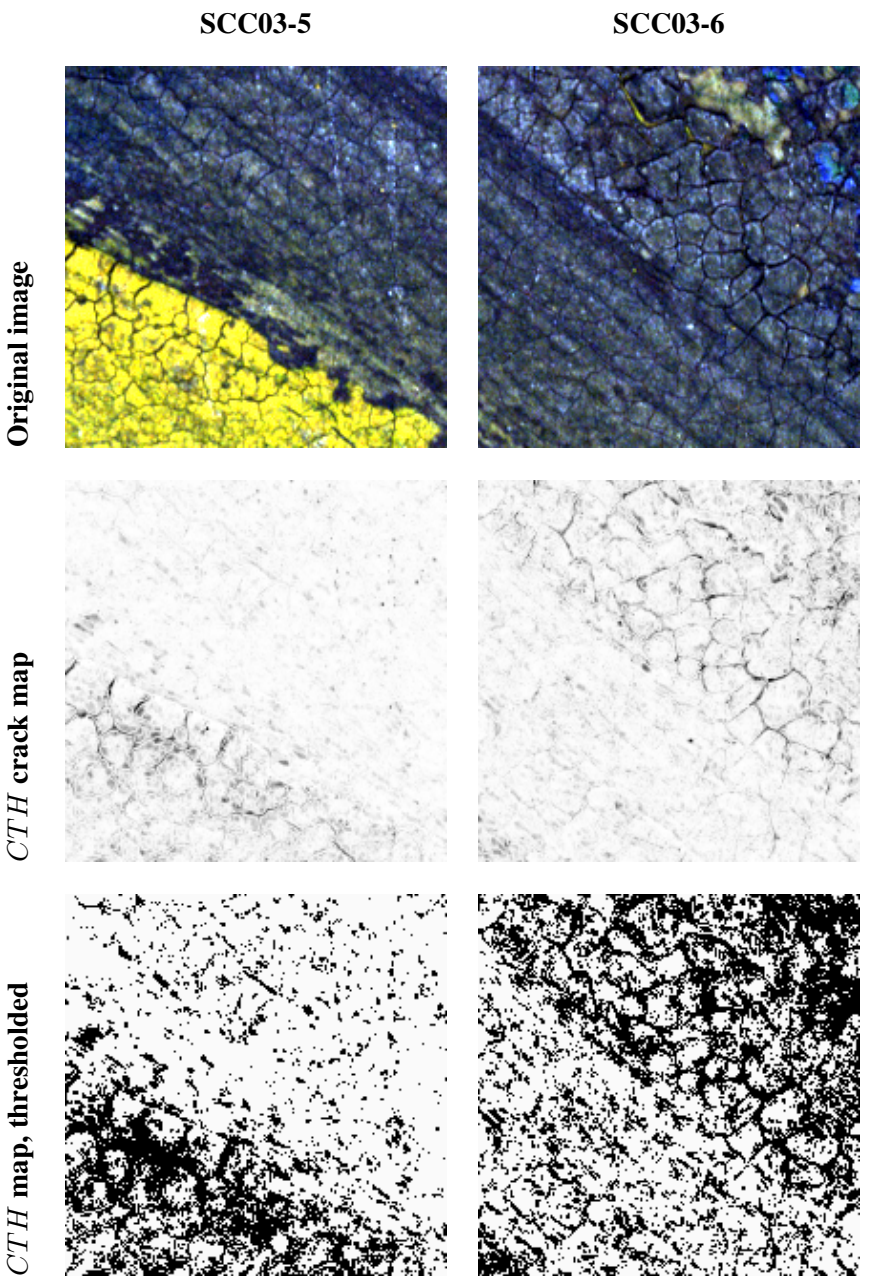

Figure 8.19 – Crack detection results of image SCC03-5 and SCC03-6. It can be said that cracks are generally well identified in the pre-thresholding images. However, thresholding operation does not seem to improve the visibility since many non-crack structures are falsely identified as cracks.

8.6 Computational Complexity

Computational complexity is a major concern when it comes to hyperspectral image processing, due to the size of the image at hand. And apart from the challenge of extending a grayscale technique to the spectral domain, computational burden is another reason why band selection and dimensionality reduction are common strategies in the processing of hyperspectral images. Thus, after being presented with good results obtained from the proposed full-band approach for crack detection, one might still think whether these results worth the required computational time and resources.

Let n_I, n_λ, n_B, and p be the number of pixels in image I, number of spectral channels, number of pixels included in SE B, and a constant value representing the number of primitive operations required for certain processing, respectively. Then, time complexity of CRA-based crack detection algorithm is as provided in Table 8.6, i.e., linear following image and SE sizes. Then, regarding crack detection, typically the crack width remains small and do not follow the size of an entire image. Thus, the SE size can remain small further reducing the computational time.

Table 8.6 – Computational complexity of CRA-based crack detection algorithm, i.e., linear complexity following the image and SE sizes. n_I, n_λ, n_B, and p be the number of pixels in image I, number of spectral channels, number of pixels included in SE B, and a constant value representing the number of primitive operations required for certain processing, respectively.

Processing steps	**# of primitive operations**	**Notes**
Distance computation (KLPD function)	$2 \times n_I \times n_\lambda \times p_{KLPD}$	2 is for distance to 2 references
CRA ordering relation	$2 \times n_I \times n_\lambda \times p_{CRA}$	2 is for the two conditions in CRA
Morphological processing	$4 \times n_I \times n_\lambda \times n_B$	4 is for erosion, dilation, opening, and closing
Top-hats (KLPD function)	$2 \times n_I \times n_\lambda \times p_{KLPD}$	2 is for both top-hats $TH^{-\infty}$ and $TH^{+\infty}$
CTH (logical OR)	$n_I \times n_\lambda$	
Complexity	$n_I \times n_\lambda \times n_B$	**Linear time**

8.7 Conclusion

In literature, crack detection task has been addressed by means of grayscale top-hat transforms, despite the availability of color or spectral images. This approach is then followed by a series of advanced processing methods in order to obtain a good enough crack maps. In this chapter, rather than reducing the spectral image at hand such that it can be processed by a grayscale approach, we have extended top-hat transforms into a full-band spectral approach. By using a full-band approach, we will be able to fully exploit the obtained spectral measure.

Several extension approaches of top-hat transforms are demonstrated. Our proposed extension employs a distance-based ordering relation, i.e., conditional ratio and angular distance ordering relation (CRA). In order to evaluate the quality of these spectral top-hat transforms, assessment criteria have also been developed using artificially generated crack images. Assessment carried out for each approach not only determines their quality, but also their corresponding optimum parameters, especially the threshold required to obtain the final crack map. Finally, after evaluation and parameter selection, the obtained top-hat transforms are applied to a real case where the images come from hyperspectral captures of cracking layers of a cultural heritage painting. Results show that clear crack maps can be obtained after top-hat transforms, without having to conduct more advanced processing techniques.

During the application of CRA-based top-hat transforms to the real images, performances 4 spectral difference functions were also evaluated. The considered functions were spectral angle, Euclidean distance, Euclidean distance of cumulative spectrum (ECS), and spectral Kullback-Leibler pseudo-divergence (KLPD) function. And among these functions, KLPD demonstrated a better performance since it creates a larger contrast between crack and non-crack structures found in the image. This has, in turn, provided better crack maps with less false identification. It has also been demonstrated that reference selection can be made according to the image content. And by doing so, the resulting crack maps will be improved.

Summary of Contributions.

- ✓ Extension of grayscale top-hat transforms to the spectral domain for solving crack detection task. The full-band approach is enabled through the use of conditional ratio and angular distance ordering relation (CRA).
- ✓ Quality assessment protocol for crack detection algorithms using artificially generated crack images.
- ✓ Efficient spectral top-hat transforms which run in linear time and are able to produce good results without pre- and post-processing steps.

Part III

Conclusion

Chapter 9

Conclusion

9.1 Summary of Contributions

Hyperspectral imaging has been increasingly employed for various application tasks such as quality control and inspection of materials. The cultural heritage domain is one of the many fields which has also been exploring the potential of this imaging technology. The high spatial and spectral resolutions of a hyperspectral image are expected to provide the field with more advanced and accurate analyses of cultural heritage objects. And, in turn, this will aid conservation and/or restoration works of the objects. However, with the existing image processing approaches, exploitation of the information rich images cannot reach its full potential. In order to do so, we have identified a need for a metrological spectral image processing framework, where accuracy, uncertainty, and bias are addressed and managed at every step of the processing chain.

One of the application tasks we have addressed in this study is the crack detection of cultural heritage paintings. In literature, despite the availability of color and spectral images, the image processing typically remains in the grayscale domain. And if we are to use grayscale image processing tools, the hyperspectral images we have at hand must be reduced to the grayscale domain. However, we believe that such practice defeats the purpose of conducting a hyperspectral acquisition whose cost and complexity are high. This is because accuracy will be lost during the reduction process. With this consideration, we have extended the state of the art crack detection method, i.e., morphological top-hat transforms, to the spectral domain. A quality assessment protocol has also been proposed for validating the extended crack detection method. Results of applying the spectral top-hat transforms to real crack images have shown that our approach is able to obtain good

crack maps. Furthermore, the spectral top-hat transforms are shown to be effective since they do not require any pre- or post-processing steps to obtain the aforementioned results. All this work can be found in Chapter 8 Crack Detection for Cultural Heritage Paintings.

The aforementioned crack detection method has been made possible through the development of a distance-based spectral image processing framework, specifically using the well-established mathematical morphology (MM) framework. At the first step of the development, we set out to identify the most suitable mathematical definition of a spectral function. The search for a correct definition has been motivated by the aspects of metrology which regards a spectral image as a measure and not only a digital or mathematical object. The definition of a spectral function is inherent in the construction of a spectral distance function. Thus, in Chapter 3 From Definition of Spectral Function to Spectral Difference, we have classified the existing distance, similarity, and divergence functions based on their inherent assumptions of what a spectral function is. Following this classification, we have formulated assessment protocols which encompass both theoretical requirements of a distance function and the metrological constraints. Then the protocols are employed to evaluate the existing distance functions we have previously classified. Our first proposal of a suitable spectral distance function can also be found in this chapter, i.e., Euclidean distance of cumulative spectrum (ECS). However, since this first proposal, a more suitable spectral difference measure has been introduced by Richard *et al*. [145], i.e., spectral Kullback-Leibler pseudo-divergence (KLPD) function. In order to follow this latest development of a spectral distance function, all of the following image processing and analysis tools have been implemented using the KLPD function.

The notion of distance is almost inseparable to the question of reference. We cannot compute the distance of a spectral function without having to define a reference point. To address this question, in Chapter 5 Hyperspectral Image Analysis through Spectral Differences we have provided the protocol for spectral reference selection, which will be useful for various distance-based image processing and analysis tools. We have also further demonstrated the use and implementation of this protocol in the context of pigment discrimination for a given image. Throughout the study, this question of reference have always emerged. Thus, we have not only addressed the question in Chapter 5, but also in other chapters. In Chapter 7 First Levels of Spectral Mathematical Morphology, we have shown how to select spectral reference pair for erosion, dilation, opening, and closing when given certain applications goals. We have also briefly demonstrated the impact of reference selection to crack detection results in Chapter 8 Crack Detection for Cultural Heritage Paintings.

The next step in the development of the distance-based spectral mathematical morphology framework is to define a suitable spectral ordering relation. And just as what has been carried out for the identification of spectral distance function, in Chapter 4 Spectral Ordering Relation and Its Expected Properties we have formulated metrological tests in addition to the known theoretical requirements of an ordering relation. Prior to using these evaluation protocols, we have studied the existing multivariate ordering relations and selected the ones which are relevant for the spectral domain. After the theoretical and metrological evaluations, the novel conditional ratio and angular distance ordering relation (CRA), which we proposed in this chapter was found to be the most suitable spectral ordering relation.

MM is a nonlinear image processing framework useful for the analysis of spatial structures in an image. And while this framework has matured for the binary and grayscale images, its extension to the multivariate domain remains an open research question. Due to the preceding works in Chapter 3 and 4, we have been able to extend the framework to the spectral domain using the distance-based spectral ordering relation. The extensions of basic morphological operators erosion, dilation, opening, and closing are relatively straightforward and can be found in Chapter 7 First Levels of Spectral Mathematical Morphology. But more than only extending the framework to the spectral domain, we have also assessed and validated the obtained tools according to various theoretical and metrological criteria. In this chapter, we have also demonstrated how to use the operators for specific application goals, at the same time proving the interests of a full-band approach to spectral image processing.

Three new distance-based spectral morphological gradients have been defined in Chapter 7 First Levels of Spectral Mathematical Morphology. The developed gradients were further used as an entry point to a full-band approach of spectral segmentation using morphological watershed transformation. Given a specific image, we have also demonstrated how to select a spectral gradient among the three, which will maximize the relevance of watershed segmentation results. In this chapter, we have not been able to fully develop a metrological assessment protocol for the use of spectral gradients in watershed segmentation. Nevertheless, we have begun a preliminary work in assessing the stability spectral gradients in watershed segmentation. Still in the same chapter, we have extended the grayscale top-hat transforms to the spectral domain, using a distance-based approach. And it is this extension which has been used as to solve the crack detection task in Chapter 8 Crack Detection for Cultural Heritage Paintings.

During the development stages leading up to the spectral MM framework, we have been able to develop other powerful spectral image processing and analysis tools. Based on spectral difference function we defined in Chapter 3, new graphical

representations of spectral differences have been introduced in Chapter 5 Hyperspectral Image Analysis through Spectral Differences. A bidimensional histogram of spectral differences (BHSD) given in the chapter had been first introduced by Richard *et al*. [145]. Then, we have extended this BHSD into the n-dimensional space, with demonstration given for a three-dimensional one, i.e., the tridimensional histogram of spectral differences (THSD). A modified BHSD can also be found in Chapter 7 First Levels of Spectral Mathematical Morphology where it was first introduced and employed to analyze the impact of our distance-based erosion and dilation operators. Going back to the context of Chapter 5, the usefulness and interests of these graphical representations have been demonstrated in two application tasks, i.e., pigment discrimination in a painting image and the identification of noisy spectral bands in a given spectral image. Finally, these graphical representations offer perhaps the first solution to the analysis of spectral distributions, allowing to identify existing spectral groups within an image. And together with the reference selection protocol, an operational analysis tool for the cultural heritage domain has been obtained.

In Chapter 6 Spectral Rank Order Filters another family of spectral image processing tools is introduced. We have been able to extend rank order filters (ROF) to the spectral domain using our distance-based CRA ordering relation. To ensure that the obtained spectral ROF satisfy the aspects of metrology, we have also developed protocols for assessing the tools. The first metrological validation evaluates spectral ROF in their ability to suppress impulse noise. In the second validation, we employed Vector Median Filters (VMF) by Astola *et al*. [18] as the reference filter for the case of edge preservation capability. Through these series of tests, we have been able to identify the limitations and advantages of our new approach. Then, we have also discovered that the state of the art of multivariate median filter, i.e., VMF, is not always superior to our approach. While VMF generally blurs an input image, in our approach the edges are better preserved. However, there are also certain cases where our approach produces grainy artifacts in the filtered images, and VMF does not. The chapter was closed by comparing the time and space complexities of our approach to the reference filter, i.e., VMF. Through this analysis, we have shown that our approach provides a significantly lower computational complexity than VMF. And in turn, this would be an attractive solution for more advanced spectral ROF.

9.2 Discussions and Perspectives

By the end of this study, KLPD function [145] has been found to be the most suitable spectral difference function. However, we have also encountered challenges when using this function. In particular, the use of logarithmic function in KLPD

could potentially cause numerical artifacts, especially when used with reflectance images whose value range from 0 to 1. Despite having addressed the issue with several implementation strategies, this clearly shows that there is room for improving the current spectral difference function.

In Chapter 4 Spectral Ordering Relation and Its Expected Properties we were able to define a dataset which would allow assessing the performance of multivariate ordering relations with regards to two spectral transformations we had previously identified, i.e., magnitude change and standard deviation change. The datasets were composed of color scales found in a pigment image datasets. Nevertheless, the assessment protocol can be improved by adding another dataset which would enable the assessment of multivariate ordering relations with respect to translation, which is a spectral transformation corresponding to hue shift in the color domain.

In Chapter 6 Spectral Rank Order Filters, we have extended impulse noise model to the spectral domain for assessing the performance of spectral ROF. And while this has allowed us to identify the limitations and advantages of our approach, a more realistic noise model would certainly give us a better idea of the performance of our approach in a real case. Then, despite having defined the protocol for reference selection in Chapter 5 Hyperspectral Image Analysis through Spectral Differences, we have not applied this to spectral ROF. Nevertheless, with a better reference selection following a specific goal, the results of spectral ROF can certainly be improved.

We have defined new spectral morphological gradients and used them for gradient-based watershed segmentation in Chapter 7 First Levels of Spectral Mathematical Morphology. However, the work we conducted here was only at a preliminary stage. Assessment protocols need to be defined, addressing both theoretical and metrological constraints. Additionally, to take fully into account the potential of the distance-based spectral morphological gradients, several models of gradient combination can be formulated to improve the final results of spectral image segmentation.

In Chapter 8 Crack Detection for Cultural Heritage Paintings, we have developed a full-band approach to spectral crack detection which was shown to be efficient. However, there are still plenty of rooms for improvements. First of all, the crack model can be improved such that it better represents a real case of cracking paint layer. For example, the crack width can be made non-uniform. Then, as for the method itself, more advanced morphological filters can be employed to improve the crack detection results. As of now we have only used top-hat transforms which are limited in the sense that it only works in a single scale. But in a real case, cracks do vary is their sizes. Thus, a multiscale morphological approach such as

the Multiple Objects Matching using Probing (MOMP) which was first introduced by Barat *et al*. [22] should certainly be employed. And having defined the spectral difference function and ordering relation, the extension of MOMP to the spectral domain will be straightforward.

The spectral MM framework we have obtained by the end of this study is by no means finished. We have only given the basic morphological tools from erosion and dilation to top-hat transforms. And as depicted in Fig. 9.1, there are a lot more tools to be developed. Various morphological filters can be obtained, allowing multiscale analysis of shape in an image. Fractal and texture analyses, classification purposes, pattern spectrum, they all can be further achieved and developed. And in addition to this spectral MM framework, the obtained spectral ROF will also lead to further developments of more advanced spectral nonlinear filters.

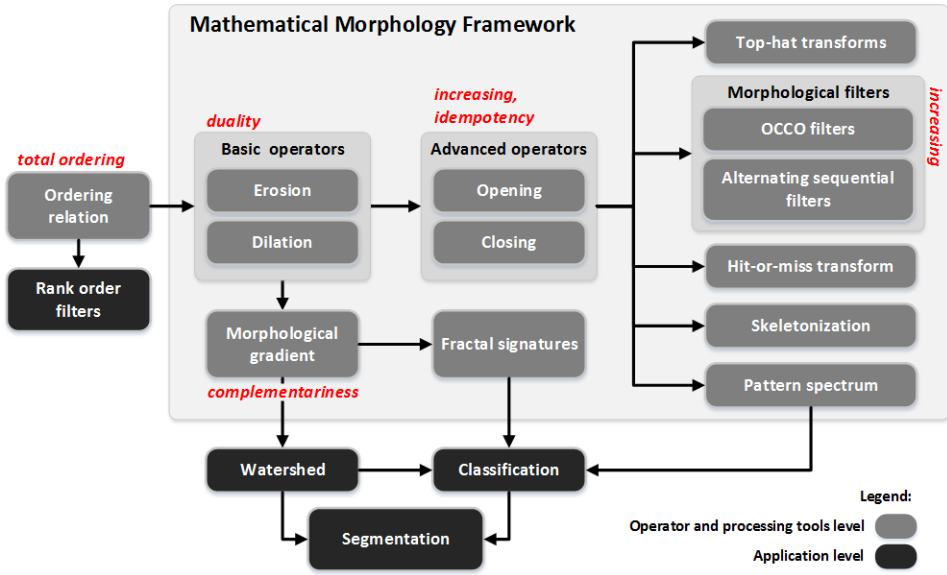

Figure 9.1 – Flowchart of the possible spectral image processing tools after the basic morphological tools.

Last but not least, the graphical representations of spectral differences we have introduced in Chapter 5 Hyperspectral Image Analysis through Spectral Differences can be further developed and used in classification purposes. Despite having only demonstrated them up to a three-dimensional case, by employing more spectral references we can obtain an n-dimensional feature space for a given image. And, ultimately, this feature space can be used in more advanced classification purposes.

9.3 Concluding Remarks

This study had been started with a believe that we need a hyperspectral image processing framework which respects the metrological aspects of a hyperspectral image, that it is a measure instead of only a mathematical or digital objects. This entails that one of the most common ways to deal with a hyperspectral image, i.e., through dimensionality reduction or band selection, cannot be considered as a solution. This is because the process will throw away the high resolution measures, at the same time losing accuracy. Thus, throughout the study, we have striven for a full-band spectral approach by means of a distance function.

Aiming to obtain a metrological framework, we have claimed that being mathematically valid is insufficient. Following the claim, in all stages of our image processing framework, we have assessment protocols for both theoretical and metrological constraints. These steps were usually followed by validation of usefulness in a real application task.

Through the different tools and their corresponding results, we have shown that imposing metrology to image processing is possible. And the rigorous validation works, starting from theoretical images to images from a real case where neither ground truth nor reference images are available, in the end has provided us with reliable image processing tools. And with such tools, we know what to expect and we can be sure of the relevance of our image processing results. It is such framework that we want to use for, e.g., quality control purposes.

Finally, the novel tools and operators we have developed might become obsolete in the future as research continues to progress. Nevertheless, one of the valuable contributions we have made lies in the quality assessment protocols we have formulated and developed. And the protocols, even though they can certainly be improved, has provided standards for hyperspectral image processing framework to develop in the future.

Part IV

Appendices

Appendix A

Comprehensive State of the Art of Spectral Difference Functions

Mathematical expressions for spectral distance functions included in Chapter 3 are provided in this appendix. However, note that spectral distance functions that were mentioned but did not come with mathematical formula will be excluded from the discussion in this appendix.

A.1 Vector Distance in the Euclidean Space

Many distance functions in this category can be generalized as the variations of L_p norms below.

$$d_{L_p}(S_1, S_2) = \left(\int_{\lambda_{\min}}^{\lambda_{\max}} |s_1(\lambda) - s_2(\lambda)|^p \, d\lambda \right)^{\frac{1}{p}}$$

Varying the order p will give us **fractional Minkowski** ($p < 1$) [5], **Manhattan** (p=1), **Euclidean** (p=2), and **Chebyshev** (p=∞) distance functions. Chebyshev distance can also be written as

$$d_{Che}(S_1, S_2) = \max_{\lambda}(|s_1(\lambda) - s_2(\lambda)|).$$

A.1.1 Weighted Manhattan Distance

Canberra distance [101], just as Manhattan distance, calculates energy or intensity difference but normalized by the total energy. It is written as

$$d_{Can}(S_1, S_2) = \int_{\lambda_{\min}}^{\lambda_{\max}} \frac{|s_1(\lambda) - s_2(\lambda)|}{|s_1(\lambda)| + |s_2(\lambda)|} \, d\lambda.$$

Sørensen distance [161], or also known as **Bray-Curtis distance**, uses cumulative energy over the entire spectrum as its weighting function. Note that Bray-Curtis distance is not to be confused with Bray-Curtis similarity. The distance formula is

$$d_{Sor}(S_1, S_2) = \frac{\int_{\lambda_{\min}}^{\lambda_{\max}} |s_1(\lambda) - s_2(\lambda)| \, d\lambda}{\int_{\lambda_{\min}}^{\lambda_{\max}} (s_1(\lambda) + s_2(\lambda)) \, d\lambda}.$$

Kulczynski distance [65] whose expression is as follows, normalizes intensity difference by the integral of overlapping region between two spectral functions,

$$d_{Kul}(S_1, S_2) = \frac{\int_{\lambda_{\min}}^{\lambda_{\max}} |s_1(\lambda) - s_2(\lambda)| \, d\lambda}{\int_{\lambda_{\min}}^{\lambda_{\max}} \min\{s_1(\lambda), s_2(\lambda)\} \, d\lambda}.$$

Lorentzian distance [65] can be regarded as Manhattan distance with logarithmic weight given to the intensity difference, see the formulation below. This weight is given such that the big differences do not have a greater significance than the smaller or median ones in the integration process.

$$d_{Lor}(S_1, S_2) = \int_{\lambda_{\min}}^{\lambda_{\max}} \ln(1 + |s_1(\lambda) - s_2(\lambda)|) \, d\lambda.$$

A.1.2 Weighted Euclidean Distance

An example of weighted Euclidean distance are **root mean square (RMS)** distance. Originally RMS is expressed as follows,

$$d_{RMS}(S_1, S_2) = \left(\frac{1}{n} \sum_{i=0}^{n-1} | \, s_1(\lambda_i) - s_2(\lambda_i) \, |^2 \right)^{\frac{1}{2}}$$

where a spectral function is expressed as a discrete array instead of a continuous function. Adapting the expression to a continuous definition, formula below is obtained. Note that the averaging factor n in the initial formula is modified into the range of spectral functions in use, i.e., $\lambda_{\max} - \lambda_{\min}$. This is because in the continuous form, spectral channel count n is no more defined.

$$d_{RMS}(S_1, S_2) = \left(\frac{1}{\lambda_{\max} - \lambda_{\min}} \int_{\lambda_{\min}}^{\lambda_{\max}} |s_1(\lambda) - s_2(\lambda)|^2 \, d\lambda \right)^{\frac{1}{2}}$$

There are also the two χ^2 distances whose formula are as follows. Per band intensity differences in χ_1^2 and χ_2^2 are normalized by squared total intensity and total

intensity, respectively.

$$d_{\chi_1^2}(S_1, S_2) = \int_{\lambda_{\min}}^{\lambda_{\max}} \frac{(s_1(\lambda) - s_2(\lambda))^2}{(s_1(\lambda) + s_2(\lambda))^2}\, d\lambda$$
$$d_{\chi_2^2}(S_1, S_2) = \frac{1}{2} \int_{\lambda_{\min}}^{\lambda_{\max}} \frac{(s_1(\lambda) - s_2(\lambda))^2}{s_1(\lambda) + s_2(\lambda)}\, d\lambda$$

Geman-McClure function [75] can be considered as squared Euclidean distance but normalized per spectral band with squared intensity difference. The formula is

$$d_{GMC}(S_1, S_2) = \int_{\lambda_{\min}}^{\lambda_{\max}} \frac{(s_1(\lambda) - s_2(\lambda))^2}{1 + (s_1(\lambda) - s_2(\lambda))^2}\, d\lambda.$$

A.1.3 Angular Distance

Distance functions that consider angular distance are, e.g., **cosine distance**

$$d_{cos}(S_1, S_2) = 1 - sim_{\cos}(S_1, S_2)$$

and **spectral angle**, which was originally developed in the context of Spectral Angle Mapper [97].

$$d_{SAM}(S_1, S_2) = \cos^{-1}(sim_{\cos}(S_1, S_2)).$$

As can be seen, the two functions are based on the calculation of cosine similarity between two spectra S_1 and S_2. The similarity function is written as

$$sim_{\cos}(S_1, S_2) = \frac{\int_{\lambda_{\min}}^{\lambda_{\max}} (s_1(\lambda) \cdot s_2(\lambda))\, d\lambda}{\left(\int_{\lambda_{\min}}^{\lambda_{\max}} s_1(\lambda)^2\, d\lambda\right)^{\frac{1}{2}} \left(\int_{\lambda_{\min}}^{\lambda_{\max}} s_2(\lambda)^2\, d\lambda\right)^{\frac{1}{2}}}.$$

A.2 Distance in N-Dimensional Manifold

Goodness-of-fit coefficient (GFC) [82] is developed based on Schwartz's inequality. In the Euclidean space, it is basically the cosine distance. Since GFC is originally a similarity function, the distance formulation is as follows,

$$d_{GFC}(S_1, S_2) = 1 - \frac{\left|\int_{\lambda_{\min}}^{\lambda_{\max}} s_1(\lambda) \cdot s_2(\lambda)\, d\lambda\right|}{\sqrt{\left|\int_{\lambda_{\min}}^{\lambda_{\max}} s_1(\lambda)^2\, d\lambda\right|} \sqrt{\left|\int_{\lambda_{\min}}^{\lambda_{\max}} s_2(\lambda)^2\, d\lambda\right|}}.$$

Let $\mathcal{S} = \{S_i, i = [0, L-1]\}$ be a set of spectral functions, distance between two spectral functions S_a and S_b is expressed by **isometric feature mapping (Isomap)** [170] as the sum of local distances d_{local} between S_i and S_j, where the list of S_i forms the shortest path $\mathcal{P}$ between S_a and S_b. In other words, the shortest path between S_a and S_b is formed by a chain of P spectra, see equation below where $S_0 = S_a,\ S_L = S_b,\ P \leq L$, and $S_i \neq S_j, \forall i \neq j$. d_{local} is typically Euclidean distance or dot product.

$$d_{isomap}(S_a, S_b) = \min\left(\sum_{i=0}^{P-1} d_{local}(S_i, S_{i+1})\right)$$

A.3 Distance between Distributions

Distance measures in this category consider a spectral function either as probability distribution function (PDF), cumulative distribution function (CDF), or discrete probability distribution (most commonly known as *histogram*). Then, depending on which definition is assumed, the following terms and expressions will be incorporated in the distance measures.

Total energy k and **average energy** m of a spectral function

$$k = \int_{\lambda_{\min}}^{\lambda_{\max}} s(\lambda)\, d\lambda \quad \text{and} \quad m = \frac{k}{\lambda_{\max} - \lambda_{\min}}$$

Average spectral function S_m

$$S_m = \frac{S_1 + S_2}{2} = \left\{ s_m(\lambda) = \frac{s_1(\lambda) + s_2(\lambda)}{2},\ \forall\lambda \in [\lambda_{\min}, \lambda_{\max}] \right\}$$

Standardized spectral function $\hat{S}$

$$\hat{S} = \{\hat{s}(\lambda) = s(\lambda) - m,\ \forall\lambda \in [\lambda_{\min}, \lambda_{\max}]\}$$

Normalized spectral function $\bar{S}$

$$\bar{S} = \left\{ \bar{s}(\lambda) = \frac{s(\lambda)}{k},\ \forall\lambda \in [\lambda_{\min}, \lambda_{\max}] \right\}$$

Average-normalized spectral function $\bar{S}_m$

$$\bar{S}_m = \frac{\bar{S}_1 + \bar{S}_2}{2} = \left\{ \bar{s}_m(\lambda) = \frac{\bar{s}_1(\lambda) + \bar{s}_2(\lambda)}{2},\ \forall\lambda \in [\lambda_{\min}, \lambda_{\max}] \right\}$$

A.3.1 Correlation-Based

Spectral correlation [54], originally a measure of similarity, is defined as follows.

$$R(S_1, S_2) = \frac{\int_{\lambda_{\min}}^{\lambda_{\max}} \widehat{s}_1(\lambda) \cdot \widehat{s}_2(\lambda)\, d\lambda}{\left(\int_{\lambda_{\min}}^{\lambda_{\max}} \widehat{s}_1(\lambda)^2\, d\lambda\right)^{\frac{1}{2}} \left(\int_{\lambda_{\min}}^{\lambda_{\max}} \widehat{s}_2(\lambda)^2\, d\lambda\right)^{\frac{1}{2}}}$$

Then, to fit our context of distance, the mathematical formulation of spectral correlation is modified into the equation below. Spectral correlation was said to be an improvement of spectral angle [54] for its capability to detect false positives.

$$d_{Cor}(S_1, S_2) = 1 - \frac{1 + R(S_1, S_2)}{2}$$

Pearson's χ^2, defined by the equation below, is a measure of how unlikely one distribution (or *spectral function*) was drawn from the population distribution (or *spectral set*) as represented by the average S_m. This measure is also known as χ^2 **statistic** [142, 149].

$$d_{Pea}(S_1, S_2) = \int_{\lambda_{\min}}^{\lambda_{\max}} \frac{(s_1(\lambda) - s_m(\lambda))^2}{s_m(\lambda)}$$

A.3.2 Measure of Area Under Curves

Smith distance measures the amount of intersection between two PDFs or histograms. Then it uses the minimum of total energy as normalizing factor. The function is formalized as the following.

$$d_{Smi}(S_1, S_2) = 1 - \frac{\int_{\lambda_{\min}}^{\lambda_{\max}} \min(s_1(\lambda), s_2(\lambda))\, d\lambda}{\min\left(\int_{\lambda_{\min}}^{\lambda_{\max}} s_1(\lambda)\, d\lambda, \int_{\lambda_{\min}}^{\lambda_{\max}} s_2(\lambda)\, d\lambda\right)}$$

Manhattan distance and its variations in Appendix A.1 can also be regarded as measures for area under curves, albeit with different assumptions of spectral function definition.

A.3.3 f-divergences

Given two spectral functions S_1 and S_2, f**-divergence** is defined as

$$div(\bar{S}_1, \bar{S}_2) = \int_{\lambda_{\min}}^{\lambda_{\max}} \bar{S}_1(\lambda) \cdot f\left(\frac{\bar{S}_1(\lambda)}{\bar{S}_2(\lambda)}\right)\, d\lambda,$$

where the normalized spectral functions are used instead of the initial ones.

Kullback-Leibler divergence [98], or shortly **KL-divergence**, is f-divergence functions employing $\ln$. Although non-negative, as seen in the equation below, KL-divergence is not symmetric since $KL(\bar{S}_1, \bar{S}_2) \neq KL(\bar{S}_2, \bar{S}_1)$.

$$KL(\bar{S}_1, \bar{S}_2) = \int_{\lambda_{\min}}^{\lambda_{\max}} \bar{S}_1(\lambda) \cdot \ln \frac{\bar{S}_1(\lambda)}{\bar{S}_2(\lambda)} \, d\lambda$$

Jeffrey divergence or **J-divergence** [85] was constructed to obtain a symmetric divergence. It is defined by

$$d_{JEF}(S_1, S_2) = div_J(\bar{S}_1, \bar{S}_2) = KL(\bar{S}_1, \bar{S}_2) + KL(\bar{S}_2, \bar{S}_1).$$

Spectral Information Divergence (**SID**) [42] is a measure commonly used in remote sensing field. Looking at its mathematical formulation, this measure is essentially a J-divergence.

K-divergence [112] is yet another directed divergence as KL-divergence. It is defined by

$$K(\bar{S}_1, \bar{S}_2) = KL(\bar{S}_1, \bar{S}_m) = \int_{\lambda_{\min}}^{\lambda_{\max}} \bar{S}_1(\lambda) \cdot \ln \frac{\bar{S}_1(\lambda)}{\bar{S}_m(\lambda)} \, d\lambda.$$

As can be observed from the equation above, K-divergence is also not symmetric. Using Jeffrey's symmetrization, **Jensen-Shannon divergence** [112] or **JS-divergence** is obtained. Its formula is as follows.

$$\begin{aligned} d_{JS}(S_1, S_2) &= div_{JS}(\bar{S}_1, \bar{S}_2) \\ &= \frac{1}{2} \left(K(\bar{S}_1, \bar{S}_2) + K(\bar{S}_2, \bar{S}_1) \right) \\ &= \frac{1}{2} \left(KL(\bar{S}_1, \bar{S}_m) + KL(\bar{S}_2, \bar{S}_m) \right) \end{aligned}$$

It should also be noted that several studies [114, 142, 149] uses **empirical Jeffrey divergence** to deal with histogram values. This empirically-derived J-divergence is said to be numerically stable, symmetric, and robust with respect to noise and the size of histogram bins [142]. See the mathematical expression below.

$$d_{EJ}(S_1, S_2) = 2 \cdot (KL(S_1, S_m) + KL(S_2, S_m))$$

A.3.4 Other Distance Functions

Other distance functions include, e.g.,**Squared chord distance** [132]

$$d_{SqC}(S_1, S_2) = \int_{\lambda_{\min}}^{\lambda_{\max}} \left(\sqrt{s_1(\lambda)} - \sqrt{s_2(\lambda)} \right)^2,$$

and the transformation-cost based distance, i.e., **Earth mover's distance** (EMD) [149]. EMD computes the necessary minimal cost to transform one distribution to another. The first step is to find a flow $F = [f_{ij}]$ which minimizes the overall cost $EMD(S_1, S_2, F)$ below. Then, EMD distance d_{EMD} is a normalized version of EMD cost. More details of EMD distance implementation and constraints can be found in [149].

$$EMD(S_1, S_2, F) = \sum_{i=1}^{m} \sum_{j=1}^{n} d_{ij} \cdot f_{ij}$$

$$d_{EMD}(S_1, S_2) = \frac{EMD(S_1, S_2, f)}{\sum_{i=1}^{m} \sum_{j=1}^{n} f_{ij}}$$

In order to embed intensity differences in the distance measure, EMD distance was further developed into a Combined EMD [104] as follows,

$$d_{C_{EMD}}(S_1, S_2) = \frac{1}{\alpha} \cdot d_{EMD}(S_1, S_2) + \frac{1}{\beta} \cdot (\|S_1\| - \|S_2\|)$$

where α and β are two parameters required to manage the importance of each part of the distance function. In our implementation, we modify $\beta = 1 - \alpha$.

Appendix B

Hyperspectral Image Datasets

In the following, hyperspectral image dataset employed throughout the study will be described. Visualization methods used to generate the color images can be seen in Chapter 2. Also, note that due to considerations which have been elaborated in Chapter 5, the first and last 10 bands from the spectral images are never taken into account in computation. The number of spectral bands mentioned in the following are numbers of acquired spectral bands, prior to the removal of 10 bands at each of the extremities.

B.1 Pigment-56

Several pigment charts were acquired by hyperspectral scanner A (see Section B.5) and their reflectance signals were obtained (see Section B.6). Each acquired images consist of 160 spectral bands, from 414.62 to 992.50 nm, in 3.63 nm interval. An example of the pigment charts is shown in Fig. B.1. As seen in the figure, a pigment chart contains several pigment patches. Pigment-56 dataset is composed of 56 isolated pigment patches, each of different hues. Examples of the isolated pigment patches can be seen in Fig. B.2. Then, since each pigment patch consists of four different brightness levels, in the dataset there are a total of 56×4 different color patches. Example spectral reflectance functions taken from two pigment patches, each with 4 different brightness levels, can be seen in Fig. B.3.

Figure B.1 – An example of hyperspectrally acquired pigment chart, which is the origin of Pigment-56 dataset.

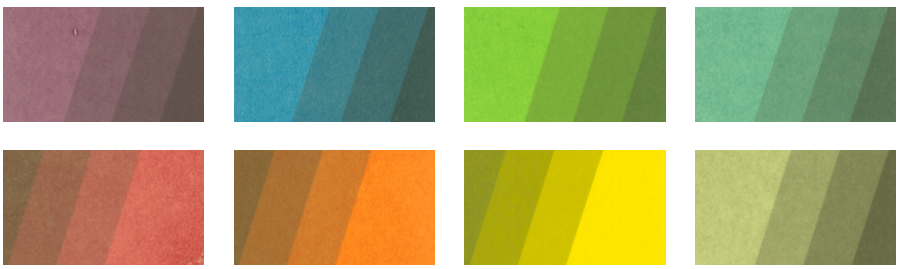

Figure B.2 – Several isolated pigment patches in the Pigment-56 dataset. Shown color images were generated using CLTR visualization method.

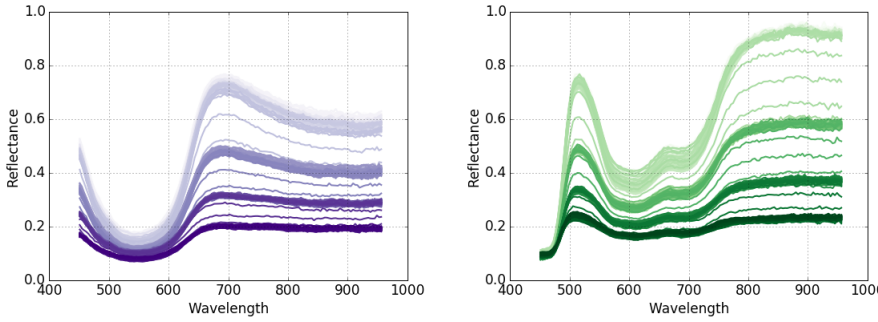

Figure B.3 – Spectral reflectance functions obtained from two pigment patches.

Using an equi-energetic black and white spectral reflectance functions S_{Bk} and S_{Wh} as references, distributions of spectral difference values of these colors in a bidimensional histogram of spectral differences (BHSD) can be observed in Fig. B.4. Note that the 56 colors shown in the BHSDs are obtained at random from their corresponding color patches. From the two BHSDs we can observe that spectral variations which exist in the dataset are dominated by intensity rather than shape differences. To further observe distribution of spectral differences within each individual pigment patches, BHSDs obtained using S_{Wh} as reference from some of the patches are shown in Fig. B.5.

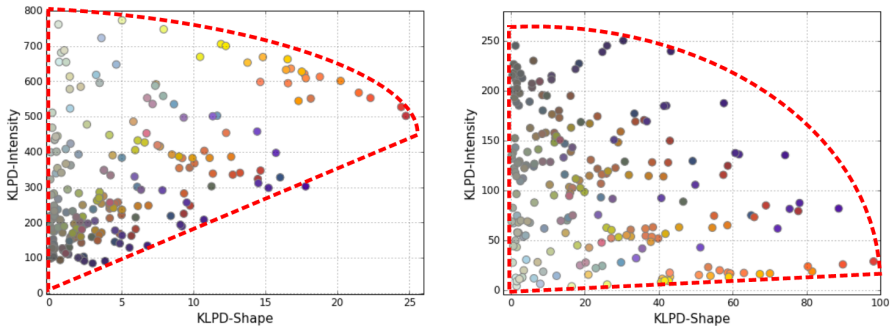

(a) BHSD relative to S_{Bk}

(b) BHSD relative to S_{Wh}

Figure B.4 – Distribution of spectral differences of spectral functions found in Pigment-56, shown in BHSDs obtained using two references, i.e., equi-energetic black S_{Bk} and white S_{Wh}.

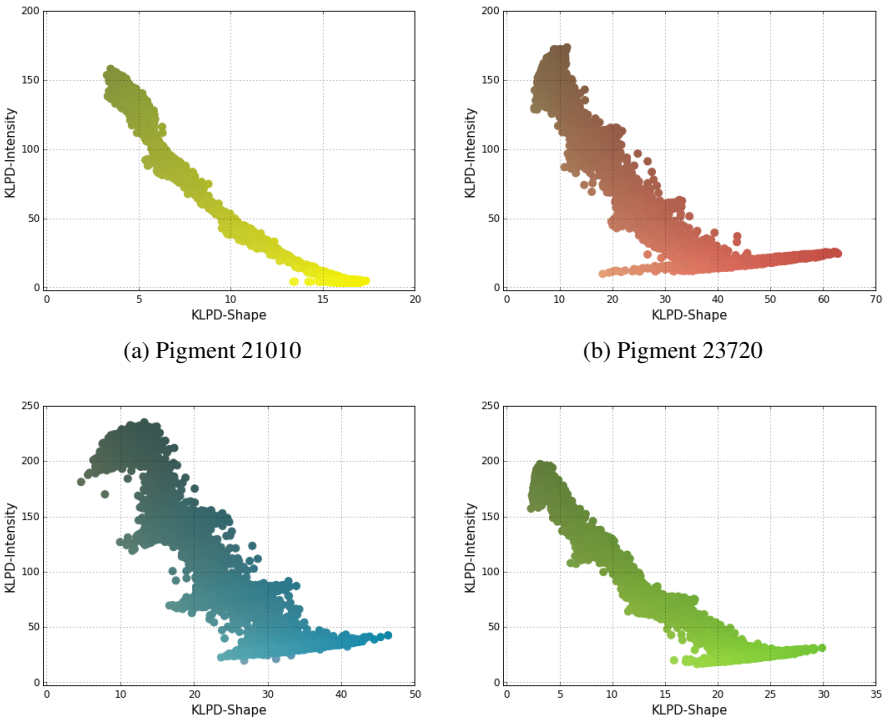

(a) Pigment 21010

(b) Pigment 23720

(c) Pigment 45080

(d) Pigment 44500

Figure B.5 – BHSDs of several pigment patches, obtained by employing an equi-energetic white spectral function S_{Wh} as reference. Horizontal and vertical axes of all BHSDs are KLPD-Shape and KLPD-Intensity, respectively.

B.2 Subsets-250

In Subsets-250 dataset, in total there are 8 images originating from various hyperspectrally acquired objects, see Fig. B.6, each represented in terms of spectral reflectance and of spatial dimension 250×250 pixels. Detailed description of the images are provided in the following.

FN1, FN2 These two images are subsets of a painting by Fritz Thaulow, i.e., The Old Factory, Akerselva (1901). The painting itself is owned/ exhibited at the Lillehammer Kunstmuseum in Lillehammer, Norway. The hyperspectral image is originally of 160 spectral bands, i.e., within spectral range of 414.20 and 993.67 nm, in 3.64 nm interval. They were acquired using scanner A (Section B.5). The maximum reflectance value of the original image exceeds 1. And since the implementation of framework developed in this study requires value range between 0 and 1, each subset image $\mathcal{S}_I$ is normalized according to the following formula.

$$\tilde{I}(x) = \frac{I(x) - \min(\mathcal{S}_I)}{\max(\mathcal{S}_I) - \min(\mathcal{S}_I)}$$

NP1, NP2 The two images are subsets of two documents provided by the Norwegian National Library, acquired using scanner A (Section B.5). NP1 and NP2 are of identical spectral resolution to FN1 and FN2.

PN1, PN2 The two images are subsets of a pastel painting of unknown painter, originating from a private collection. The acquired hyperspectral image was of 182 spectral bands, from 412.45 to 989.77 nm, in 3.19 nm interval. They were acquired using scanner B (Section B.5). The original reflectance image has a maximum value which exceeds 1. Therefore, the two subsets are normalized/ scaled using the same procedure as FN1 and FN2.

SC1, SC2 The two image are subsets of The Scream (1893) painting by Edvard Munch, taken from the front side (*recto*) of the painting. The Scream (1893) itself is located in the National Gallery, Oslo, Norway. The original hyperspectral image is of 160 spectral bands, from 414.62 to 992.50 nm, in 3.63 nm interval. They were acquired using scanner A (Section B.5).

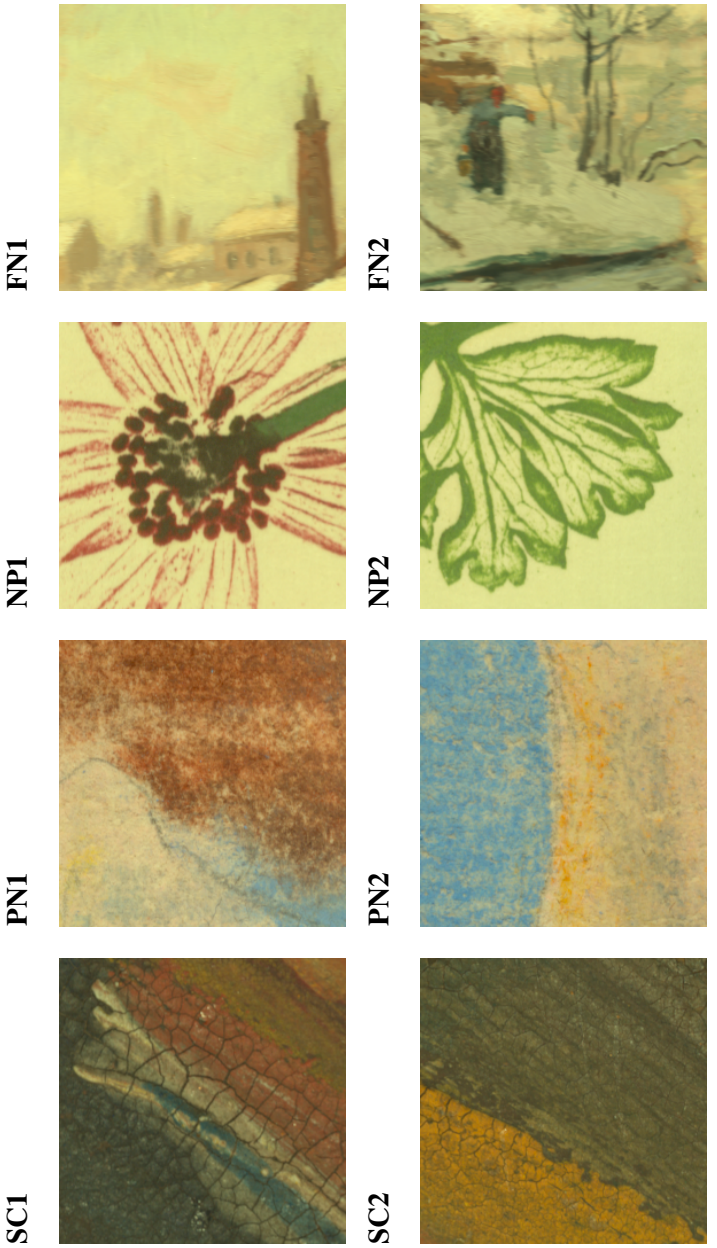

Figure B.6 – All 8 images in the Subsets-250 dataset. Shown color images were generated using CLTR visualization method.

B.3 Cracks-200

Cracks-200 dataset consists of subsets of The Scream (1893) painting by Edvard Munch, where each image subset has the spatial dimension of 200×200 pixels. In total, there are 15 subset images, taken from various locations of the front side (*recto*) of the painting where cracks occur. All of the images are shown in Fig. B.7 and B.8. Shown color images are generated using ENVI software platform [69].

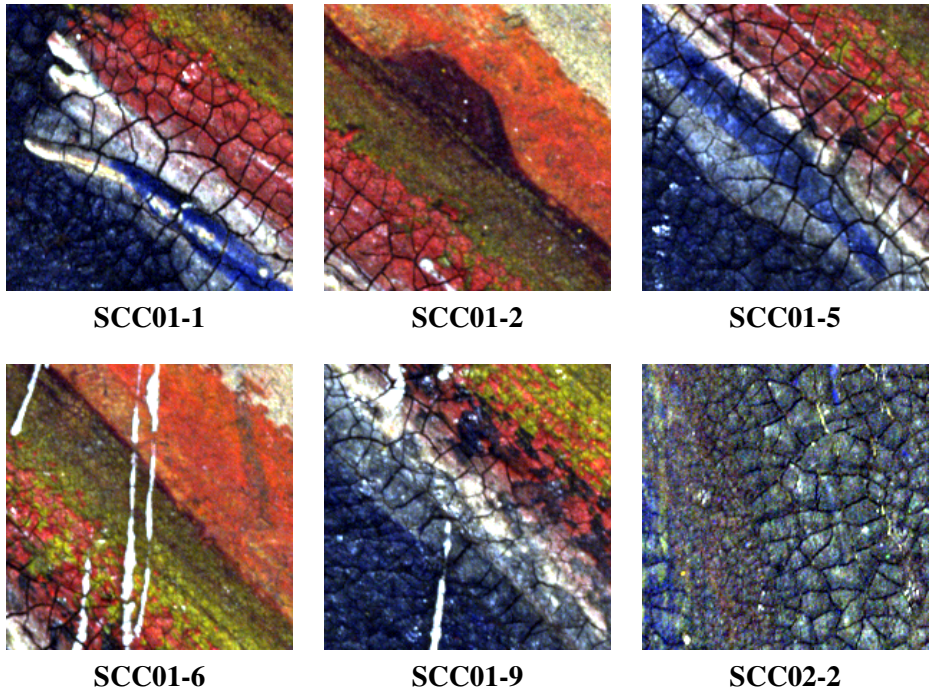

SCC01-1 **SCC01-2** **SCC01-5**

SCC01-6 **SCC01-9** **SCC02-2**

Figure B.7 – Six out of 15 images from the Cracks-200 dataset. Shown color images are generated using ENVI software platform.

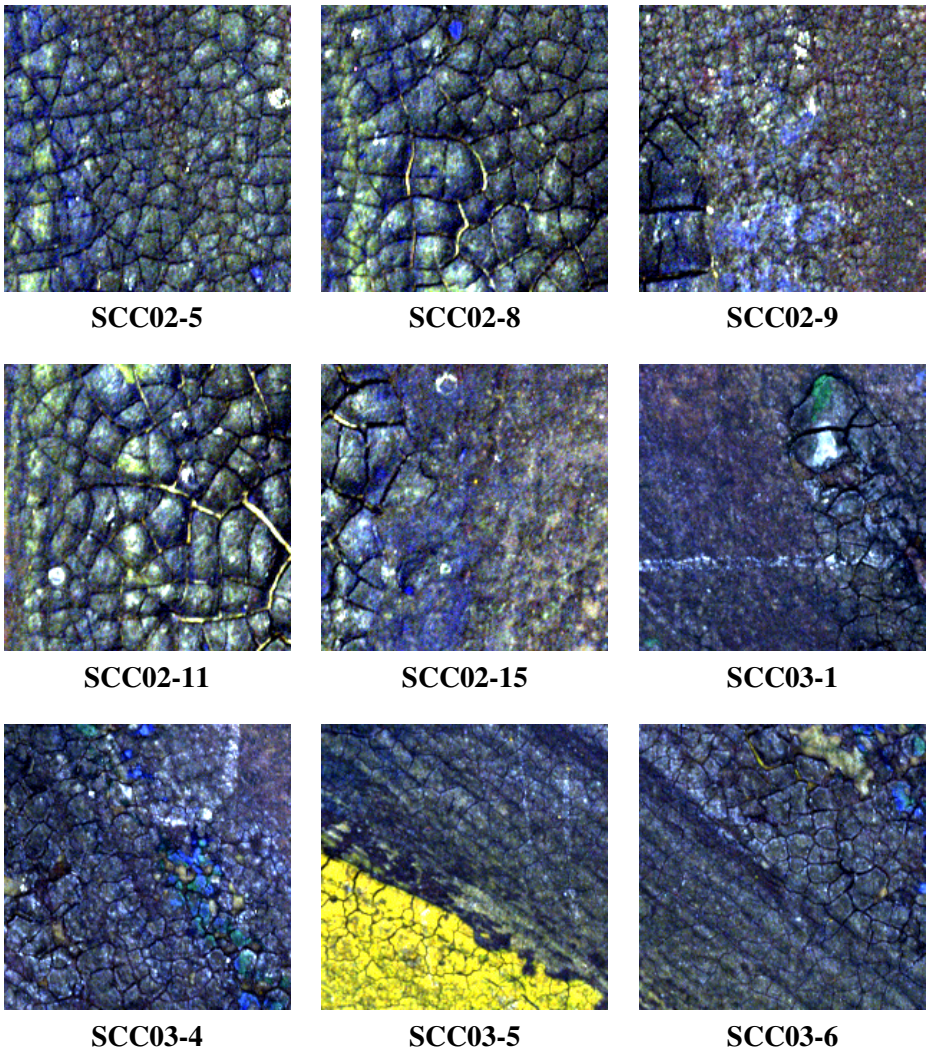

Figure B.8 – Nine out 15 images from the Cracks-200 dataset. Shown color images are generated using ENVI software platform.

B.4 Image Naming Convention

In the following are consensus used to name each figure from all datasets in the previous sections.

Pigment-56 The number **56** in Pigment-56 is to state that there are 56 pigment images in the dataset. Then, each pigment patch is named with a 5-digit number, e.g., 21010, which corresponds to its pigment number which can be found in the corresponding pigment chart, see Fig. B.1.

Subsets-250 Name of the dataset is derived from the fact that images in this dataset are subsets of larger images and they are of size 250×250 pixels. **FN** and **PN** are abbreviations of **Fritz Normalized** and **Pastel Normalized**, respectively. FN images are from a painting by **Fritz Thaulow**. PN images come from a **pastel** painting. **NP** is an abbreviation of **Natural Printing**, which is the original filename of the larger images where NP1 and NP2 are extracted from. **SC** images are subsets from The **Scream** painting.

Cracks-200 Name of the dataset was given to describe that images in this dataset came from cracking layers of a painting, i.e., The Scream (1896) by Edvard Munch, and that each image is of size 200×200 pixels. Images in this dataset are named **SCC** to stand for **Scream, Cracks**. The two digits following SCC, e.g., SCC01, is used to identify the different regions of interests (ROIs) in the original painting where crack occurs. Then, the rest of the digits are to indicate the number of partition in each ROI.

B.5 Specifications of Hyperspectral Scanners

In the following are two hyperspectral scanners employed to capture all the aforementioned hyperspectral images.

Scanner A is a hyperspectral line scanner HySpex VNIR-1600 manufactured by NEO. It captures images in the visible and near infrared spectral range, from 400 to 1000 nm with 160 spectral bands. The VNIR-1600 has a spectral sampling of 3.6 nm and captures 1600 spatial pixels across the field of view. Detailed specification of HySpex VNIR-1600 can be found in [128].

Scanner B is a hyperspectral line scanner HySpex VNIR-1800 manufactured by NEO. It operates in the visible and the near infrared (VNIR) region of the electromagnetic spectrum, between 400 and 1000 nanometer, with a spectral sampling interval of 3.26 nm and captures 182 bands. Detailed specification of HySpex VNIR-1800 can be found in [129].

B.6 Reflectance Estimation Procedure

In each hyperspectral acquisition, the object of interest is captured together with a calibration target, e.g., Spectralon® Diffuse Reflectance Standards [100]. Since the spectral reflectance measures of this target is known, spectral power distribution (SPD) of the light source used at the acquisition can be retrieved by the following equation, where "observed radiance" is the amount of light recorded by the hyperspectral scanner.

$$\text{light source SPD} = \frac{\text{observed radiance}}{\text{spectralon reflectance}}$$

Then, reflectance of the captured object or scene can be obtained by the following equation.

$$\text{object reflectance} = \frac{\text{observed radiance}}{\text{light source SPD}}$$

Acknowledgment

Pigment-56 Hyperspectral acquisition of the pigment charts was conducted by Norsk Elektro Optikk AS (NEO). Reflectance estimation of the acquired radiance data were carried out by Dr. Sony George (SG).

Subsets-250: FN1, FN2 Hyperspectral acquisition and spectral reflectance estimation were both carried out by SG [76].

Subsets-250: NP1, NP2 Hyperspectral acquisition of the images was carried out under "Hyperspectral Imaging and Analysis of Ancient Manuscripts" project, funded by the Regional Research Foundation Innlandet, by a team of researchers from NTNU Gjøvik (Gjøvik University College at the time). The Norwegian National Library, who provided the manuscripts, was one of the partners in the project. Reflectance estimation of the acquired images was conducted by SG.

Subsets-250: PN1, PN2 Hyperspectral acquisition and spectral reflectance estimation were both carried out by NEO.

Subsets-250: SC1, SC2; Cracks-200 Hyperspectral acquisition was carried out by a team of researchers from NEO and NTNU Gjøvik (Gjøvik University College at the time) within the context of HyPerCept project, see [81].

Bibliography

[1] Colorimetry, 3rd ed. Technical Report 15:2004, Commission Internationale de L'Éclairage, Vienna, Austria, 2004.

[2] F. S. Abas and K. Martinez. Craquelure analysis for content-based retrieval. In *Digital Signal Processing, 2002 14th International Conference on*, volume 1, pages 111–114 vol.1, 2002.

[3] F. M. Abed. *Pigment Identification of Paintings Based on Kubelka–Munk Theory and Spectral Images*. PhD thesis, Rochester Institute of Technology, Rochester, NY, USA, Jul 2014.

[4] S. Agarwal, R. Sharma, and R. Dubey. Sketch based image retrieval using watershed transformation. In *Computational Intelligence Communication Technology (CICT), 2016 Second International Conference on*, pages 160–165, Feb 2016.

[5] C. C. Aggarwal, A. Hinneburg, and D. A. Keim. On the surprising behavior of distance metrics in high dimensional space. In J. Van den Bussche and V. Vianu, editors, *Database Theory — ICDT 2001*, volume 1973 of *Lecture Notes in Computer Science*, pages 420–434. Springer Berlin Heidelberg, 2001.

[6] N. Alajlan and E. Jernigan. *An Effective Detail Preserving Filter for Impulse Noise Removal*, pages 139–146. Springer Berlin Heidelberg, Berlin, Heidelberg, 2004.

[7] M. S. Alam and P. Sidike. Trends in oil spill detection via hyperspectral imaging. In *Electrical Computer Engineering (ICECE), 2012 7th International Conference on*, pages 858–862, Dec 2012.

[8] J. Angulo and J. Serra. Morphological coding of color images by vector connected filters. In *Signal Processing and Its Applications, 2003 Seventh International Symposium on*, volume 1, pages 69–72, Jul 2003.

[9] J. Angulo. Unified morphological color processing framework in a lum/sat/hue representation. In C. Ronse, L. Najman, and E. Decencière, editors, *Mathematical Morphology: 40 Years On*, volume 30 of *Computational Imaging and Vision*, pages 387–396. Springer Netherlands, 2005.

[10] J. Angulo. Morphological colour operators in totally ordered lattices based on distances: Application to image filtering, enhancement and analysis. *Computer Vision and Image Understanding*, 107(1-2):56–73, 2007.

[11] E. Aptoula, N. Courty, and S. Lefèvre. An end-member based ordering relation for the morphological description of hyperspectral images. In *Image Processing (ICIP), 2014 IEEE International Conference on*, pages 5097–5101, Oct 2014.

[12] E. Aptoula and S. Lefèvre. A comparative study on multivariate mathematical morphology. *Pattern Recognition*, 40(11):2914–2929, Feb 2007.

[13] E. Aptoula and S. Lefèvre. Pseudo multivariate morphological operators based on α-trimmed lexicographical extrema. In *Image and Signal Processing and Analysis, 2007 5th International Symposium on*, pages 367–372, Sep 2007.

[14] E. Aptoula and S. Lefèvre. α-trimmed lexicographical extrema for pseudo-morphological image analysis. *Journal of Visual Communication and Image Representation*, 19(3):165–174, Apr 2008.

[15] E. Aptoula and S. Lefèvre. On lexicographical ordering in multivariate mathematical morphology. *Pattern Recognition Letters*, 29(2):109–118, Jan 2008.

[16] E. Aptoula, S. Lefèvre, and C. Collet. Mathematical morphology applied to the segmentation and classification of galaxies in multispectral images. In *14th European Signal Processing Conference (EUSIPCO)*, pages 1–5, Sep 2006.

[17] J. Astola, P. Haavisto, P. Heinonen, and Y. Neuvo. Median type filters for color signals. In *Circuits and Systems, IEEE International Symposium on*, volume 2, pages 1753–1756, Jun 1988.

[18] J. Astola, P. Haavisto, and Y. Neuvo. Vector median filters. *Proceedings of the IEEE*, 78(4):678–689, Apr 1990.

[19] T. L. Austin Jr. An approximation to the point of minimum aggregate distance. *Metron*, 19:10–21, 1959.

[20] X. Bai and F. Zhou. New alternating sequential filters and the application for impulsive noise removal. In *Image and Signal Processing (CISP), 2010 3rd International Congress on*, volume 3, pages 1088–1091, Oct 2010.

[21] L. Bar, A. Brook, N. Sochen, and N. Kiryati. Color image deblurring with impulsive noise. In N. Paragios, O. Faugeras, T. Chan, and C. Schnörr, editors, *Variational, Geometric, and Level Set Methods in Computer Vision*, volume 3752 of *Lecture Notes in Computer Science*, pages 49–60. Springer Berlin Heidelberg, 2005.

[22] C. Barat, C. Ducottet, and M. Jourlin. Pattern matching using morphological probing. In *Image Processing, 2003. ICIP 2003. Proceedings. 2003 International Conference on*, volume 1, pages 369–372, Sep 2003.

[23] V. Barnett. The ordering of multivariate data. *Journal of the Royal Statistical Society. Series A (General)*, 139(3):318–355, 1976.

[24] M. Barni, F. Bartolini, and V. Cappellini. Image processing for virtual restoration of artworks. *IEEE MultiMedia*, 7(2):34–37, Apr 2000.

[25] M. Barni and V. Cappellini. On the computational complexity of multivariate median filters. *Signal Processing*, 71(1):45–54, 1998.

[26] M. Bartkowiak and M. Domanski. Vector median filters for processing of color images in various color spaces. In *Image Processing and its Applications, 1995 Fifth International Conference on*, pages 833–836, Jul 1995.

[27] C. B. Bell and H. S. Haller. Bivariate symmetry tests: Parametric and nonparametric. *The Annals of Mathematical Statistics*, 40(1):259–269, 1969.

[28] S. Beucher and F. Meyer. The morphological approach to segmentation: the watershed transformation. In E. Dougherty, editor, *Mathematical morphology in image processing*, volume 34 of *Optical Engineering*, chapter 12, pages 433–481. Marcel Dekker, New York, 1993.

[29] S. Bhattacharya, K. S. Malyavantham, R. Acharya, and R. Berezney. Fractal analysis of replication site images of the human cell nucleus. In *Engineering in Medicine and Biology Society (IEMBS), 2004 26th Annual International Conference of the IEEE*, volume 1, pages 1443–1446, Sep 2004.

[30] F. Brackx, N. De Schepper, and F. Sommen. The Clifford-Fourier transform. *Journal of Fourier Analysis and Applications*, 11(6):669–681, Nov 2005.

[31] M. Brand. Charting a manifold. In *Advances in Neural Information Processing Systems*, volume 15, pages 961–968. MIT Press, 2003.

[32] J.-C. Bricola, M. Bilodeau, and Serge. A multi-scale and morphological gradient preserving contrast. In *Stereology and Image Analysis, 14th International Congress for*, pages 1–4, Jul 2015.

[33] S. Bucklow. The effect of craquelure on the perception of the pictorial image. *Zeitschrift für Kunsttechnologie und Konservierung*, 8(1):104–111, 1994.

[34] S. Bucklow. The description and classification of craquelure. *Studies in Conservation*, 44(4):233–244, 1999.

[35] J. B. Campbell and R. H. Wynne. *Introduction to Remote Sensing*, chapter Electromagnetic Radiation, pages 31–58. Guilford Press, 5th edition, Jun 2011.

[36] J. B. Campbell and R. H. Wynne. *Introduction to Remote Sensing*, chapter Hyperspectral Remote Sensing, pages 429–444. Guilford Press, 5th edition, Jun 2011.

[37] J. B. Campbell and R. H. Wynne. *Introduction to Remote Sensing*, chapter Digital Imagery, pages 101–129. Guilford Press, 5th edition, Jun 2011.

[38] P. Carré, P. Denis, and C. Fernandez-Maloigne. Spatial color image processing using Clifford algebras: application to color active contour. *Signal, Image and Video Processing*, 8(7):1357–1372, 2014.

[39] A. Casini, F. Lotti, and M. Picollo. Imaging spectroscopy for the non-invasive investigation of paintings. In T. Asakura, editor, *International Trends in Optics and Photonics: ICO IV*, pages 343–356. Springer Berlin Heidelberg, Berlin, Heidelberg, 1999.

[40] M. E. Celebi, H. A. Kingravi, and Y. A. Aslandogan. Nonlinear vector filtering for impulsive noise removal from color images. *Journal of Electronic Imaging*, 16(3):033008–033008–21, Oct 2007.

[41] R. H. Chan, C.-W. Ho, and M. Nikolova. Salt-and-pepper noise removal by median-type noise detectors and detail-preserving regularization. *Image Processing, IEEE Transactions on*, 14(10):1479–1485, Oct 2005.

[42] C.-I. Chang. Spectral information divergence for hyperspectral image analysis. In *Geoscience and Remote Sensing Symposium (IGARSS), 1999 IEEE International Conference on*, volume 1, pages 509–511 vol.1, 1999.

[43] J. Chanussot and P. Lambert. Bit mixing paradigm for multivalued morphological filters. In *Image Processing and Its Applications, 6th IEE International Conference on*, volume 2, pages 804–808, Jul 1997.

[44] J. Chanussot and P. Lambert. Watewater approaches for color image segmentation. In *Nonlinear Signal and Image Processing, IEEE Workshop on*, pages 129–133, Jun 1999.

[45] E. Chevallier and J. Angulo. Image adapted total ordering for mathematical morphology on multivariate images. In *Image Processing (ICIP), IEEE International Conference on*, pages 2943–2947, Oct 2014.

[46] G. K. Choudhary and S. Dey. Crack detection in concrete surfaces using image processing, fuzzy logic, and neural networks. In *Advanced Computational Intelligence (ICACI), 2012 IEEE Fifth International Conference on*, pages 404–411, Oct 2012.

[47] D. C. Comer. *Petra and the Paradox of a Great City Built by Nomads: An Explanation Suggested by Satellite Imagery*, pages 73–83. Springer New York, New York, NY, Nov 2013.

[48] B. Cornelis, A. Dooms, F. Leen, A. Munteanu, and P. Schelkens. Multispectral imaging for digital painting analysis: a Gauguin case study. *Proc. SPIE*, 7798:77980I–77980I–13, 2010.

[49] N. Courty, E. Aptoula, and S. Lefèvre. A classwise supervised ordering approach for morphology based hyperspectral image classification. In *Pattern Recognition (ICPR), 2012 21st International Conference on*, pages 1997–2000, Nov 2012.

[50] M. M. Crawford, L. Ma, and W. Kim. Exploring nonlinear manifold learning for classification of hyperspectral data. In S. Prasad, L. M. Bruce, and J. Chanussot, editors, *Optical Remote Sensing*, volume 3 of *Augmented Vision and Reality*, pages 207–234. Springer Berlin Heidelberg, 2011.

[51] A. Căliman, M. Ivanovici, N. Richard, and G. Toacşe. A multivariate mathematical morphology based on orthogonal transformation, probabilistic extrema estimation and distance optimization. In C. L. L. Hendriks, G. Borgefors, and R. Strand, editors, *Mathematical Morphology and Its Applications*

to Signal and Image Processing, volume 7883 of *Lecture Notes in Computer Science*, pages 255–266. Springer Berlin Heidelberg, 2013.

[52] F. J. Damerau. A technique for computer detection and correction of spelling errors. *Commun. ACM*, 7(3):171–176, Mar 1964.

[53] B. B. Damodaran and R. R. Nidamanuri. Dynamic linear classifier system for hyperspectral image classification for land cover mapping. *Selected Topics in Applied Earth Observations and Remote Sensing, IEEE Journal of*, 7(6):2080–2093, Jun 2014.

[54] O. de Carvalho Jr., R. Guimaraes, R. Gomes, A. de Carvalho, N. da Silva, and E. Martins. Spectral multiple correlation mapper. In *Geoscience and Remote Sensing Symposium (IGARSS), 2006 IEEE International Conference on*, pages 2773–2776, Jul 2006.

[55] H. Deborah, N. Richard, and J. Y. Hardeberg. On the quality evaluation of spectral image processing algorithms. In *Signal-Image Technology and Internet-Based Systems (SITIS), 2014 Tenth International Conference on*, pages 133–140, Nov 2014.

[56] H. Deborah, N. Richard, and J. Y. Hardeberg. A comprehensive evaluation of spectral distance functions and metrics for hyperspectral image processing. *Selected Topics in Applied Earth Observations and Remote Sensing, IEEE Journal of*, 8(6):3224–3234, Jun 2015.

[57] H. Deborah, N. Richard, and J. Y. Hardeberg. Hyperspectral crack detection in paintings. In *Colour and Visual Computing Symposium (CVCS)*, pages 1–6, Aug 2015.

[58] H. Deborah, S. George, and J. Y. Hardeberg. Pigment mapping of The Scream (1893) based on hyperspectral imaging. In A. Elmoataz, O. Lezoray, F. Nouboud, and D. Mammass, editors, *Image and Signal Processing*, volume 8509 of *Lecture Notes in Computer Science*, pages 247–256. Springer International Publishing, Jun 2014.

[59] H. Deborah, N. Richard, and J. Y. Hardeberg. Spectral ordering assessment using spectral median filters. In J. A. Benediktsson, J. Chanussot, L. Najman, and H. Talbot, editors, *Mathematical Morphology and Its Applications to Signal and Image Processing*, volume 9082 of *Lecture Notes in Computer Science*, pages 387–397. Springer International Publishing, May 2015.

[60] H. Deborah, N. Richard, and J. Y. Hardeberg. Vector crack detection for cultural heritage paintings. In *Traitement et Analyse de l'Information Méthodes et Applications (TAIMA)*, May 2015.

[61] H. Deborah, N. Richard, and J. Hardeberg. Spectral impulse noise model for spectral image processing. In A. Trémeau, R. Schettini, and S. Tominaga, editors, *Computational Color Imaging*, volume 9016 of *Lecture Notes in Computer Science*, pages 171–180. Springer International Publishing, Feb 2015.

[62] C.-H. Demarty and S. Beucher. Color segmentation algorithm using an HLS transformation. In *Mathematical Morphology and Its Applications to Image and Signal Processing, 1998 Fourth International Symposium on*, ISMM '98, pages 231–238, Norwell, MA, USA, 1998. Kluwer Academic Publishers.

[63] P. Denis, P. Carré, and C. Fernandez-Maloigne. Spatial and spectral quaternionic approaches for colour images. *Computer Vision and Image Understanding*, 107(1-2):74–87, 2007. Special issue on color image processing.

[64] S. D. Desai, K. V. Horadi, P. Navaneet, B. Niriksha, and V. Siddeshvar. Detection and removal of cracks from digitized paintings and images by user intervention. In *Advanced Computing, Networking and Security, 2013 2nd International Conference on*, pages 51–55, Dec 2013.

[65] E. Deza and M.-M. Deza. *Dictionary of Distances*. Elsevier Science, Amsterdam, The Netherlands, 2006.

[66] M. C. d'Ornellas and J. A. T. Borges da Costa. Color mathematical morphology based on partial ordering of spectra. In *Computer Graphics and Image Processing, XX Brazilian Symposium on*, pages 37–44, 2007.

[67] J. Dumont, T. Hirvonen, V. Heikkinen, M. Mistretta, L. Granlund, K. Himanen, L. Fauch, I. Porali, J. Hiltunen, S. Keski-Saari, M. Nygren, E. Oksanen, M. Hauta-Kasari, and M. Keinänen. Thermal and hyperspectral imaging for Norway spruce (Picea abies) seeds screening. *Computers and Electronics in Agriculture*, 116:118–124, Mar 2015.

[68] M. T. Eismann. *Hyperspectral Remote Sensing*. SPIE Press, 2012.

[69] Exelis Visual Information Solutions, Inc. ENVI software platform. `http://www.harrisgeospatial.com/ProductsandSolutions/GeospatialProducts/ENVI.aspx`. Retrieved October 2016.

[70] W. Fang and W. Youxian. Detecting preserved eggshell crack using machine vision. In *Information Technology, Computer Engineering and Management Sciences (ICM), 2011 International Conference on*, volume 3, pages 62–65, Sep 2011.

[71] A. M. Fernandes, C. Franco, A. Mendes-Ferreira, A. Mendes-Faia, P. L. da Costa, and P. Melo-Pinto. Brix, pH and anthocyanin content determination in whole Port wine grape berries by hyperspectral imaging and neural networks. *Computers and Electronics in Agriculture*, 115:88–96, Jul 2015.

[72] L. Gan and Q. Liu. Eye detection based on rank order filter and projection function. In *Computer Design and Applications (ICCDA), 2010 International Conference on*, volume 1, pages V1–642–V1–645, Jun 2010.

[73] S. Garg and G. Sahoo. Crack classification and interpolation of old digital paintings. *Journal of Computer Sciences and Applications*, 1(5):85–90, 2013.

[74] D. G. Gavin, W. Oswald, E. R. Wahl, and J. W. Williams. A statistical approach to evaluating distance metrics and analog assignments for pollen records. *Quaternary Research*, 60(3):356–367, 2003.

[75] S. Geman and D. McClure. Statistical methods for tomographic image reconstruction. *Bulletin of the International Statistical Institute*, II:4–5, 1987.

[76] S. George and J. Y. Hardeberg. Estimation and correction of geometric distortion in pushbroom hyperspectral system for imaging art paintings. *Electronic Imaging: Image Sensors and Imaging Systems*, 2016(12):1–4, 2016.

[77] P. Ghamisi, J. A. Benediktsson, G. Cavallaro, and A. Plaza. Automatic framework for spectral-spatial classification based on supervised feature extraction and morphological attribute profiles. *IEEE Journal of Selected Topics in Applied Earth Observations and Remote Sensing*, 7(6):2147–2160, Jun 2014.

[78] I. Giakoumis, N. Nikolaidis, and I. Pitas. Digital image processing techniques for the detection and removal of cracks in digitized paintings. *IEEE Transactions on Image Processing*, 15(1):178–188, Jan 2006.

[79] R. C. Gonzalez and R. E. Woods. *Digital Image Processing*. Prentice-Hall, Inc., Upper Saddle River, NJ, USA, 3rd edition, 2006.

[80] R. W. Hamming. Error detecting and error correcting codes. *Bell System Technical Journal*, 29(2):147–160, 1950.

[81] J. Y. Hardeberg, S. George, F. Deger, I. Baarstad, and J. E. H. Palacios. Spectral scream: Hyperspectral image acquisition and analysis of a masterpiece. In T. Frøysaker, N. Streeton, H. Kutzke, B. Topalova-Casadiego, and F. Hanssen-Bauer, editors, *Public paintings by Edvard Munch and some of his contemporaries. Changes and conservation challenges.* Archetype Publications, London, 2015.

[82] J. Hernández-Andrés, J. Romero, A. García-Beltrán, and J. L. Nieves. Testing linear models on spectral daylight measurements. *Appl. Opt.*, 37(6):971–977, Feb 1998.

[83] J. Herranz, J. Nin, and M. Sole. Optimal symbol alignment distance: A new distance for sequences of symbols. *IEEE Transactions on Knowledge and Data Engineering*, 23(10):1541–1554, Oct 2011.

[84] P. Howarth and S. Rüger. Fractional distance measures for content-based image retrieval. In D. E. Losada and J. M. Fernández-Luna, editors, *Advances in Information Retrieval*, volume 3408 of *Lecture Notes in Computer Science*, pages 447–456. Springer Berlin Heidelberg, 2005.

[85] H. Jeffreys. An invariant form for the prior probability in estimation problems. *Proceedings of the Royal Society of London A: Mathematical, Physical and Engineering Sciences*, 186(1007):453–461, 1946.

[86] Z. Ji, H. Liao, X. Zhang, and Q. H. Wu. Simple and efficient soft morphological filter in periodic noise reduction. In *TENCON 2006 - 2006 IEEE Region 10 Conference*, pages 1–4, Nov 2006.

[87] L. Joyeux, O. Buisson, B. Besserer, and S. Boukir. Detection and removal of line scratches in motion picture films. In *Computer Vision and Pattern Recognition, 1999. IEEE Computer Society Conference on.*, volume 1, page 553 Vol. 1, 1999.

[88] B. Justusson. Median filtering: Statistical properties. In *Two-Dimensional Digital Signal Processing II*, volume 43 of *Topics in Applied Physics*, pages 161–196. Springer Berlin Heidelberg, Jun 1981.

[89] A. C. Karaca, A. Ertürk, M. K. Güllü, M. Elmas, and S. Ertürk. Plastic waste sorting using infrared hyperspectral imaging system. In *Signal Processing and Communications Applications Conference (SIU), 2013 21st*, pages 1–4, Apr 2013.

[90] M. G. Kendall. Discrimination and classification. In *Multivariate analysis*, pages 165–185. Academic Press, New York, USA, 1966.

[91] T. Kinsman, M. Fairchild, and J. Pelz. Color is not a metric space implications for pattern recognition, machine learning, and computer vision. In *Image Processing Workshop (WNYIPW), 2012 Western New York*, pages 37–40, Nov 2012.

[92] V. Kober, M. Mozerov, and J. Álvarez-Borrego. *Automatic Removal of Impulse Noise from Highly Corrupted Images*, pages 34–41. Springer Berlin Heidelberg, Berlin, Heidelberg, 2005.

[93] M. Köppen and K. Franke. Pareto-dominated hypervolume measure: An alternative approach to color morphology. In *7th International Conference on Hybrid Intelligent Systems (HIS 2007)*, pages 234–239, Sep 2007.

[94] M. Köppen and K. Franke. *Fuzzy Morphologies Revisited*, pages 39–48. Springer London, London, 2000.

[95] M. Köppen and K. Franke. A color morphology based on pareto-dominance relation and hypervolume measure. *Conference on Colour in Graphics, Imaging, and Vision*, 2008(1):423–426, 2008.

[96] C. Kotropoulos and I. Pitas. Multichannel L filters based on marginal data ordering. *Signal Processing, IEEE Transactions on*, 42(10):2581–2595, Oct 1994.

[97] F. A. Kruse, A. B. Lefkoff, J. W. Boardman, K. B. Heidebrecht, A. T. Shapiro, P. J. Barloon, and A. F. H. Goetz. The spectral image processing system (SIPS) – interactive visualization and analysis of imaging spectrometer data. *Remote Sensing of Environment*, 44(2-3):145–163, 1993.

[98] S. Kullback and R. A. Leibler. On information and sufficiency. *The Annals of Mathematical Statistics*, 22(1):79–86, 1951.

[99] M. Kurdy and D. Jeulin. Directional mathematical morphology operations. *Acta Stereologica*, 8(2):473–480, 1989.

[100] Labsphere. Spectralon®Diffuse Reflectance Standards. `https://www.labsphere.com/`. Retrieved October 2016.

[101] G. N. Lance and W. T. Williams. Computer programs for hierarchical polythetic classification ("similarity analyses"). *The Computer Journal*, 9(1):60–64, 1966.

[102] A. Landstrom and M. J. Thurley. Morphology-based crack detection for steel slabs. *IEEE Journal of Selected Topics in Signal Processing*, 6(7):866–875, Nov 2012.

[103] A. Ledoux, N. Richard, and A. S. Capelle-Laizé. Color hit-or-miss transform (CMOMP). In *Signal Processing Conference (EUSIPCO), 2012 Proceedings of the 20th European*, pages 2248–2252, Aug 2012.

[104] A. Ledoux, N. Richard, and A.-S. Capelle-Laizé. How to specify or identify the most accurate multispectral distance function for mathematical morphology? In *Colour and Visual Computing Symposium (CVCS)*, pages 1–7, Sep 2013.

[105] A. Ledoux, N. Richard, and A.-S. Capelle-Laizé. Limitations et comparaisons d'ordonnancement utilisant des distances couleur. In *Atelier Traitement et Analyse des Images, Méthodes et Applications (TAIMA)*, Oct 2011.

[106] A. Ledoux, N. Richard, A.-S. Capelle-Laizé, and C. Fernandez-Maloigne. Perceptual color hit-or-miss transform: application to dermatological image processing. *Signal, Image and Video Processing*, 9(5):1081–1091, 2015.

[107] T. Lei, Y. Wang, G. Wang, and Y. Fan. Multivariate mathematical morphology based on fuzzy extremum estimation. *Image Processing, IET*, 8(9):548–558, Sep 2014.

[108] R. Lerallut, Étienne Decencière, and F. Meyer. Image filtering using morphological amoebas. *Image and Vision Computing*, 25(4):395–404, 2007. International Symposium on Mathematical Morphology 2005.

[109] V. I. Levenshtein. Binary codes capable of correcting deletions, insertions, and reversals. *Soviet Physics Doklady*, 10(8):707–710, 1966.

[110] O. Lezoray and A. Elmoataz. Nonlocal and multivariate mathematical morphology. In *Image Processing (ICIP), 2012 19th IEEE International Conference on*, pages 129–132, Sep 2012.

[111] O. Lezoray, A. Elmoataz, and C. Meurie. Mathematical morphology in any color space. In *Image Analysis and Processing Workshops, 2007. ICIAPW 2007. 14th International Conference on*, pages 183–187, Sep 2007.

[112] J. Lin. Divergence measures based on the shannon entropy. *IEEE Transactions on Information Theory*, 37(1):145–151, Jan 1991.

[113] D. Liu, J. Ma, D.-W. Sun, H. Pu, W. Gao, J. Qu, and X.-A. Zeng. Prediction of color and pH of salted porcine meats using visible and near-infrared hyperspectral imaging. *Food and Bioprocess Technology*, 7(11):3100–3108, Nov 2014.

[114] H. Liu, D. Song, S. Rüger, R. Hu, and V. Uren. Comparing dissimilarity measures for content-based image retrieval. In H. Li, T. Liu, W.-Y. Ma, T. Sakai, K.-F. Wong, and G. Zhou, editors, *Information Retrieval Technology*, volume 4993 of *Lecture Notes in Computer Science*, pages 44–50. Springer Berlin Heidelberg, 2008.

[115] P. Maragos and R. Schafer. Morphological filters–part i: Their set-theoretic analysis and relations to linear shift-invariant filters. *Acoustics, Speech and Signal Processing, IEEE Transactions on*, 35(8):1153–1169, Aug 1987.

[116] P. Maragos and R. Schafer. Morphological filters–part ii: Their relations to median, order-statistic, and stack filters. *Acoustics, Speech and Signal Processing, IEEE Transactions on*, 35(8):1170–1184, Aug 1987.

[117] J. Martin, J. Krueger, and D. Gareau. Hyperspectral imaging for melanoma screening. In *Proc. SPIE*, volume 8926, pages 892611–892611–7, 2014.

[118] K. Martinez. High resolution digital imaging of paintings: The Vasari project. *Microcomputers for Information Management*, 8(4):277–283, Dec 1991.

[119] G. Matheron. *Éléments pour une théorie des milieux poreux*. Masson, Paris, 1967.

[120] G. Matheron. *Random sets and integral geometry*. Wiley, New York, 1975.

[121] F. Meyer. Un algorithme optimal de ligne de partage des eaux. In *Reconnaisance des Formes et Intelligence Artificielle, 8e congrès*, pages 847–857, Lyon-Villeurbanne, 1991.

[122] S. K. Mitra and G. L. Sicuranza, editors. *Nonlinear Image Processing*. Communications, Networking and Multimedia. Elsevier Inc., 2001.

[123] T. Mohammadi Moghaddam, S. M. A. Razavi, and M. Taghizadeh. Applications of hyperspectral imaging in grains and nuts quality and safety assessment: a review. *Journal of Food Measurement and Characterization*, 7(3):129–140, Aug 2013.

[124] K. Møllersen, J. Y. Hardeberg, and F. Godtliebsen. Divergence-based colour features for melanoma detection. In *Colour and Visual Computing Symposium (CVCS), 2015*, pages 1–6, Aug 2015.

[125] M. S. Nair, K. Revathy, and R. Tatavarti. Removal of salt-and pepper noise in images: a new decision-based algorithm. In *International MultiConference of Engineers and Computer Scientists (IMECS)*, volume I, 2008.

[126] K. Nallaperumal, J. Varghese, S. Saudia, R. Selvakumar, K. Krishnaveni, and S. Vinsley. Selective switching median filter for the removal of salt amp; pepper impulse noise. In *Wireless and Optical Communications Networks, 2006 IFIP International Conference on*, pages 1–5, 2006.

[127] S. Naqvi, N. Gallagher, and E. Coyle. An application of median filters to digital television. In *Acoustics, Speech, and Signal Processing, IEEE International Conference on ICASSP '86.*, volume 11, pages 2451–2454, Apr 1986.

[128] Norsk Elektro Optikk AS. HySpex VNIR-1600. `http://www.hyspex.no/products/vnir_1600.php`. Retrieved October 2016.

[129] Norsk Elektro Optikk AS. HySpex VNIR-1800. `http://www.hyspex.no/products/vnir_1800.php`. Retrieved October 2016.

[130] K. J. Nowicki, C. S. Edwards, and P. R. Christensen. Removal of salt-and-pepper noise in THEMIS infrared radiance and emissivity spectral data of the martian surface. In *Hyperspectral Image and Signal Processing: Evolution in Remote Sensing (WHISPERS), 2013 5th Workshop on*, 2013.

[131] F. G. Ortiz Zamora, F. Torres-Medina, J. Lopez-Angulo, and S. Puente Mendez. Comparative study of vectorial morphological operations in different color spaces. In *Proc. SPIE*, volume 4572, pages 259–268, Oct 2001.

[132] J. Overpeck, T. Webb, and I. Prentice. Quantitative interpretation of fossil pollen spectra: Dissimilarity coefficients and the method of modern analogs. *Quaternary Research*, 23(1):87–108, 1985.

[133] J. Pastor-Pellicer, M. Z. Afzal, M. Liwicki, and M. J. Castro-Bleda. Complete system for text line extraction using convolutional neural networks and watershed transform. In *2016 12th IAPR Workshop on Document Analysis Systems (DAS)*, pages 30–35, Apr 2016.

[134] L. Peng, W. Chao, L. Shuangmiao, and F. Baocai. Research on crack detection method of airport runway based on twice-threshold segmentation. In *2015 Fifth International Conference on Instrumentation and Measurement, Computer, Communication and Control (IMCCC)*, pages 1716–1720, Sep 2015.

[135] R. Pike, G. Lu, D. Wang, Z. G. Chen, and B. Fei. A minimum spanning forest-based method for noninvasive cancer detection with hyperspectral imaging. *IEEE Transactions on Biomedical Engineering*, 63(3):653–663, Mar 2016.

[136] I. Pitas and P. Tsakalides. Multivariate ordering in color image filtering. *Circuits and Systems for Video Technology, IEEE Transactions on*, 1(3):247–259, 295–6, Sep 1991.

[137] I. Pitas and A. Venetsanopoulos. Order statistics in digital image processing. *Proceedings of the IEEE*, 80(12):1893–1921, Dec 1992.

[138] I. Pitas. Marginal order statistics in color image filtering. *Optical Engineering*, 29(5):495–503, 1990.

[139] A. Plaza, P. Martinez, J. Plaza, and R. Perez. Dimensionality reduction and classification of hyperspectral image data using sequences of extended morphological transformations. *IEEE Transactions on Geoscience and Remote Sensing*, 43(3):466–479, Mar 2005.

[140] A. Plaza, P. Martinez, R. Perez, and J. Plaza. A new approach to mixed pixel classification of hyperspectral imagery based on extended morphological profiles. *Pattern Recognition*, 37(6):1097–1116, Jun 2004.

[141] W. K. Pratt. *Digital Image Processing*. John Wiley & Sons, Inc., New York, NY, USA, 1978.

[142] J. Puzicha, T. Hofmann, and J. M. Buhmann. Non-parametric similarity measures for unsupervised texture segmentation and image retrieval. In *Computer Vision and Pattern Recognition, 1997. Proceedings., 1997 IEEE Computer Society Conference on*, pages 267–272, Jun 1997.

[143] S.-E. Qian and G. Chen. A new nonlinear dimensionality reduction method with application to hyperspectral image analysis. In *Geoscience and Remote Sensing Symposium, 2007. IGARSS 2007. IEEE International*, pages 270–273, Jul 2007.

[144] A. Ribés, F. Schmitt, R. Pillay, and C. Lahanier. Calibration and spectral reconstruction for CRISATEL: An art painting multispectral acquisition system. *Journal of Imaging Science and Technology*, 49(6):563–573, Nov 2005.

[145] N. Richard, D. Helbert, C. Olivier, and M. Tamisier. Pseudo-divergence and bidimensional histogram of spectral differences for hyperspectral image processing. *Journal of Imaging Science and Technology*, 60(5):50402–1–50402–13, Sep 2016.

[146] J.-F. Rivest, P. Soille, and S. Beucher. Morphological gradients. *Journal of Electronic Imaging*, 2(4):326–336, Oct 1993.

[147] C. Rodarmel and J. Shan. Principal component analysis for hyperspectral image classification. *Surveying and Land Information Systems*, 62(2):115–122, 2002.

[148] S. T. Roweis and L. K. Saul. Nonlinear dimensionality reduction by locally linear embedding. *Science*, 290(5500):2323–2326, Dec 2000.

[149] Y. Rubner, C. Tomasi, and L. Guibas. The earth mover's distance as a metric for image retrieval. *International Journal of Computer Vision*, 40(2):99–121, 2000.

[150] T. Ružić, B. Cornelis, L. Platiša, A. Pižurica, A. Dooms, W. Philips, M. Martens, M. De Mey, and I. Daubechies. Virtual restoration of the ghent altarpiece using crack detection and inpainting. In *Advanced Concepts for Intelligent Vision Systems*, volume 6915 of *Lecture Notes in Computer Science*, pages 417–428. Springer Berlin Heidelberg, 2011.

[151] A. Sáez, J. Sánchez-Monedero, P. A. Gutiérrez, and C. Hervás-Martínez. Machine learning methods for binary and multiclass classification of melanoma thickness from dermoscopic images. *IEEE Transactions on Medical Imaging*, 35(4):1036–1045, Apr 2016.

[152] A. Schneider, G. Gonnet, and G. Cannarozzi. SynPAM–a distance measure based on synonymous codon substitutions. *IEEE/ACM Transactions on Computational Biology and Bioinformatics*, 4(4):553–560, Oct 2007.

[153] M. A. Schulze. An edge-enhancing nonlinear filter for reducing multiplicative noise. *Proc. SPIE*, 3026:46–56, 1997.

[154] J. Serra. *Image Analysis and Mathematical Morphology*, volume I. Academic Press, Inc., London, 1982.

[155] J. Serra. Alternating sequential filters. In *Image analysis and mathematical morphology*, volume II: Theoretical Advances, chapter 10, pages 203–214. Academic Press, 1988.

[156] J. Serra, editor. *Image Analysis and Mathematical Morphology*, volume II: Theoretical Advances. Academic Press, London, 1988.

[157] A. G. Silva, M. S. Fouto, A. T. d. Silva, R. Arthur, A. M. Arthur, Y. Iano, and J. M. L. d. Faria. Segmentation of foveal avascular zone of the retina based on morphological alternating sequential filtering. In *2015 IEEE 28th International Symposium on Computer-Based Medical Systems*, pages 38–43, Jun 2015.

[158] C. B. Singh, D. S. Jayas, J. Paliwal, and N. D. White. Identification of insect-damaged wheat kernels using short-wave near-infrared hyperspectral and digital colour imaging. *Computers and Electronics in Agriculture*, 73(2):118–125, Aug 2010.

[159] P. Soille. *Morphological Image Analysis: Principles and Applications*. Springer-Verlag New York, Inc., Secaucus, NJ, USA, 2 edition, 2003.

[160] Y. Song, Y. Han, J.-S. Oh, and S. Lee. Edge preserving impulse noise reduction. *Journal of Imaging Science and Technology*, 57(6):60507–1–60507–8, Nov 2013.

[161] T. Sørensen. *A method of establishing groups of equal amplitude in plant sociology based on similarity of species content and its application to analyses of the vegetation on Danish commons*, volume 5 of *Kongelige Danske videnskabernes selskab.; Biologiske skrifter*. I kommission hos E. Munksgaard, Kopenhagen, 1948.

[162] G. S. Spagnolo and F. Somma. Virtual restoration of cracks in digitized image of paintings. *Journal of Physics: Conference Series*, 249(1):012059, 2010.

[163] S. R. Sternberg. Grayscale morphology. *Computer Graphics and Image Processing*, 35(3):333–355, Sep 1986.

[164] W. Sun, A. Halevy, J. J. Benedetto, W. Czaja, C. Liu, H. Wu, B. Shi, and W. Li. UL-Isomap based nonlinear dimensionality reduction for hyperspectral imagery classification. *ISPRS Journal of Photogrammetry and Remote Sensing*, 89:25–36, 2014.

[165] J. Sweet, J. Granahah, and M. H. Sharp. An objective standard for hyperspectral image quality. In *9th AVIRIS Earth Science Workshop*, Pasadena, CA, 2000.

[166] D. Talukdar and R. Acharya. Estimation of fractal dimension using alternating sequential filters. In *Image Processing, 1995. Proceedings., International Conference on*, volume 1, pages 231–234, Oct 1995.

[167] T. Tao. *An Introduction to Measure Theory*. American Mathematical Society, 2011.

[168] Y. W. Teh and S. T. Roweis. Automatic alignment of hidden representations. In *Advances in Neural Information Processing Systems*, volume 15, pages 841–848. MIT Press, 2002.

[169] K. Tempfli, N. Kerle, G. C. Huurneman, and L. L. F. Janssen, editors. *Principles of Remote Sensing*. The International Institute for Geo-Information Science and Earth Observation (ITC), Enschede, The Netherlands, 4 edition, 2009.

[170] J. B. Tenenbaum, V. de Silva, and J. C. Langford. A global geometric framework for nonlinear dimensionality reduction. *Science*, 290(5500):2319–2323, 2000.

[171] The Joint Committee for Guides in Metrology (JCGM). International vocabulary of metrology – Basic and general concepts and associated terms. Technical report, 2012.

[172] S. G. Tyan. Median filtering: Deterministic properties. In *Two-Dimensional Digital Signal Processing II*, volume 43 of *Topics in Applied Physics*, pages 197–217. Springer Berlin Heidelberg, 1981.

[173] L. J. van Vliet, I. T. Young, and G. L. Beckers. A nonlinear laplace operator as edge detector in noisy images. *Computer Vision, Graphics, and Image Processing*, 45(2):167–195, 1989.

[174] M. A. Veganzones and M. Graña. Lattice auto-associative memories induced supervised ordering defining a multivariate morphology on hyperspectral data. In *Hyperspectral Image and Signal Processing: Evolution in Remote Sensing (WHISPERS), 2012 4th Workshop on*, pages 1–4, Jun 2012.

[175] S. Velasco-Forero and J. Angulo. Multiclass ordering for filtering and classification of hyperspectral images. In *Hyperspectral Image and Signal Processing: Evolution in Remote Sensing (WHISPERS), 2011 3rd Workshop on*, pages 1–4, Jun 2011.

[176] S. Velasco-Forero and J. Angulo. Supervised ordering in $\mathbb{R}^p$: Application to morphological processing of hyperspectral images. *IEEE Transactions on Image Processing*, 20(11):3301–3308, Nov 2011.

[177] S. Velasco-Forero and J. Angulo. Random projection depth for multivariate mathematical morphology. *Selected Topics in Signal Processing, IEEE Journal of*, 6(7):753–763, Nov 2012.

[178] C. Vertan, V. Popescu, and V. Buzuloiu. Morphological like operators for color images. In *8th European Signal Processing Conference (EUSIPCO)*, pages 165–168, 1996.

[179] D.-h. Wang, X.-k. Yang, and Y. Zhao. A hyperspectral image endmember extraction algorithm based on generalized morphology. *Optoelectronics Letters*, 10(5):387–390, 2014.

[180] G. Wang, Y. Wang, H. Li, X. Chen, H. Lu, Y. Ma, C. Peng, Y. Wang, and L. Tang. Morphological background detection and illumination normalization of text image with poor lighting. *PLoS ONE*, 9(11):1–22, Nov 2014.

[181] X. Wang. Multiscale median filter for image denoising. In *Signal Processing (ICSP), 2010 IEEE 10th International Conference on*, pages 2617–2620, Oct 2010.

[182] K. R. Weber and S. T. Acton. On connected filters in color image processing. *Journal of Electronic Imaging*, 13(3):619–629, Jul 2004.

[183] Wikimedia Commons. EM spectrum. `https://commons.wikimedia.org/wiki/File:EM_spectrum.svg`. Retrieved July 2016.

[184] S. Wilczyński, R. Koprowski, M. Marmion, P. Duda, and B. Błońska-Fajfrowska. The use of hyperspectral imaging in the VNIR (400-1000 nm) and SWIR range (1000-2500 nm) for detecting counterfeit drugs with identical API composition. *Talanta*, 160:1–8, Nov 2016.

[185] D. Wu, S. Wang, N. Wang, P. Nie, Y. He, D.-W. Sun, and J. Yao. Application of time series hyperspectral imaging (TS-HSI) for determining water distribution within beef and spectral kinetic analysis during dehydration. *Food and Bioprocess Technology*, 6(11):2943–2958, Nov 2013.

[186] T.-S. Yan, X.-H. Hu, H.-M. Li, and J.-W. Zhou. Online detection of glass bottle crack based on evolutionary neural network and computer vision. In *Consumer Electronics, Communications and Networks (CECNet), 2012 2nd International Conference on*, pages 418–421, Apr 2012.

[187] H. Yang, Q. Du, and G. Chen. Unsupervised hyperspectral band selection using graphics processing units. *Selected Topics in Applied Earth Observations and Remote Sensing, IEEE Journal of*, 4(3):660–668, Sep 2011.

[188] H. Yang, Q. Du, and G. Chen. Particle swarm optimization-based hyperspectral dimensionality reduction for urban land cover classification. *Selected Topics in Applied Earth Observations and Remote Sensing, IEEE Journal of*, 5(2):544–554, Apr 2012.

[189] C.-W. Yeh and D. Pycock. Similarity colour morphology. In *Computer Science and Electronic Engineering Conference (CEEC), 2013 5th*, pages 71–76, Sep 2013.

[190] A. Zare and P. Gader. Hyperspectral band selection and endmember detection using sparsity promoting priors. *Geoscience and Remote Sensing Letters, IEEE*, 5(2):256–260, Apr 2008.

[191] W. Zhang, Z. Zhang, D. Qi, and Y. Liu. Automatic crack detection and classification method for subway tunnel safety monitoring. *Sensors*, 14(10):19307–19328, Oct 2014.